

# UC Berkeley

## UC Berkeley Electronic Theses and Dissertations

### Title

Leveraging *Xenopus* frog species to study architectural diversity of the mitotic spindle and mechanisms underlying hybrid inviability

### Permalink

<https://escholarship.org/uc/item/1bq8h77f>

### Author

Kitaoka, Maiko

### Publication Date

2022

Peer reviewed|Thesis/dissertation

Leveraging *Xenopus* frog species to study architectural diversity of the mitotic spindle  
and mechanisms underlying hybrid inviability

By

Maiko Kitaoka

A dissertation submitted in partial satisfaction of the

requirements for the degree of

Doctor of Philosophy

in

Molecular and Cell Biology

in the

Graduate Division

of the

University of California, Berkeley

Committee in charge:

Professor Rebecca Heald, Chair  
Associate Professor Dirk Hockemeyer  
Professor Gary H. Karpen  
Professor Rasmus Nielsen

Spring 2022

Leveraging *Xenopus* frog species to study architectural diversity of the mitotic spindle  
and mechanisms underlying hybrid inviability

Copyright 2022  
by  
Maiko Kitaoka

## Abstract

Leveraging *Xenopus* frog species to study architectural diversity of the mitotic spindle and mechanisms underlying hybrid inviability

by

Maiko Kitaoka

Doctor of Philosophy in Molecular and Cell Biology

University of California, Berkeley

Professor Rebecca Heald, Chair

Cell division is crucial to life. Across all eukaryotes, this dramatic and complex process relies on the mitotic spindle to segregate chromosomes faithfully into new daughter cells, ensuring the health and survival of the next generation. Despite its conserved components and universal function of transmitting a complete genome, the cell division machinery, including the central mitotic spindle, varies widely across the tree of life in size and morphology. Interestingly, chromosome segregation defects, genome elimination, and embryonic lethality are frequently observed upon hybridization of closely related species. However, whether and how divergent cell division machinery leads to functional defects is unknown. This dissertation is comprised of four projects that span comparative evolutionary, cell, and developmental biology to examine the basis and consequences of divergent cell division machineries by using *X. laevis*, *X. tropicalis*, and *X. borealis* frogs. I develop the use of *X. borealis* to understand divergence in spindle assembly mechanisms and examine how spindle architecture varies even among closely related frog species. I adapt expansion microscopy for *Xenopus* extract systems, combining an unparalleled in vitro physiological reconstitution system with high-resolution imaging to measure and dissect microtubule organization to better define spindle morphometrics. We leverage the full power of the *Xenopus* systems to establish the most tractable vertebrate model for investigating the cellular and molecular mechanisms underlying hybridization outcomes, incompatibility, and genome elimination. Altogether, this work provides important molecular insight and understanding to mechanisms that contribute to spindle assembly and scaling, hybrid inviability, and speciation.

## **Dedication**

To those who struggle because there are limits.  
Take advantage of what you have, and run the world.

# Table of Contents

Abstract	1
Dedication	i
Table of Contents	ii
List of Figures and Tables	iv
Acknowledgements	vi
<b>Chapter 1: Introduction</b>	<b>1</b>
1.1 Making the mitotic spindle	1
1.2 Pulling apart chromosomes from the centromere	2
1.3 Evolution of cell division machinery leads to speciation barriers	4
1.4 Powering the cell cycle with the <i>Xenopus</i> egg extract	5
1.5 <i>Xenopus</i> interspecies comparisons reveal molecular mechanisms of intracellular scaling and evolutionary divergence	6
1.6 <i>Xenopus</i> hybrids provide cell biological insight into mechanisms of size control, species barriers, genome evolution, and reproductive isolation	7
<b>Chapter 2: Spindle assembly in egg extracts of the Marsabit clawed frog, <i>X. borealis</i></b>	<b>11</b>
2.1 Abstract	11
2.2 Introduction	12
2.3 Results	14
2.4 Discussion	34
2.5 Methods	35
<b>Chapter 3: Ultrastructure expansion microscopy of <i>Xenopus</i> egg extract spindles</b>	<b>41</b>
3.1 Abstract	41
3.2 Introduction	42
3.3 Results	45
3.4 Discussion	53
3.5 Methods	55
<b>Chapter 4: Paternal chromosome loss and metabolic crisis contribute to hybrid inviability in <i>Xenopus</i></b>	<b>59</b>
4.1 Abstract	59
4.2 Results and Discussion	60
4.3 Methods	80
<b>Chapter 5: Molecular conflicts disrupting centromere assembly contribute to <i>Xenopus</i> hybrid inviability</b>	<b>89</b>
5.1 Abstract	89
5.2 Introduction	90
5.3 Results	92

5.4	Discussion	112
5.5	Methods	114
<b>Chapter 6: Conclusions</b>		<b>121</b>
<b>References</b>		<b>126</b>

## List of Figures and Tables

### Chapter 1: Introduction

Figure 1.1. <i>Xenopus</i> hybrid crosses are asymmetric, depending on which species provides the egg vs. sperm	9
---	---

### Chapter 2: Spindle assembly in egg extracts of the Marsabit clawed frog, *X. borealis*

Figure 2.1. Characterization of the Marsabit clawed frog, <i>X. borealis</i>	14
Figure 2.2. <i>X. borealis</i> sperm nuclei length comparison and quantification	16
Figure 2.3. <i>X. borealis</i> egg extracts at a glance	17
Figure 2.4. <i>X. borealis</i> CSF egg extracts reconstitute spindle assembly	19
Figure 2.5. Analysis of <i>X. borealis</i> cycled spindles	20
Figure 2.6. Analysis of <i>X. borealis</i> CSF spindle properties	22
Figure 2.7. Sensitivity of <i>X. borealis</i> spindles to perturbation of the RanGTP gradient	23
Figure 2.8. Titration of <i>X. borealis</i> egg extract with other <i>Xenopus</i> egg extracts	26
Figure 2.9. Effects of cytoplasmic mixing on microtubule distribution	27
Figure 2.10. Localization of XMAP215 on <i>X. borealis</i> spindles	29
Figure 2.11. Localization of scaling factors katanin and TPX2 on <i>X. borealis</i> spindles	30
Figure 2.12. Protein sequence alignments of <i>Xenopus</i> katanin	32
Figure 2.13. Protein sequence alignments of <i>Xenopus</i> TPX2	33
Table 2.1. Ran perturbation phenotypes	25

### Chapter 3: Ultrastructure expansion microscopy of *Xenopus* egg extract spindles

Figure 3.1. Workflow for expansion of <i>Xenopus</i> egg extract spindle samples	46
Figure 3.2. Comparison of expansion factors and microtubule distribution between different expansion protocols	48
Figure 3.3. Evaluation of the expansion-induced deformations between the different protocols	49
Figure 3.4. Our adapted U-ExM protocol can faithfully maintain the structure of an intact <i>X. laevis</i> egg extract spindle	50
Figure 3.5. Expansion microscopy can increase resolution of centromere puncta	51

### Chapter 4: Paternal chromosome loss and metabolic crisis contribute to hybrid inviability in *Xenopus*

Figure 4.1. Role of the <i>X. laevis</i> genome in $t_e \times l_s$ hybrid embryo death	61
Figure 4.2. Occurrence of micronuclei, role of ploidy and spindle architecture	63
Figure 4.3. Compatibility of <i>X. laevis</i> chromosomes with <i>X. tropicalis</i> cytoplasm	65
Figure 4.4. Characterization of micronuclei in $t_e \times l_s$ hybrid embryos and link to embryo death	66



Figure 4.5. Gene expression and metabolic changes preceding $t_e \times l_s$ hybrid embryo death	69
Figure 4.6. Whole genome sequencing of $tt_e \times l_s$ rescued embryos and metabolic profiling of $t_e \times l_s$ and $t_e \times b_s$ hybrid embryos	71
Figure 4.7. Chromosomal loss in exogastrulating $t_e \times b_s$ hybrid embryos	77
Figure 4.8. Characterization of micronuclei in $t_e \times b_s$ hybrid embryos	78
Table 4.1. Embryonic development in <i>Xenopus</i> haploids and cybrids generated from <i>X. tropicalis</i> irradiated eggs	61
Table 4.2. Effects of drug treatments on $t_e \times t_s$ embryos	68
Table 4.3. Sub-genome distribution of lost compared to retained DNA in $t_e \times l_s$ , $tt_e \times l_s$ , and $t_e \times b_s$ hybrids	72
Table 4.4. Chromosome distribution of lost vs. remaining DNA in $t_e \times l_s$ , $tt_e \times l_s$ , and $t_e \times b_s$ hybrids	73
Table 4.5. Overrepresentation test of all or metabolism-only 3L and 4L lost genes	76
<b>Chapter 5: Molecular conflicts disrupting centromere assembly contribute to <i>Xenopus</i> hybrid inviability</b>	
Figure 5.1. Comparison of <i>X. laevis</i> , <i>X. tropicalis</i> , and <i>X. borealis</i> core centromere sequences	93
Figure 5.2. Comparison of centromere DNA and CENP-A protein sequences	94
Figure 5.3. Loss of centromeric CENP-A is cell cycle-dependent	95
Figure 5.4. CENP-A is lost from <i>X. laevis</i> chromosomes 3L and 4L	96
Figure 5.5 Driving CENP-A assembly rescues centromere localization in interphase, which persists on mitotic <i>X. laevis</i> , but not on <i>X. borealis</i> chromosomes	99
Figure 5.6 Driving CENP-A assembly with proteins expressed in reticulocyte lysate	100
Figure 5.7 Mitotic replication stress leads to <i>X. borealis</i> centromere and chromosome morphology defects	102
Figure 5.8 Characterization of chromosome morphology defects that can be induced by aphidicolin and rescued by p97 inhibition	103
Figure 5.9 Replication-transcription conflicts at rDNA on <i>X. borealis</i> chromosomes can be rescued by inhibiting RNA Pol I	105
Figure 5.10 Pol I transcription inhibition does not affect <i>X. tropicalis</i> or <i>X. laevis</i> chromosomes, while Pol III inhibition had no effect on any species	107
Figure 5.11 Treatments that rescue CENP-A localization in egg extracts reduce micronuclei formation in hybrid embryos, but inviability persists	108
Figure 5.12 Microinjection with reticulocyte lysate does not affect embryo development or chromosome segregation.	109

## Acknowledgements

I am very thankful to many people in my life who challenged me, believed in me, pushed me to re-examine myself and my science, and overall made my PhD experience so unique. I have grown and learned immensely as a scientist, colleague, and member of society. This entire thesis grew out of collaborations and conversations with so many people, and I am grateful to all of you for helping me to survive and flourish.

Thank you, firstly, to Rebecca Heald. Thank you for being an unfailingly positive and encouraging mentor, happy to hear from me even when the updates were not good, and willing to spend a significant portion of your energy and time with me. More than anyone else, you believed in me, trusted me, and advocated for me at every step. You have given me so many opportunities, freedom, and lessons in your lab, scientifically and personally. Thank you for demonstrating every single day that kindness is not only possible in science but the best path forward. I am a more thoughtful, kinder scientist because of you and my experiences with you.

I have learned that my favorite part of science is the incredible, brilliant people I get to talk to, about both experiments and life. I've been extremely fortunate and grateful to collaborate with Owen Smith and Aaron Straight throughout most of my PhD – thank you for always answering my (many) questions, I have always walked away from our conversations with a smile. Though I cannot list everyone here, I am thankful to all the people I've met and talked to at various meetings – thank you for your critiques and new angles, for posing questions that made me sink into various rabbit holes, and for making a young, very green graduate student scientist feel as though she was doing ok amongst the more seasoned crowd of postdocs and PIs. Thank you to my thesis committee, Gary Karpen, Dirk Hockemeyer, and Rasmus Nielsen, for advice and guidance when I needed it most. I must give a special shout-out to Gary for being a much-needed expert on centromeres, and for teaching me by example to be skeptical and ask many questions. I'd also like to thank Sylvia Erhardt, Iain Cheeseman, and Sam Corless – organizing a conference together for 4 years (unexpectedly) has been a large part of my PhD, and I'm so grateful to do it with such lovely, kind people. I'd especially like to acknowledge Iain for becoming another mentor to me, after unintentionally being in the same circles from my undergraduate days to today. I am blown away by your wisdom, boundless enthusiasm, and generosity.

I would never have made it to Berkeley, and I would not be a scientist if not for Terry Orr-Weaver and the TOW Zone. Thank you, Terry, for giving me a chance as an undergraduate after a cold email – I didn't know it fully at the time, but the opportunity and mentoring from you were invaluable. Special thanks to my postdoc mentor, Boryana Petrova, for fostering my nascent experimental hands, and to Brian Hua, Jessie Von Stetina, Emir Avilés-Pagán, Laura Frawley, Jess Alexander, Masatoshi Hara, Iva Kronja, and Jared Nordman for making the TOW Zone my first scientific home and forever family.

Thank you to all of the Healdies that I've had the pleasure of overlapping with in the lab – all of you have made me a better scientist, friend, and colleague every single

day, and words do not describe how fondly I will cherish all of our experiences and antics on the 3<sup>rd</sup> floor of LSA. I thank Romain Gibeaux for immediately taking me under his wing and kickstarting my PhD experiments from my rotation, and continuing to be a friend, collaborator, and mentor since then. I have had the best bay mate ever in Kelly Miller – thank you for making me look forward to every day in the lab because you were around, for gushing with me about musicals, and instilling your love and wisdom for frogs to all of us. To Mina Sun, Ambika Nadkarni, Coral Zhou, and Helena Cantwell, I have been eternally grateful for your postdoc advice, perspectives, and excellent examples. While our lab may be postdoc-heavy most of the time, I have to thank Guadalupe Sepulveda-Peña for being my grad student companion and buddy for several years. To Lupe Coy, thank you for making sure our lab stayed functional, but also for being a warm presence to talk to in the quieter morning hours. Lastly to everyone else that I have had the immense fortune of calling my lab mate: Andrew Grenfell, Xiao Zhou, Chris Brownlee, Elizabeth Earley, Tracy Lou, Christian Erikson, Justin Peng, Clotilde Cadart, Xiao Liu, Martin Liu, Cordell Clark, and Megan Onyundo. I'm very thankful to have met, worked with, and know all of you; thank you for our many conversations and laughter. Lastly, thank you to our frogs and facility managers – none of this would be possible without you!

My friends from MCB, especially my 2016 cohort: you are all amazing, and I'm so lucky to have been a part of this fantastic, talented group of people throughout graduate school. I am especially thankful to have made some life-long friends here. To Jack, Jana, Josh, and Andrea – I'm so happy JJJAMM has grown and flourished from our row in MCB 200. Thank you, Andrea, for consistent, weekly cups of tea that served as an excellent release valve when necessary, but usually were just a fun excuse to take a mental break in the sunshine. I also have to credit you with getting me started with cross-stitch! Jana, for inspiring my DIY habits further, making me laugh in the middle of sentences, and always being willing to drive us all around. Josh, for your spicy hot takes. Jack, for your boisterous energy that always brings me out of my shell. JJJAMM hangouts and Dairy gals' nights are a highlight, thank you all!

Thesis acknowledgements would not be complete without mentioning family. Mine is small but more than enough. Thank you, Eiko and Hisaya, and Christiane, John, and Nicole for the constant support.

Finally, thank you to my partner, Mark J. Khoury. Graduate school would be a different world without you, and I'm so happy we did this together and independently. Thank you for being the brave one, for being there when everything fell apart, and for helping me put it all back together again and again. You're the one I always turn to, and your capacity for knowledge, reason, and patience never ceases to astound me. Thank you for being the best friend and partner-in-crime for all of our adventures in and out of the lab. I can't wait for more.

# Chapter 1

## Introduction

Cell division is a fundamental and crucial process in all eukaryotes with the central goal of accurately distributing the DNA blueprint encoded on chromosomes to two new daughter cells. During this process, the cell reorganizes dramatically to assemble a mitotic spindle from thousands of microtubules, condense chromosomes to package the genetic information and attach it to the spindle, which then physically pulls replicated chromosomes apart so that each daughter cell receives a complete set. Errors in cell division lead to loss or rearrangements of genetic material and serious downstream consequences that impair gene expression, cellular physiology, and cause disease and lethality (Holland and Cleveland, 2012). Thus, understanding the carefully orchestrated choreography of molecules and structures involved in this cellular dance and its conservation across species is of great interest and importance.

### 1.1 Making the mitotic spindle

At the center of this process is the mitotic spindle, a highly dynamic, self-organizing, microtubule-based macromolecular apparatus. First observed in the late 1800s by Walter Flemming (Flemming, 1882), it remains a central focus for researchers due to its complexity and importance in cellular function, physiology, and viability. The spindle consists of thousands of microtubules, long filamentous polymer “cables” made up of arrays of tubulin dimers. These cables self-organize into a bipolar, football-shaped structure with two focused poles. An extensive array of microtubule-associated proteins including molecular motors, as well as non-protein components like RNA (Blower et al., 2007; Grenfell et al., 2016a; Chang et al., 2004), work together to build the spindle, integrate complex spatial information and cellular signals, and generate the force necessary to physically separate replicated sister chromatids to daughter cells synchronously (Petry, 2016; Elting et al., 2018).

Three main populations of microtubules make up the spindle. Kinetochore or k-fibers attach to mitotic chromosomes so that the kinetochores of replicated sister chromatids are connected to opposite spindle poles, directly facilitating the spindle’s key function (McDonald et al., 1992). Spindle, or interpolar, microtubules are densely packed and bundled in overlapping antiparallel arrays throughout the spindle for structural integrity and stability (Mastronarde et al., 1993). Finally, astral microtubules emanate outwards from the centrosomes at spindle poles away from the metaphase plate and towards the cell cortex. This provides the force and cues necessary for spindle orientation, particularly in asymmetric divisions that are important for cell fate and differentiation (Grill et al., 2003). Interestingly, astral microtubules are not found in most meiotic spindles (Crowder et al., 2015). Microtubules are nucleated through two main pathways: via centrosomes and chromatin. Centrosomes are the microtubule organizing centers, typically found at the spindle poles, that generate new microtubule assembly by recruiting and activating the template  $\gamma$ -tubulin (Mitchison and Kirschner, 1984a; Zheng et al., 1995). The second pathway, chromatin-mediated microtubule nucleation, relies on the RanGTP gradient generated by RCC1 (Regulator of Chromosome Condensation 1),

a guanine nucleotide exchange factor, around mitotic chromosomes. This gradient causes release of spindle assembly factors from importins around the mitotic chromatin, leading to microtubule nucleation and stabilization (Cavazza and Vernos, 2016; Kalab and Heald, 2008). Remarkably, microtubules nucleated around DNA- or RCC1-coated beads are capable of self-organizing into a bipolar spindle structure in the complete absence of kinetochores and centrosomes (Heald et al., 1996; Halpin et al., 2011).

Accurate cell division and faithful chromosome segregation are essential for organismal health, physiology, and survival over generations, and the cellular machinery devoted to this process is highly conserved. Even so, the principle macromolecular structure of cell division, the mitotic spindle, adapts to the cellular environment and varies dramatically among different cell types and sizes, and across the tree of life (Crowder et al., 2015). How do the components of the mitotic spindle, especially its main microtubule network, create morphologically distinct spindles? How does this architecture lend itself to the essential function of the spindle to accurately pull apart chromosomes? What evolutionary or cellular forces drive these distinctions to create “specialized” spindles across species and cell types? Previous biochemical, genetic, and sequencing data have provided a nearly complete parts list necessary to assemble the spindle and facilitate chromosome segregation, and cell biological investigations have assessed spindle morphometrics at a whole-structure, micron-level scale (Helmke et al., 2013; Petry, 2016). However, we currently lack an understanding of how features of microtubule dynamics, bundling, and motor-dependent movements relate to spindle function and how its structure is tailored according to cell type, fate, size, shape, and species. The development and application of new computational analysis methods and high-resolution imaging technologies, such as super-resolution techniques, expansion microscopy, focused ion beam electron microscopy and tomography, among others, to a wide variety of model systems and cell types will test current models, measurements, and predictions and provide a new window into the spindle’s parts, architectures, and function.

## **1.2 Pulling apart chromosomes from the centromere**

During cell division, the genome undergoes a dramatic remodeling process as the interphase nuclear DNA transforms into highly compact, condensed mitotic chromosomes. Packaging the genome into these rod-shaped structures facilitates the genome’s accurate segregation and partitioning into the resulting two daughter cells, as each chromosome resolves and can become physically attached to the spindle. This key interaction between chromosomes and microtubules occurs at the centromere, the epigenetically-defined recruitment center that specifies the assembly site for kinetochore proteins to form the large complex necessary to attach to the spindle microtubules (Westhorpe and Straight, 2014; McKinley and Cheeseman, 2016). The centromere is specified epigenetically by the presence of a specific histone H3 variant, CENP-A (Earnshaw and Rothfield, 1985; Earnshaw and Migeon, 1985; Palmer et al., 1991; Guse et al., 2011; Mendiburo et al., 2011), which is required to localize nearly all other constitutive centromere associated network (CCAN) and kinetochore components to enable faithful mitotic chromosome segregation (Régnier et al., 2005; Foltz et al., 2006; Fachinetti et al., 2013). CENP-A chromatin is recognized by other centromere-specific

factors, including HJURP, CENP-C, and CENP-N, to maintain its location and function (Moree et al., 2011; Carroll et al., 2010; Falk et al., 2015; Pentakota et al., 2017; Chittori et al., 2018; Tian et al., 2018). Unlike other histones, new CENP-A deposition is uncoupled from DNA replication and is not replenished in S phase, instead being loaded onto chromatin during G1 (Jansen et al., 2007), and newly replicated sister chromatids progress through mitosis with half-maximal occupancy of CENP-A histones. This temporal control outside of S phase is conserved across multiple organisms (Jansen et al., 2007; Mellone et al., 2011; Shukla et al., 2018) and serves as one of many layered mechanisms in place to regulate CENP-A incorporation and preserve centromeric identity.

Paradoxically, despite their evolutionary conservation, essential function and importance, centromere DNA and associated protein sequences are rapidly evolving, even among closely related species (Henikoff et al., 2001; Malik and Henikoff, 2001; Cooper and Henikoff, 2004; Malik et al., 2002; Rosin and Mellone, 2016). Across species, there are various “flavors” of centromere protein networks, such that not every species relies predominantly on CENP-A. Most vertebrate and metacentric species, including humans, adopt a network of proteins comprised of the CENP-A nucleosome, CCAN, and KMN (Knl1/Mis12/Ndc80 complexes) proteins (Weir et al., 2016; Westhorpe and Straight, 2014). However, a miniaturized version of this network that includes only Cid, CAL1, and CENP-C, equivalent to the vertebrate CENP-A, HJURP/Mis18 complex, and CENP-C, respectively, is sufficient for centromere propagation and identity in *Drosophila* (Roure et al., 2019; Erhardt et al., 2008; Chen et al., 2014). Even more strikingly, insect species with holocentric chromosomes, such as Lepidoptera (butterflies and moths), have repeatedly lost CENP-A throughout evolution (Drinnenberg et al., 2014), and instead use a CENP-T-centric network to establish and maintain centromeric chromatin (Cortes-Silva et al., 2020). In an extreme example, the *Trypanosoma* family of kinetoplastids have CENP-A-independent centromeres and build kinetochores with evolutionarily distinct KKT proteins that do not resemble the canonical CCAN proteins (Akiyoshi and Gull, 2014).

The centromere thus provides a unique comparative window into the evolution of species due to its rapid divergence, co-evolution between proteins and DNA, and species-specific differences (Rosin and Mellone, 2016; Kumon et al., 2021). In addition to the variation of protein networks described above, CENP-A/Cid has undergone tissue-specific specialization, duplication, and divergence in many *Drosophila* species (Kursel and Malik, 2017; Kursel et al., 2021), and the regulation and interactions between centromeric proteins can differ between tissues within a single species, particularly in the germline where centromere maintenance and establishment becomes critically important for the fitness of the next generation (Raychaudhuri et al., 2012; Dunleavy and Collins, 2017; Swartz et al., 2019; Das et al., 2017). For example, unlike canonical histones, CENP-A is not exchanged for protamines during spermatogenesis, thus providing a template for centromere location in the next generation (Palmer et al., 1990; Milks et al., 2009; Dunleavy et al., 2012; Raychaudhuri et al., 2012). Centromere biology and dysfunction has also been implicated in various interspecies hybrids where the parental genomes are partially or completely eliminated (Fujiwara et al., 1997; Sakai et al., 2007; Sanei et al., 2011; Kuppuppu et al., 2015). How is the centromere directly or indirectly affected

in interspecies hybrids? Does centromere diversity contribute to speciation and reproductive barriers? Altogether, the centromere remains enigmatic in its regulation and diversity, but provides a phenomenal paradox to study by being both essential and conserved across species, as well as highly divergent and prone to dysfunction.

### 1.3 Evolution of cell division machinery leads to speciation barriers

The variation and diversity among key cell division machinery components can have profound effects on the evolution of new species as well as on species barriers. Following fertilization, multicellular organisms form a zygote that undergoes a unique period of development characterized by rapid cleavages, mitotic divisions that produce smaller cells without embryonic growth. These cleavage divisions are characterized by abbreviated cell cycles that include only DNA replication and mitosis with no gap phases or cell cycle checkpoints (Newport and Kirschner, 1984; Graham and Morgan, 1966; Clute and Masui, 1992), and the embryo relies primarily on stockpiled maternal resources. But what happens when two related species try to hybridize? Are their cellular mechanisms, especially in cell division, compatible with each other between the maternal and paternal species given their conserved but variable nature? How has evolution changed the proteins, sequences, and other various components involved in the first big events of an organism's life?

Classically, species are defined as reproductively isolated groups (Presgraves, 2010; Dobzhansky, 1937). Interspecies crosses give rise to progeny that are sterile or dead, and thus unable to pass on their genetic information to future generations. Both pre- and post-zygotic mechanisms contribute to reproductive isolation barriers, but mechanisms underlying these barriers are often difficult to study given that hybrids are genetic "dead ends" (Jagannathan and Yamashita, 2018). Hybridization can fail if the gametes from two different species are incompatible and incapable of fusing to generate the zygote and kickstart development, creating a pre-zygotic barrier. This is particularly useful for externally fertilizing organisms to prevent cross-species competition, but also saves the internally fertilizing organism from wasting the precious and costly investment of gametogenesis by forming an inviable hybrid. For this reason, fertilization is fundamental in sexual reproduction and species propagation over generations, and thus occupies a unique evolutionary paradigm whereby the mechanisms must be highly efficient and conserved, but species-specific (Gert and Pauli, 2020). Therefore, mismatches between egg and sperm are one method to ensure that species remain distinct. For example, recent work has shown that zebrafish, *Danio rerio*, encode a short, membrane-bound, maternal protein called Bouncer, which mediates sperm-egg binding and is essential for sperm entry into the zebrafish egg (Herberg et al., 2018). Cross-fertilization with the distantly-related medaka sperm leads to a robust pre-zygotic barrier, where zebrafish eggs cannot be fertilized. However, medaka sperm could fertilize zebrafish eggs expressing medaka Bouncer protein, though at a low efficiency, indicating that Bouncer is sufficient to mediate species-specificity of fertilization between fish species (Herberg et al., 2018). Importantly, fertilization factors identified in other species also demonstrate rapid evolutionary signatures, demonstrating the pressure to keep

interacting proteins from various species distinct from each other while the fundamental principles remain conserved (Gert and Pauli, 2020).

Even if cross-fertilization is feasible between species, hybridization of closely related species can lead to reduced hybrid fitness, lethality, and sterility through post-zygotic barriers, all of which drive reproductive isolation and speciation (Maheshwari and Barbash, 2011). Previous genetic work has uncovered a small number of hybrid incompatibility genes, with many of these studies relying on classical genetic mapping and viable hybrids (Maheshwari and Barbash, 2011). Interestingly, many experimental hybrids across systems demonstrate defects in genome organization and faulty chromosome segregation leading to parental genome elimination (Dion-Cote and Barbash, 2017). In many cases, only one parental genome is negatively affected (Fujiwara et al., 1997; Gernand et al., 2005; Sanei et al., 2011). Previous studies have implicated an important role for the centromere and surrounding chromatin environment, particularly in *Drosophila* and *Arabidopsis* hybrids (Ferree and Barbash, 2009; Satyaki et al., 2014; Anselm et al., 2018; Lukacs et al., 2021; Jagannathan and Yamashita, 2021; Kupp et al., 2015; Maheshwari et al., 2015; Marimuthu et al., 2021). Notably, two hybrid inviability factors, hybrid male rescue (Hmr) and lethal hybrid rescue (Lhr), interact in *Drosophila* to regulate heterochromatin repeats that suppress transposable element expression (Satyaki et al., 2014), and are involved in a number of mechanisms that are thought to maintain centromeric and pericentromeric integrity (Anselm et al., 2018; Lukacs et al., 2021). Genetic and genomic screens of *Drosophila* hybrids have additionally identified nuclear pore complex components (Presgraves et al., 2003; Tang and Presgraves, 2009) and a single cell cycle regulation gene, *gfzf*, in mediating hybrid incompatibility (Phadnis et al., 2015). Though it remains unclear if and how these interact with Hmr or Lhr, it emphasizes the importance of genome stability and cell cycle mechanisms in mediating hybrid incompatibility and evolution. Moreover, genome organization and packaging through heterochromatin and chromocenter domains appear to play key roles in mediating faithful chromosome segregation in *Drosophila* hybrids (Ferree and Barbash, 2009; Jagannathan and Yamashita, 2021). Meanwhile, the only known mammalian speciation gene is *Prdm9*, a meiotic histone H3 methyltransferase that binds to and specifies meiotic recombination hotspots (Mihola et al., 2009; Baudat et al., 2009; Forejt et al., 2021). Overall, the cellular and molecular mechanisms underlying hybrid inviability and speciation barriers are still largely unknown across various experimental systems, particularly among vertebrates, though cell cycle regulation likely plays a key role.

#### **1.4 Powering the cell cycle with the *Xenopus* egg extract**

An abundant and invasive species, the tongueless, aquatic, African clawed *Xenopus* frogs have been among the most informative model organisms in the study of the cell cycle. Upon hormone injection, *Xenopus* females lay thousands of eggs, arrested in metaphase II of meiosis by cyostatic factor (CSF) activity (Masui and Markert, 1971). Cell-free egg extracts were first prepared by Lokha and Masui, by collecting and crushing the eggs to separate their layers and make it possible to harvest undiluted egg cytoplasm (Lohka and Masui, 1983; Lohka and Maller, 1985; Murray, 1991). The *Xenopus* frog egg



is stockpiled with maternal RNAs and proteins during oogenesis to support rapid early embryonic development, providing the embryo with the necessary components to power the cell cycle. Thus, once isolated, this cell-free cytoplasmic extract contains all the necessary biomolecules and machinery necessary to recapitulate the cell cycle multiple times in a test tube with the addition of a DNA source, such as sperm nuclei or DNA-coated beads (Murray and Kirschner, 1989; Murray, 1991; Heald et al., 1996). Metaphase spindles, mitotic chromosomes, and interphase nuclei can all be formed in vitro, and several important processes, such as DNA replication, chromosome condensation, and kinetochore formation, are fully supported in extracts (Maresca and Heald, 2006; French and Straight, 2017). The egg extract system undergoes a simple and controllable cell cycle, mimicking the timing and functions of the early embryonic cleavages. These cycles lack gap phases and oscillate rapidly between S phase (DNA replication) and M phase (mitosis) without checkpoints. The extract allows for unparalleled control over the cell cycle, as it is highly synchronous, can be arrested in either metaphase or interphase, and is amenable to biochemical and pharmacological manipulations, such as protein immunodepletions and small molecule inhibitor treatments, to manipulate cell cycle-specific structures and dynamics. Thus far, *Xenopus* extracts have been key to our understanding of the fundamental principles at play in cell cycle control, spindle assembly, and chromosome segregation (Murray and Kirschner, 1989; Glotzer et al., 1991; Sawin and Mitchison, 1991; Blow and Laskey, 1986; Hirano and Mitchison, 1991; Heald et al., 1996).

### **1.5 *Xenopus* interspecies comparisons reveal molecular mechanisms of intracellular scaling and evolutionary divergence**

*Xenopus* eggs and embryos possess unique features that allow us to pose mechanistic questions about mitotic spindle and chromosome assembly, and size scaling from the level of genomes and subcellular structures to the whole organism. The egg extract's ability to recapitulate cell cycle events has been a powerful, biochemically manipulable system that allows fundamental discoveries and precise dissection of mechanisms involved in building and maintaining the mitotic spindle. In addition, the fertilized *Xenopus* embryo undergoes rapid cleavage divisions during early development without cellular growth, splitting the embryo into smaller and smaller cells. This provides a phenomenal paradigm to understand subcellular scaling throughout organismal development and cell cycle mechanisms in the absence of checkpoint regulation. Examination of *Xenopus* embryos and use of cytoplasmic embryo extracts from specific developmental stages have been instrumental in understanding spindle morphology and size control (Wühr et al., 2008; Crowder et al., 2015; Wilbur and Heald, 2013; Levy and Heald, 2010).

In addition to revealing cell division phenomena within a single species, comparisons across multiple *Xenopus* species have provided a unique evolutionary window to examine conservation and divergence of these mechanisms. In vitro egg extract systems have been developed and applied to a variety of species with different egg and genome sizes, beginning with the smaller, diploid frog, *Xenopus tropicalis* (Brown et al., 2007), and extending to *Hymenochirus boettgeri*, a tiny Pipid family frog from a

different genus (Miller et al., 2019). Spindles from the smaller *X. tropicalis* frog are shorter in length compared to *X. laevis* due to two key mechanisms: 1) increased microtubule severing activity of the enzyme katanin (Loughlin et al., 2010, 2011), and 2) elevated levels of TPX2, a spindle assembly factor that promotes microtubule bundling by kinesin-5 motor Eg5 (Helmke and Heald, 2014). These differences also lead to changes in global architecture and morphology of the spindle, specifically in the microtubule organization and density across the length of the spindle from pole-to-pole, where *X. tropicalis* spindles have more robust kinetochore fibers and shift microtubule density towards the poles rather than overlapping over the metaphase plate (Loughlin et al., 2011; Helmke and Heald, 2014; Grenfell et al., 2016b). This is not due to the difference in DNA content, but rather the cytoplasmic composition from each species. Indeed, mixing *X. laevis* and *X. tropicalis* cytoplasmic extracts results in spindles of intermediate size and morphological characteristics in a dose-dependent manner, regardless of DNA content and species, thus indicating that cytoplasmic factors are sufficient to scale these subcellular structures and build the associated morphological architecture (Brown et al., 2007; Helmke and Heald, 2014).

Remarkably, investigation of spindles from the distantly related Pipid frog *H. boettgeri* revealed that these specific mechanisms did not apply beyond the *Xenopus* genus. *H. boettgeri* spindles are similar in size to *X. tropicalis*, but katanin severing activity and TPX2 levels were more similar to *X. laevis*. Instead, spindle scaling in *H. boettgeri* depended entirely on a microtubule depolymerizing motor kif2a (Miller et al., 2019), which scales spindles during the rapid *X. laevis* embryonic cleavages (Wilbur and Heald, 2013). Though kif2a levels are consistent across *X. laevis*, *X. tropicalis*, and *H. boettgeri*, it is enriched on *H. boettgeri* spindles through phosphorylation of specific serine residue by Polo-like kinase 1 (Plk1) that is not conserved with *Xenopus* (Miller et al., 2019). Thus, these interspecies comparisons have revealed divergent mechanisms of spindle size scaling and control through the use of in vitro frog egg extract systems, allowing further exploration and potential identification of evolutionary forces and constraints on mechanisms that control spindle assembly and size scaling.

## **1.6 *Xenopus* hybrids provide cell biological insight into mechanisms of size control, species barriers, genome evolution, and reproductive isolation**

Uniquely among vertebrates, anurans exhibit extreme variability in ploidy and genome size. The *Xenopus* genus alone is extraordinary in the diversity of polyploid species that exhibit a wide range of genome sizes among the ~30 known *Xenopus* species, including eleven allotetraploid or tetraploid species, seven octaploids, and two dodecaploids (Evans et al., 2015). These frogs possess multiple intriguing evolutionary relationships that include past interspecies hybridization events (Session et al., 2016). Both *X. laevis* and *X. borealis* are allotetraploid species ( $2N = 36$  chromosomes) whose genomes contain two subgenomes, L and S (for long and short), that arose through an interspecies hybridization of two diploid *X. tropicalis*-like progenitor species ~17 million years ago (Session et al., 2016). *X. laevis* and *X. borealis* subsequently have nine pairs of homoeologous L and S chromosomes, with the ninth pair being a result of chromosomal fusion (Session et al., 2016), compared to the diploid *X. tropicalis* ( $2N =$

20). *X. tropicalis* is believed to have diverged from *X. laevis* and *X. borealis* ~48 million years ago. Prior to the detailed sequencing and knowledge of their genome evolution, various *Xenopus* species were used to generate interspecific hybrids to understand parental gene expression patterns (De Robertis and Black, 1979; Woodland and Ballantine, 1980; Bürki, 1985). Other amphibian hybrids, particularly *Rana* bullfrogs and polyploid salamanders, were used to investigate hybrid developmental arrests, cytoplasmic incompatibility, and fertilization blocks against polyspermy (Elinson, 1981, 1977a; b; Elinson and Briedis, 1981).

Viable *Xenopus* hybrids created from *X. laevis* eggs fertilized by *X. tropicalis* sperm ( $I_e \times t_s$ ) have recently been used to interrogate the relationship between the DNA-to-cytoplasmic ratio and timing of zygotic gene activation, and mechanisms of biological size control at the level of the whole organism in addition to cellular and subcellular levels. These *X. laevis*/*X. tropicalis* hybrid crosses produce an adult frog intermediate in genome size, cell size, and body length between the two parental species (Fig. 1.1) (Narbonne et al., 2011; Gibeaux, Miller et al., 2018; Jukam et al., 2021). Comparing *X. laevis*/*X. tropicalis* hybrids with cybrids, in which the maternal *X. laevis* genome was eliminated by UV crosslinking prior to fertilization, revealed that decreased DNA content in the cybrids led to delayed onset of zygotic transcription and cell cycle elongation (Jukam et al., 2021). Interestingly, DNA-to-cytoplasmic ratio manipulations led to delays in expression for all *Xenopus* genes, emphasizing its crucial contribution in zygotic genome activation and regulation (Jukam et al., 2021). The use of viable hybrids has also demonstrated that genome size correlates well with cell and organism size, but other parameters influence these relationships. In particular, transcriptome analysis revealed upregulated paternal-derived expression of DNA-binding, transcriptional regulators in hybrids (Gibeaux, Miller et al., 2018). Strikingly, overexpression of candidate transcription factors in *X. laevis* embryos can shrink the body length to match the viable hybrid, though cell and nuclear size were not affected. This suggests that gene expression from the paternal *X. tropicalis* genome at zygotic genome activation therefore influences size scaling of the hybrids, where transcription factors act to “fine tune” the cell and organismal size set by changes in genome size (Gibeaux, Miller et al., 2018).

Recently, we pioneered the use of inviable *Xenopus* hybrids as a vertebrate model system to understand speciation barriers and mechanisms of incompatibility that lead to hybrid death (Gibeaux et al., 2018; Kitaoka et al., 2022). While other model systems, particularly in *Drosophila*, have been used to investigate hybrid incompatibility through genetic approaches (Presgraves et al., 2003; Tang and Presgraves, 2009; Phadnis et al., 2015; Powell et al., 2020), it remains unclear what cellular and molecular mechanisms are mis-matched and go awry between even closely related species. Indeed, most inviable hybrids that create a post-zygotically genetic “dead end”, i.e. a lethal F1 offspring, were not considered for investigation due to their lethality and difficulty to study. However, *Xenopus* provides the ideal system to tackle mechanistic questions of hybrid incompatibility. The evolutionary history of *Xenopus*, which includes past hybridization events to create the allotetraploid genome of *X. laevis* (Session et al., 2016), provides the perfect backdrop to perform further experimental hybridizations (Fig. 1.1). Importantly, the ease of in vitro cross fertilization methods combined with the powerful egg extract system

opens the door for detailed molecular, cell biological, developmental, and evolutionary analysis of the basis of hybridization outcomes. We spearhead this unique experimental realm to understand the incompatibilities and mismatches that arise in hybrids that lead to their lethality, and provide insight into speciation and reproductive isolation barriers.

**Figure 1.1**

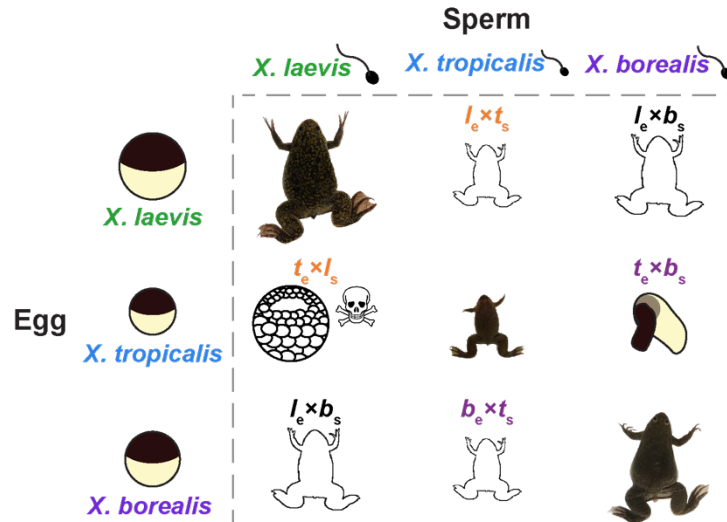


**Figure 1.1. *Xenopus* hybrid crosses are asymmetric, depending on which species provides the egg vs. sperm.** Hybrids produced from *X. tropicalis* eggs are inviable, while hybrids made from *X. laevis* or *X. borealis* eggs are viable. *X. tropicalis* sperm-based hybrids also allow for investigation of size scaling, as the hybrids produced are intermediate in size. All species nomenclature throughout this thesis denotes eggs or egg extract as subscript e and sperm or sperm chromosomes as subscript s. For example,  $t_e \times l_s$  indicates *X. tropicalis* eggs combined with *X. laevis* sperm.

My thesis spans comparative evolutionary, cell, and developmental biology to reveal novel mechanisms and address several long-standing paradoxes in cell division. Chapter 2 addresses in detail the development and characterization of a third *Xenopus* species' egg extract and spindle assembly mechanisms using *Xenopus borealis*, a closely related allotetraploid "sister" species to *X. laevis* (Kitaoka et al., 2018). This provides another comparative window to address the conservation of spindle assembly mechanisms among *Xenopus* frogs, as well as the paradoxical divergence and variation in spindle architecture. Chapter 3 delves into the complex microtubule architecture of the *Xenopus* spindle, as we attempt to glean further understanding into spindle architecture diversity by adapting expansion microscopy for the egg extract systems (Guilloux, Kitaoka, Mocaer et al., in prep). This method will begin to provide insight as to why and how various spindle architectures across species evolve and give rise to the essential function of the mitotic and meiotic spindles. Chapter 4 establishes a uniquely tractable vertebrate system for hybrid incompatibility, using *X. laevis*, *X. tropicalis*, and *X. borealis*. We investigate their asymmetric hybrid cross outcomes and discover downstream cell biological consequences that result in hybrid inviability (Gibeaux et al., 2018). Finally, Chapter 5 takes advantage of all that the *Xenopus* system has to offer to elucidate how

specific chromosomes are affected in inviable hybrids that lead to their eventual death (Kitaoka et al., 2022). This reveals genomic vulnerability of the repetitive centromere and ribosomal DNA, the most rapidly evolving and the most conserved genomic regions, respectively, and highlights the molecular conflicts that occur at these essential loci. Overall, my work uniquely leverages *Xenopus* systems to probe species-specific mechanisms at play in the essential process of cell division and uncovers how these mechanisms can clash in hybrids to create speciation barriers.

## Chapter 2

### Spindle assembly in egg extracts of the Marsabit clawed frog, *Xenopus borealis*

The following chapter contains material from a publication on which I am the first author (Kitaoka et al., 2018). This article is distributed under the terms of the Creative Commons Attribution License (CC BY 4.0), which permits unrestricted use and redistribution provided that the original author and source are credited.

#### ABSTRACT

Egg extracts of the African clawed frog *Xenopus laevis* have provided a cell-free system instrumental in elucidating events of the cell cycle, including mechanisms of spindle assembly. Comparison with extracts from the diploid Western clawed frog, *Xenopus tropicalis*, which is smaller at the organism, cellular and subcellular levels, has enabled the identification of spindle size scaling factors. We set out to characterize the Marsabit clawed frog, *Xenopus borealis*, which is intermediate in size between the two species, but more recently diverged in evolution from *X. laevis* than *X. tropicalis*. *X. borealis* eggs were slightly smaller than those of *X. laevis*, and slightly smaller spindles were assembled in egg extracts. Interestingly, microtubule distribution across the length of the *X. borealis* spindles differed from both *X. laevis* and *X. tropicalis*. Extract mixing experiments revealed common scaling phenomena among *Xenopus* species, while characterization of spindle factors katanin, TPX2, and Ran indicate that *X. borealis* spindles possess both *X. laevis* and *X. tropicalis* features. Thus, *X. borealis* egg extract provides a third in vitro system to investigate interspecies scaling and spindle morphometric variation.

## 2.1 INTRODUCTION

In all eukaryotes, cell division requires the spindle, a highly dynamic, self-organizing, microtubule-based apparatus that accurately segregates replicated chromosomes to daughter cells. Spindle microtubules assemble into a bipolar structure that attaches to chromosomes via their kinetochores and aligns them at the metaphase plate so that sister chromatids are oriented toward opposite spindle poles. Although the basic form and composition of the spindle is conserved, spindle structure adapts to changes in cell size and type, and varies dramatically both across and within species (Crowder et al., 2015; Wühr et al., 2008). While many of the molecules and mechanisms that orchestrate spindle assembly have been elucidated, it remains unclear how specific spindle architectures are established, and how this variation impacts spindle function.

Unfertilized eggs of the African clawed frog *Xenopus laevis* arrested in metaphase of meiosis II by cytostatic factor (CSF) (Masui and Markert, 1971) can be obtained in large quantities. Their fractionation by centrifugation yields a crude cytoplasmic extract that maintains the metaphase arrest and supports spindle assembly around sperm nuclei or chromatin-coated beads (Sawin and Mitchison, 1991; Heald et al., 1996). Remarkably, spindles formed in egg extracts of the smaller, related frog *Xenopus tropicalis* are shorter in length independent of DNA source, and mixing the two extracts produced spindles of intermediate size (Brown et al., 2007). It was found that compared to *X. laevis*, *X. tropicalis* possess smaller spindles due to (i) elevated activity of the hexameric AAA-ATPase microtubule severing enzyme katanin (Loughlin et al., 2010, 2011), and (ii) a higher concentration of the spindle assembly factor, TPX2 (targeting factor for Xklp2), which promotes association of the cross-linking spindle motor Eg5 and a shift of microtubule density from antiparallel overlap in the center of the spindle to the poles (Helmke and Heald, 2014). *X. tropicalis* spindles were also observed to possess distinct morphological features, including more robust kinetochore fibers and a more circular shape (Loughlin et al., 2011; Grenfell et al., 2016b). Furthermore, whereas spindle assembly in *X. laevis* extracts required a chromatin-generated gradient of RanGTP (Kalab et al., 2002; Cavazza and Vernos, 2016), *X. tropicalis* spindle assembly was not affected by disruption of this pathway (Helmke and Heald, 2014). Therefore, not only spindle size, but also spindle architecture, morphology, and assembly mechanisms differ between these two species.

To further address the conservation of spindle morphology, assembly, and scaling mechanisms across evolution, we decided to characterize a third *Xenopus* species, the Marsabit clawed frog *Xenopus borealis*. Whereas allotetraploid *X. laevis* (36 chromosomes) and diploid *X. tropicalis* (20 chromosomes) diverged 48 million years ago, *X. borealis* is more closely related to *X. laevis*, having diverged 17 million years ago (Session et al., 2016). Like *X. laevis*, *X. borealis* possesses an allotetraploid genome of 36 chromosomes. Interestingly, *X. borealis* was used extensively in the 1970s to analyze the conservation of ribosomal nucleic acids compared to *X. laevis* (Brown et al., 1972; Brown and Sugimoto, 1973; Griswold et al., 1974; Wellauer and Reeder, 1975; Leister and Dawid, 1975; Ford and Brown, 1976) and was misidentified as *Xenopus mulleri* until 1977 (Brown et al., 1977). Revisiting this species and applying the egg extract

methodology allowed us to further evaluate spindle morphometric variation and scaling in *Xenopus*. We show that *X. borealis* spindles are intermediate in size and display properties of both *X. laevis* and *X. tropicalis*, resulting in distinct features. These findings highlight the evolutionary plasticity of spindle morphology and assembly mechanisms, and introduce *X. borealis* as a third *Xenopus* species amenable to in vitro assays to investigate the molecular basis of spindle variation.



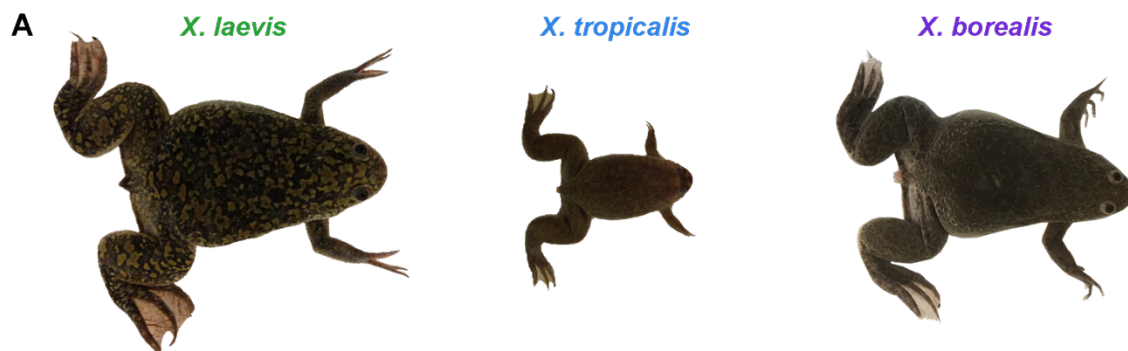
## 2.2 RESULTS

In this study, we characterized *X. borealis* and spindle assembly in its egg extracts, using the two well-characterized *Xenopus* species, *X. laevis* and *X. tropicalis*, for comparison.

### ***X. borealis* frogs, eggs, and sperm are morphologically distinct**

At ~7 cm body length, adult *X. borealis* female frogs were intermediate in size between *X. laevis* (~10 cm) and *X. tropicalis* (~4 cm) and also displayed distinct physical traits including googly eyes and a pear-like body shape (Fig. 2.1A). Measuring the size of *X. borealis* gametes revealed that *X. borealis* eggs averaged  $1.2 \pm 0.02$  mm in diameter, slightly smaller than *X. laevis* ( $1.3 \pm 0.05$  mm) and larger than *X. tropicalis* ( $0.75 \pm 0.02$  mm) (Fig. 2.1B). Interestingly, *X. borealis* sperm cells were significantly longer (average  $22 \pm 2.8$   $\mu\text{m}$ ) than those of both *X. laevis* ( $19 \pm 2.3$   $\mu\text{m}$ ) and *X. tropicalis* ( $13.5 \pm 2.1$   $\mu\text{m}$ ) (Fig. 2.1C), and similar size differences were observed comparing isolated sperm nuclei (Fig. 2.2) (Grainger, 2012). In vitro fertilization and live imaging revealed that the rate of early development of *X. borealis* and *X. laevis* embryos were similar (Fig. 2.1D and Video 2.1) (Nieuwkoop and Faber, 1994). Nuclei isolated from stage 8 (5 hpf) embryos of *X. borealis* (average  $2214 \pm 1016$   $\mu\text{m}^2$ ) were comparable in size to those from *X. laevis* ( $2010 \pm 1081$   $\mu\text{m}^2$ ), while *X. tropicalis* nuclei ( $405 \pm 116$   $\mu\text{m}^2$ ) were significantly smaller (Fig. 2.1E). In summary, although *X. borealis* display distinct traits, our measurements show that like *X. laevis* and *X. tropicalis*, *X. borealis* egg size scales with adult animal size, and that *X. borealis* development and nuclear size is very similar to that of *X. laevis*. These findings are consistent with the well-characterized phenomenon that genome size scales with nuclear and cell size among amphibians (Levy and Heald, 2016).

**Figure 2.1**



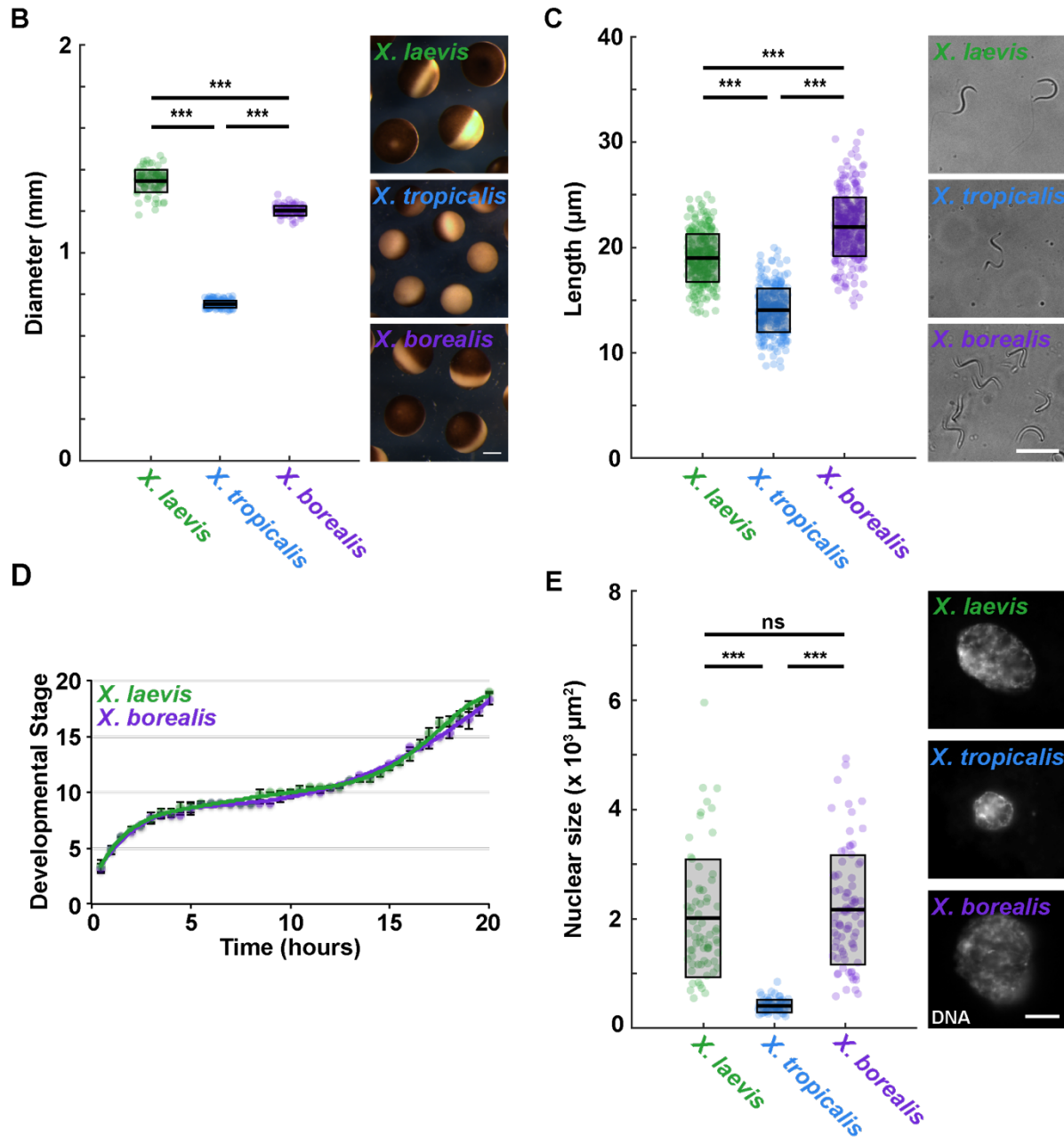


**Figure 2.1: Characterization of the Marsabit clawed frog, *X. borealis***

(A) Relative body size of *X. borealis* frogs compared to *X. laevis* and *X. tropicalis*. (B) Comparison and quantification of egg size. Egg size (diameter in mm) is plotted as boxplots for *X. laevis* (green), *X. tropicalis* (blue), and *X. borealis* (purple). Each dot represents an individual egg ( $n = 89$  for *X. laevis*,  $n = 132$  for *X. tropicalis*, and  $n = 77$  for *X. borealis*, from 3 females for each species). Representative images of eggs for each species are shown (right). Scale bar is  $200 \mu\text{m}$ . (C) Comparison and quantification of sperm size. Sperm head length ( $\mu\text{m}$ ) is plotted as boxplots for *X. laevis* (green), *X. tropicalis* (blue), and *X. borealis* (purple). Each dot represents an individual sperm cell ( $n = 288$  for *X. laevis*,  $n = 278$  for *X. tropicalis*, and  $n = 310$  for *X. borealis*, from 3 males for each species). Representative images of sperm cells for each species are shown (right). Scale bar is  $20 \mu\text{m}$ . (D) Early embryo development at room temperature for *X. laevis* and *X. borealis*. Embryos were staged according to Nieuwkoop and Faber (Nieuwkoop and Faber, 1994). Data for *X. laevis* embryos ( $n = 12$ ) are blotted in green and *X. borealis* ( $n = 12$ ) in purple. Error bars

show the standard deviation. **(E)** Stage 8 embryo nuclei comparison and quantification. Representative images of nuclei isolated from stage 8 *X. laevis*, *X. tropicalis*, and *X. borealis* embryos are shown with DNA signal. Scale bar is 10  $\mu\text{m}$ . Nuclear size (area in  $\mu\text{m}^2$ ) is plotted as boxplots for *X. laevis* (green), *X. tropicalis* (blue), and *X. borealis* (purple). Each dot represents an individual nucleus ( $n = 68$  for *X. laevis*,  $n = 71$  for *X. tropicalis*, and  $n = 84$  for *X. borealis*). In **B**, **C**, and **E**, the thicker black line indicates the average, and the outlined gray box represents the standard deviation. Statistical significance was determined by a two-tailed, two-sample unequal variance t-test.

**Video 2.1: Characterization of *X. borealis* embryo development; *X. laevis* vs. *X. borealis***

*X. laevis* (left) and *X. borealis* (right) eggs were fertilized with *X. laevis* or *X. borealis* sperm, respectively, and simultaneously imaged in separate dishes. Scale bar corresponds to 200  $\mu\text{m}$ . The video represents 20 h played in 15 s at a rate of 120 frames per second. (available online: <https://onlinelibrary.wiley.com/doi/10.1002/cm.21444>)

**Figure 2.2**

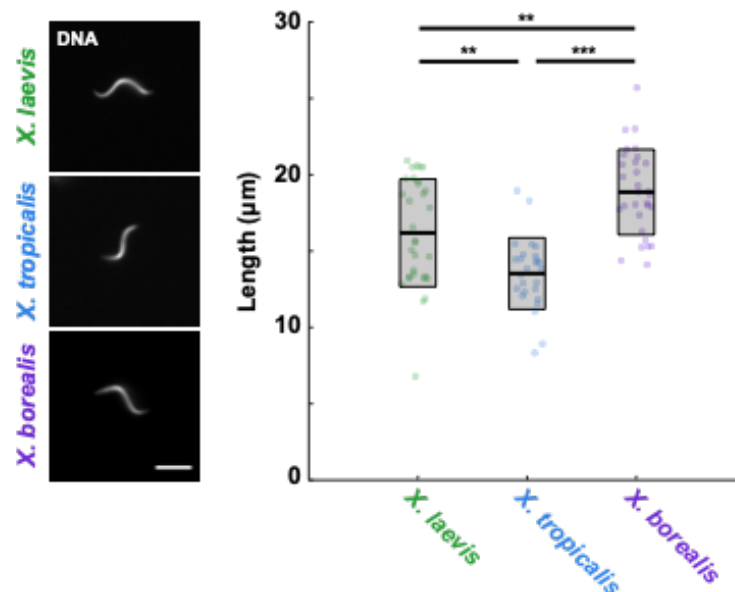


**Figure 2.2: *X. borealis* sperm nuclei length comparison and quantification**

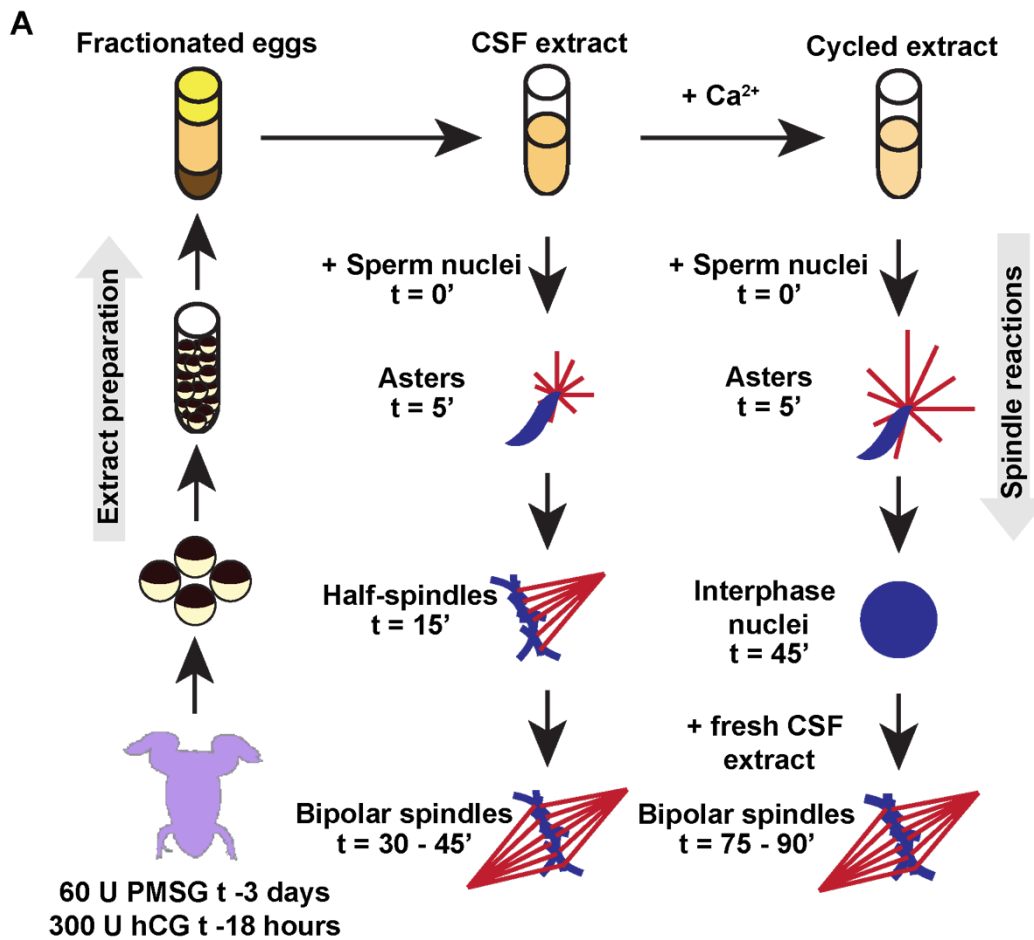
Images of sperm nuclei prepared from *X. laevis*, *X. tropicalis*, and *X. borealis*. DNA signal is shown. Scale bar is 10  $\mu\text{m}$ . Length ( $\mu\text{m}$ ) is plotted as boxplots for *X. laevis* (green), *X. tropicalis* (blue), and *X. borealis* (purple). Each dot represents an individual sperm nucleus ( $n = 31$  for *X. laevis*,  $n = 26$  for *X. tropicalis*,  $n = 30$  for *X. borealis*), the thicker black line indicates the average, and the outlined gray box represents the standard deviation. Statistical significance was determined by a two-tailed, two-sample unequal variance t-test.

***X. borealis* egg extract recapitulates cell cycle events**

To evaluate the utility of *X. borealis* eggs for in vitro assays, we adapted published ovulation procedures to reproducibly obtain metaphase II, CSF-arrested eggs in sufficient amounts to prepare egg extracts (see **Materials and Methods**). *X. borealis* eggs were dejellied and fractionated using standard protocols (Maresca and Heald, 2006; Hannak and Heald, 2006; Brown et al., 2007), and produced similar yields of cytoplasmic extract compared to *X. laevis* despite their smaller body and egg size. *X. borealis* egg extract

was then combined with *X. borealis* sperm nuclei and assayed for spindle assembly. When added directly to CSF extract, sperm nuclei induced the formation of asters ( $t = 5'$ ), followed by half-spindles ( $t = 15'$ ) and bipolar CSF spindles ( $t = 30 - 45'$ ) (Fig. 2.3A, B). Addition of calcium together with sperm nuclei induced exit from metaphase arrest and formation of interphase nuclei within 45 min. Following the addition of fresh CSF extract, bipolar “cycled” spindles assembled from 75 min to 90 min (Fig. 2.3A, C). We noted that *X. borealis* extracts formed spindles more quickly than *X. laevis*, almost as rapidly as *X. tropicalis* (unpublished data). These experiments show that, as for the other *Xenopus* species, *X. borealis* egg extracts are fully capable of recapitulating the cell cycle and assembling spindles in vitro.

**Figure 2.3**



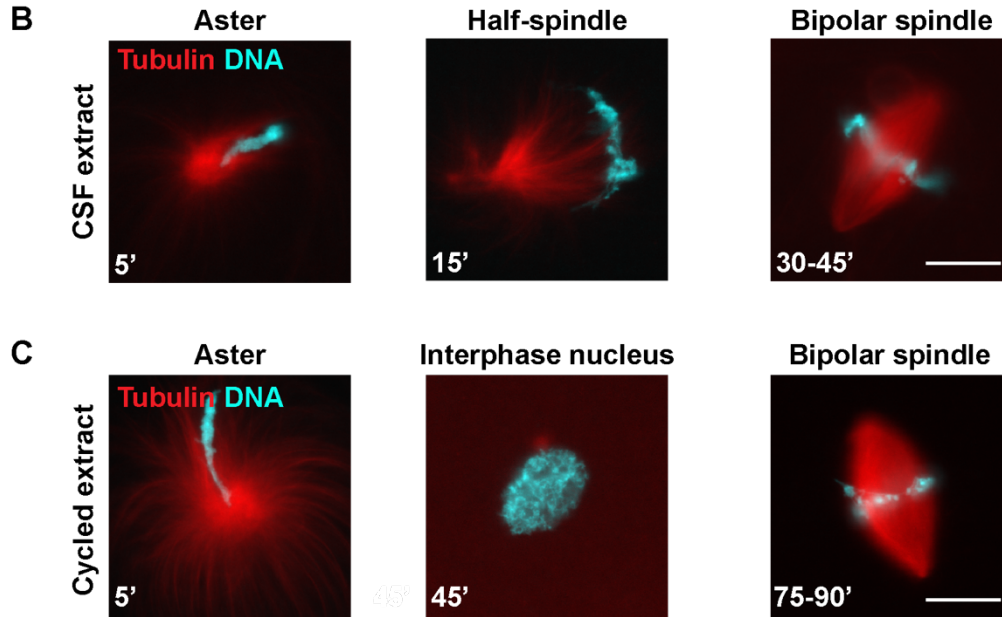


**Figure 2.3: *X. borealis* egg extracts at a glance**

**(A)** Schematic of extract preparation and spindle assembly reactions. **(B)** Images of spindle assembly intermediates in CSF extract reactions. **(C)** Images of spindle assembly intermediates in cycled extract reactions. Images in **B-C** of representative structures are shown with tubulin (red) and DNA (blue) signal. Scale bar is 20  $\mu\text{m}$ .

### ***Xenopus* species possess distinct spindle morphometrics**

We next examined some parameters of *X. borealis* spindle size and microtubule organization and compared them to *in vivo* meiosis II spindles as well as to spindles assembled in *X. laevis* and *X. tropicalis* egg extracts. *X. borealis* spindles assembled *in vitro* were similar in length from pole-to-pole and width at the metaphase plate to meiotic spindles imaged in metaphase II-arrested eggs (length/width average  $43.9 \pm 5.5 \mu\text{m}/21.7 \pm 3.6 \mu\text{m}$  *in vivo* vs.  $44.4 \pm 5.5 \mu\text{m}/23.4 \pm 5.9 \mu\text{m}$  in extract) (Fig. 2.4A). *X. borealis* extract was also capable of inducing bipolar spindle assembly around stage 8 *X. borealis* embryo nuclei and 10  $\mu\text{m}$  diameter chromatin-coated beads (Halpin et al., 2011). Embryo nuclei spindles were slightly smaller than those formed around sperm nuclei (average length  $39.7 \pm 4.4 \mu\text{m}$ , width  $25.1 \pm 4.7 \mu\text{m}$ ) (Fig. 2.4B), while spindles assembled around DNA-coated beads were considerably shorter (average  $22.4 \pm 3.9 \mu\text{m}$ ) (Fig. 2.4C). These measurements demonstrate that like *X. laevis* and *X. tropicalis*, spindles formed in *X. borealis* egg extract mimic the size and morphology of the meiotic egg spindle, and that spindle assembly *in vitro* occurs in the presence or absence of centrosomes.

**Figure 2.4**

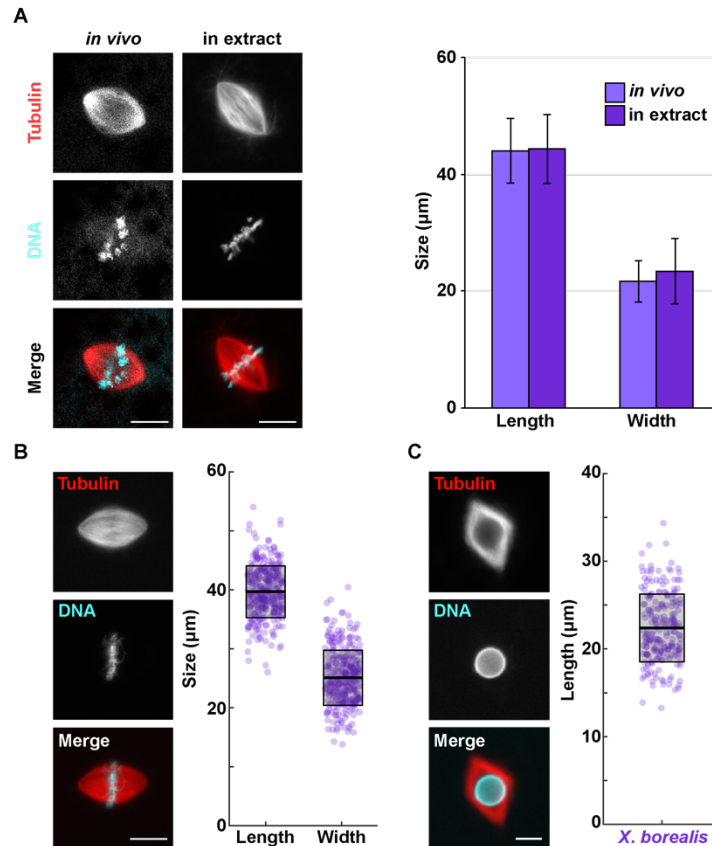


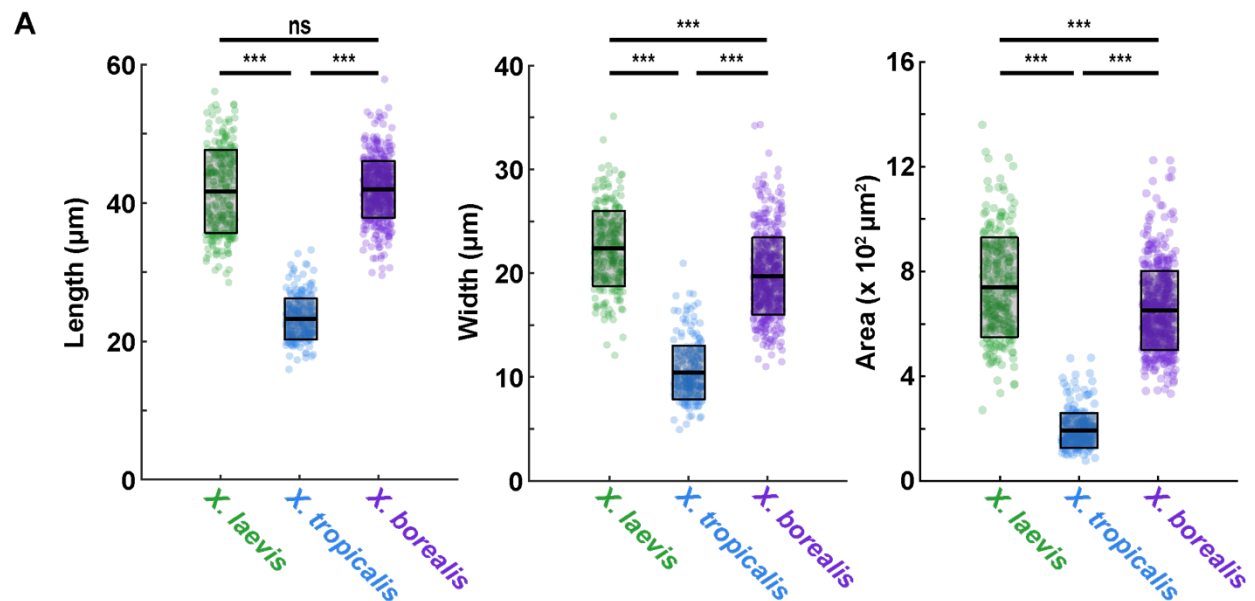
**Figure 2.4: *X. borealis* CSF egg extracts reconstitute spindle assembly**

**(A)** *In vivo* *X. borealis* metaphase-arrested egg spindles compared to spindles assembled in CSF extract. Scale bar is 20 μm. Spindle length (left) and width (right) are plotted (μm) as columns for *X. borealis* spindles from *in vivo* metaphase-arrested eggs (light purple) and formed in *in vitro* egg extract (dark purple). Error bars represent the standard deviation. **(B)** Spindles assembled around stage 8 *X. borealis* embryo nuclei added to *X. borealis* egg extract. Scale bar is 20 μm. Spindle length (left) and width (right) are plotted (μm) as boxplots. Each dot represents an individual spindle measurement (n = 310, from 3 independent egg extracts). **(C)** Spindles assembled around single 10 μm chromatin-coated beads in *X. borealis* egg extract. Scale bar is 10 μm. Length (μm) is plotted as a boxplot. Each dot represents an individual spindle measurement (n = 219, from 4 independent egg extracts). Representative images in **A-C** are shown with tubulin (top) and DNA (middle) signals individually and merged (bottom). In **B-C**, the thicker black line indicates the average, and the outlined gray box represents the standard deviation.

Despite their smaller egg size, we found that cycled *X. borealis* spindles were similar in length to *X. laevis* (average  $41.9 \pm 4.1$  μm vs.  $41.6 \pm 6.0$  μm), but significantly narrower (average  $19.7 \pm 3.7$  μm vs.  $22.4 \pm 3.6$  μm), thereby reducing spindle area and therefore total microtubule content. *X. borealis* spindles were both longer and wider than *X. tropicalis* spindles (average  $23.2 \pm 3.0$  μm in length,  $10.4 \pm 2.6$  μm in width) (Fig. 2.5A). Thus, *X. borealis* spindles scale with egg size and are intermediate in size between those of *X. laevis* and *X. tropicalis*. Interestingly, the three species each displayed unique spindle microtubule distributions across the spindle. As previously reported, *X. laevis*

spindles showed a consistent plateau of tubulin intensity along the length of the spindle indicating the presence of an overlapping, tiled array of microtubules (Loughlin et al., 2010). In contrast, *X. tropicalis* tubulin intensity was greater at the poles and reduced in the center of the spindle at the metaphase plate (Helmke and Heald, 2014). Interestingly, *X. borealis* spindles displayed a similar increase in microtubule density at the poles as *X. tropicalis*, a similar density at the metaphase plate as *X. laevis*, and a unique dip in tubulin intensity between the poles and metaphase plate (Fig. 2.5B). While similar microtubule distribution patterns were observed in CSF spindles, they were less distinct than in cycled spindles, potentially due to the absence of sister kinetochores and associated microtubules (Grenfell et al., 2016b). *X. borealis* CSF spindles were also longer and wider than both *X. laevis* and *X. tropicalis* (Fig. 2.6). A difference in spindle morphology between spindles with replicated (cycled) and unreplicated (CSF) chromosomes has been observed previously and emphasizes the fact that spindle morphology can vary in different cellular contexts (Grenfell et al., 2016b; Levy and Heald, 2016). We decided to focus on cycled spindle assembly for subsequent experiments, as these form around duplicated chromosomes with assembled kinetochores and thus are more physiologically relevant. Therefore, *X. borealis* fits into the *Xenopus* interspecies scaling regime, as the animals, eggs and meiotic spindles are all intermediate in size between the other two species. However, *X. borealis* microtubule arrays share some similarity with both species, leading to a unique spindle architecture.

**Figure 2.5**



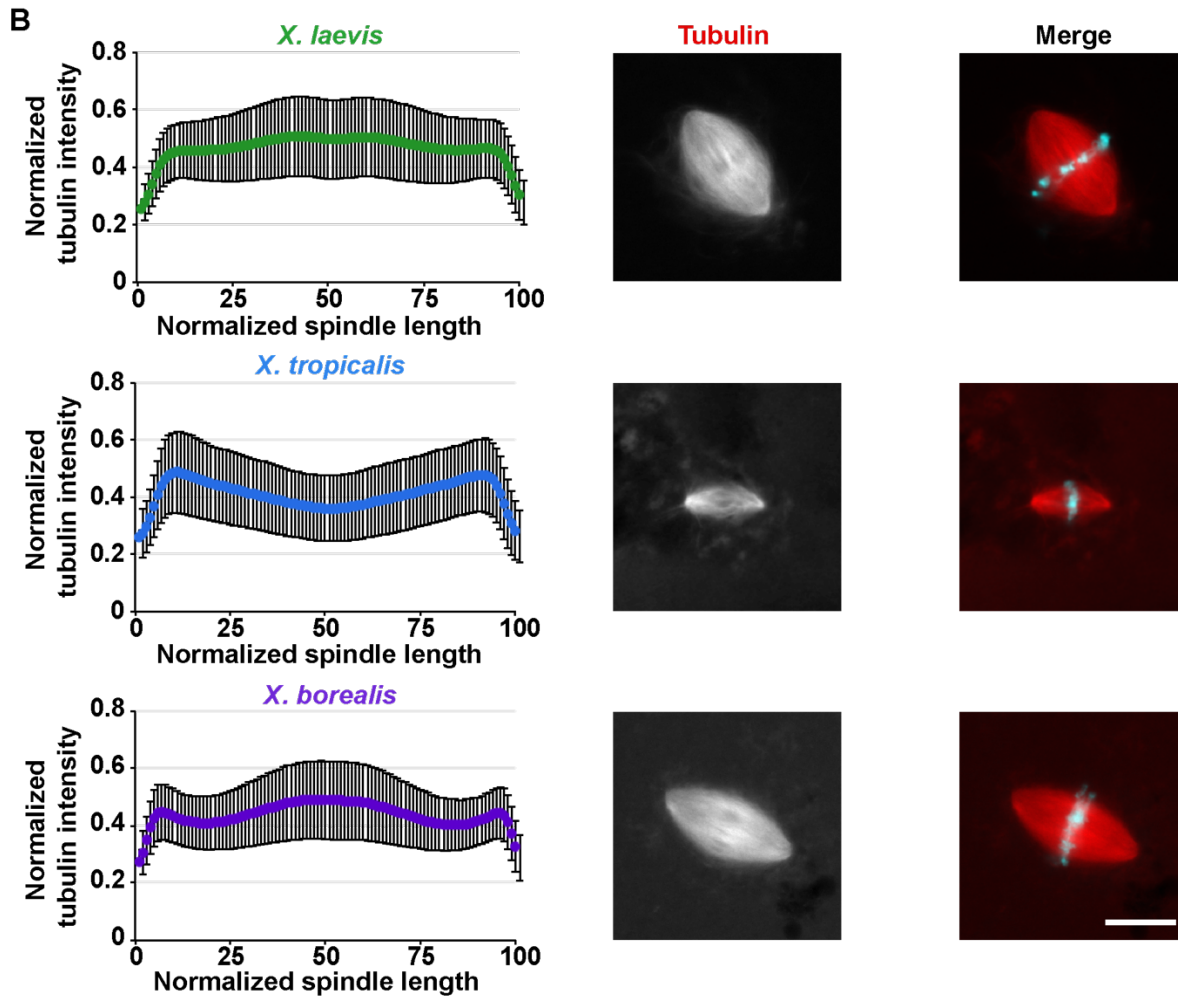


**Figure 2.5: Analysis of *X. borealis* cycled spindles**

**(A)** Quantification of *X. borealis* cycled spindle dimensions. Length (left), width (middle), and area approximated as an ellipse (right) are plotted ( $\mu\text{m}$  or  $\mu\text{m}^2$ ) as boxplots for *X. laevis* (green), *X. tropicalis* (blue), and *X. borealis* (purple) spindles. Each dot represents an individual spindle measurement ( $n = 256$  spindles for *X. laevis*,  $n = 241$  for *X. tropicalis*, and  $n = 493$  for *X. borealis*, from 3 independent egg extracts for each species), the thicker black line indicates the average, and the outlined gray box represents the standard deviation. Statistical significance was determined by a two-tailed, two-sample unequal variance t-test. **(B)** Microtubule fluorescence intensity distribution in *X. laevis* (green), *X. tropicalis* (blue), and *X. borealis* (purple) spindles. Line scans of rhodamine-tubulin signal along the length of the spindle were measured ( $n = 257$  spindles for *X. laevis*,  $n = 242$  for *X. tropicalis*, and  $n = 470$  for *X. borealis*, from 3 independent egg extracts for each species). Spindle length was normalized to 100% and tubulin intensities were normalized within each dataset. Average tubulin intensities were plotted for each species' spindles. Error bars represent the standard deviation. Representative images of spindles formed from *X. laevis*, *X. tropicalis*, and *X. borealis* sperm nuclei in their respective egg extracts are shown with tubulin signal individually (left) and merged with DNA signal (right). Scale bar is 20  $\mu\text{m}$ .



Figure 2.6

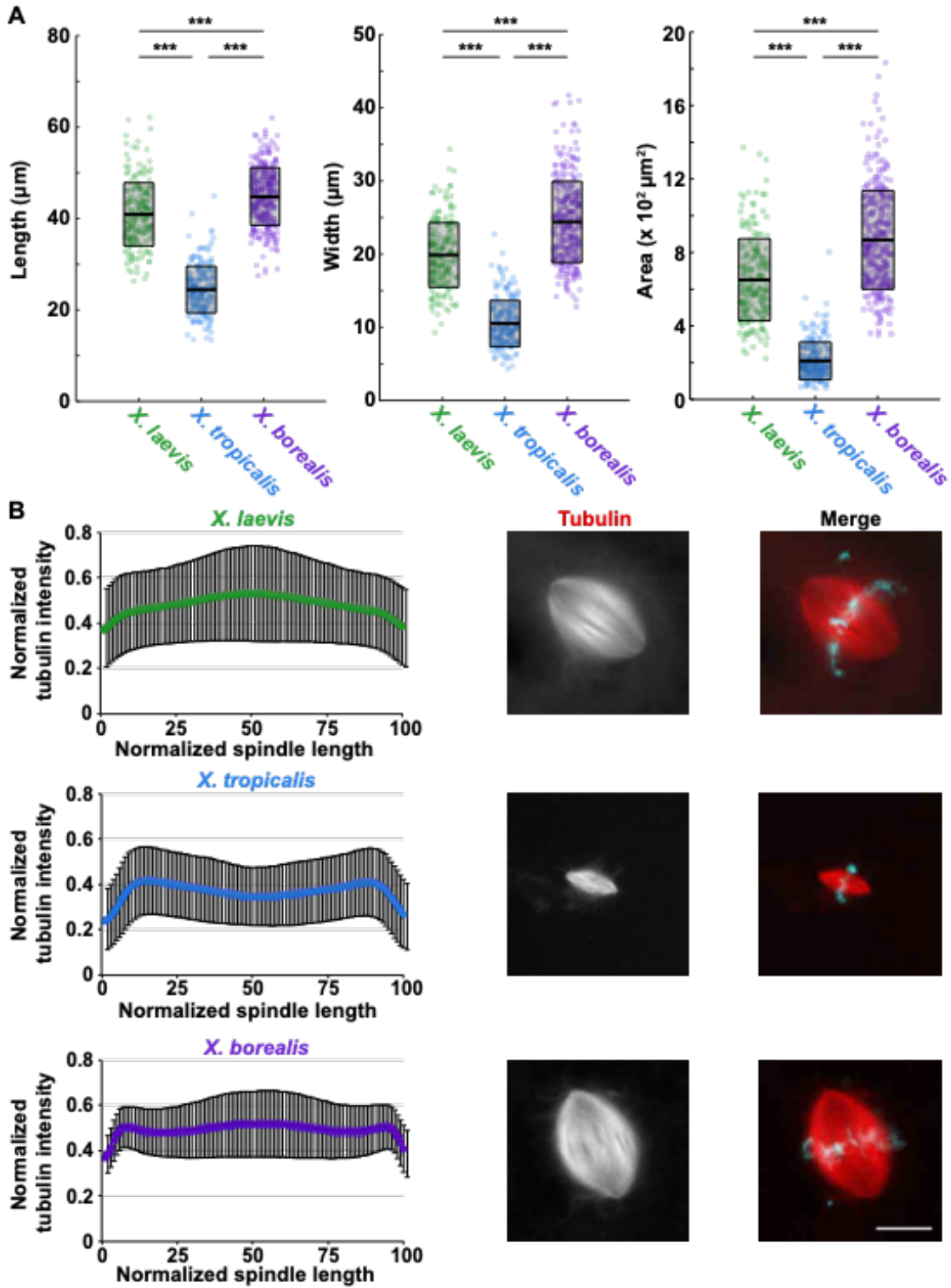


Figure 2.6: Analysis of *X. borealis* CSF spindle properties

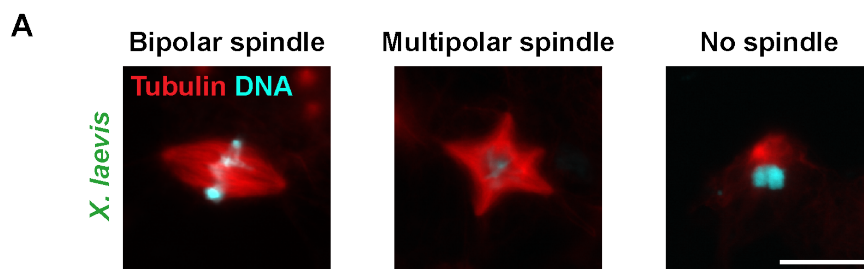
(A) Quantification of *X. borealis* CSF spindle dimensions. Length (left), width (middle), and area approximated as an ellipse (right) are plotted ( $\mu\text{m}$  or  $\mu\text{m}^2$ ) as boxplots for *X. laevis* (green), *X. tropicalis* (blue), and *X. borealis* (purple) spindles. Each dot represents an individual spindle

measurement (n = 196 spindles for *X. laevis*, n = 202 for *X. tropicalis*, and n = 304 for *X. borealis*), the thicker black line indicates the average, and the outlined gray box represents the standard deviation. Statistical significance was determined by a two-tailed, two-sample unequal variance t-test. **(B)** Microtubule distribution in *X. laevis* (green), *X. tropicalis* (blue), and *X. borealis* (purple) spindles. Line scans of rhodamine-tubulin signal along the length of the spindle were measured (n = 243 spindles for *X. laevis*, n = 313 for *X. tropicalis*, and n = 316 for *X. borealis*). Spindle length was normalized to 100% and tubulin intensities were normalized within each dataset. Average tubulin intensities were plotted for each species' spindles. Error bars represent the standard deviation. Representative images of spindles formed from *X. laevis*, *X. tropicalis*, and *X. borealis* sperm nuclei in their respective egg extracts are shown with tubulin signal individually (left) and merged with DNA signal (right). Scale bar is 20  $\mu\text{m}$ . Data in **A-B** were reproduced in 3 independent egg extracts for each species. All 3 were used for microtubule distribution analysis in **B**. Measurements in **A** were quantified from 2 extracts, processed as squashes for accurate absolute size measurements.

### ***X. borealis* spindles are sensitive to perturbation of the RanGTP gradient**

To compare spindle assembly mechanisms among the three species, we examined the role of the RanGTP gradient, which acts to release nuclear localization signal (NLS)-containing spindle assembly factors from importins near mitotic chromatin where the guanine nucleotide exchange factor RCC1 (Regulator of Chromosome Condensation 1) is localized, thereby promoting microtubule nucleation, stabilization, and crosslinking (Cavazza and Vernos, 2016). Perturbing the RanGTP gradient by the addition of Ran mutants, such as a dominant negative (T24N) or constitutively active, GTP-bound (Q69L) form, is detrimental to *X. laevis* spindle assembly, abolishing it completely or increasing ectopic microtubule nucleation and formation of multipolar spindles, respectively (Kalab et al., 1999, 2002). In contrast, we showed previously that *X. tropicalis* spindles are much less affected by perturbation of the RanGTP gradient (Helmke and Heald, 2014). To test the role of this pathway in *X. borealis*, we added the Ran mutants at the onset of spindle assembly. Upon addition of RanT24N, spindle assembly was strongly impaired, with dramatically reduced microtubule nucleation around sperm nuclei, while RanQ69L increased the number of multipolar spindle structures (Fig. 2.7 and Table 2.1). Thus, like *X. laevis*, *X. borealis* bipolar spindle assembly depends on the RanGTP gradient.

**Figure 2.7**



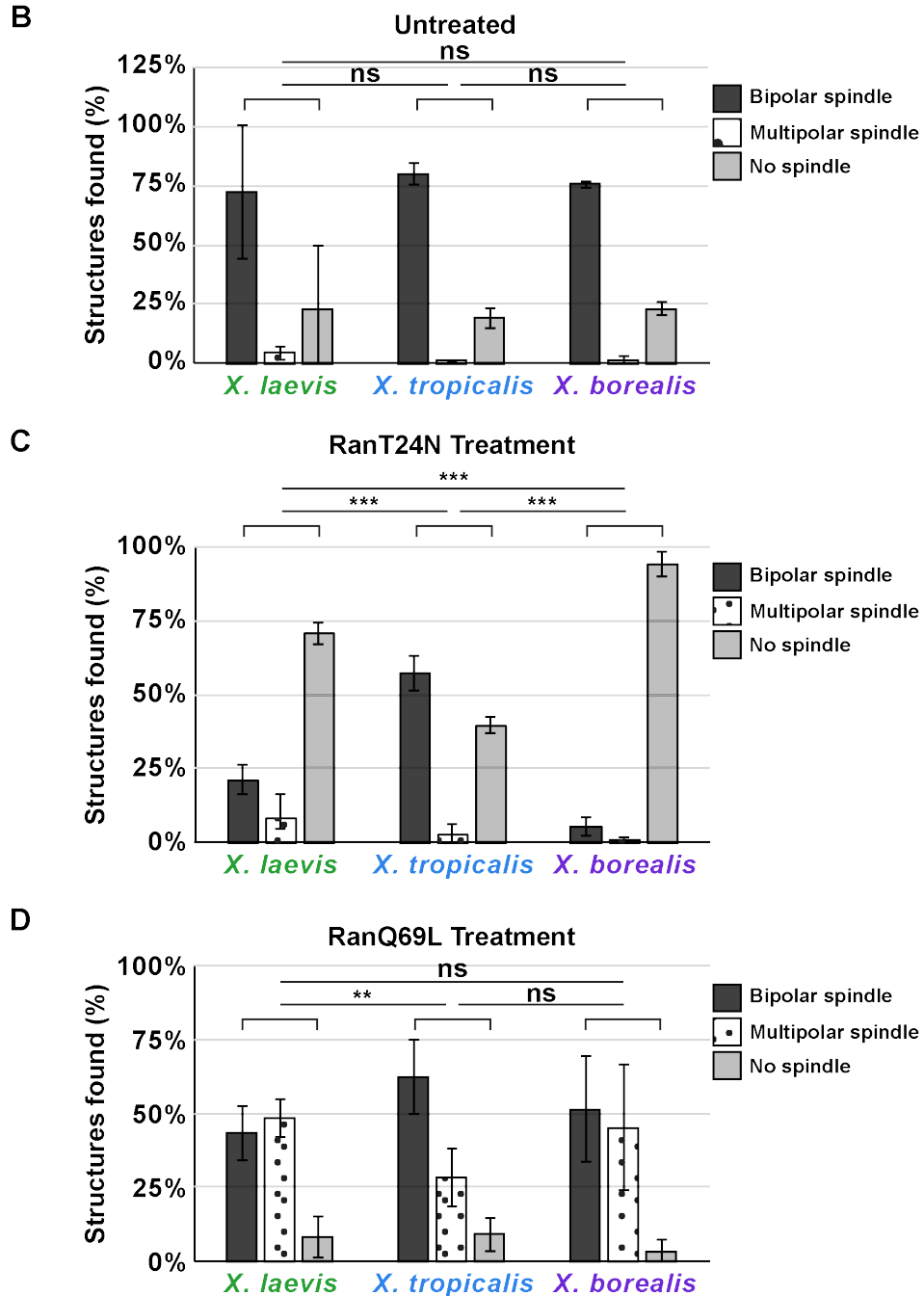


**Figure 2.7: Sensitivity of *X. borealis* spindles to perturbation of the RanGTP gradient**

(A) Phenotype categories quantified in *Xenopus* egg extract spindle assembly reactions containing Ran mutants. Representative images in *X. laevis* extracts are shown with tubulin (red) and DNA (blue) signals. Scale bar is 20  $\mu\text{m}$ . Bar graphs of the percentage of spindles in each category are shown for (B) untreated extracts, (C) RanT24N treated extracts, and (D) RanQ69L treated in *Xenopus* extracts. In B-D, percentages of bipolar (dark gray), multipolar (polka dots), and no spindles found (light gray) are plotted for *X. laevis*, *X. tropicalis*, and *X. borealis* extracts (3 independent extracts were quantified for each species). Error bars represent the standard deviation. Statistical significance was determined by a two-tailed, 3x2 Fisher Exact test.

**Table 2.1**

	<b>Bipolar spindles</b> Average % ± SD (N)	<b>Multipolar spindles</b> Average % ± SD (N)	<b>No spindles</b> Average % ± SD (N)
<i>X. laevis</i>	72.5% ± 0.3 (1221)	4.5% ± 0.03 (74)	23.0% ± 0.3 (407)
T24N	21.3% ± 0.05 (406)	8.0% ± 0.1 (246)	70.7% ± 0.03 (1496)
Q69L	43.4% ± 0.1 (1101)	48.4% ± 0.1 (1048)	8.2% ± 0.1 (85)
<i>X. tropicalis</i>	79.8% ± 0.04 (906)	1.1% ± 0.002 (12)	19.1% ± 0.04 (217)
T24N	57.4% ± 0.1 (803)	3.0% ± 0.03 (45)	39.7% ± 0.03 (565)
Q69L	62.4% ± 0.1 (748)	28.4% ± 0.1 (319)	9.2% ± 0.1 (122)
<i>X. borealis</i>	75.7% ± 0.02 (1177)	1.4% ± 0.01 (23)	23.0% ± 0.03 (347)
T24N	5.3% ± 0.03 (98)	0.7% ± 0.01 (19)	94.0% ± 0.04 (1371)
Q69L	51.4% ± 0.2 (621)	45.2% ± 0.2 (783)	3.4% ± 0.04 (32)

**Table 2.1: Ran perturbation phenotypes**

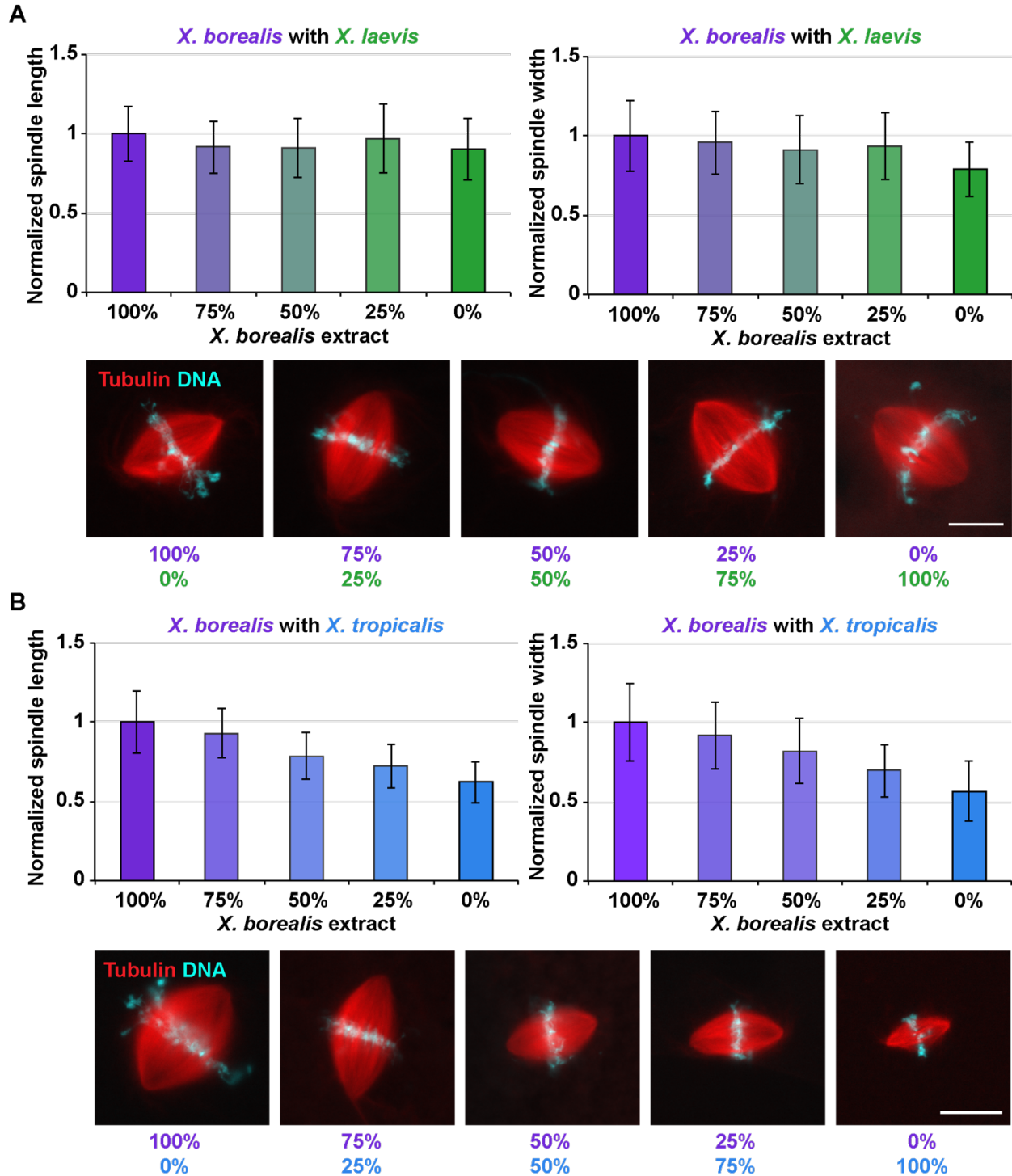
Quantification of spindle phenotypes observed in egg extract reactions containing RanT24N or RanQ69L. Data are from 3 independent experiments for each species. Statistical significance was determined by a two-tailed 3x2 Fisher's exact test. Untreated reactions are not significantly different between species. T24N reactions are all significantly different between species. Q69L reactions are only significantly different between *X. laevis* and *X. tropicalis*.

### **Common spindle scaling mechanisms operate among *Xenopus* species**

It has been shown that hybrid embryos can be generated by fertilization of *X. borealis* eggs with sperm from either *X. laevis* and *X. tropicalis* (De Robertis and Black, 1979; Gibeaux et al., 2018), indicating compatibility between the *X. borealis* cytoplasm and the chromosomes of both species. Addition of either *X. laevis* or *X. tropicalis* sperm nuclei to *X. borealis* extract did not alter spindle microtubule distribution (Fig. 2.9A), consistent with previous studies indicating that egg cytoplasm composition is the primary determinant of spindle morphology (Brown et al., 2007). To determine whether maternal cytoplasmic factors affect spindle size similarly among the three *Xenopus* species, we mixed *X. borealis* egg extract with either *X. laevis* or *X. tropicalis* extract in the presence of *X. laevis* or *X. tropicalis* sperm nuclei, respectively. Whereas titration of *X. borealis* extract with *X. laevis* did not affect spindle dimensions (Fig. 2.8A), *X. tropicalis* extract caused *X. borealis* spindles to shrink proportionately with the amount added (Fig. 2.8B). Analysis of spindle microtubule distributions in mixed extracts revealed that these were also affected proportionately, favoring the tubulin distribution of the more abundant extract (Fig. 2.9B and C). These results are consistent with cytoplasmic mixing of *X. laevis* with *X. tropicalis* extracts, which also caused spindle shrinkage in a dose-dependent manner

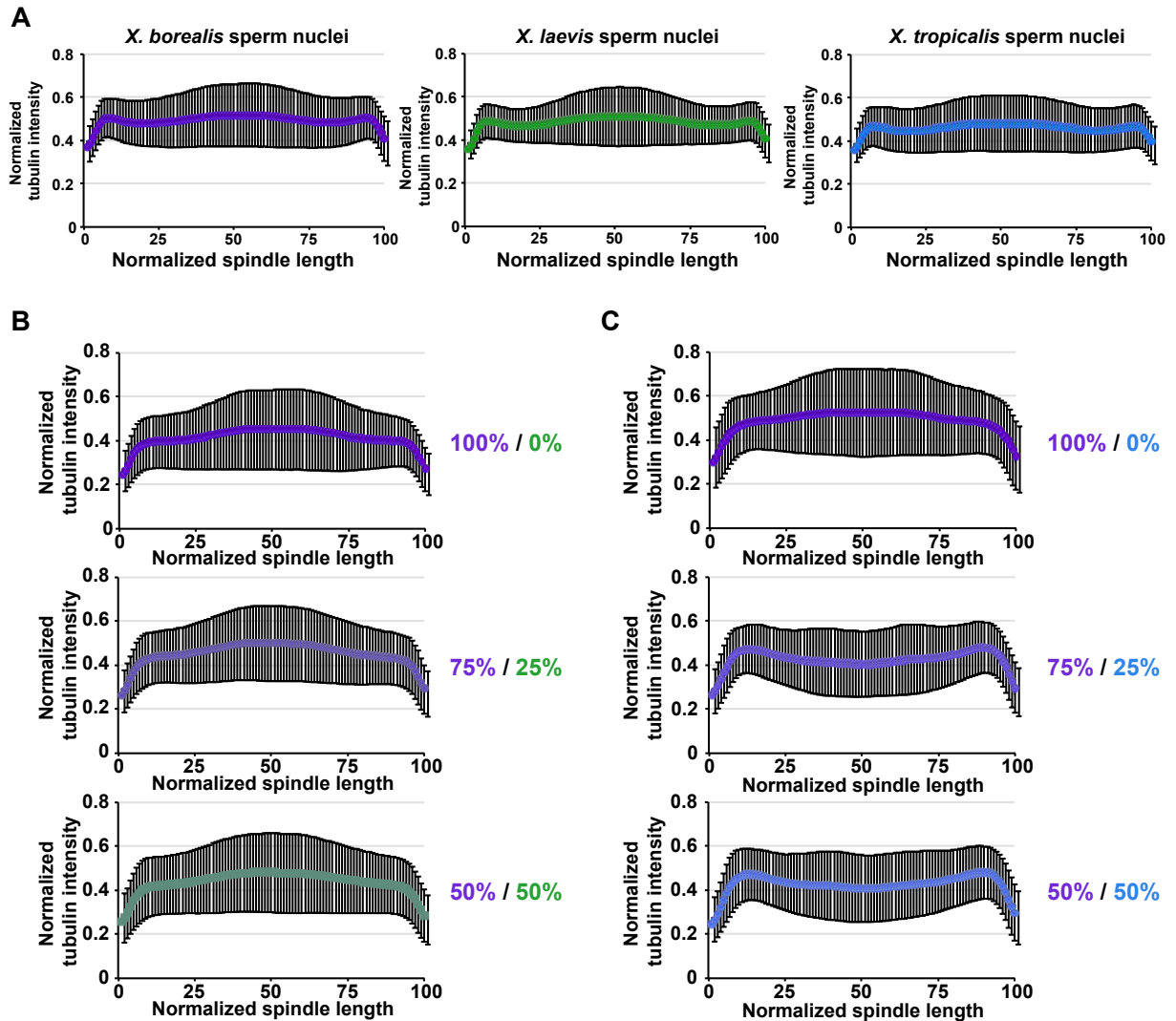
(Brown et al., 2007). Altogether, these data indicate that common scaling and microtubule organization mechanisms operate among the three *Xenopus* species.

**Figure 2.8**



**(A)** *X. borealis* extract mixed with *X. laevis* extract. Spindle length (left panel) and width (right panel) are plotted as columns, with colors proportionate to the amount of *X. laevis* (green) added to *X. borealis* (purple) (n = 341 for 100% *X. borealis*, 0% *X. laevis*; n = 350 for 75% *X. borealis*, 25% *X. laevis*; n = 331 for 50% *X. borealis*, 50% *X. laevis*; n = 313 for 25% *X. borealis*, 75% *X. laevis*; and n = 267 for 0% *X. borealis*, 100% *X. laevis* over 3 independent experiments). **(B)** *X. borealis* extract mixed with *X. tropicalis* extract. Spindle length (left panel) and width (right panel) are plotted as columns, with colors proportionate to the amount of *X. tropicalis* (blue) added to *X. borealis* (purple) (n = 295 for 100% *X. borealis*, 0% *X. tropicalis*; n = 306 for 75% *X. borealis*, 25% *X. tropicalis*; n = 295 for 50% *X. borealis*, 50% *X. tropicalis*; n = 337 for 25% *X. borealis*, 75% *X. tropicalis*; and n = 334 for 0% *X. borealis*, 100% *X. tropicalis* over 3 independent experiments). In **A-B**, spindle length and width were normalized to the length and width, respectively, of 100% *X. borealis* CSF spindles. Error bars represent the standard deviation. Representative images are shown with tubulin (red) and DNA (blue) signal. Scale bar is 20  $\mu\text{m}$ .

**Figure 2.9**



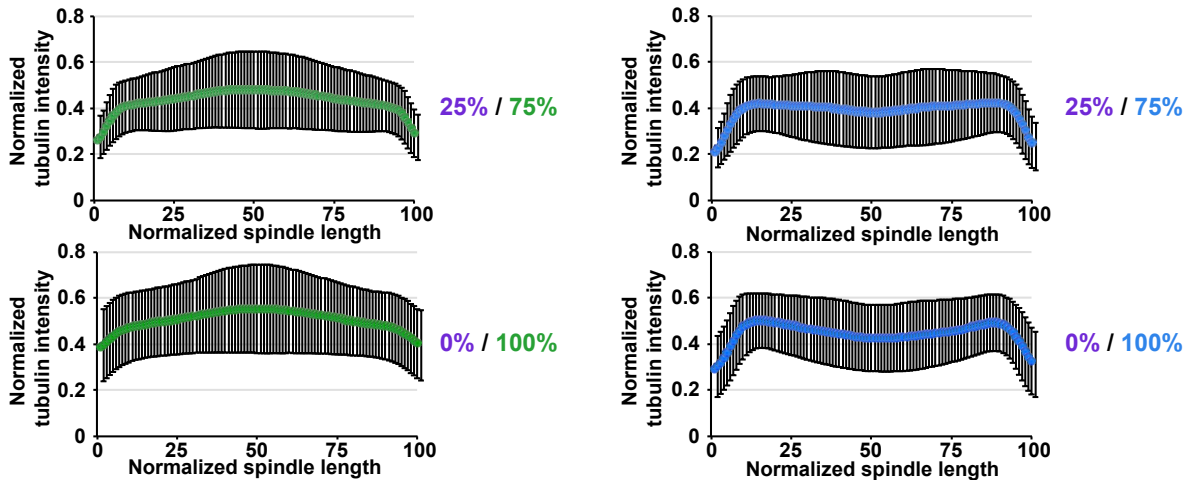


**Figure 2.9: Effects of cytoplasmic mixing on microtubule distribution**

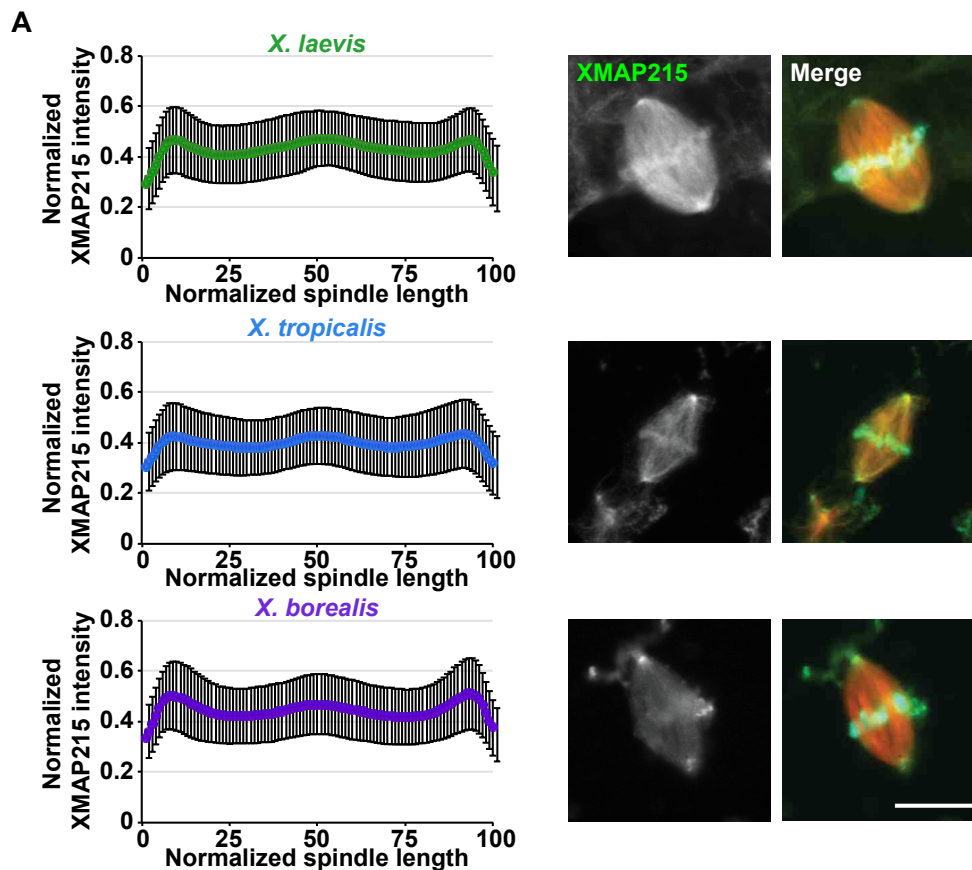
**(A)** Microtubule intensity distribution in spindles formed around *X. borealis* (purple), *X. laevis* (green), and *X. tropicalis* (blue) sperm nuclei in *X. borealis* egg extract ( $n = 316$  for *X. borealis* sperm nuclei,  $n = 307$  spindles for *X. laevis* sperm nuclei, and  $n = 307$  for *X. tropicalis* sperm nuclei, from 3 independent *X. borealis* egg extracts). **(B)** Microtubule distribution in spindles formed in mixed extracts of *X. laevis* (green) and *X. borealis* (purple) ( $n = 301$  for 100% *X. borealis*, 0% *X. laevis*;  $n = 338$  for 75% *X. borealis*, 25% *X. laevis*;  $n = 322$  for 50% *X. borealis*, 50% *X. laevis*;  $n = 295$  for 25% *X. borealis*, 75% *X. laevis*; and  $n = 240$  for 0% *X. borealis*, 100% *X. laevis* over 3 independent experiments). **(C)** Microtubule distribution in spindles formed in mixed extracts of *X. tropicalis* (blue) and *X. borealis* (purple) ( $n = 283$  for 100% *X. borealis*, 0% *X. tropicalis*;  $n = 272$  for 75% *X. borealis*, 25% *X. tropicalis*;  $n = 260$  for 50% *X. borealis*, 50% *X. tropicalis*;  $n = 272$  for 25% *X. borealis*, 75% *X. tropicalis*; and  $n = 305$  for 0% *X. borealis*, 100% *X. tropicalis* over 3 independent experiments). In **A-C**, line scans of rhodamine-tubulin signal along the length of the spindle were measured. Spindle length was normalized to 100% and tubulin intensities were normalized within each dataset. Average tubulin intensities were plotted. Error bars represent the standard deviation.

### ***X. borealis* spindles combine scaling factor features of both *X. laevis* and *X. tropicalis***

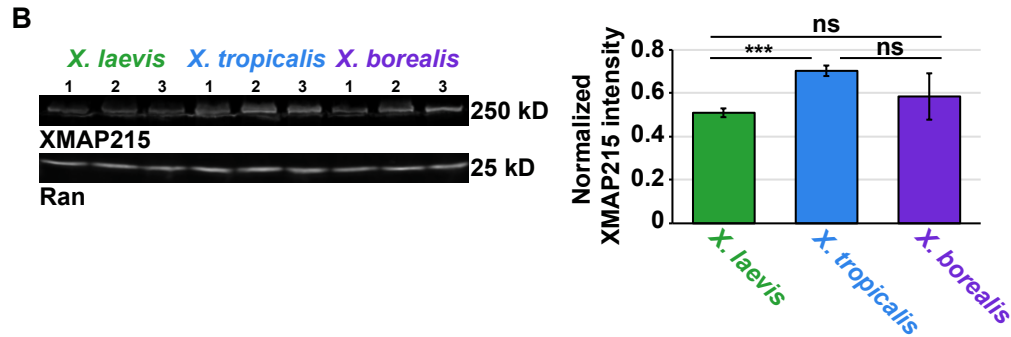
To investigate the molecular basis of *X. borealis* spindle size and morphology, we compared the localization, abundance, and sequence of katanin and TPX2, two spindle scaling factors that contribute to spindle size differences between *X. laevis* and *X. tropicalis*, as well as the microtubule polymerase XMAP215, levels of which have been shown to regulate spindle length in *Xenopus* (Reber et al., 2013). XMAP215 levels and localization were similar for all three *Xenopus* species (Fig. 2.10). Katanin, a microtubule severing AAA-ATPase, has higher activity in *X. tropicalis* due to the absence of an inhibitory phosphorylation site (Serine 131) found in the *X. laevis* protein (Loughlin et al., 2011). Immunofluorescence and line scan analysis of spindles revealed that katanin localization on the *X. borealis* spindle displays a small but distinct increase at the metaphase plate as well as the spindle poles, while the localization on *X. laevis* spindles is more uniform and *X. tropicalis* shows katanin enrichment solely at the poles (Fig. 2.11A). By Western blot, katanin levels did not differ significantly across the three species (Fig. 2.11B). Although the amino acid sequence of *X. borealis* katanin is over 97% identical to that of both *X. tropicalis* and *X. laevis*, it contains the key inhibitory serine residue that regulates katanin activity in *X. laevis* (Fig. 2.12). It remains to be determined

whether katanin activity is similarly regulated in *X. borealis*. TPX2 is a Ran-regulated microtubule-associated protein that is found at three-fold higher concentrations in *X. tropicalis* compared to *X. laevis*. Increasing the level of TPX2 in *X. laevis* extracts to that of *X. tropicalis* was previously shown to reduce spindle length through its increased recruitment of the spindle motor Eg5 to spindle poles (Helmke and Heald, 2014). Interestingly, *X. borealis* spindles displayed an overall TPX2 localization more similar to *X. tropicalis*, with higher intensity at the spindle poles, but also possessed a central smaller peak of TPX2 reminiscent of *X. laevis* (Fig. 2.11C). Levels of TPX2 in *X. borealis* egg extracts were two-fold higher than in *X. laevis*, but not elevated to *X. tropicalis* levels. (Fig. 2.11D). Notably, the amino acid sequence of *X. borealis* TPX2 is more similar to *X. laevis* compared to *X. tropicalis* and contains the seven amino acid residues thought to reduce microtubule nucleation activity of *X. laevis* TPX2 (Fig. 2.13) (Helmke and Heald, 2014; Grenfell et al., 2016b). Altogether, these results suggest that *X. borealis* spindle length results from its lower katanin activity similar to *X. laevis*, while its microtubule distribution is likely affected by increased levels of TPX2, which is more reminiscent of *X. tropicalis*.

**Figure 2.10**



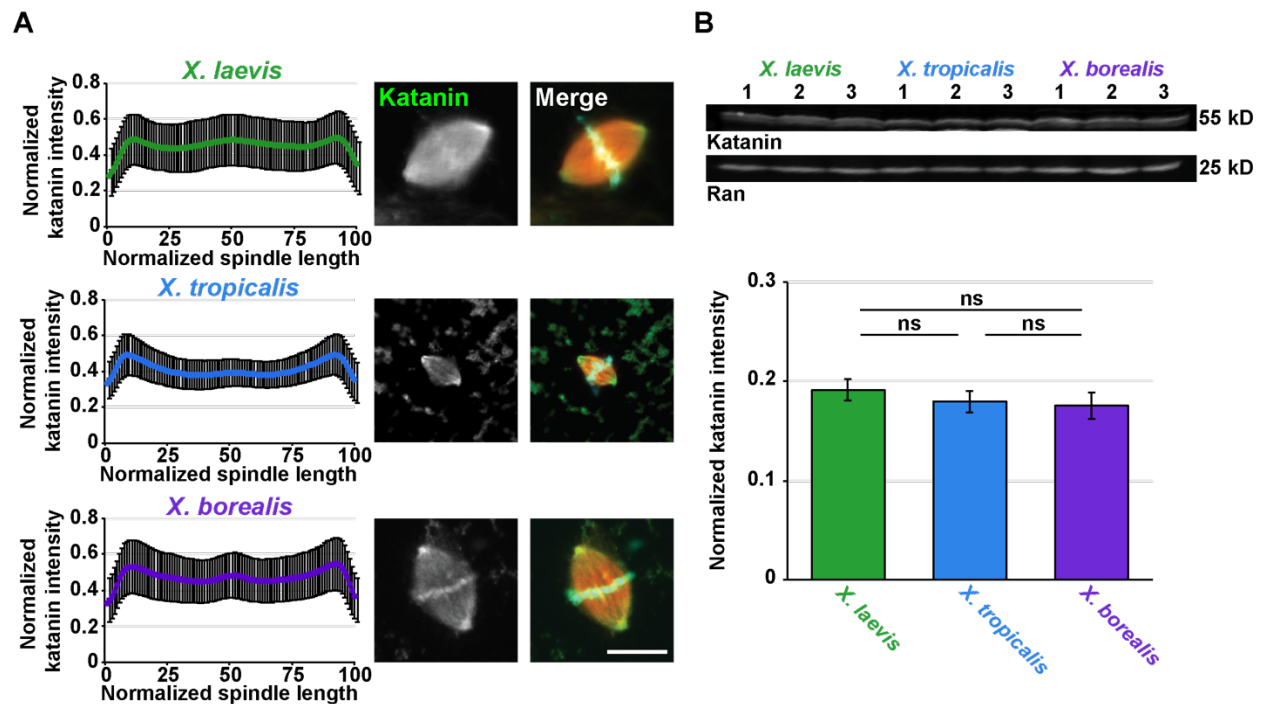




**Figure 2.10: Localization of XMAP215 on *X. borealis* spindles**

(A) XMAP215 localization in *X. laevis* (green), *X. tropicalis* (blue), and *X. borealis* (purple) spindles. Line scans of Alexa Fluor 488 signal along the length of the spindle were measured (n = 420 spindles for *X. laevis*, n = 390 for *X. tropicalis*, and n = 338 for *X. borealis*, from 3 independent egg extracts for each species). Spindle length was normalized to 100%, and XMAP215 intensities were normalized within each dataset. Average XMAP215 intensities were plotted for each species' spindles. Error bars represent the standard deviation. Representative images of spindles formed around *X. laevis*, *X. tropicalis*, and *X. borealis* sperm nuclei in their respective egg extracts are shown with XMAP215 signal in gray scale (left) and merged with tubulin and DNA signals (right). Scale bar is 20  $\mu$ m. (B) Western blot of *X. laevis*, *X. tropicalis*, and *X. borealis* extracts probed for XMAP215. XMAP215 band integrated density is plotted as columns for *X. laevis* (green), *X. tropicalis* (blue), and *X. borealis* (purple) extracts, with 3 independent extracts analyzed for each species. Band intensity was normalized to the integrated density of the corresponding Ran loading control. Error bars represent the standard deviation. Statistical significance was determined by a two-tailed, two-sample unequal variance t-test.

**Figure 2.11**



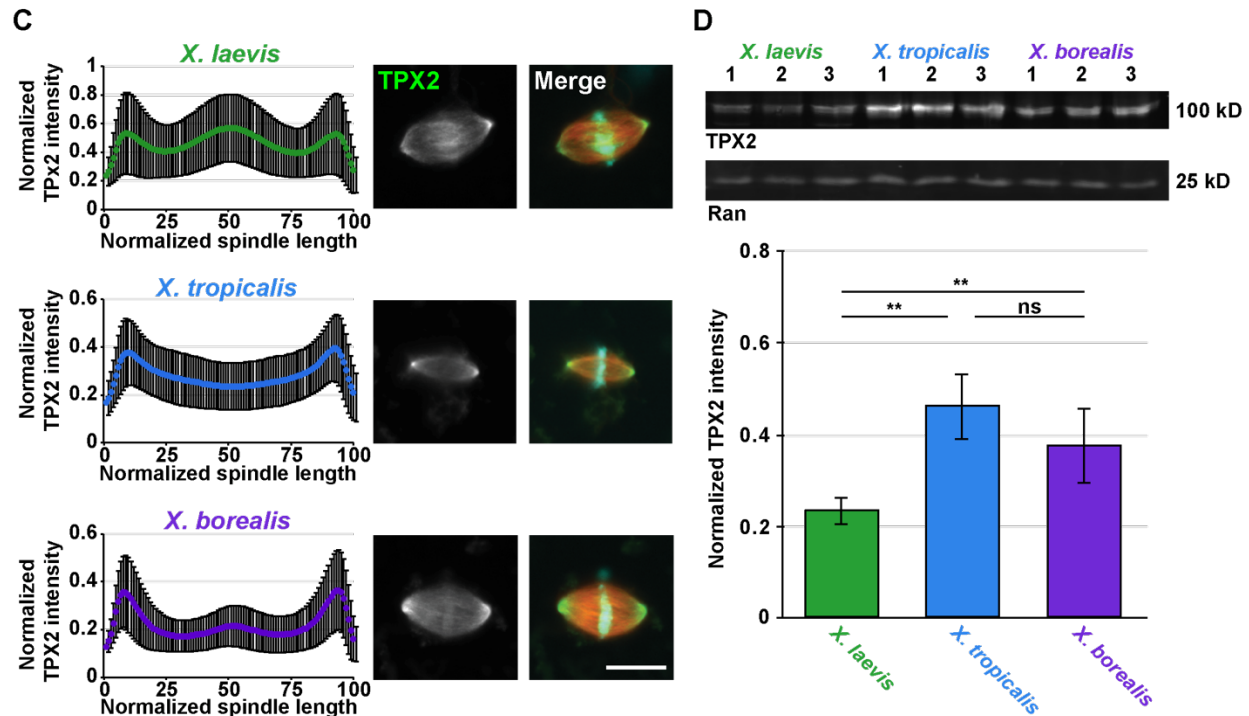


**Figure 2.11: Localization of scaling factors katanin and TPX2 on *X. borealis* spindles**

(A) Katanin immunofluorescence staining of *X. laevis* (green), *X. tropicalis* (blue), and *X. borealis* (purple) spindles. Line scans of Alexa Fluor 488 signal along the length of the spindle were measured ( $n = 385$  spindles for *X. laevis*,  $n = 408$  for *X. tropicalis*, and  $n = 348$  for *X. borealis*, from 3 independent egg extracts for each species). (B) Western blots of *X. laevis*, *X. tropicalis*, and *X. borealis* extracts probed for katanin. (C) TPX2 immunofluorescence staining of *X. laevis* (green), *X. tropicalis* (blue), and *X. borealis* (purple) spindles. Line scans of Alexa Fluor 488 signal along the length of the spindle were measured ( $n = 406$  spindles for *X. laevis*,  $n = 433$  for *X. tropicalis*, and  $n = 418$  for *X. borealis*, from 3 independent egg extracts for each species). (D) Western blots of *X. laevis*, *X. tropicalis*, and *X. borealis* extracts, probed for TPX2. In A and C, spindle length was normalized to 100% and katanin or TPX2 intensities, respectively, were normalized within each dataset. Average TPX2 intensities were plotted for each species' spindles. Error bars represent the standard deviation. Representative images of spindles formed from *X. laevis*, *X. tropicalis*, and *X. borealis* sperm nuclei in their respective egg extracts are shown with katanin or TPX2 grayscale signal (left) and merged with tubulin and DNA signals (right). Scale bar is 20  $\mu\text{m}$ . In B and D, katanin or TPX2 band integrated densities are plotted as columns for *X. laevis* (green), *X. tropicalis* (blue), and *X. borealis* (purple) extracts (3 independent extracts are shown for each species). Band intensities were normalized to the integrated density of the corresponding Ran loading control. Error bars represent the standard deviation. Statistical significance was determined by a two-tailed, two-sample unequal variance t-test.

**Figure 2.12**

KATANIN		
X. tropicalis	MSLLMISENVKLALEYALLGNYSAMVYYQGVLDQMNKYLVSVDKTFLQQKWQQVWQEQIN	60
X. laevis.S	MSLLMISENVKLALEYALLGNYSAMVYYQGVLDQMNKYLVSVDKTFLQQKWQQVWQEQIN	60
X. borealis.S	MSLLMISENVKLALEYALLGNYSAMVYYQGVLDQMNKYLVSVDKTFLQQKWQQVWQEQIN *****	60
X. tropicalis	MEAKHVKDIMSTLEGFKLDNSPVKTTQHEFFPAHDGEVWSLPVPVRRRPSFGPRKRQSVQC	120
X. laevis.S	MECKHVKDIMSTLEGFKLDSSPVKTTQHEFFPSHDGEVWSLPVPVRRRPSFGPRKRQSVQC	120
X. borealis.S	MEAKHVKDIMSTLEGFKLDNSPVKTTQHEFFPAHDGEVWSLPVPVRRRPSFGPRKRQSVQC **.*.....*.....*.....*.....*.....*.....*	120
X. tropicalis	NDNKSHNNRFGA-GKGNLPSKNTNNVVKMFPVRAREKKDFTLKVDEKNKSSVDVSETE	179
X. laevis.S	NDNKSHNNRFSAAAKGNLPSARNANNVVKMFPVRAREKKDALIK----NKSSADVSETE	175
X. borealis.S	NDNKSHNNRFSAAAKGNLPSARNANNVVKMFPVRAREKKDALLKVKDEKNKSSVDVSETE *****.*.....*.....*.....*.....*.....*.....*	180
X. tropicalis	VKKFDGTGYDKDLIEALERDIISQNPNIIRWDDIADLEAKKLLKEAVVLEPMWPEFFKGI	239
X. laevis.S	VKRFDGSGYDKDLIEALERDIISQNPNIIRWDDIADLEAKKLLKEAVVLEPMWPEFFKGI	235
X. borealis.S	VKKFDGAGYDKDLIEALERDIISQNPNIIRWDDIADLEAKKLLKEAVVLEPMWPEFFKGI **.*.....*.....*.....*.....*.....*.....*	240
X. tropicalis	RRPWKGLVMGPPGTGKTLAKAVATECKTTFNIISSSTLTSKYRGESEKLVRLLFEMAR	299
X. laevis.S	RRPWKGLVMGPPGTGKTLAKAVATECKTTFNIISSSTLTSKYRGESEKLVRLLFEMAR	295
X. borealis.S	RRPWKGLVMGPPGTGKTLAKAVATECKTTFNIISSSTLTSKYRGESEKLVRLLFEMAR *****	300
X. tropicalis	FYAPTTIFIDEIDSICSRRTSEHEASRRVKAELLVQMDGVGGASENEDPSKMVMVLAA	359
X. laevis.S	FYAPTTIFIDEIDSICSRRTSEHEASRRVKAELLVQMDGVGGASENEDPSKMVMVLAA	355
X. borealis.S	FYAPTTIFIDEIDSICSRRTSEHEASRRVKAELLVQMDGVGGASENEDPSKMVMVLAA *****	360
X. tropicalis	TNFPWDIDEALRRRLEKRIYIPLPSAKGRELLRINLKELELADDVNIETIAENMDGYSG	419
X. laevis.S	TNFPWDIDEALRRRLEKRIYIPLPSAKGRELLRINLKELELADDVNIETIAENMDGYSG	415
X. borealis.S	TNFPWDIDEALRRRLEKRIYIPLPSTKGRELLRINLKELELADDVNIETIAENMDGYSG *****	420
X. tropicalis	ADITNVCRDASLMAMRRRIEGLTPEEIRNLSRDDMHMPTMEDFEMALKKVSQSASDI	479
X. laevis.S	ADITNVCRDASLMAMRRRIEGLTPEEIRNLSRDDMHMPTMEDFEMALKKVSQSASDI	475
X. borealis.S	ADITNVCRDASLMAMRRRIEGLTPEEIRNLSRDDMHMPTMEDFEMALKKVSQSASDI *****	480
X. tropicalis	EKYEKWIEEFGSC	492
X. laevis.S	EKYEKWIEEFGSC	488
X. borealis.S	EKYEKWIEEFGSC *****	493

**Figure 2.12: Protein sequence alignments of *Xenopus* katanin**

Protein sequences of *X. tropicalis*, *X. laevis*, and *X. borealis* katanin were aligned using Clustal Omega (default parameters). The *X. borealis* sequence is 97.6% identical to that of *X. tropicalis*, and 97.0% identical to *X. laevis*. The red box indicates the key regulatory serine residue at position 131.

Figure 2.13

TPX2		
X. tropicalis	MAEAQDLYTFDAPSTFINFTAFHEDHGADSWFDKVTNAENIPDQRLSEIPAVNAEQNG	60
X. laevis.L	MEDTQDITYSDAPSIIF-NFSSFHDDHNADSWFDQVTNAENIPDQRLSET-SVNTSEQNS	58
X. laevis.S	MADAQDITYSDAPSIIF-NFSSFHDDHNADSWFDQLTNAENIPDQKPLSET-SVNAEQNC	58
X. borealis	MADAQDSYTYDAPSIIF-NFSSFNEDHNADSWFDQVTNAENIPDPIQLSEN-SVNAEQNC	58
X. tropicalis	MVEPEETSPSKETVSESAAHFSDGKSQARRSSRRMSRKHQRKLLVKMRETRLEKETAQSD	120
X. laevis.L	KVEPVQTTSPKDDVSNATHVCDVKSQKRSSRRMSRKHQRKLLVKMMDTHLEKETAPPE	118
X. laevis.S	KVEPGKITPSKEEVKSTTHVCDVKSQTKRSARRMSRKHQRKLLVKMETHLEKETAQSE	118
X. borealis	EVEPGKETPSKEEVKRTTHVCDVKSQTKRSARRMSRKHQRKLLVKMKE---KETTQSE	114
X. tropicalis	CPPTKKLKGSSTKGARTPVIRGQPPRSGHGNSNTPRPKAPLTLPTPTVLKRNVMVKPKS	180
X. laevis.L	YPPCKKLGSSSKGRHAPVIKQSTSSHSMSTSPKPAQLTMPSTPTVLKRRNVLVKAKN	178
X. laevis.S	YPPCKKLGSSTKDRQAPVIRGQPTSSHGHTSPKPAQLTMPPTPTVLKRRNVLAKSKS	178
X. borealis	YPPCKKLGSSTKDRHAPVIRGQPTSHLGTASPKPAHLMPPTPTVLKRRNMLAKCKN	174
X. tropicalis	SEEQELRMQELQKEMLENLKNNEHSMKAAISGTPSVKSAVPITKPVDFHFKTDDRPK	240
X. laevis.L	SEEQELKMQELQKEMLENLKNNEHSMKVAITGAGQVPK-TFIPVTKPVDFHFKTDDRKL	237
X. laevis.S	SEEQELKMQALQKEMLENLKNNEHSMKVAISGAGQVPK-NFIPVTKPVDFHFKTDDRKL	237
X. borealis	SEEQELKMQELQKEMLEHLKNEQSMKVAISGAGQVPK-NVIPVTKPVDFHFKTDDRKL	233
X. tropicalis	RVADQPKGEYKEVDFAAALRKHPPSPV--SKAALVTPKPFNLKGRKRHEEASEFVSTA	298
X. laevis.L	RTANQPEGDGYKAVDFASLVRKHPPSPVQVTKGGHTVPPKPFNLKGRKRHEEASDVSTA	297
X. laevis.S	RNANPPEGDGYKEVDFASVLRKPPSPVQVTKGGHTVPPKPFNLKGRKRHEEASDFVSTA	297
X. borealis	RSANLEPGDGYKEVDFASLVRKPPSPVQVTKGGHTVPPKPFNLKGRKRHEEASDFVSTA	293
X. tropicalis	EQVIFSFKKTPARYHLRSRQRELEGPSFVKMVRPKLTNPKTPLLQTKQRLRPVMCKSAAE	358
X. laevis.L	EQVIAFYKRTTPARYHLRSRQREMEGPSFVKMKTKLTNPKTPLLQTKGRHRPVTCKSAAE	357
X. laevis.S	EQVVAFYRRTTPARYHLRSRQREMEGPSFVKMLKPKLTNPKTPLLQTKQRHRPVTCKSAAE	357
X. borealis	EQVVAFYRRTTPARYHLRSRQREMEGPSFVKMMKPKLTNPKTPLLQTKQRHRPVTCKSAAE	353
X. tropicalis	LEAEELERIQYKFKAQELDSRILEGAQVLPKPKPVKEPTKAIGFDLEIEKRIQQREKRD	418
X. laevis.L	LEAEELMINQYKFKAQELDTRILEGGPVLKPKPLVKEPTKAIGFDLEIEKRIQQREKKE	417
X. laevis.S	LEAEELDMIHQYKFKAQELDTRILEGGPVLKPKPSVKEPTKAIGFDLEIEKRIQQREKRD	417
X. borealis	LEAEELERIHQYKFKARELDTKILEGAPVLPKPKPSVKEPTKAIGFDLEIEKRIQQREKRD	413
X. tropicalis	EGEEEAFTFHSRCPCKILLTEVVGVPKLLPVTVPSPFALKNRVRLPAREEK-EEEV	477
X. laevis.L	EIEEETFTFHSRCPCKMLTDVVGVPKLLPVTVPQSPAFALKNRVRIPAQEEKQEMV	477
X. laevis.S	EVEEEAFTFHSRCPCKILADVVGVPQKLLPVTVPQSPAFALKNRVRIPAQEEK-EEEV	476
X. borealis	EGEEEAFTFHSRCPCKILADVVGVPQKLLPVTVPQSPAFALKNRVRIPAQEEQEEEV	473
X. tropicalis	PAIKATAMPHYGVPPKPLVQQRQVEVCPFSFDQDRERLLRKEKMEELRKEEVHKFKA	537
X. laevis.L	PVIKATAMPHYGVPPKPLVQQRQVDCVCPFSFCDRDKERLQKPKRLDELRLKDEVPKFA	537
X. laevis.S	PVIKATAMPHYGVPPKPLVQKQVEACPFSCERDKERLQKPKRLDELRLKDEEVKFA	536
X. borealis	PVIKATAMPHYGVPPKPLVQKQVEACPFSCERDKERLQKPKRLDELRLKDEEVKFA	533
X. tropicalis	QPLPEFGHVSLEPKRVKMPQQEPPFVLEIDKRGAPLQRWQQQVKEEQKQKEMAVFKAR	597
X. laevis.L	QPLPQFDNIRLPEKKVKMPTQQEPPFLEIDKRGASKLQRWQQQIQEELKQKEMVVFAR	597
X. laevis.S	QRLPQFDHISLPEKKVKMPTQQEPPFLEIDKRGATKLRWQHQIKBELKQKEMVVFAR	596
X. borealis	QPLPQFDHISLPEKKVKIPTQQEPPFLEIDKRGASKLQRWQIQIKELKQKEMVVFAR	593
X. tropicalis	PNTVVHQEPFVPKKESRCLTA-----TEGFELATEKRAKERQEFKSLAEMEAQKSL	650
X. laevis.L	PNTVVHQEPFVPKKENSRLTESLSGSIQEGFELATAKRAKERQEFKCLAETAQKSL	657
X. laevis.S	PNTVVHQEPFVPKKENSRLTDSLGSMIQEGFELATAKRAKERQEFKCLAEMEAQKSL	656
X. borealis	PNTVVHQEPFVPKKENSRLTDSLGSASIIQEGFELATAKRAKERQEFKCLAEMEAQKSL	653
X. tropicalis	EEETRQRQEEEEEREEISHLRKLKLVHKAQPIRKYKAVDVKASDTPLTIPESFNFSDFK	709
X. laevis.L	EEEIRKRREEEKKEEISQLRQELVHKAQPIRKYRAVEVKASDVPLTVPSFNFSDFK	716
X. laevis.S	EEETRQRQEEEEEREEINQLRQELVHKAQPIRKYKAVEVKASDVPLTVPSFNFSDFK	715
X. borealis	EEETRKRREEEEREEISQLRQELVHKAQPIRKYRAVEVKASDVPLTVPSFNFSDFK	712

Figure 2.13: Protein sequence alignments of *Xenopus* TPX2

Protein sequences of *X. tropicalis*, *X. laevis*, and *X. borealis* TPX2 were aligned using Clustal Omega (default parameters). The *X. borealis* sequence is 75.7% identical to *X. tropicalis*, and 85.8% and 91.3% identical to sequences from the two subgenomes of *X. laevis*, L and S, respectively. The red box indicates the key 7 amino acids at position 619-624 that are absent from *X. tropicalis* and regulate microtubule nucleation activity.

## 2.3 DISCUSSION

Overall, these observations reveal that *X. borealis* meiotic spindles, although more similar in size and RanGTP-dependence to *X. laevis*, also possess some structural and molecular features characteristic of *X. tropicalis*. These findings support the idea that katanin and TPX2 are important spindle length control and assembly factors in *Xenopus*. Katanin-mediated microtubule severing activity has been shown to regulate spindle size in several organisms, including *Caenorhabditis elegans*, *Xenopus*, and human cells (McNally et al., 2006; Loughlin et al., 2011; Joly et al., 2016; Jiang et al., 2017), which is consistent with results from meiotic spindle assembly simulations showing that altering microtubule depolymerization rates robustly scales spindle length (Loughlin et al., 2010).

The role of TPX2 in spindle assembly and size control is more complicated. Depletion of the TPX2 ortholog D-TPX2 from *Drosophila melanogaster* syncytial embryos and S2 cells resulted in spindle shortening (Goshima, 2011; Hayward and Wakefield, 2014), and human cells require phosphorylation of TPX2 by Aurora A for normal spindle length (Bird and Hyman, 2008; Fu et al., 2015). In contrast, addition of recombinant TPX2 to *X. laevis* extracts decreased spindle length (Helmke and Heald, 2014), and we have observed similar effects on *X. borealis* spindles (unpublished data). Spindle-shrinking effects in *Xenopus* did not depend on Aurora A, but rather on a change in spindle microtubule distribution caused by increased recruitment of the cross-linking Eg5 motor to spindle poles (Helmke and Heald, 2014). TPX2 also regulates microtubule nucleation in the spindle (Alfaro-Aco et al., 2017; Petry et al., 2013; Scrofani et al., 2015; Petry, 2016). TPX2 has thus emerged as a central player of spindle assembly and organization in a wide variety of cell types (Ma et al., 2011; Helmke et al., 2013; Fu et al., 2015; Levy and Heald, 2016) and is overexpressed in many cancers (Chang et al., 2012; Neumayer et al., 2014). Our results highlight the importance of TPX2 levels and localization as determinants of meiotic spindle microtubule architecture. TPX2 localization (Fig. 2.11C) correlates well with the distribution of tubulin intensity across all three species (Fig. 2.5B), particularly at the spindle poles (Ma et al., 2011; Helmke and Heald, 2014). Despite having higher TPX2 levels, the greater sequence similarity of *X. borealis* TPX2 to the *X. laevis* protein (Fig. 2.13) may explain the increased sensitivity to Ran inhibition in *X. borealis* (Fig. 2.7C), since a 7 amino acid sequence shown to decrease microtubule nucleation activity relative to *X. tropicalis* is present in both *X. borealis* and *X. laevis* TPX2 (Fig. 2.11D) (Helmke and Heald, 2014). Altogether, our results provide clues to how TPX2 levels may tune meiotic spindle architecture and assembly pathways by altering microtubule nucleation and organization.

In summary, *Xenopus borealis* provides a robust in vitro egg extract that adds to the characterized *X. laevis* and *X. tropicalis* systems, enabling further investigation of spindle assembly and interspecies scaling. Our findings highlight that egg meiosis II spindle architecture varies across *Xenopus* species and suggest that *X. borealis* spindles assemble with a combination of *X. laevis* as well as *X. tropicalis* features.

## 2.4 MATERIALS and METHODS

### Chemicals

Unless otherwise stated, all chemicals were purchased from Sigma-Aldrich, St. Louis, MO.

### Frog care

All animal experimentation in this study was performed according to our Animal Use Protocol approved by the UC Berkeley Animal Care and Use Committee. Mature *X. laevis*, *X. tropicalis*, and *X. borealis* frogs were obtained from NASCO, WI. *X. laevis*, *X. tropicalis*, and *X. borealis* females were ovulated with no harm to the animals with a 6-, 3-, and 4-month rest interval, respectively. To obtain testes, males were euthanized by over-anesthesia through immersion in ddH<sub>2</sub>O containing 0.15% MS222 (Tricaine) neutralized with 5 mM sodium bicarbonate prior to dissection, and then frozen at -20°C.

### Sperm nuclei purification

*X. laevis* and *X. tropicalis* sperm nuclei were prepared and purified as previously described (Grainger, 2012). The following modifications were made for *X. borealis* sperm nuclei purification. *X. borealis* males were primed with 40 U of PMSG 3 days prior to dissection and boosted with 100 U hCG 12-24 h before dissection. Testes were removed and cleaned from all blood vessels and fat with forceps. Testes were then washed 3X in cold 1X MMR (1X MMR: 100 mM NaCl, 2 mM KCl, 2 mM CaCl<sub>2</sub>, 1 mM MgCl<sub>2</sub> and 5 mM HEPES-NaOH pH 7.6, 0.1 mM EDTA) and 3X in cold Nuclear Preparation Buffer (NPB) (2X NPB: 500 mM sucrose, 30 mM HEPES, 1 mM spermidine trihydrochloride, 0.4 mM spermine tetrahydrochloride, 2 mM dithiothreitol, 2 mM EDTA) and placed in 1 mL of cold NPB for homogenization with scissors and a pestle. Samples were briefly spun to pellet the remaining tissue before transferring the supernatant to a new tube for centrifugation at 1500 g for 10 min at 4°C to pellet sperm. The pellet was resuspended in 1 mL NPB supplemented with 50 µL of 10 mg/mL lysolecithin and incubated for 5 min at RT. The resuspended pellet was then added to 4 mL of cold NPB supplemented with 3% BSA and spun at 3,000 RPM for 10 min at 4°C. The resulting pellet was resuspended in 2 mL of cold NPB with 0.3% bovine serum albumin (BSA) and 30% filtered glycerol. Finally, the pellet was resuspended in 500 µL of cold NPB with 0.3% BSA and 30% filtered glycerol. Sperm nuclei were adjusted to a concentration of 10<sup>8</sup> nuclei per mL using cold NPB with 0.3% BSA and 30% glycerol to make a 200X stock, aliquoted, frozen in liquid nitrogen, and stored at -80°C.

### In vitro fertilization

*X. borealis* males were injected with 300 U of human chorionic gonadotropin hormone (hCG) 12-24 h before dissection and testes were collected in Leibovitz L-15 Medium (Gibco – Thermo Fisher Scientific, Waltham, MA) supplemented with 10% Fetal Bovine Serum (FBS; Gibco) for immediate use. *X. laevis* males were injected with 500 U of hCG 12-24 h before dissection and testes were stored at 4°C in 1X MR (100 mM NaCl, 1.8 mM KCl, 2 mM CaCl<sub>2</sub>, 1 mM MgCl<sub>2</sub> and 5 mM HEPES-NaOH pH 7.6) for 1-2 weeks. *X. borealis* and *X. laevis* females were primed with 60 U and 100 U, respectively, of pregnant mare serum gonadotrophin (PMSG, National Hormone and Peptide Program,

Torrance, CA) at least 48 h before use and boosted with 300 U and 500 U, respectively, of hCG 12-24 h before the experiment. *X. borealis* and *X. laevis* frogs were kept at 16°C in 0.5X and 1X MMR, respectively. *X. borealis* eggs were picked from the tub and deposited onto petri dishes coated with 1.5% agarose in 1/10X MMR. *X. laevis* females were squeezed gently to deposit eggs onto petri dishes coated with 1.5% agarose in 1/10X MMR. Two *X. borealis* testes or 2/3 of an *X. laevis* testis were collected and homogenized using scissors and a pestle in 1 mL of L-15 and 10% FBS. Any excess liquid in the petri dishes was removed, and the eggs were fertilized with 500 µL of sperm solution per dish. Eggs were swirled in the solution to individualize eggs as much as possible and incubated for 5 min. Dishes were flooded with ddH<sub>2</sub>O, swirled and incubated for 10 min, followed by buffer exchange to 1/10X MMR and incubation for 10 min. The embryo jelly coats were then removed with a 3% cysteine solution in ddH<sub>2</sub>O-NaOH, pH 7.8. After extensive washing (>4X) with 1/10X MMR, embryos were incubated at 23°C. At stage 2-3, fertilized embryos were sorted and placed in fresh 1/10X MMR in new petri dishes coated with 1.5% agarose in 1/10X MMR.

All embryos were staged according to Nieuwkoop and Faber (Nieuwkoop and Faber, 1994).

### **Embryo video imaging**

Imaging dishes were prepared using a homemade PDMS mold designed to print a pattern of 1 mm large wells in agarose that allowed us to image 4 *X. borealis* or *X. laevis* embryos simultaneously within the 3X4 mm camera field of view for each condition. Embryos were imaged from stage 2-3. Videos were taken simultaneously using two AmScope MD200 USB cameras (AmScope, Irvine, CA) each mounted on an AmScope SE305R stereoscope. Time lapse movies were acquired at a frequency of 1 frame every 10 s for 20 h and saved as Motion JPEG using a MATLAB (The MathWorks, Inc., Natick, MA) script. Movie post-processing (cropping, concatenation, resizing, addition of scale bar) was done using MATLAB and Fiji (Schindelin et al., 2012). All MATLAB scripts written for this study are available upon request. Two of the scripts used here were obtained through the MATLAB Central File Exchange: “videoMultiCrop” and “concatVideo2D” by Nikolay S.

### **Embryo nuclei purification**

Following in vitro fertilization, *X. borealis* embryos were arrested at stage 8 (~5 hpf) in late interphase using 150 µg/mL cycloheximide in 1/10X MMR for 60 min. Embryos were washed several times in Egg Lysis Buffer (ELB; 250 mM sucrose, 50 mM KCl, 2.5 mM MgCl<sub>2</sub>, and 10 mM HEPES pH 7.8) supplemented with LPC (10 µg/mL each leupeptin, pepstatin, chymostatin), cytochalasin D (100 µg/mL), and cycloheximide (100 µg/mL), packed in a tabletop centrifuge at 200 g for 1 min, crushed with a pestle, and centrifuged at 10,000 g for 10 min at 16°C. The cytoplasmic extract containing endogenous embryonic nuclei was collected, supplemented with 8% glycerol, aliquoted, frozen in liquid nitrogen, and stored at -80°C.

### ***X. borealis* egg extract**

*X. borealis* metaphase-arrested egg extracts were prepared similarly to *X. laevis* and *X. tropicalis* (Maresca and Heald, 2006; Brown et al., 2007), with the following modifications.

*X. borealis* female frogs were primed with 60 U PMSG at least 48 hours before use and boosted with 300 U hCG 12-24 hours before the experiment. Frogs were kept at 16°C in 0.5X MMR. The eggs were dejellied in a 3% cysteine solution in 1X XB-salts (20X: 2M KCl, 20 mM MgCl<sub>2</sub>, 2 mM CaCl<sub>2</sub>), pH 7.8, and washed in CSF-XB (100 mM KCl, 0.1 mM CaCl<sub>2</sub>, 3 mM MgCl<sub>2</sub>, 50 mM sucrose, 10 mM K-EGTA, 10 mM K-HEPES, pH 7.8). CSF-XB buffer was exchanged for CSF-XB supplemented with LPC (10 µg/mL) (CSF-XB+). 1 mL of CSF-XB+ supplemented with cytochalasin D (100 µg/mL) was added to the bottom of an ultracentrifuge tube (SW-55, Beckman) before loading eggs into the tube. Extract tubes were placed in adapter tubes and spun at 1600 g for 1 min to pack the eggs. The excess liquid was removed and the eggs crushed by centrifugation at 10,200 rpm for 16 min at 16°C. The cytoplasmic fraction was then removed and supplemented with LPC (1:1000 dilution; 10 mg/mL stock), cytochalasin D (1:500 dilution; 10 mg/mL stock), energy (1:50 dilution; 50X stock: 190 mM creatine phosphate, 25 mM adenosine triphosphate, 25 mM MgCl<sub>2</sub>, 2.5 mM K-EGTA pH 7.7), and rhodamine-tubulin (1:300 dilution; 65.8 µg/uL stock) for spindle assembly reactions. Sperm nuclei, embryo nuclei, or 10 µm chromatin-coated beads, prepared as previously described (Halpin et al., 2011), were used as a source of DNA for spindle assembly.

### ***X. laevis* and *X. tropicalis* egg extracts and mixing experiments**

*X. laevis* and *X. tropicalis* metaphase arrested egg extracts were prepared and spindle reactions conducted as previously described (Maresca and Heald, 2006; Brown et al., 2007). *X. laevis* or *X. tropicalis* extracts were mixed in different proportions to *X. borealis* extract and supplemented with either *X. laevis* or *X. tropicalis* sperm nuclei, respectively.

### **Extract treatments**

To examine sensitivity to perturbations of the RanGTP gradient, *X. laevis*, *X. tropicalis*, and *X. borealis* sperm nuclei were added to their respective egg extracts and cycled through interphase. Ran T24N (final concentration 1 µM) and Q69L (final concentration 5 µM) mutant proteins, purified as previously described (Helmke and Heald, 2014), were added to the interphase extract reaction when fresh CSF extract was added to induce the extract to cycle back to mitosis.

### **Spindle spin-down and immunofluorescence**

Spindle reactions were prepared, spun-down, and processed for immunofluorescence as previously described (Hannak and Heald, 2006). Briefly, the extract reactions were fixed for 5-10 minutes with 2.5% formaldehyde and spun down at 10,200 rpm for 16 min at 16°C. The coverslips were incubated for 30 s in cold methanol, washed in PBS+NP40, and blocked overnight in PBS + 5% BSA at 4°C. The anti-TPX2 (1:150 dilution, unpublished), anti-katanin p60 (1:500 dilution) (Loughlin et al., 2011), or anti-XMAP215 (1:200, Tony Hyman & Kazu Kinoshita) rabbit antibodies were added for 1 h in PBS + 5% BSA. After washing with PBS+NP40, the coverslips were incubated with 1:1000 anti-rabbit antibody coupled to Alexa Fluor 488 (Invitrogen – Thermo Fisher Scientific, Waltham, MA) for 30 min and then with 1:1000 Hoechst for 5 min. The coverslips were then washed and mounted for imaging with Vectashield (Vector Laboratories, Burlingame, CA).



### **Egg whole mount immunofluorescence**

Metaphase-arrested *X. borealis* eggs were fixed for 1-3 h at RT using MAD fixative (2 parts of methanol (Thermo Fisher Scientific, Waltham, MA), 2 parts of acetone (Thermo Fisher Scientific, Waltham, MA), 1 part of DMSO), and stored overnight at -20°C in fresh MAD fixative. Embryos were then processed as previously described (Lee et al., 2008a) with some modifications. Following gradual rehydration in 0.5X SSC (1X SSC: 150 mM NaCl, 15 mM Na citrate, pH 7.0), embryos were bleached with 2% H<sub>2</sub>O<sub>2</sub> (Thermo Fisher Scientific, Waltham, MA) in 0.5X SSC containing 5% formamide for 2-3 h under light, then washed in PBT, a PBS solution containing 0.1% Triton X-100 (Thermo Fisher Scientific, Waltham, MA) and 2 mg/ml BSA. Embryos were blocked in PBT supplemented with 10% goat serum (Gibco – Thermo Fisher Scientific, Waltham, MA) and 5% DMSO for 1-3 h and incubated overnight at 4°C in PBT supplemented with 10% goat serum and the primary antibodies. We used the following antibodies: 1:500 mouse anti-beta tubulin (E7; Developmental Studies Hybridoma Bank, Iowa City, IA), 1:350 rabbit anti-histone H3 (ab1791; Abcam, Cambridge, MA). Embryos were then washed 4 X 2 h in PBT and incubated overnight in PBT supplemented with 1:500 goat anti-mouse secondary antibody coupled to Alexa Fluor 488 and 1:500 goat anti-rabbit secondary antibody coupled to Alexa Fluor 568 (Invitrogen – Thermo Fisher Scientific, Waltham, MA). Embryos were then washed 4 X 2 h in PBT and gradually dehydrated in methanol. Embryos were finally cleared in Murray's clearing medium (2 parts of Benzyl Benzoate, 1 part of Benzyl Alcohol). Embryos were placed in a chamber made using a flat nylon washer (Grainger, Lake Forest, IL) attached with nail polish (Sally Hansen, New York, NY) to a slide and covered by a coverslip, and filled with Murray's clearing medium for confocal microscopy.

### **Confocal microscopy**

Confocal microscopy was performed on an upright Zeiss LSM 780 NLO AxioExaminer using the Zeiss Zen software. Embryos were illuminated with an LED light source (X-cite 120LED). For the imaging of histone H3 and tubulin, embryos were imaged using a Plan-Apochromat 20x/1.0 Water objective and laser powers of 12%, on multiple 1024x1024 px plans spaced of 0.683 µm in Z. Images are mean averages of 2 scans with a depth of 16 bits. Channels were acquired simultaneously, and pinhole size was always chosen to correspond to 1 airy unit.

### **Imaging and quantification**

Eggs were imaged using the Leica Application Suite (v4.9; Leica Microsystems, Buffalo Grove, IL) with a Wild M7A stereoscope equipped with a Leica MC170HD camera. Sperm cells, sperm nuclei, embryo nuclei, and spindles were imaged using micromanager software (Edelstein et al., 2014) with an Olympus BX51 microscope equipped with an ORCA-ER camera (Hamamatsu Photonics, Hamamatsu city, Japan), and with an Olympus UPlan FL 40x/0.75 air objective. All measurements were made using Fiji. The spindle tubulin, katanin, TPX2, and XMAP215 intensity line scans were measured using an automated Java ImageJ plugin developed by Xiao Zhou (Heald lab, UC Berkeley; <https://github.com/XiaoMutt/AiSpindle>).

### **Western blot and analysis**

1  $\mu$ L of egg extract for 3 independent extracts for each species was subjected to SDS-PAGE (12% gel for katanin, 8% gel for TPX2 and XMAP215) and transferred to a nitrocellulose membrane. The anti-TPX2 (1:500 dilution, unpublished), anti-katanin p60 (1:1000 dilution) (Loughlin et al., 2011), or anti-XMAP215 (1:1000, Tony Hyman & Kazu Kinoshita) rabbit antibodies and anti-Ran (1:2000 dilution, BD Biosciences, San Jose, CA) mouse antibody were added for 1 h or overnight at 4°C in PBS + 0.1% Tween-20 + 5% milk. Secondary antibodies (goat anti-rabbit IRDye 800 or goat anti-mouse IRDye 680) were added at 1:10,000 for 1 h in PBS + 0.1% Tween-20. Blots were scanned with an Odyssey Infrared Imaging System (LI-COR Biosciences), and band intensity was quantified with Fiji.

### **Protein sequence alignments**

Multiple sequence alignments were performed using Clustal Omega (default parameters). Sequence similarities were determined by pairwise alignments using EMBOSS Needle (default parameters).

## **ACKNOWLEDGEMENTS**

We thank members of the Heald lab for support and fruitful discussions, in particular Xiao Zhou for his line scan plugin and Ambika Nadkarni for the purification of Ran mutants. We thank Sofia Medina-Ruiz, Austin Mudd, and Dan Rokhsar for providing early access to *X. borealis* katanin, TPX2, and XMAP215 sequences. The confocal microscopy performed in this work was done at the UC Berkeley CRL Molecular Imaging Center, supported by NSF DBI-1041078. MK was supported by the UC Berkeley MCB department NIH training grant 4T32GM007232-40. RH was supported by NIH R35 GM118183 and the Flora Lamson Hewlett Chair. RG was supported by an HFSP long term fellowship LT 0004252014-L.

## **AUTHOR CONTRIBUTIONS**

M.K. performed the experiments and analyzed the data, with help from R.G. M.K. prepared the figures and wrote the manuscript with input from R.H. and R.G.

## Chapter 3

### Ultrastructure expansion microscopy of *Xenopus* egg extract spindles

#### ABSTRACT

Across the eukaryotic tree of life, the dynamic, microtubule-based mitotic spindle executes the essential task of faithfully segregating chromosomes to daughter cells during cell division. Despite its universal function and conserved components, the spindle varies greatly in shape, size, and structure. How specific spindle architectures are formed and contribute to the fidelity of spindle function remains unclear. *Xenopus* egg extracts provide a powerful, cell-free, manipulable in vitro system instrumental in understanding mitotic spindle assembly and function. Here, we adapted ultrastructure expansion microscopy, which increases the size of a biological sample for greater spatial resolution, for spindles assembled in *Xenopus* egg extract in conjunction with directly labelled tubulin and immunofluorescence. This method leaves the biochemical power of *Xenopus* extracts untouched but attempts to boost resolution to allow us to correlate morphological differences in spindle architecture across species and cell types with spindle function.

### 3.1 INTRODUCTION

In all eukaryotes, the mitotic spindle performs the essential function of segregating replicated sister chromatids faithfully to daughter cells. This highly dynamic and self-organizing structure is built from thousands of microtubules that assemble to form a bipolar structure that allows chromosomes to be physically pulled apart toward opposite spindle poles. The protein composition and function of the mitotic spindle is conserved, but spindle structure changes according to cell type, shape, and size, thus varying dramatically across and within species (Crowder et al., 2015; Wühr et al., 2008). How specific spindle architectures are established and how this contributes to the spindle's essential function of chromosome segregation fidelity is still an open question, despite our current detailed understanding of the many molecules and mechanisms required to orchestrate spindle assembly (Helmke et al., 2013; Petry, 2016).

Cytoplasmic extracts prepared from *Xenopus* frog eggs have been an instrumental model system in advancing our knowledge of the cell cycle, mitotic spindle, and the cytoskeleton. Maternal stockpiles of biomolecules from oogenesis are used in extracts to power and recapitulate cellular activities, including key cell cycle events like chromosome condensation and mitotic spindle assembly, without bulk gene expression and transcription (Lohka and Masui, 1983; Lohka and Maller, 1985). The extract system provides unparalleled control over synchronized cell cycle states, as it can be arrested in either metaphase or interphase, and switching between the two states multiple times is fast and technically simple (Murray and Kirschner, 1989). The cell-free, membrane-less nature of the cytoplasmic extract system can be biochemically and pharmacologically treated to interrogate cell division dynamics, structure, and function in a highly physiological reconstitution system. Specific protein functions can be determined by antibody-based depletions, and add-back experiments with recombinant wild-type and mutant proteins or mRNAs that are translated in the extract can test specific domain activities (Murray, 1991; Jenness et al., 2018). Lastly, the extract is highly amenable to fluorescence microscopy techniques.

Interspecies comparisons with different *Xenopus* species extracts have also enabled our understanding of mechanisms that scale spindle size appropriately for different cell sizes (Brown et al., 2007; Loughlin et al., 2010, 2011; Helmke and Heald, 2014; Kitaoka et al., 2018). Extracts made from fertilized *X. laevis* embryos have uncovered how spindle and nuclear size is regulated during the rapid embryonic cleavages that create progressively smaller cells without growth (Wilbur and Heald, 2013; Good et al., 2013; Levy and Heald, 2010). Even among closely related *Xenopus* frogs, spindle architecture varies across the length of the spindle (Kitaoka et al., 2018), but why this is the case and how these differences arise is still unclear. *Xenopus* frogs provide a unique paradigm and an excellent system to tackle questions of microtubule organization and dynamics, and how spindle architecture relates to its essential function within and across species.

One challenge to understanding spindle architecture has been limited by the density and complexity of this macromolecular structure, which is made up of thousands

of microtubules and hundreds of associated proteins (Sauer et al., 2005; Liska et al., 2004). The dynamic instability of microtubules dictates that each microtubule polymer cycles between polymerization and depolymerization phases, when new tubulin dimers are added and removed to grow and shrink the length of the microtubule, respectively (Mitchison and Kirschner, 1984b). However, the density of microtubules across the entire spindle and current microscopy techniques have limited our investigation of their organization, including the number, distribution, and bundling of microtubules, as these cannot be resolved well with either light or super-resolution fluorescence microscopy within an intact, whole spindle. Light microscopy is limited by the diffraction limit of light, which can only resolve points that are 250 nm apart, while the width of a single microtubule is 25 nm in diameter (Chretien et al., 1992). Rather, global morphometric observations of mitotic spindles with light microscopy have been and continue to be instrumental to our understanding of spindle assembly mechanisms (Heald et al., 1996; Walczak et al., 1998; Helmke et al., 2013; Petry, 2016). On the other hand, electron microscopy regularly reaches nanometer resolutions, so its use has significantly advanced our knowledge of spindle microtubules (McDonald et al., 1992; Mastronarde et al., 1993). While studying large 3D volumes with tomographic reconstructions has been achieved to investigate spindle microtubule organization, it has proven technically challenging and time-consuming (Redemann et al., 2018; Müller-Reichert et al., 2018; Tranfield et al., 2014). The large size of the entire spindle and current technical restrictions make it unrealistic to examine the entire structure with electron microscopy alone. There is a clear need to combine technologies to bridge this gap in resolution to provide clarity on questions surrounding microtubule organization and dynamics. For example, while microtubule bundles are commonly described, it remains unclear how many individual microtubules make up a bundle, how tightly or loosely they are bound together, and how this organization impacts force generation within and around the spindle.

Recently, expansion microscopy (ExM) has emerged as a revolutionary technique that increases the physical size of the biological sample by embedding it into a swellable hydrogel polymer (Chen et al., 2015; Tillberg et al., 2016; Chozinski et al., 2016; Gambarotto et al., 2018). This physical increase in sample size creates space between proteins within a structure so that they can be separated to a range that can be resolved with classical light microscopy techniques without disrupting the overall architecture. ExM promises to bridge the resolution gap between existing light, super-resolution, and electron microscopy techniques. The affordability and compatibility of EM with conventional cell biological techniques, such as immunofluorescence, rather than relying on advanced optics, makes it accessible to all laboratories and model systems. Though originally developed for cultured cells and brain tissue to examine neuron connectivity (Chen et al., 2015), ExM and variations on the original method have already been applied to diverse model systems, often in combination with super-resolution microscopy techniques to maximize resolution. Recent studies have examined the microtubule cytoskeletal organization of the pathogen *Giardia* (Halpern et al., 2017), centriolar structural integrity (Le Guennec et al., 2020), and even whole *C. elegans* (Yu et al., 2020) and zebrafish larvae (Sim et al., 2021), demonstrating the fast-growing popularity of the technique.

Notably, the mitotic spindle from a Ptk1 cell was first imaged with expansion microscopy in (Chozinski et al., 2016). Subsequently, several groups have begun to examine specific proteins associated with mitotic spindle structures, such as Hec1/Ndc80 at the kinetochore and kinesin Kif25 at centrosomes (Chozinski et al., 2016; Decarreau et al., 2017). ExM can re-evaluate past results with increased spatial resolution and further interrogate the functional roles for specific microtubule architectures and their associated proteins within the mammalian spindle. Bridging fibers that connect and balance tension between sister kinetochore fibers were discovered recently as a result of applying ExM (Kajtez et al., 2016; Vukusic et al., 2017; Ponjavić et al., 2021).

Here, we set out to adapt ExM for the *Xenopus* egg extract to combine a versatile and powerful in vitro system ideal for studying the mitotic spindle with significant increases in resolution that could enable us to identify finer architectural details within an intact mitotic spindle that relate to its essential function. We describe an optimized protocol for the cell-free *Xenopus* extract spindle, and highlight key aspects that are essential for faithfully maintaining the entire structure throughout expansion. Applying this protocol to various species to create an expanded “spindle zoo” will provide new insight to the spindle diversity seen across species, cell sizes, types, and fates, leading us to a better understanding of how specific microtubule dynamics and organization lead to optimal spindle function and chromosome segregation fidelity.

## 3.2 RESULTS

To adapt previous ExM protocols for *Xenopus* egg extracts, we prepared metaphase II-arrested *X. laevis* egg extracts, isolated the cytoplasmic fraction, and proceeded to assemble spindles with rhodamine-labeled tubulin after induction of interphase and DNA replication with the addition of calcium (Hannak and Heald, 2006). We chose to use cycled mitotic spindles that formed after sperm nuclei had been replicated in interphase, rather than CSF spindles assembled directly in metaphase egg extract, as these were the most stable in our hands after fixation and spindown. Once spindles had fully formed, individual reactions were fixed with formaldehyde and spun down onto circular coverslips in order to be further processed for ExM, allowing us to treat several spindle structures at once on the same coverslip. Coverslips were then incubated in ice-cold methanol for 5 minutes to promote microtubule sticking and faithful fixation of mitotic spindle structures (Gambarotto et al., 2018). Shorter methanol incubations were not sufficient to withstand further ExM processing steps and resulted in lost microtubule structures, though incubations from 30 seconds to 5 minutes are perfectly acceptable if the sample is not processed for ExM. Coverslips were rehydrated and washed following methanol fixation before proceeding with further ExM treatments (Fig. 3.1A).

It was crucial that we could be able to measure the same spindle both pre- and post-expansion to develop and validate our protocol from one extract to another. To achieve this with minimal damage to the pre-expansion spindles on coverslips, we designed a custom slide chamber that keeps the sample immersed in neutral PBS buffer while we imaged with an upright objective (Fig. 3.1B). No mounting media or sealing reagents were necessary, therefore allowing us to retrieve the coverslip after pre-expansion imaging for further ExM processing steps.

Briefly, expansion microscopy works as follows: After fixation and immunofluorescence labelling of relevant biomolecules, acryloyl X-SE (AcX) is added to the sample to attach chains that will covalently bind to the gelation polymer. Upon gel polymerization, the biological structures will be completely embedded within the gel and connected to both the gel and biomolecules. Expansion of the sample at this step can cause shearing and breaking of the bonds between biomolecules such that the original structure is no longer faithfully maintained in the gel. To prevent this, the biological structure is “loosened” so that the labeled proteins are now only connected to the gel polymer, which holds them in their appropriate spatial configuration. After this point, the gel can be expanded with water, pushing the proteins apart from each other and creating more space between proteins as the gel and sample grow physically larger together.



**Figure 3.1**

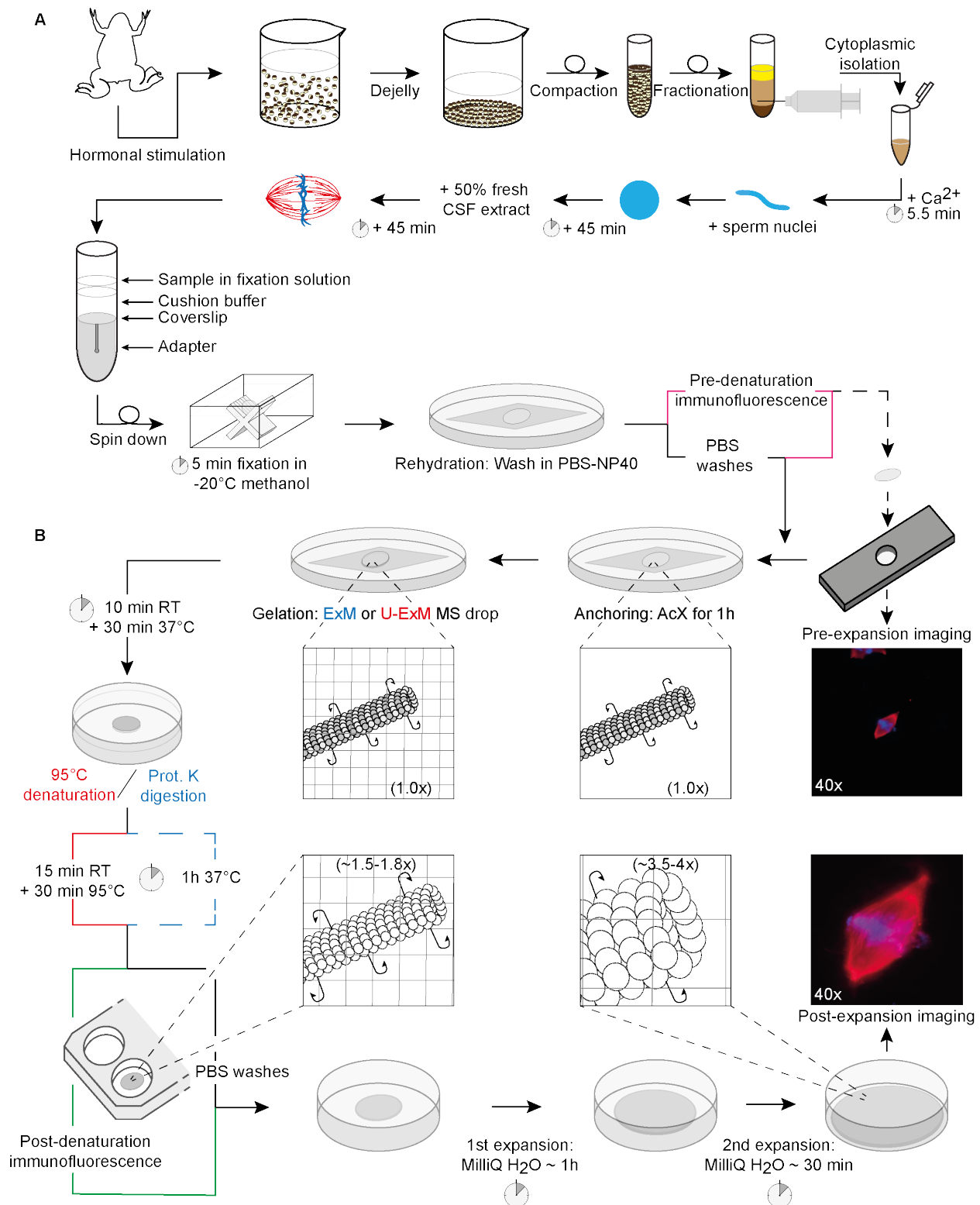


**Figure 3.1. Workflow for expansion of *Xenopus* egg extract spindle samples.** A. Preparation of egg extract spindles for expansion microscopy, including major steps of egg extract preparation, spindle assembly and spin-down. B. Expansion microscopy-specific steps from

anchoring and gelation to disruption and expansion. Note that immunofluorescence for pre-expansion imaging is performed after sample fixation and prior to anchoring and that immunofluorescence for post-expansion imaging is done after disruption and prior to expansion. If these steps are not performed, they are replaced by PBS washes. Insets demonstrate a single microtubule undergoing chemical modifications necessary to tether proteins to the gel polymer and expansion in water. (O/N: overnight; RT: Room Temperature; ExM: Expansion Microscopy; U-ExM: Ultrastructure ExM).

### **Validation of ExM protocols on *Xenopus* egg extract spindles**

We adapted our workflow (Fig. 3.1) based on existing ExM literature, but it required validation in *Xenopus* egg extracts, which is a cell-free environment for spindle assembly that lacks membranes and other forces in a cell that can contribute to its shape and integrity. Our aim was to further visualize the extremely dense microtubule network within the mitotic spindle, so it was key that the entire spindle structure be maintained faithfully throughout expansion. To accomplish this, we compared published variations of the original ExM method compatible with immunofluorescence (Chen et al., 2015; Tillberg et al., 2016; Chozinski et al., 2016) and the ultrastructure ExM (U-ExM) protocols (Gambarotto et al., 2018). Notably, expansion microscopy was first used to examine neuron connectivity in brain tissues and cell culture systems, both of which encapsulate cellular structures safely in membranes. With the cell-free *Xenopus* extract, we had a unique situation where we needed to keep the fragile, free-floating cytoskeletal structures intact.

Immunofluorescence steps can be taken pre-expansion after fixation for most antibodies and post-expansion immunofluorescence could also be successful just before expansion with water for certain antibodies. However, when pre-expansion tubulin immunofluorescence alone was used, expanded spindles were often unlabeled in the center of the spindle, indicating low binding occupancy and difficulty accessing deeper, denser microtubule regions of the spindle prior to expansion. With post-expansion immunofluorescence, antibodies must be able to recognize the appropriate protein antigens, which was not always successful after proteins are loosened. In our hands, post-denaturation immunofluorescence was most successful for tubulin antibodies, perhaps because antibodies were able to access the protein antigens more easily once the sample had been denatured, thus allowing for more faithful staining even in the center of the spindle. However, directly-labelled tubulin, such as rhodamine-tubulin commonly used with egg extracts, was by far the most successful and abundant fluorescent label, likely due to the small size of the fluorophore and labeling density per tubulin dimer. Throughout this work, we use rhodamine-tubulin in conjunction with other antibodies to probe spindle structure.

To carefully optimize a working ExM protocol for the cell-free *Xenopus* egg extract spindles, we compared two key steps in the protocol with either the original ExM or U-ExM methods: the recipe for the gel polymer itself, and the method of “loosening” up the protein from the gel prior to expansion. U-ExM uses a higher percentage of sodium acrylate and lower percentage of acrylamide compared to the original ExM method, which preserved the overall architecture of small organelles, such as centrioles, best (Chen et al., 2015; Tillberg et al., 2016; Chozinski et al., 2016; Gambarotto et al., 2018). After

gelation, ExM utilizes Proteinase K digestion of all proteins embedded in the gelled sample, while U-ExM uses a gentler thermal denaturation that keeps proteins intact but floppy. We used four experimental conditions to examine the effects of each of these on spindle structure and integrity (Fig. 3.2). All four conditions resulted in ~4x expansion, indicating that any combination produced the expected physical size increase (Fig. 3.2, center panels).

### The structural integrity of expanded *X. laevis* mitotic spindles depends disruption treatments more than gel composition

To assess the structural fidelity of expanded mitotic spindles, we measured line scans of tubulin intensity across the length of the spindle from pole to pole and compared the distribution of pre- and post-expansion spindles. Proteinase K digestion had the most detrimental effect on the expanded spindles, as tubulin intensity decreased significantly in the center of the spindle after expansion with both gel recipes (Figure 3.2A, B). The tubulin density at spindle poles also increased significantly with Proteinase K digestion, while thermal denaturation did not affect the tubulin density across the spindle (Figure 3.2C, D). Proteinase K digestion also resulted in larger ranges of expansion factors, demonstrating that digestion is not always even across the spindle, while thermal denaturation consistently led to a 3.5-4x expansion factor (Fig. 3.2 A, B vs. C, D center panels).

**Figure 3.2**

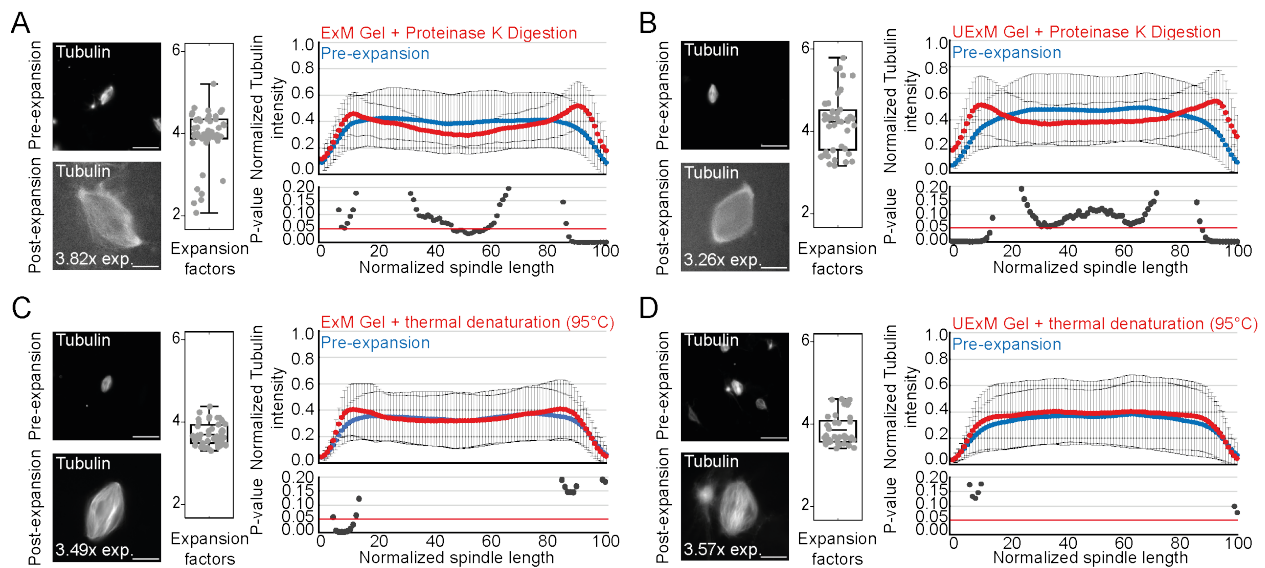
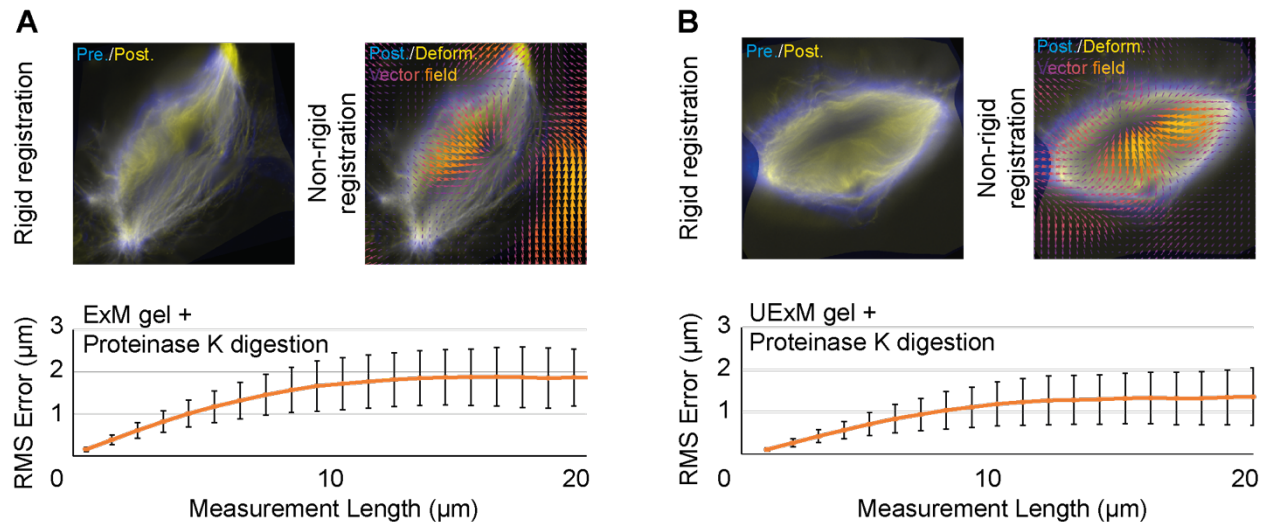


**Figure 3.2. Comparison of expansion factors and microtubule distribution between different expansion protocols.** The four tested conditions differing by the acrylamide composition of the gels and the nature of the disruption method are shown: ExM gel + Digestion (A), U-ExM gel + Digestion (B), ExM gel + Denaturation (C), and U-ExM gel + Denaturation (D). For each, left panels are representative images of unexpanded (top) and expanded (bottom) spindles, with rhodamine-labeled tubulin shown in gray. The expansion factor of the shown spindle is indicated. Scale bar is 40  $\mu\text{m}$ . Center panels are boxplots showing individual spindle expansion factors (grey dots;  $n = 51$ ,  $n = 47$ ,  $n = 47$ ,  $n = 41$ , respectively for A, B, C, and D), the center line is the mean, the box indicates the 25%-75% quantiles and the error bars the minimum

and maximum values. Average expansion factors were: (A)  $3.74 \pm 0.20$ , (B)  $4.28 \pm 0.48$ , (C)  $3.74 \pm 0.15$ , (D)  $3.92 \pm 0.14$  (average value  $\pm$  SD). Right panels are the average normalized fluorescence intensity distributions  $\pm$  Standard Deviation (top) for unexpanded (blue) and expanded (red) spindles, and the p-values calculated along the spindle axis comparing the distributions (bottom) shown only from 0 to 0.2. The red line indicates the p-value threshold of 0.05. Compared to middle panels, here, only spindles that kept enough rhodamine signal after expansion were used for analysis ( $n = 34$ ,  $n = 29$ ,  $n = 47$ ,  $n = 41$ , respectively for A, B, C and D).

We next tested whether significant deformations were introduced into the mitotic spindle as a result of expansion in our four experimental conditions, as all ExM protocols rely on the assumption that the sample grows isotropically. For this analysis, we imaged the same spindles pre- and post-expansion, then used Elastix and Mathematica software as previously described to quantify the resulting deformations (Chozinski et al., 2016). We registered these images as “rigid registrations”, and overlaid them on top of each other to visualize a “global match” between identical pre- and post-expansion spindles. We also created non-rigid registrations of the expanded spindle images to overlay the rigid and non-rigid registrations and determine the amount of deformation in the expanded image, visualized as a vector field to indicate the direction of local deformations. This analysis showed that thermal deformation led to less deformations and decreased root-mean-square (RMS) error in expanded spindles compared to Proteinase K digestion, which introduced more significant errors in addition to lost intensity at the spindle midzone (Fig. 3.3A, B vs. C, D). From these measurements, it’s clear that the mode of sample disruption greatly influences the integrity of the expanded structure and its fidelity to the original, unexpanded structure. While ExM and U-ExM gels performed similarly in this analysis (Fig. 3.3), we decided to move forward with the U-ExM formula since this gave the most consistent results across multiple extracts and sample preparations, particularly regarding tubulin intensity, distribution, and expansion factors (Fig. 3.2).

**Figure 3.3**



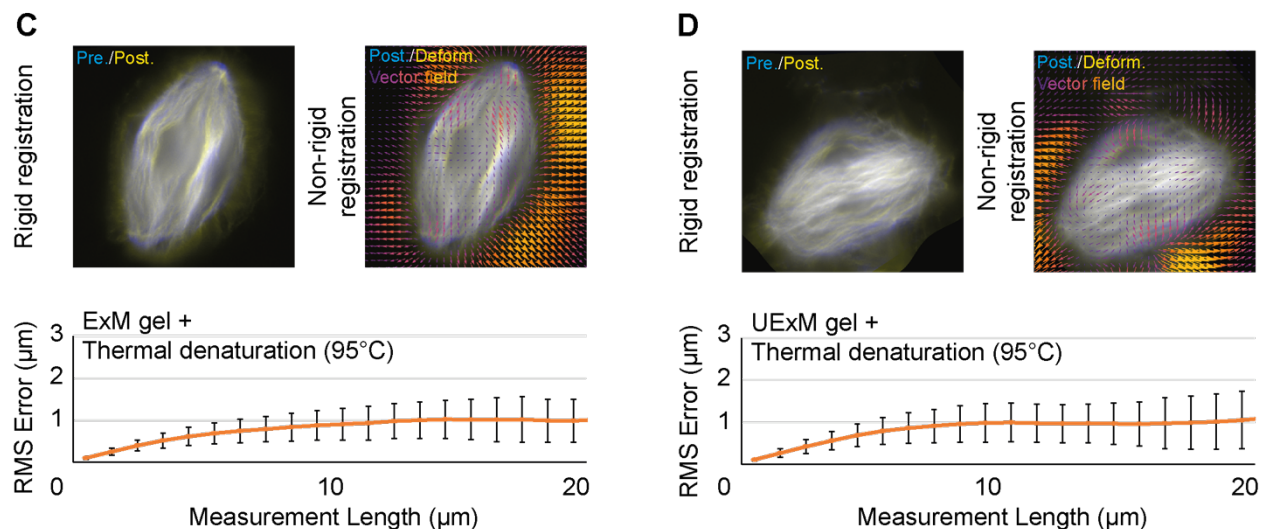


**Figure 3. Evaluation of the expansion-induced deformations between the different protocols.** A, B, C, and D show our four tested conditions. The top images show the rigid registration (left) made between the enlarged unexpanded spindle (blue) and the expanded spindle (yellow) to obtain a global match, as well as the non-rigid registration (right) made between the expanded spindle (blue) and the matrix (yellow) made during the rigid alignment (the vector fields in purple to yellow show the local deformations and their direction). The bottom graph represents the Root-Mean-Square length measurement error according to pre-expansion length computed from pre- and post-expansion images. The orange line shows the average and the error bars, the standard deviation ( $n = 51$ ,  $n = 47$ ,  $n = 47$ ,  $n = 41$ , respectively for A, B, C, and D).

**Figure 3.4**

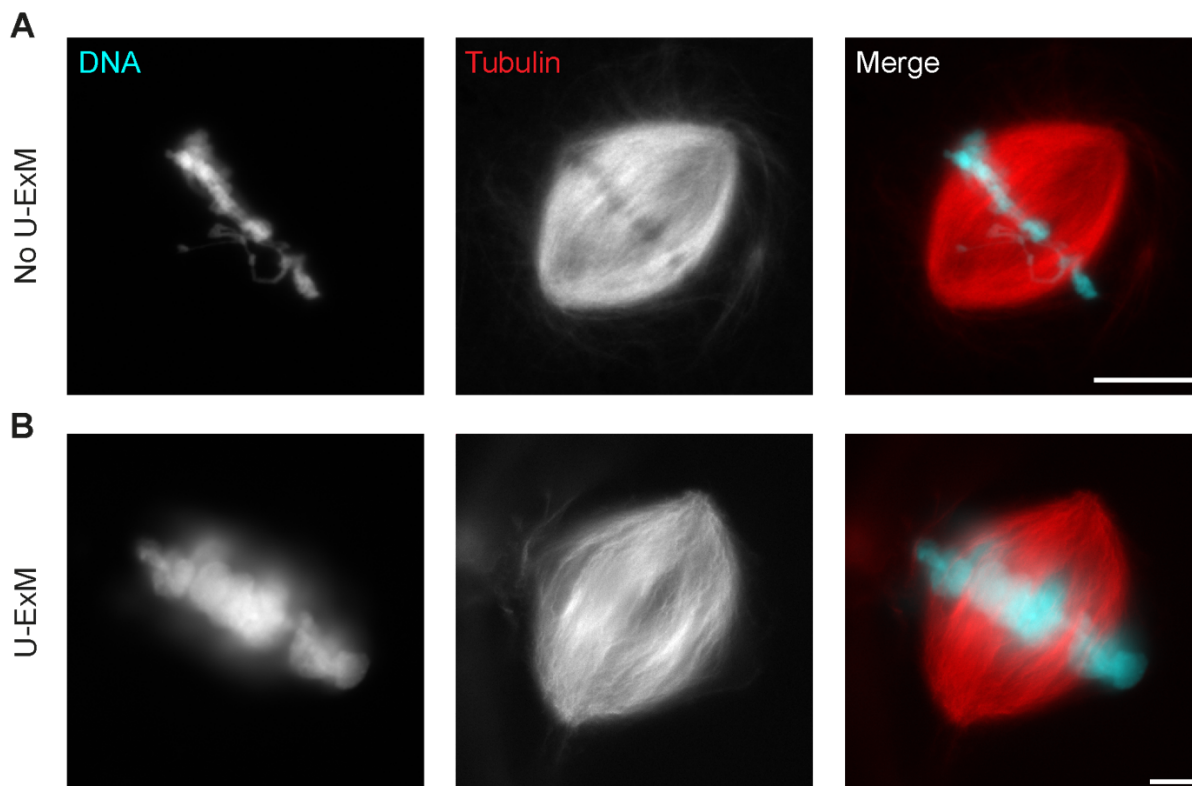


**Figure 3.4. Our adapted U-ExM protocol can faithfully maintain the structure of an intact *X. laevis* egg extract spindle.** Representative images of (A) untreated and (B) U-ExM-treated spindles. DNA is in cyan, tubulin in red. Scale bars are both 20  $\mu\text{m}$ .

### Examining other *Xenopus* species and mitotic structures

As a result of these optimizations and validations, our adapted U-ExM method was able to faithfully maintain the structure of the cycled *X. laevis* extract spindle and increase its size by approximately four times (Fig. 3.4, compare A and B). This prompted us to examine an additional structure within the mitotic spindle: the centromere, which provides the specific location and signaling for the large kinetochore protein complex to assembly so that it can attach chromosomes to the spindle microtubules. This key interaction is essential for faithful partitioning to daughter cells during cell division (Cheeseman, 2014). In parallel with our optimizations of the U-ExM method for *X. laevis* spindles, we also verified its use on *X. tropicalis* spindles. We used both *X. laevis* and *X. tropicalis* spindles to examine CENP-A, the centromeric histone variant, with immunofluorescence. Our expansion microscopy protocols were able to detect distinct centromeric foci and could even resolve specific doublets around the duplicated sister chromatids (Fig. 3.5A, B). In addition, we quantified the number of CENP-A doublets per spindle, and found that spindles assembled in egg extract often do not contain exactly one genome's worth of DNA (Fig. 3.5C). This is likely due to the lack of no membranes in *Xenopus* extracts to keep nuclei, chromosomes, and spindle structures packaged together, and mitotic spindles fuse together when in close proximity to each other (Gatlin et al., 2009). Importantly, this quantification would have been more imprecise without the increased spatial resolution offered by U-ExM, highlighting its immediate utility and potential.

**Figure 3.5**

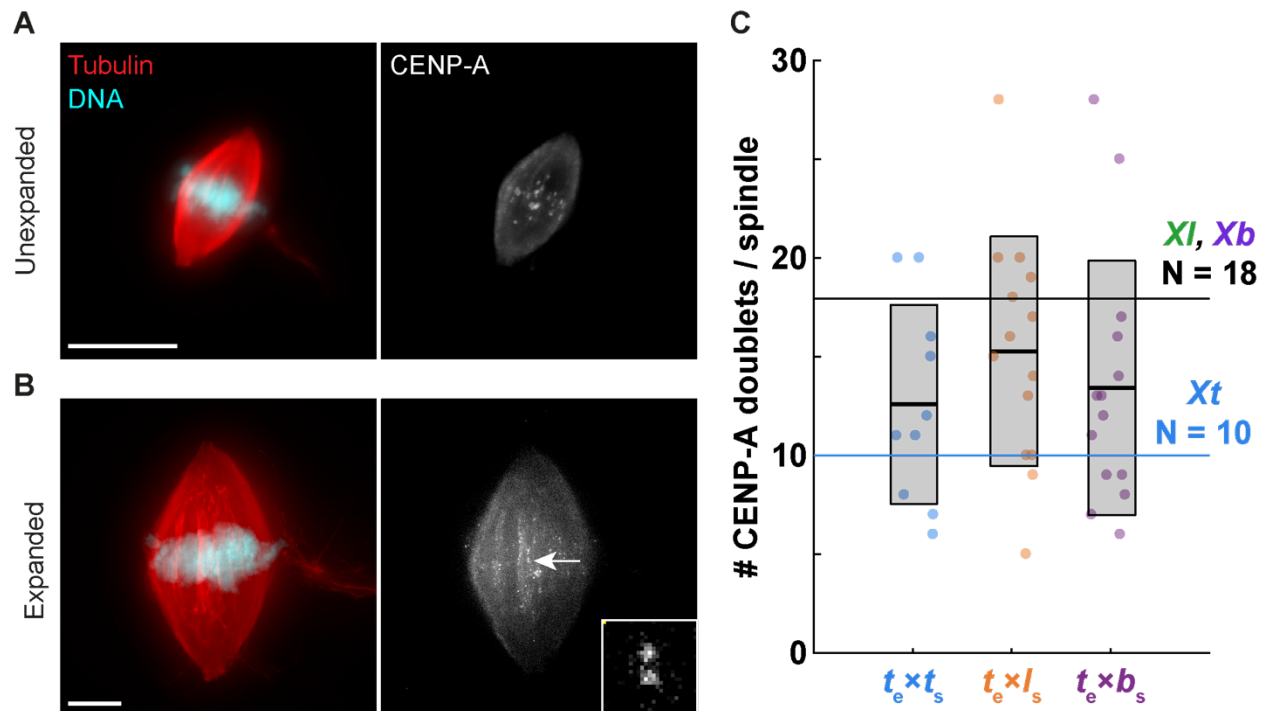


**Figure 3.5. Expansion microscopy can increase resolution of centromere puncta.** Representative images of the same (A) unexpanded and (B) expanded *X. tropicalis* spindles with CENP-A immunofluorescence. Inset demonstrates the spatial resolution gained to visualize CENP-A doublets. (C) Box plot demonstrating that extract spindles do not have exactly one genome. DNA is in cyan, tubulin in red, CENP-A in gray. Scale bars are both 20  $\mu\text{m}$ .

### 3.3 DISCUSSION

Our results demonstrate the successful adaptation and development of ultrastructure expansion microscopy for the *Xenopus* egg extract, the first time this technique has been applied to a cell-free in vitro system. We show isotropic expansion of mitotic spindles and preserve their native microtubule-based architecture, specifically using thermal denaturation and higher sodium acrylate/lower acrylamide gels. We demonstrate that the technique can be applied to other *Xenopus* species and mitotic spindle structures. At the time of this writing, we have not been able to directly address how specific spindle architectures form and contribute to function using U-ExM with the full power and range of *Xenopus* extracts. Our experiments here serve as the proof-of-principle for this method. Our adaptation of U-ExM for the *Xenopus* extract systems prompts us and others to ask more detailed questions about microtubule distribution, organization, and metrics throughout the macromolecular spindle structure with conventional fluorescence microscopy techniques. More high-resolution microscopy techniques and computational analyses will be crucial to answer these questions, and these are currently under development.

ExM provides several key advantages that make it an attractive and accessible method for many biological questions. However, there are drawbacks and limitations to consider. Each new sample type requires careful optimization, and every new variation of ExM has first gone through extensive validation similar to our methods presented here. In addition, fluorophore brightness can be severely affected after expansion, limiting fluorophore options (Chen et al., 2015; Chozinski et al., 2016). While antibodies can work well in most cases, they were not sufficient for highly abundant proteins, such as tubulin in mitotic spindles. Direct tubulin labeling, such as rhodamine-labeled tubulin commonly used among *Xenopus* extract users, provides much higher labeling density per tubulin subunit and more coverage across all microtubules in the spindle. Anti-tubulin antibodies were excellent on the surface of the spindle, but could not penetrate the dense, bundled network in the center, even with post-expansion immunofluorescence. Additionally, though samples are expected to become physically larger, the resulting thickness can make imaging more difficult because most high magnification objectives have short working distances (Gao et al., 2017). Imaging time also increases when the sample is 4x larger in both x and y dimensions as well, so it's more likely for fluorophores to be bleached over time. Expanded samples are ~99% water, making them optically clear, but finding the sample can be difficult. Lastly, ExM is limited to fixed samples, as the original proteins are cross-linked to the surrounding gel and disrupted before expansion.

Despite these limitations, ExM continues to develop rapidly to provide new windows into whole cellular structures that were too small to image clearly previously. Even though global morphometrics of the mitotic spindle have been well investigated by conventional light microscopy, combining the manipulable, biochemically tractable *Xenopus* egg extracts with U-ExM can pave the way for further studies to investigate how spindle architecture adapts to the cellular environment and lends itself to function across different species, cell types, and developmental stages. Previous comparative work has



already identified key differences in spindle architecture across *Xenopus* and Pipid family frog species and the mechanisms involved in mediating spindle scaling and structure (Brown et al., 2007; Loughlin et al., 2011; Helmke and Heald, 2014; Kitaoka et al., 2018; Miller et al., 2019), providing an ideal starting point to dissect these spindles further with U-ExM, high resolution imaging, computational analysis, and modeling. We will use U-ExM to get a closer look at these key differences, with the goal of identifying further structural details, defining microtubule organization and bundling metrics, and probing how these spindle architecture differences correlate with the essential function of dividing DNA faithfully to daughter cells.

### 3.4 MATERIALS and METHODS

Unless otherwise stated, all reagents were purchased from Sigma-Aldrich.

#### **Frog care**

All frogs were used and maintained in accordance with standards established by the UC Berkeley Animal Care and Use Committee and approved in our Animal Use Protocol. Mature *Xenopus laevis* and *X. tropicalis* frogs were obtained from Nasco (Fort Atkinson, WI), the National *Xenopus* Resource (Woods Hole, MA), or Centre de Ressources Biologique *Xénopes*, Université de Rennes 1, France. *Xenopus* frogs were housed in a recirculating tank system with regularly monitored temperature and water quality (pH, conductivity, and nitrate/nitrite levels). *X. laevis* were housed at 20-23°C, and *X. tropicalis* were housed at 23-26°C. All animals were fed Nasco frog brittle. *X. laevis* and *X. tropicalis* females were ovulated with no harm to the animals with a 6- and 3-month rest interval, respectively.

#### ***Xenopus* egg extracts and spindowns**

*X. laevis* and *X. tropicalis* metaphase-arrested egg extracts and spindle reactions were prepared as previously described (Hannak and Heald, 2006; Brown et al., 2007). Briefly, extract reactions were fixed for 1 min with 2.5% formaldehyde and spun down at 10,200 rpm for 16 min at 16°C onto 12 mm coverslips. The coverslips were incubated for 5 min in ice cold methanol, washed 3x in PBS + 0.1% NP40.

#### **Pre-expansion immunofluorescence**

Coverslips were blocked either for 1 h at room temperature (RT) or overnight at 4°C in PBS + 3% BSA. The antibodies (mouse DM1a tubulin, 1:500, add other ab specifics) were added for 1 h in PBS + 3% BSA. Coverslips were washed 3x in PBS-NP40, then incubated with 1:500 secondary Alexa Fluor antibodies (Invitrogen-Thermo Fisher Scientific) for 30 min in PBS-NP40, followed by Hoechst (1:500, 10 mg/mL stock) for 5 min in PBS-NP40. Finally, coverslips were washed with PBS-NP40 3x, and once with PBS. Coverslips were either imaged in a custom-built chamber to acquire specific pre-expansion images prior to the U-ExM protocol (below), or mounted with Vectashield (Vector Laboratories) as non-expanded controls.

#### **Ultrastructure expansion microscopy for *Xenopus* egg extract spindles**

Coverslips were incubated in 1 µg/mL AcX (Acryloyl-X, SE, 6-((acryloyl) amino) hexanoic Acid, Succinimidyl Ester, Thermo Fisher, A20770) diluted in PBS for 1 h at RT. The monomer solutions were prepared in advance, aliquoted, and stored at -20°C. For U-ExM, the following recipe was used: 19% sodium acrylate (Sigma, 408220), 10% acrylamide (Interchim, UP873376), 0.1% N,N'-methylenebisacrylamide (Sigma, M1533) in 1x PBS. ExM samples used the following monomer solution: 2.5% acrylamide, 8.625% sodium acrylate, 0.15% N,N'-methylenebisacrylamide in 1X PBS supplemented with 2M NaCl. Monomer solution, APS, and TEMED were thawed on ice. Gelation reactions (monomer solution, 0.2% TEMED, 0.2% APS) were prepared on parafilm with the sample face-down into a 75 µL drop of gelation solution, and incubated for 10 min at RT, followed by 30 min at 37°C. Once solidified, the gel and attached coverslip were transferred to a

glass petri dish (Corning), and incubated for 15 min at RT in disruption buffer (50 mM Tris pH 8, 200 mM SDS, 200 mM NaCl, prepared fresh and warmed). The buffer is exchanged for fresh disruption buffer, and gels were incubated at 95°C for 30 min. The coverslip and gel should disassociate naturally during this incubation. After careful removal from heat, gels were washed 3x in fresh PBT (PBS + 0.1% Triton X) and transferred to a 6-well plate for storage overnight at 4°C in PBS or expanded immediately with 2 x 30 min washes with MilliQ water for imaging. Following imaging, gels were shrunk in 2 x 30 min washes with 1x PBS and stored at 4°C long-term.

When the original ExM protocol was used, the gel and attached coverslip were transferred to a glass petri dish (Corning), and incubated for 1 hour at 37°C in digestion buffer (50 mM Tris (pH 8), 1 mM EDTA, 0.5% Triton X-100, 0.8 M guanidine HCl) with 8 units/mL of Proteinase K (Roche, 03115828001). Gels were washed 3x for 5 min in PBT.

### **Post-denaturation immunofluorescence**

Gels were incubated in primary antibodies (1:500, mouse DM1a tubulin, rabbit CENP-A (generously gifted from Aaron Straight)) for 1 h at RT in PBS-BSA, shaking gently, followed by 3 washes in PBT. Secondary antibodies (Alexa Fluors 488, 568, 647, 1:500, Invitrogen) were added for 30 min at RT in PBT and gently shaking, followed by Hoechst (1:500) for 5 min at RT. All antibody incubations used 1 mL/gel. Gels were washed 3x in PBT and either stored in 1X PBS at 4°C or expanded immediately for imaging.

### **Widefield imaging**

Unexpanded and expanded spindles were imaged using Micromanager 1.4 software (Edelstein et al., 2014) with an upright Olympus BX51 microscope equipped with an Prime BSI camera (Photometrics) and Olympus UPlan 40X/0.75 air objective.

### **Distortion analysis and quantification**

Using Elastix and Mathematica software, the Root Mean Square error (RMS error) was calculated between images of the same spindle before and after expansion as previously described (Chozinski et al., 2016). The pre-expansion image was enlarged four-fold in FIJI to match the size of the post-expansion image. Rigid registration (translation, rotation, linear scaling) was performed in Elastix by superimposing the two images to create a global “best match”. Non-rigid registration then allowed images to be deformed to correct local deformations. Mathematica was then used to calculate the RMS error to represent the sample’s deformations.

### **Quantification and statistical analysis**

Spindle length and fluorescence intensity line scans were measured by drawing a line across the length of the spindle from pole to pole using FIJI and quantified using an automated Java ImageJ plugin developed by Dr. Xiao Zhou (Heald Lab, UC Berkeley, <https://github.com/XiaoMutt/AiSpindle>). All data were normalized to the maximum intensity of all datasets and the length of the spindle to calculate the average distribution across the spindle. All experiments and data are representative of three independent biological extracts. For all box plots, the thick line inside the box indicates the average across biological replicates, and the upper and lower box boundaries indicate the

standard deviation. P values were calculated with two-tailed, two-sample unequal variance t-tests in Microsoft Excel. Fluorescence intensity profiles were plotted in Excel with error bars indicating the standard deviation. The number of egg extracts used, individual spindles counted, and p-values are listed in the figure legends.

## **ACKNOWLEDGEMENTS**

We thank the France-Berkeley Fund #24-2018 for providing financial support for research exchanges between the Heald lab and the TIPs (now MiToS) group at the Institute Genetics and Development Rennes, led by Denis Chrétien and Romain Gibeaux. We thank Karel Mocaer, Den A. Lipata, and Gabriel Guilloux for help with experiments to M.K. We thank Romain Gibeaux for project development and guidance. We thank past and present members of the Heald laboratory, the TIPs/MiToS team at the IGDR, Srigokul Upadhyayula, and Mark J. Khoury for support and fruitful discussions. M.K. was supported by a National Science Foundation GRFP fellowship. R.H. was supported by NIH MIRA grant R35 GM118183 and the Flora Lamson Hewlett Chair.

## **AUTHOR CONTRIBUTIONS**

M.K., R.H., and R.G. designed and initiated the project. R.H. and R.G. supervised the project. M.K. and K.M. performed early optimizations and adaptations on the originally published ExM protocol. G.G. completed and validated the adapted protocol with R.G., including the analyses comparing unexpanded and expanded spindles (tubulin line scans, rigid and non-rigid registrations). M.K. performed the confocal microscopy and species comparison experiments and analyses. G.G. and R.G. prepared Figures 1-3. M.K. prepared the remaining figures and wrote the manuscript with input from all authors.

## Chapter 4

### Paternal chromosome loss and metabolic crisis contribute to hybrid inviability in *Xenopus*

The following chapter contains material from a publication on which I am a co-author (Gibeaux et al., 2018). This article is distributed under the terms of the Creative Commons Attribution License (CC BY 4.0), which permits unrestricted use and redistribution provided that the original author and source are credited.

#### ABSTRACT

Hybridization of eggs and sperm from closely related species can give rise to genetic diversity, or can lead to embryo inviability due to incompatibility. Although central to evolution, the cellular and molecular mechanisms underlying postzygotic barriers that drive reproductive isolation and speciation remain largely unknown (Seehausen et al., 2014; Presgraves, 2010). Species of the African Clawed frog *Xenopus* provide an ideal system to study hybridization and genome evolution. *Xenopus laevis* is an allotetraploid with 36 chromosomes that arose through interspecific hybridization of diploid progenitors, whereas *Xenopus tropicalis* is a diploid with 20 chromosomes that diverged from a common ancestor ~48 million years ago (Session et al., 2016). Differences in genome size between the two species are accompanied by organism size differences, and size scaling of the egg and subcellular structures such as nuclei and spindles formed in egg extracts (Brown et al., 2007). Nevertheless, early development transcriptional programs, gene expression patterns, and protein sequences are generally conserved (Hirsch et al., 2002; Yanai et al., 2011). Whereas the hybrid produced when *X. laevis* eggs are fertilized by *X. tropicalis* sperm is viable, the reverse hybrid dies prior to gastrulation (Bürki, 1985; Narbonne et al., 2011). Here we apply cell biological tools and high-throughput methods to study the mechanisms underlying hybrid inviability. We reveal that two specific *X. laevis* chromosomes are incompatible with the *X. tropicalis* cytoplasm and are mis-segregated during mitosis, leading to unbalanced gene expression at the maternal to zygotic transition, followed by cell-autonomous catastrophic embryo death. These results reveal a cellular mechanism underlying hybrid incompatibility that is driven by genome evolution and contributes to the process by which biological populations become distinct species.

## 4.1 RESULTS and DISCUSSION

Hybrids produced through fertilization of *X. laevis* eggs with *X. tropicalis* sperm ( $l_e \times t_s$ ) are viable, whereas *X. tropicalis* eggs fertilized by *X. laevis* sperm ( $t_e \times l_s$ ) are not (Fig. 4.1a) (Bürki, 1985; Narbonne et al., 2011). Although cleavage divisions and rate of development of  $t_e \times l_s$  hybrids were initially similar to *X. tropicalis* ( $t_e \times t_s$ ) (Fig. 4.1b), hybrid embryos died abruptly as late blastulae and never initiated gastrulation. Before their death, hybrid embryos took on a deformed mushroom-like shape before lysing from the vegetal pole (Fig. 4.1c and Video 4.1). Explants prepared from the opposite pole (animal caps) of mid-blastula  $t_e \times l_s$  embryos also died within a few hours, indicating that embryo death is cell autonomous and not a result of faulty developmental cues (Fig. 4.1d and Video 4.2). In contrast to  $t_e \times l_s$  hybrids that die as embryos, haploid *Xenopus* embryos develop to the tadpole stage (Hamilton, 1957; Narbonne et al., 2011), suggesting that hybrid death is due to factors brought in by the *X. laevis* sperm to the *X. tropicalis* egg during fertilization. Irradiation of *X. laevis* sperm prior to fertilization, which destroys the DNA (Goda et al., 2006; Wühr et al., 2008), resulted in a haploid phenotype (Fig. 4.1e and Videos 4.3, 4.4), indicating that  $t_e \times l_s$  embryo death is due to the presence of the *X. laevis* genome. Cybrid embryos generated by irradiating *X. tropicalis* eggs, destroying the maternal DNA (Narbonne et al., 2011) before fertilization with *X. laevis* sperm, died before gastrulation similar to  $t_e \times l_s$  embryos, indicating that hybrid inviability does not result from a conflict between the paternal and maternal genomes (Table 4.1).

### **Video 4.1. Characterization of $t_e \times l_s$ hybrid embryo death; *X. tropicalis* vs. $t_e \times l_s$**

*X. tropicalis* eggs were fertilized with *X. tropicalis* (left) or *X. laevis* sperm (right) and simultaneously imaged in separate dishes. The video plays 20h in 15s (rate of 120 fps) and the scale bar corresponds to 200  $\mu\text{m}$ . (All videos presented here are available online: <https://www.nature.com/articles/nature25188#Sec23>)

### **Video 4.2. Cell death in $t_e \times l_s$ hybrid animal cap; *X. tropicalis* vs. $t_e \times l_s$**

*X. tropicalis* eggs were fertilized with *X. tropicalis* sperm (left) or *X. laevis* sperm (right). At stage 8, animal caps were isolated and simultaneously imaged in separate dishes. The video plays 20h in 15s (rate of 120 fps) and the scale bar corresponds to 200  $\mu\text{m}$ .

### **Video 4.3. Role of *X. laevis* DNA in $t_e \times l_s$ hybrid embryo death; $t_e \times l_s$ vs $t_e \times [l_s]$**

*X. tropicalis* eggs were fertilized with *X. laevis* sperm (left) or UV-irradiated *X. laevis* sperm (right) and simultaneously imaged in separate dishes. The video plays 20h in 15s (rate of 120 fps) and the scale bar corresponds to 200  $\mu\text{m}$ .

### **Video 4.4. Development of *X. tropicalis* haploid embryos; $t_e \times [t_s]$ vs $t_e \times [l_s]$**

*X. tropicalis* eggs were fertilized with UV-irradiated *X. tropicalis* sperm (left) or UV-irradiated *X. laevis* sperm (right) and simultaneously imaged in separate dishes. The video plays 20h in 15s (rate of 120 fps) and the scale bar corresponds to 200  $\mu\text{m}$ .

**Table 4.1**

Embryo	Normal	Regular	Died between	Exogastrulae	Normal	Abnormal	Tadpoles	
	Stage 2 <sup>†</sup> (n)	Stage 9 (%)	9-13 (%)		tailbuds	tailbuds	Stunted (%)	Normal (%)
$[t_e] \times t_s$	402 (5)	402 (100)	6 (1)	131 (33)	209 (52)	56 (14)	191 (48)	18 (4)
$[t_e] \times l_s^\ddagger$	25 (7)	25 (100)	25 (100)	0 (0)	0 (0)	0 (0)	0 (0)	0 (0)

**Table 4.1: Embryonic development in *Xenopus* haploids and hybrids generated from *X. tropicalis* irradiated eggs.**

Symbol *n* indicates the number of different male-female combinations from which results were compiled.

† Unfertilized eggs and embryos that showed an abnormal or incomplete first cleavage were excluded from this analysis.

‡ Fertilization efficiency of irradiated *X. tropicalis* eggs with *X. laevis* sperm was very low (~4%).

To visualize the dynamics of hybrid cell divisions, we injected mRNAs encoding fluorescent fusion proteins to label embryo chromosomes and mitotic spindles, and observed animal caps at early stage 9, which revealed anaphase defects and chromosome mis-segregation (Fig. 4.1f and Video 4.5). Immunofluorescence of whole embryos confirmed the presence of lagging chromosomes and chromosome bridges in cells throughout hybrid blastulae, as well as the formation of micronuclei in interphase, whereas no such defects were observed in *X. tropicalis* embryos (Fig. 4.1g) or in the reverse viable hybrid (data not shown). Imaging of  $t_e \times l_s$  embryos from stage 4 (8 cells) to stage 9 (thousands of cells) revealed micronuclei in 6-10% of the cells throughout hybrid development, but not in the *X. tropicalis* control (Fig. 4.2a, b), indicating that chromosome mis-segregation in  $t_e \times l_s$  hybrid embryos is unrelated to changes in gene expression at the onset of zygotic genome activation (ZGA). Because the regular ploidy supported by the *X. tropicalis* egg is N=20 chromosomes, but the  $t_e \times l_s$  hybrid zygote must accommodate 28 chromosomes, we tested whether an increase in ploidy was causing chromosome mis-segregation and embryo death by applying a cold shock to *X. tropicalis* zygotes a few minutes after fertilization to suppress polar body extrusion and increase their ploidy to N=30 chromosomes (Fig. 4.2c). Micronuclei were not observed in cold-shocked embryos, which developed to the tailbud stage similarly to haploid embryos (Fig. 4.2d). Thus, increasing the ploidy of *X. tropicalis* embryos does not cause chromosome mis-segregation or cell death, indicating a specific role for the *X. laevis* genome in hybrid inviability.

**Figure 4.1**





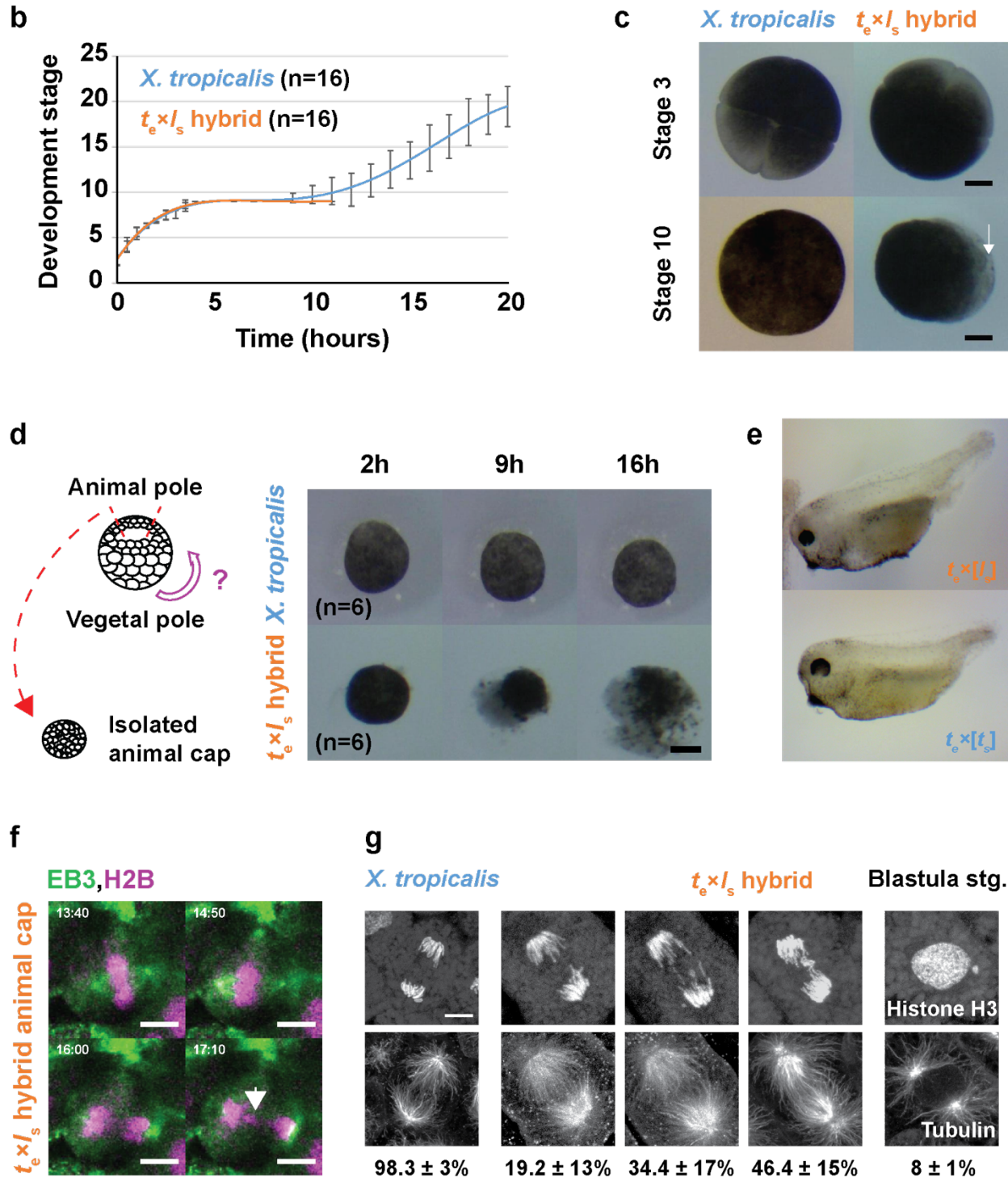


**Figure 4.1: Role of the *X. laevis* genome in  $t_e \times I_s$  hybrid embryo death.**

**a**, Schematic of *X. laevis* and *X. tropicalis* cross-fertilization outcomes. **b**, Developmental timing in *X. tropicalis* and  $t_e \times I_s$  hybrid embryos. Error bars show standard deviation. **c**, Images of *X. tropicalis* and  $t_e \times I_s$  hybrid embryos at stages 3 and 10. The arrow indicates vegetal cells where death initiates. **d**, Schematic of animal cap assay and images of at 2, 9 and 16 h after isolation. Scale bars in **c** and **d**, 200  $\mu$ m. **e**, Images showing haploid phenotype following fertilization of *X. tropicalis* eggs with UV-irradiated sperm. **f**, Time-lapse images of dividing cell in a  $t_e \times I_s$  hybrid

animal cap (Video 4.5). The arrow indicates a mis-segregated chromosome. Time is in mm:ss. **g**, Immunofluorescence images showing chromosome bridges, mis-segregated chromosomes, and micronuclei throughout  $t_e \times l_s$  hybrid embryos. Scale bars in f and g are 10  $\mu\text{m}$ . Quantification of  $n = 81$  *X. tropicalis* and  $n = 78$   $t_e \times l_s$  hybrid anaphases in  $n = 17$  and 16 embryos, respectively, show a significant difference by Fisher 2 by 3 contingency test. Quantification of micronuclei in  $t_e \times l_s$  hybrid embryos is detailed in Figure 4.2b.

#### Video 4.5. Mitosis in $t_e \times l_s$ hybrid animal cap

*X. tropicalis* eggs were fertilized with *X. laevis* sperm. In vitro transcribed mRNA coding for the microtubule end binding protein EB3 labeled with GFP and histone H2B labeled with RFP was injected into stage 2 embryos. At stage 8, animal caps were isolated, mounted and imaged using live confocal microscopy. Histone H2B-RFP (shown in magenta) and EB3-GFP (shown in green) signals were imaged in a single plane with a frame size of 1024x1024 pixels, every 5s. The movie plays 20 min in 8s (rate of 30 fps). The time is in mm:ss and the scale bar is 20  $\mu\text{m}$ .

**Figure 4.2**

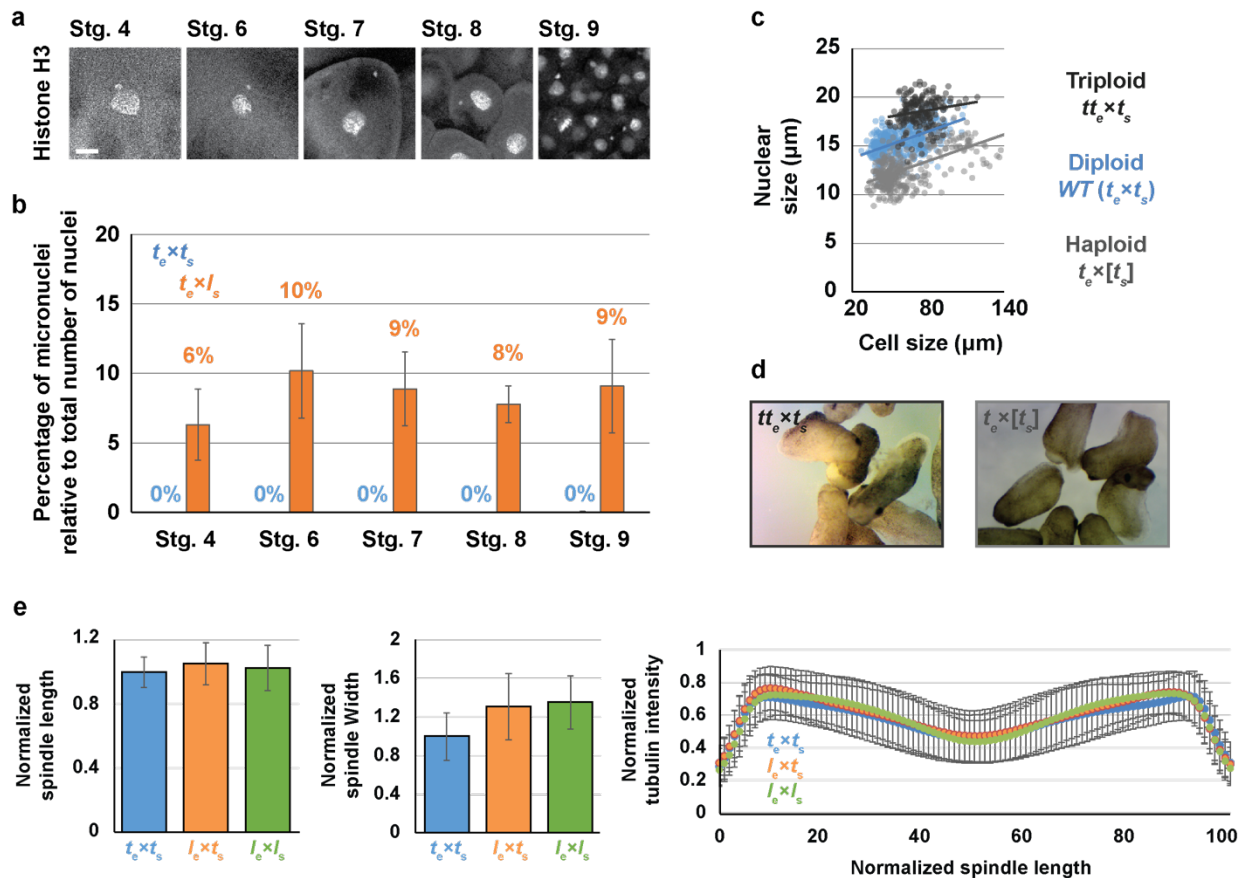


**Figure 4.2: Occurrence of micronuclei, role of ploidy and spindle architecture.**

**a**, Micronuclei in  $t_e \times l_s$  hybrid embryos at various developmental stages. Whole mount embryo immunofluorescence was performed in  $t_e \times l_s$  hybrid embryos using anti-histone H3 antibody at stages 4, 6, 7, 8 and 9. Scale bar is 10  $\mu\text{m}$ . **b**, Quantification of micronuclei in *X. tropicalis* (blue) and  $t_e \times l_s$  hybrid (orange) embryos. The percentage of micronuclei was calculated as the number of micronuclei in the imaged portion of the embryo divided by the total number of nuclei in the same imaged portion. The average percentage of micronuclei for several embryos at stage 4 ( $n$

= 16 *X. tropicalis* embryos with a total of 58 nuclei and 18  $t_e \times l_s$  hybrids with 63 nuclei), stage 6 (n = 13/84 and 17/115), stage 7 (n = 5/148 and 10/351), stage 8 (n = 4/480 and 8/1119) and stage 9 (n = 5/5526 and 3/2004) is shown. Error bars indicate the standard error of the mean. **c**, Nuclear size in *X. tropicalis* embryos with varying ploidy. Nuclear size relative to cell size (diameters in  $\mu\text{m}$ ) is plotted for triploid ( $tt_e \times t_s$ ; dark grey, n = 175), diploid (*X. tropicalis*,  $t_e \times t_s$ ; blue, n = 453) and haploid ( $t_e \times [t_s]$ ; light grey, n = 346) embryos. Each dot indicates an individual data point and the solid lines indicate a linear fit. **d**, *X. tropicalis* embryos with varying ploidy at tailbud stage. Images of triploid ( $tt_e \times t_s$ ; left) and haploid ( $t_e \times [t_s]$ ; right) tailbuds were taken under identical conditions. **e**, Size and microtubule distribution in *X. tropicalis* spindles assembled from different embryo nuclei DNA (n = 198, 157 and 224 spindles quantified for *X. tropicalis*,  $l_e \times t_s$  hybrids, and *X. laevis* embryo nuclei, respectively, from 3 different egg extracts). Spindle length (left) and width (middle) were normalized to the *X. tropicalis* control, averages are plotted and the error bars indicate the standard deviation. Line scans of rhodamine-tubulin signal along spindle length were taken (right). Spindle lengths were normalized to 100% and tubulin intensities were normalized among datasets. The average intensities are plotted for the three spindle types, error bars indicate standard deviation and colors are as in Figure 2a. The number of spindles quantified is n = 198 for *X. tropicalis*, n = 157 for  $l_e \times t_s$  hybrid, and n = 224 for *X. laevis* embryo nuclei from 3 different egg extracts.

To determine whether assembly and function of the mitotic apparatus was affected, we used the in vitro egg extract system to examine spindle assembly and mitotic chromosome morphology. Metaphase-arrested *X. tropicalis* egg extract reconstituted spindle formation around nuclei isolated from stage 8 *X. tropicalis* (N=20), *X. laevis* (N=36), and viable hybrid embryos ( $l_e \times t_s$ ; N=28) (Fig. 4.3a). Spindle width scaled slightly with increasing genome size, but microtubule distribution was not affected by either genome size or content (Fig. 4.2e), indicating that the presence of *X. laevis* DNA did not impair spindle assembly in *X. tropicalis* cytoplasm. To investigate chromosome morphology, *X. laevis* sperm nuclei were cycled through S phase in either *X. laevis* or *X. tropicalis* egg extract, induced to arrest in metaphase, and then stained with a DNA dye and antibodies to either CENP-A, the core centromeric histone variant, or Ndc80, an outer kinetochore component essential for linking centromeres to spindle microtubules (Cheeseman, 2014). Two fluorescent spots per chromosome were often visible in either extract, suggesting that the *X. tropicalis* extract is capable of replicating the *X. laevis* genome to generate duplicated sister chromatids. However, we observed 13.5% fewer CENP-A-labeled and 12% fewer Ndc80-labeled chromosomes in *X. tropicalis* extract compared to *X. laevis* extract (Fig. 4.3b), suggesting that approximately two *X. laevis* chromosomes do not possess centromeres that become competent for kinetochore assembly following a cell cycle in *X. tropicalis* cytoplasm. Whole-genome sequencing of embryos at stage 9 prior to cell death revealed the specific loss of 228 Mb of *X. laevis* sequence from  $t_e \times l_s$  hybrids (Fig. 4.3c), 96% of which was missing from just two chromosomes, 3L and 4L. By contrast, no genomic deletions were detected in viable  $l_e \times t_s$  hybrid embryos (data not shown). Chromosome regions adjacent to breakpoints were heterogeneous in abundance (Fig. 4.3d), consistent with stochastic chromosome breakage and loss. Notably, major breakpoints localized to a gap in the genome assembly, indicating the presence of repetitive elements. Chromosome loss and partial deletion has been observed in nonviable hybrids in fish (Fujiwara et al., 1997; Sakai et al., 2007) and *Drosophila* (Ferree and Barbash, 2009), but the underlying mechanisms were unclear. Our results suggest that  $t_e \times l_s$  hybrid incompatibility may be due to

divergence of centromeric sequences, which are poorly characterized in *Xenopus* but known to evolve rapidly (Kalitsis and Choo, 2012), or to other unidentified repetitive DNA elements that lead to chromosome instability and ultimately prevent kinetochore assembly on chromosomes 3L and 4L.

**Figure 4.3**

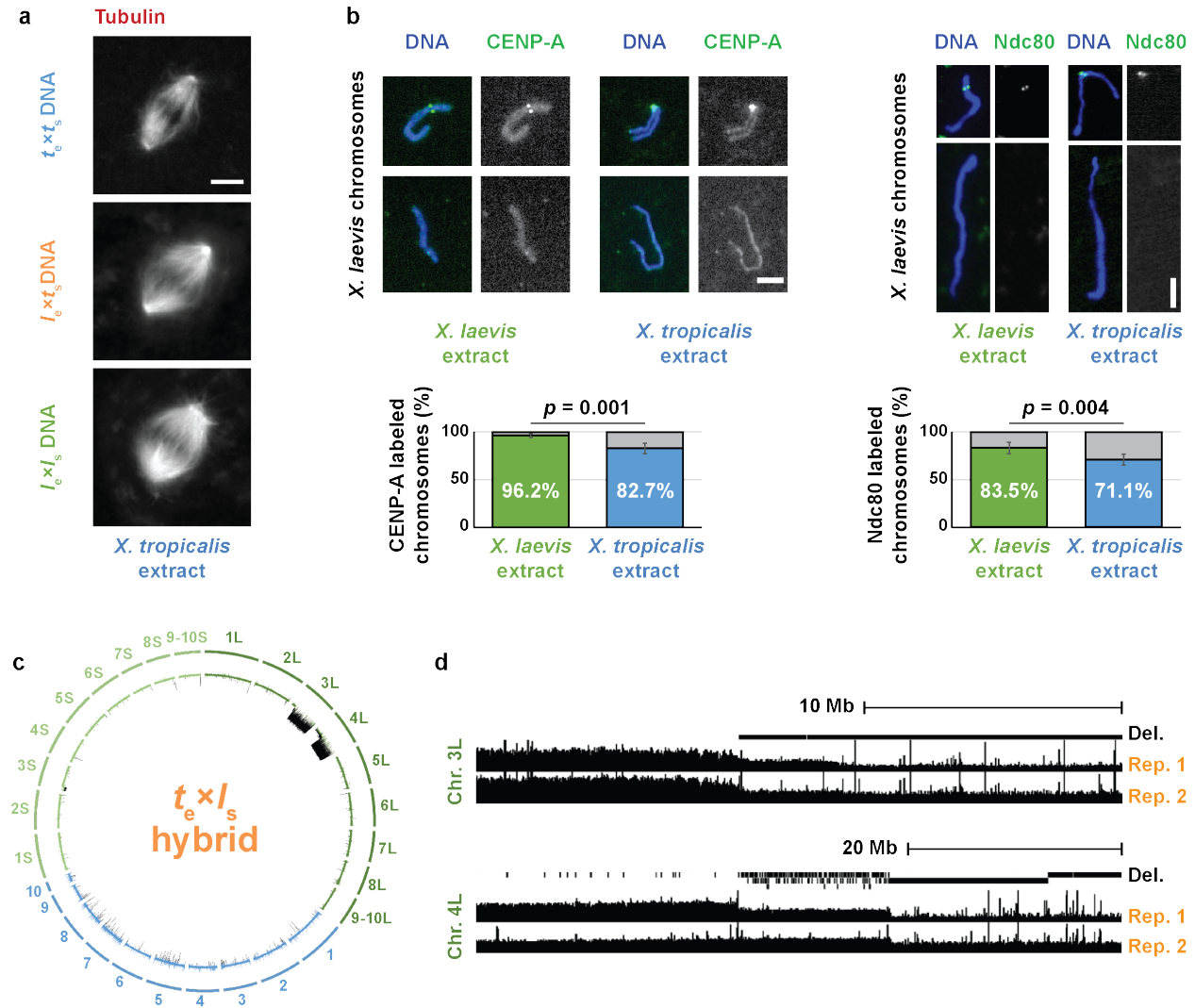


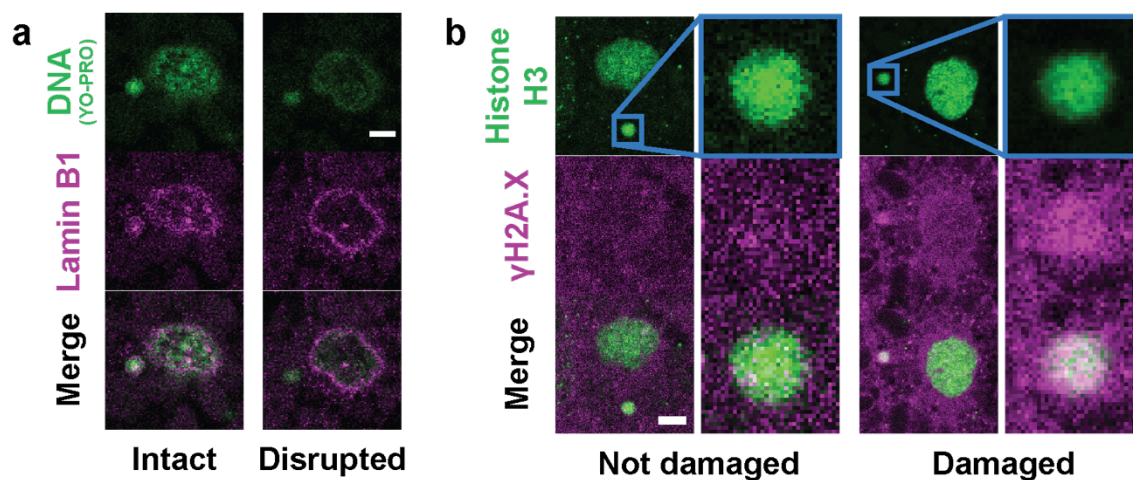
**Figure 4.3: Compatibility of *X. laevis* chromosomes with *X. tropicalis* cytoplasm.**

**a**, Fluorescence images of spindles formed around *X. tropicalis*,  $l_e \times t_s$  hybrid and *X. laevis* chromosomes in *X. tropicalis* egg extract. Scale bar, 10  $\mu$ m. See Fig. 3.2e for quantification. **b**, Fluorescence images of *X. laevis* chromosomes stained for CENP-A or Ndc80 following replication in *X. laevis* or *X. tropicalis* egg extract. CENP-A and Ndc80 labeling was quantified from  $n = 1792$  and  $n = 1959$  chromosomes, respectively in *X. laevis* extract, and  $n = 2692$  and  $n = 1930$ , respectively, in *X. tropicalis* extract. Scale bars, 5  $\mu$ m. Error bars are standard deviation,  $p$  values determined by two-tailed heteroscedastic t-test. **c**, Circle plot of whole genome sequencing data for  $t_e \times l_s$  hybrid embryos aligned and normalized to the genomes of *X. tropicalis*

(blue) and *X. laevis* (green), with underrepresented genome regions in black. **d**, Expanded view of chromosome 3L and 4L breakpoints with deleted regions indicated in two biological replicates.

We next investigated the link between chromosome loss and  $t_e \times I_s$  hybrid embryo death. Micronuclei in cancer cells accumulate DNA damage (Crasta et al., 2012; Hatch et al., 2013; Terradas et al., 2009) and, in *Xenopus*, DNA damage was shown to trigger apoptosis at the onset of gastrulation (Hensey and Gautier, 1997). As in cancer cells, micronuclei in  $t_e \times I_s$  hybrid embryos often lost envelope integrity and contained damaged DNA (Fig. 4.4a, b). However,  $t_e \times I_s$  hybrid death did not resemble TUNEL-positive apoptotic death induced by chemical inhibitors of DNA replication or protein synthesis in *X. tropicalis* embryos (Fig. 4.4c; Table 4.2; Videos 4.6, 4.7). We hypothesized that chromosome loss could lead to cell death by affecting gene expression at zygotic genome activation. To assess the effects of blocking gene expression globally, we treated *X. tropicalis* embryos with the transcription initiation inhibitor triptolide and observed a phenotype reminiscent of the timing and manner of the catastrophic  $t_e \times I_s$  hybrid embryo death, although lysis did not initiate from the vegetal side (Table 4.2; Videos 4.8, 4.9). To test whether altering gene dosage could rescue hybrid viability, we applied cold shock to the hybrid zygote to suppress polar body extrusion and introduce a second copy of the *X. tropicalis* genome. Although extremely inefficient, a total of 9 triploid hybrid  $tt_e \times I_s$  embryos were obtained in 4 separate experiments and survived to tailbud/tadpole stages (Fig. 4.5a). Rescued embryos possessed significantly higher DNA content than diploid *X. tropicalis* embryos at stage 21 (Fig. 4.5b), but whole genome sequencing revealed that *X. laevis* DNA was eliminated by the tadpole stage (Fig. 4.6a, Table 4.3, 4.4). Our results link  $t_e \times I_s$  hybrid inviability with altered gene expression that can be rescued with a second copy of the *X. tropicalis* genome, and indicate that  $t_e \times I_s$  hybrid embryo inviability is caused by defects at the onset of zygotic genome activation, and not by DNA damage and apoptosis.

**Figure 4.4**



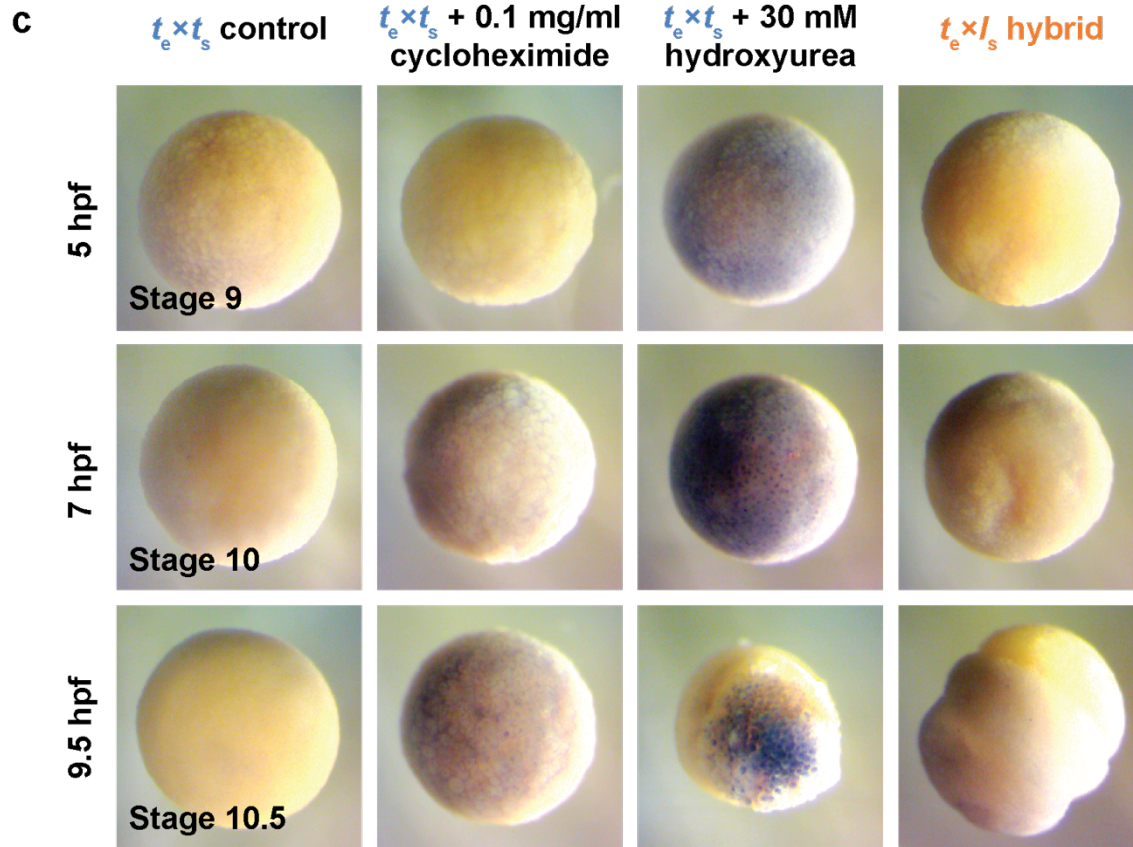


**Figure 4.4: Characterization of micronuclei in  $t_e \times I_s$  hybrid embryos and link to embryo death.**

**a**, Disrupted micronuclei envelopes in  $t_e \times I_s$  hybrid embryos. Whole mount embryo immunofluorescence was performed in  $t_e \times I_s$  hybrid embryos using the YO-PRO DNA dye (top) and anti-Lamin B1 antibody (middle), corresponding channels are shown in green and magenta, respectively. The merged images are shown below. Intact (left) and disrupted (right) envelopes were observed. Scale bar is 10  $\mu$ m. **b**, DNA damage in  $t_e \times I_s$  hybrid embryo micronuclei. Whole mount embryo immunofluorescence was performed in  $t_e \times I_s$  hybrid embryos using anti-histone H3 (top) and anti- $\gamma$ H2A.X (middle) antibodies, corresponding channels are shown in green and magenta, respectively. The merge images are shown below. Micronuclei with undamaged (left; negative  $\gamma$ H2A.X signal) and damaged (right; positive  $\gamma$ H2A.X signal) DNA were observed. Zoomed images of micronuclei are shown on the right of each image. Scale bar is 10  $\mu$ m. **c**, TUNEL assay in apoptotic *X. tropicalis* and  $t_e \times I_s$  hybrid embryos. *X. tropicalis* (left), *X. tropicalis* treated with cycloheximide (middle left) or hydroxyurea (middle right) as indicated, and  $t_e \times I_s$  hybrid (right) embryos were prepared for TUNEL assay 5 h post fertilization (hpf; equivalent stage 9; top), 7 hpf (equivalent stage 10; middle) and 9.5 hpf (equivalent stage 10.5; bottom). Representative images are shown and were taken under identical conditions.

**Table 4.2**

Drug	Inhibition	Time of addition	Concentration	Phenotype	Product details
Cycloheximide	Protein synthesis	stage 6.5	0.1 mg/ml	Cell cycle arrest at stage 7 followed by apoptosis	C7698 (Sigma-Aldrich)
Hydroxyurea	DNA replication	stage 3	30 mM	Apoptosis at late stage 8	AC151680050 (Thermo Fisher Sc.)
Triptolide	Transcription	stage 2	25 $\mu$ M	Cell lysis at stage 9	T3652 (Sigma-Aldrich)
Olygomycin	ATP Synthase	stage 2	40 $\mu$ M	Cell cycle arrest at stage 9	75351 (Sigma-Aldrich)
AP-III-a4	Enolase (incl. 'moonlighting' functions)	stage 2	30 $\mu$ M	Arrest at stage 7 and followed by cell lysis	19933 (Cayman Chemical)
Iodoacetic acid	Glyceraldehyde-3-P dehydrogenase	stage 2	50 mM	Cell lysis at stage 9	I4386 (Sigma-Aldrich)
CP-91,149	Glycogen phosphorylase	stage 2	270 $\mu$ M	Cell death at stage 9 from the vegetal side	PZ0104 (Sigma-Aldrich)

**Table 4.2: Effects of drug treatments on  $t_e \times t_s$  embryos**

*X. tropicalis* embryos were treated with different drugs at different stages. Phenotypes of effects are listed. When unspecified, apoptosis or lysis initiated at random locations in the embryo.

**Video 4.6. Phenotype of embryo death induced by inhibition of protein synthesis**

*X. tropicalis* eggs were fertilized with *X. tropicalis* sperm and imaged while incubated from stage 6.5 in 1/10X MMR containing 0.1 mg/ml cycloheximide. The video plays 20h in 15s (rate of 120 fps) and the scale bar corresponds to 200  $\mu$ m.

**Video 4.7. Phenotype of embryo death induced by inhibition of DNA replication**

*X. tropicalis* eggs were fertilized with *X. tropicalis* sperm and imaged while incubated from stage 3 in 1/10X MMR containing 30 mM hydroxyurea. The video plays 20h in 15s (rate of 120 fps) and the scale bar corresponds to 200  $\mu$ m.

**Video 4.8. Phenotype of embryo death induced by inhibiting transcription using triptolide**

*X. tropicalis* eggs were fertilized with *X. tropicalis* sperm and imaged in separate dishes while incubated from stage 2 in 1/10X MMR containing 25  $\mu$ M triptolide (left) or a corresponding amount of DMSO (right). The video plays 20h in 15s (rate of 120 fps) and the scale bar corresponds to 200  $\mu$ m.

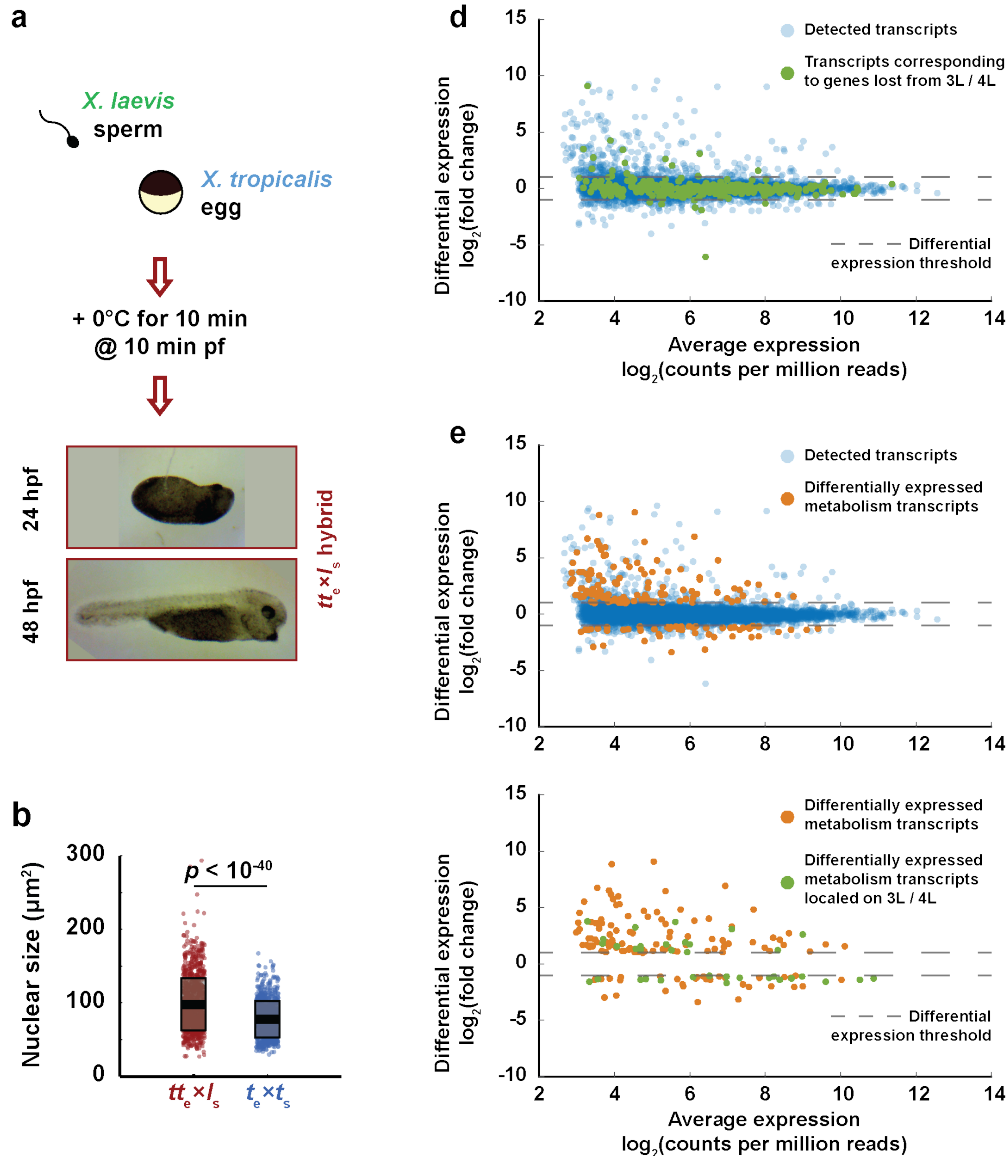
**Video 4.9. Effect of triptolide treatment on  $t_e \times I_s$  hybrid embryos**

*X. tropicalis* eggs were fertilized with *X. laevis* sperm and imaged in separate dishes while incubated from stage 2 in 1/10X MMR containing 25  $\mu$ M triptolide (left) or a corresponding amount of DMSO (right). The video plays 20h in 15s (rate of 120 fps) and the scale bar corresponds to 200  $\mu$ m.

Since metabolite pools are known to become crucial before gastrulation (Vastag et al., 2011), we subjected  $t_e \times I_s$  hybrid embryos to metabolic profiling just prior to the characteristic deformation preceding lysis (7 hpf). Levels of 17 out of 179 metabolites detected were significantly altered (Fig. 4.5c). Reduction in lactic acid, the final product of fermentation, and tricarboxylic acid cycle intermediates revealed that glycolytic metabolism was impaired in the cytoplasm of  $t_e \times I_s$  hybrid embryos, which could in turn alter lipid metabolites including neutral lipids such as diacylglycerols (DAGs) and monoacylglycerols (MAGs), as well as fatty acid oxidation metabolites such as acyl carnitines (ACs) (Fig. 4.6b). While inhibition of mitochondrial ATP synthase led to a cell cycle arrest at stage 9 (Video 4.10), perturbing the early steps of glycolysis in  $t_e \times t_s$

embryos induced cell death and lysis (Video 4.11, Table 4.2). In particular, inhibition of glycogen phosphorylase to block the release of glucose from glycogen, led to cell death at stage 9 initiated from the vegetal side (Video 4.12). These results are consistent with glycolytic defects as a primary cause of  $t_e \times l_s$  hybrid embryo death. However, other defects that contribute to hybrid incompatibility could be masked by the abrupt cell lysis, such as conflicts between the paternal genome and maternal mitochondria (Ma et al., 2016; Lee et al., 2008b).

**Figure 4.5**





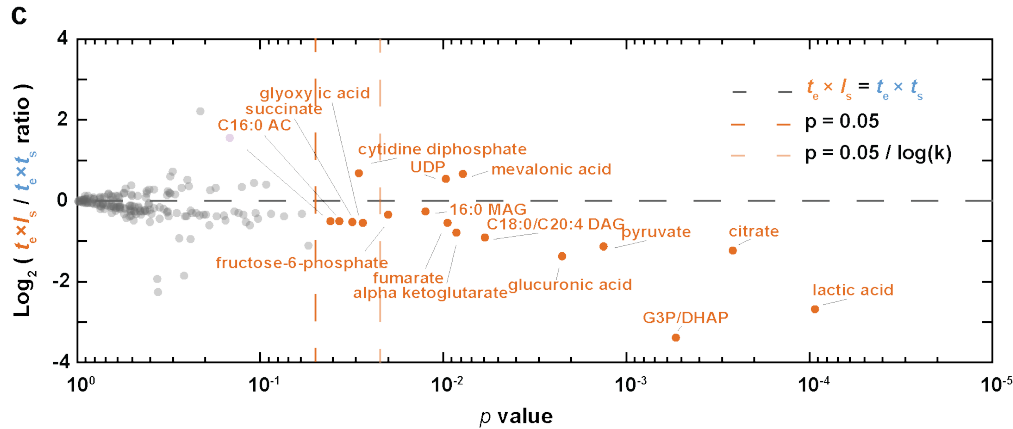


**Figure 4.5: Gene expression and metabolic changes preceding  $t_e \times I_s$  hybrid embryo death.** **a**, Schematic of polar body suppression experiment and images of  $t_e \times I_s$  rescued embryos 24 h and 48 h post-fertilization (hpf). **b**, Box plot of nuclear sizes ( $n = 988$  nuclei for  $t_e \times I_s$  and  $n = 777$  for *X. tropicalis*) showing the average area and standard deviation, p values determined by two-tailed heteroscedastic t-test. **c**, Levels of 179 metabolites in *X. tropicalis* and  $t_e \times I_s$  hybrid embryos 7 hpf (see Methods). **d**, Differential gene expression between  $t_e \times I_s$  and  $t_e \times t_s$  (see Methods). All detected transcripts ( $n = 8379$ ) are plotted in blue. Transcripts corresponding to genes lost from chromosomes 3L and 4L ( $n = 270$ ) are plotted in green. **e**, Differential expression of metabolism genes between  $t_e \times I_s$  and  $t_e \times t_s$  (see Methods). Differentially expressed metabolism transcripts ( $n = 165$ ) are plotted in orange, all detected transcripts ( $n = 8379$ ) in blue (top), and differentially expressed metabolism transcripts located on chromosomes 3L and 4L ( $n = 35$ ) in green (bottom).

#### Video 4.10. Effect of inhibiting ATP synthase on *X. tropicalis* embryos

*X. tropicalis* eggs were fertilized with *X. tropicalis* sperm and imaged in separate dishes while incubated from stage 2 in 1/10X MMR containing 40  $\mu\text{M}$  oligomycin (left) or a corresponding amount of DMSO (right). The video plays 20h in 15s (rate of 120 fps) and the scale bar corresponds to 200  $\mu\text{m}$ .

#### Video 4.11. Effect of inhibiting glyceraldehyde-3-P dehydrogenase on *X. tropicalis* embryos

*X. tropicalis* eggs were fertilized with *X. tropicalis* sperm and imaged in separate dishes while incubated from stage 2 in 1/10X MMR containing 50 mM iodoacetic acid (left) or a corresponding amount of ddH<sub>2</sub>O (right). The video plays 20h in 15s (rate of 120 fps) and the scale bar corresponds to 200  $\mu\text{m}$ .

#### Video 4.12. Effect of inhibiting glycogen phosphorylation on *X. tropicalis* embryos

*X. tropicalis* eggs were fertilized with *X. tropicalis* sperm and imaged in separate dishes while incubated from stage 2 in 1/10X MMR containing 270  $\mu\text{M}$  CP-91,149 (left) or a corresponding amount of DMSO (right). The video plays 20h in 15s (rate of 120 fps) and the scale bar corresponds to 200  $\mu\text{m}$ .

**Figure 4.6**

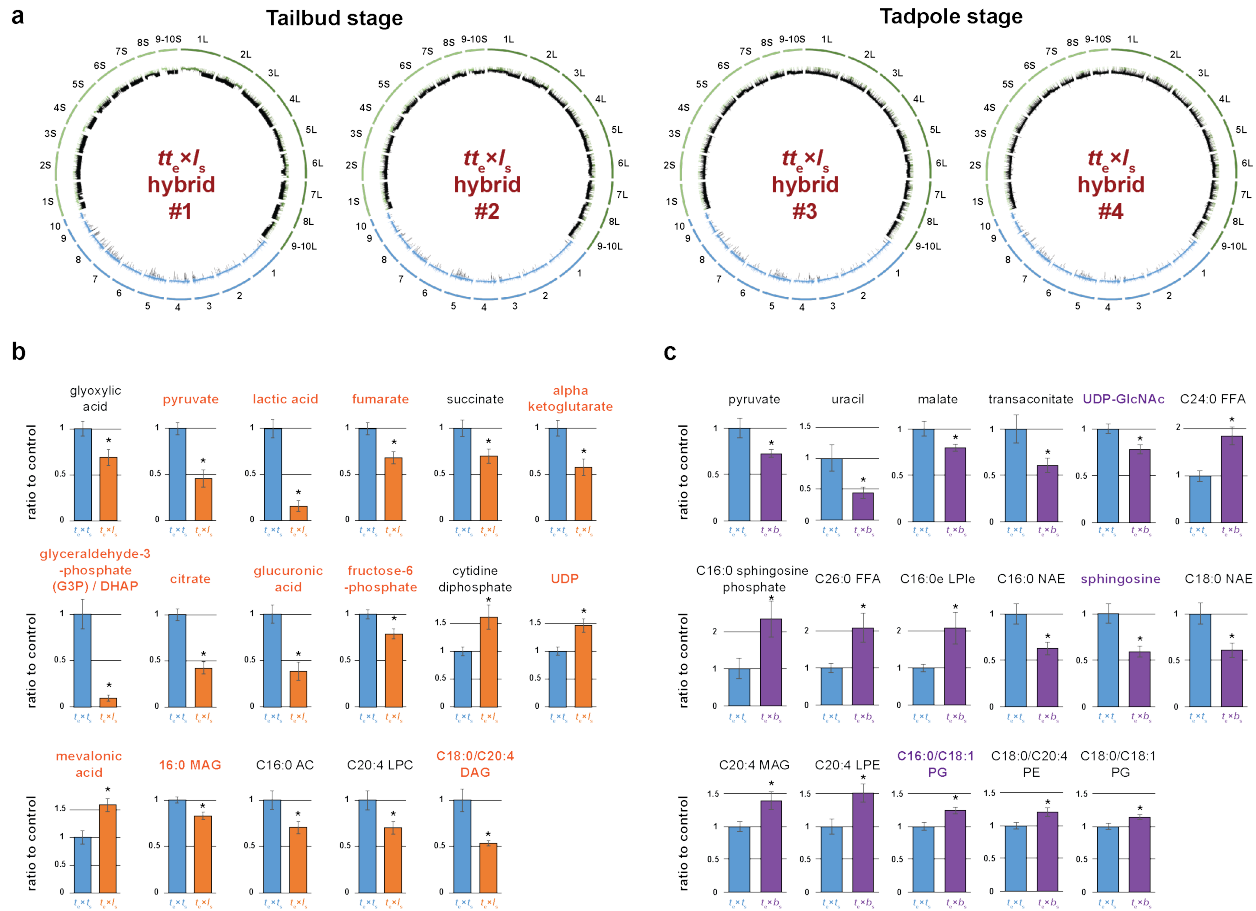


**Figure 4.6: Whole genome sequencing of  $tt_e \times I_s$  rescued embryos and metabolomic profiling of  $t_e \times I_s$  and  $t_e \times b_s$  hybrid embryos.**

**a**, The genomes of 4  $tt_e \times I_s$  rescued embryos were sequenced, aligned, and normalized to the genomes of *X. tropicalis* (blue) and *X. laevis* (green) for which sub-genomes S and L were distinguished (S in light green and L in dark green). Underrepresented regions of the genomes are color-coded in black. The  $tt_e \times I_s$  embryo genomes 1-2 were prepared from tailbuds, and 3-4 from tadpoles. **b**, Metabolites differentially represented between  $t_e \times I_s$  hybrid and *X. tropicalis* embryos 7 h post fertilization. Among the 179 metabolites detected, 17 were significantly altered in  $t_e \times I_s$  hybrid embryos and are shown as a ratio to the *X. tropicalis* control. Values for *X. tropicalis* are shown in blue and the  $t_e \times I_s$  hybrid in orange. Stars indicate statistical significance ( $p < 0.05$ ; two-tailed homoscedastic t-test). Metabolites with p values below the penalized Bonferroni corrected threshold are labeled in orange. **c**, Metabolites differentially represented between  $t_e \times b_s$  hybrid and *X. tropicalis* embryos 7 h post fertilization. Among the 241 metabolites detected, 17 were significantly altered in  $t_e \times b_s$  hybrid embryos and are shown as a ratio to the *X. tropicalis* control. Values for *X. tropicalis* are shown in blue and the  $t_e \times b_s$  hybrid in purple. Stars indicate statistical significance ( $p < 0.05$ ; two-tailed homoscedastic t-test). Metabolites with p values below the penalized Bonferroni corrected threshold are labeled in purple.

**Table 4.3**

<b><math>t_e \times I_s</math> hybrid</b>					
<b>Sub genome</b>	<b>Total (bp)</b>	<b>Lost (bp)</b>	<b>Remaining (bp)</b>	<b>Lost (%)</b>	<b>Remaining (%)</b>
<i>X.laevis</i> L	1368982762	237294229	1131688533	17.33	82.67
<i>X.laevis</i> S	1139955720	11850000	1128105720	1.04	98.96
<i>X.tropicalis</i>	1272999256	3452000	1269547256	0.27	99.73

<b><math>tt_e \times I_s</math> hybrid #1</b>					
<b>Sub genome</b>	<b>Total (bp)</b>	<b>Lost (bp)</b>	<b>Remaining (bp)</b>	<b>Lost (%)</b>	<b>Remaining (%)</b>
<i>X.laevis</i> L	1368982762	1084660643	284322119	79.23	20.77
<i>X.laevis</i> S	1139955720	946048452	193907268	82.99	17.01
<i>X.tropicalis</i>	1272999256	5686000	1267313256	0.45	99.55

<b><math>tt_e \times I_s</math> hybrid #2</b>					
<b>Sub genome</b>	<b>Total (bp)</b>	<b>Lost (bp)</b>	<b>Remaining (bp)</b>	<b>Lost (%)</b>	<b>Remaining (%)</b>
<i>X.laevis</i> L	1368982762	1259268028	109714734	91.99	8.01
<i>X.laevis</i> S	1139955720	1003939197	136016523	88.07	11.93
<i>X.tropicalis</i>	1272999256	2964000	1270035256	0.23	99.77

<b><math>tt_e \times I_s</math> hybrid #3</b>					
<b>Sub genome</b>	<b>Total (bp)</b>	<b>Lost (bp)</b>	<b>Remaining (bp)</b>	<b>Lost (%)</b>	<b>Remaining (%)</b>
<i>X.laevis</i> L	1368982762	1360054762	8928000	99.35	0.65
<i>X.laevis</i> S	1139955720	1131571720	8384000	99.26	0.74
<i>X.tropicalis</i>	1272999256	3728000	1269271256	0.29	99.71

<b><math>tt_e \times I_s</math> hybrid #4</b>					
<b>Sub genome</b>	<b>Total (bp)</b>	<b>Lost (bp)</b>	<b>Remaining (bp)</b>	<b>Lost (%)</b>	<b>Remaining (%)</b>
<i>X.laevis</i> L	1368982762	1361764762	7218000	99.47	0.53
<i>X.laevis</i> S	1139955720	1134337720	5618000	99.51	0.49
<i>X.tropicalis</i>	1272999256	3240000	1269759256	0.25	99.75

<b><math>t_e \times b_s</math> hybrid</b>					
<b>Sub genome</b>	<b>Total (bp)</b>	<b>Lost (bp)</b>	<b>Remaining (bp)</b>	<b>Lost (%)</b>	<b>Remaining (%)</b>
<i>X.borealis</i> L	1428994000	108866000	1320128000	7.62%	92.38%
<i>X.borealis</i> S	1201786000	30804000	1170982000	2.56%	97.44%
<i>X.tropicalis</i>	1273010000	11592000	1261418000	0.91%	99.09%

**Table 4.3: Sub-genome distribution of lost compared with retained DNA in  $t_e \times I_s$ ,  $tt_e \times I_s$ , and  $t_e \times b_s$  hybrids**

Percentage of lost and remaining DNA for each sub-genome is shown for all hybrids sequenced. Sub-genomes are color-coded as in Figs 4.3c and 4.7e.

Table 4.4

<b><i>t<sub>e</sub> × I<sub>s</sub></i> hybrid</b>							
Sub genome	Chromosome	Total (bp)	Lost (bp)	Remaining (bp)	Lost (%)	Remaining (%)	
<i>X.laevis</i>	1L	219879705	118000	219761705	0.05	99.95	
<i>X.laevis</i>	2L	181296326	90000	181206326	0.05	99.95	
<i>X.laevis</i>	3L	144228235	123166235	21062000	85.40	14.60	
<i>X.laevis</i>	4L	144109994	113375994	30734000	78.67	21.33	
<i>X.laevis</i>	5L	159431385	132000	159299385	0.08	99.92	
<i>X.laevis</i>	6L	155092408	132000	154960408	0.09	99.91	
<i>X.laevis</i>	7L	126865703	98000	126767703	0.08	99.92	
<i>X.laevis</i>	8L	120180497	146000	120034497	0.12	99.88	
<i>X.laevis</i>	9_10L	117898509	36000	117862509	0.03	99.97	
<i>X.laevis</i>	1S	180018555	46000	179972555	0.03	99.97	
<i>X.laevis</i>	2S	159817000	50000	159767000	0.03	99.97	
<i>X.laevis</i>	3S	120503335	11260000	109243335	9.34	90.66	
<i>X.laevis</i>	4S	121299787	110000	121189787	0.09	99.91	
<i>X.laevis</i>	5S	136612523	36000	136576523	0.03	99.97	
<i>X.laevis</i>	6S	128404278	52000	128352278	0.04	99.96	
<i>X.laevis</i>	7S	89697455	20000	89677455	0.02	99.98	
<i>X.laevis</i>	8S	98992745	118000	98874745	0.12	99.88	
<i>X.laevis</i>	9_10S	104610042	158000	104452042	0.15	99.85	
<i>X.tropicalis</i>	1	194899139	206000	194693139	0.11	99.89	
<i>X.tropicalis</i>	2	170236069	482000	169754069	0.28	99.72	
<i>X.tropicalis</i>	3	137289692	388000	136901692	0.28	99.72	
<i>X.tropicalis</i>	4	133513928	118000	133395928	0.09	99.91	
<i>X.tropicalis</i>	5	146597336	578000	146019336	0.39	99.61	
<i>X.tropicalis</i>	6	135158710	126000	135032710	0.09	99.91	
<i>X.tropicalis</i>	7	117244592	536000	116708592	0.46	99.54	
<i>X.tropicalis</i>	8	117649117	622000	117027117	0.53	99.47	
<i>X.tropicalis</i>	9	80450090	338000	80112090	0.42	99.58	
<i>X.tropicalis</i>	10	39960583	58000	39902583	0.15	99.85	
<b><i>tt<sub>e</sub> × I<sub>s</sub></i> hybrid #1</b>							
Sub genome	Chromosome	Total (bp)	Lost (bp)	Remaining (bp)	Lost (%)	Remaining (%)	
<i>X.laevis</i>	1L	219879705	86227705	133652000	39.22	60.78	
<i>X.laevis</i>	2L	181296326	132870000	48426326	73.29	26.71	
<i>X.laevis</i>	3L	144228235	142672235	1556000	98.92	1.08	
<i>X.laevis</i>	4L	144109994	142801994	1308000	99.09	0.91	
<i>X.laevis</i>	5L	159431385	152592000	6839385	95.71	4.29	
<i>X.laevis</i>	6L	155092408	107582000	47510408	69.37	30.63	
<i>X.laevis</i>	7L	126865703	117713703	9152000	92.79	7.21	
<i>X.laevis</i>	8L	120180497	98994497	21186000	82.37	17.63	
<i>X.laevis</i>	9_10L	117898509	103206509	14692000	87.54	12.46	
<i>X.laevis</i>	1S	180018555	145138555	34880000	80.62	19.38	
<i>X.laevis</i>	2S	159817000	158427000	1390000	99.13	0.87	
<i>X.laevis</i>	3S	120503335	119061335	1442000	98.80	1.20	
<i>X.laevis</i>	4S	121299787	87753787	33546000	72.34	27.66	
<i>X.laevis</i>	5S	136612523	95608000	41004523	69.98	30.02	
<i>X.laevis</i>	6S	128404278	106972278	21432000	83.31	16.69	
<i>X.laevis</i>	7S	89697455	88329455	1368000	98.47	1.53	
<i>X.laevis</i>	8S	98992745	82818000	16174745	83.66	16.34	
<i>X.laevis</i>	9_10S	104610042	61940042	42670000	59.21	40.79	
<i>X.tropicalis</i>	1	194899139	434000	194465139	0.22	99.78	
<i>X.tropicalis</i>	2	170236069	184000	170052069	0.11	99.89	
<i>X.tropicalis</i>	3	137289692	366000	136923692	0.27	99.73	
<i>X.tropicalis</i>	4	133513928	616000	132897928	0.46	99.54	
<i>X.tropicalis</i>	5	146597336	552000	146045336	0.38	99.62	
<i>X.tropicalis</i>	6	135158710	326000	134832710	0.24	99.76	
<i>X.tropicalis</i>	7	117244592	1282000	115962592	1.09	98.91	
<i>X.tropicalis</i>	8	117649117	1360000	116289117	1.16	98.84	
<i>X.tropicalis</i>	9	80450090	526000	79924090	0.65	99.35	
<i>X.tropicalis</i>	10	39960583	40000	39920583	0.10	99.90	

<b><i>tt<sub>e</sub> × I<sub>s</sub></i> hybrid #2</b>						
Sub genome	Chromosome	Total (bp)	Lost (bp)	Remaining (bp)	Lost (%)	Remaining (%)
<i>X.laevis</i>	1L	219879705	147509705	72370000	67.09	32.91
<i>X.laevis</i>	2L	181296326	173164000	8132326	95.51	4.49
<i>X.laevis</i>	3L	144228235	143472235	756000	99.48	0.52
<i>X.laevis</i>	4L	144109994	143293994	816000	99.43	0.57
<i>X.laevis</i>	5L	159431385	158345385	1086000	99.32	0.68
<i>X.laevis</i>	6L	155092408	140646000	14446408	90.69	9.31
<i>X.laevis</i>	7L	126865703	125951703	914000	99.28	0.72
<i>X.laevis</i>	8L	120180497	109526497	10654000	91.14	8.86
<i>X.laevis</i>	9_10L	117898509	117358509	540000	99.54	0.46
<i>X.laevis</i>	1S	180018555	153918555	26100000	85.50	14.50
<i>X.laevis</i>	2S	159817000	159061000	756000	99.53	0.47
<i>X.laevis</i>	3S	120503335	119983335	520000	99.57	0.43
<i>X.laevis</i>	4S	121299787	89435787	31864000	73.73	26.27
<i>X.laevis</i>	5S	136612523	111200000	25412523	81.40	18.60
<i>X.laevis</i>	6S	128404278	112342278	16062000	87.49	12.51
<i>X.laevis</i>	7S	89697455	89193455	504000	99.44	0.56
<i>X.laevis</i>	8S	98992745	98228745	764000	99.23	0.77
<i>X.laevis</i>	9_10S	104610042	70576042	34034000	67.47	32.53
<i>X.tropicalis</i>	1	194899139	336000	194563139	0.17	99.83
<i>X.tropicalis</i>	2	170236069	72000	170164069	0.04	99.96
<i>X.tropicalis</i>	3	137289692	148000	137141692	0.11	99.89
<i>X.tropicalis</i>	4	133513928	290000	133223928	0.22	99.78
<i>X.tropicalis</i>	5	146597336	462000	146135336	0.32	99.68
<i>X.tropicalis</i>	6	135158710	88000	135070710	0.07	99.93
<i>X.tropicalis</i>	7	117244592	682000	116562592	0.58	99.42
<i>X.tropicalis</i>	8	117649117	682000	116967117	0.58	99.42
<i>X.tropicalis</i>	9	80450090	180000	80270090	0.22	99.78
<i>X.tropicalis</i>	10	39960583	24000	39936583	0.06	99.94

<b><i>tt<sub>e</sub> × I<sub>s</sub></i> hybrid #3</b>						
Sub genome	Chromosome	Total (bp)	Lost (bp)	Remaining (bp)	Lost (%)	Remaining (%)
<i>X.laevis</i>	1L	219879705	218841705	1038000	99.53	0.47
<i>X.laevis</i>	2L	181296326	180206326	1090000	99.40	0.60
<i>X.laevis</i>	3L	144228235	143394235	834000	99.42	0.58
<i>X.laevis</i>	4L	144109994	143469994	640000	99.56	0.44
<i>X.laevis</i>	5L	159431385	158607385	824000	99.48	0.52
<i>X.laevis</i>	6L	155092408	152752408	2340000	98.49	1.51
<i>X.laevis</i>	7L	126865703	126041703	824000	99.35	0.65
<i>X.laevis</i>	8L	120180497	119286497	894000	99.26	0.74
<i>X.laevis</i>	9_10L	117898509	117454509	444000	99.62	0.38
<i>X.laevis</i>	1S	180018555	178884555	1134000	99.37	0.63
<i>X.laevis</i>	2S	159817000	159149000	668000	99.58	0.42
<i>X.laevis</i>	3S	120503335	119961335	542000	99.55	0.45
<i>X.laevis</i>	4S	121299787	120783787	516000	99.57	0.43
<i>X.laevis</i>	5S	136612523	135652523	960000	99.30	0.70
<i>X.laevis</i>	6S	128404278	125498278	2906000	97.74	2.26
<i>X.laevis</i>	7S	89697455	89209455	488000	99.46	0.54
<i>X.laevis</i>	8S	98992745	98318745	674000	99.32	0.68
<i>X.laevis</i>	9_10S	104610042	104114042	496000	99.53	0.47
<i>X.tropicalis</i>	1	194899139	400000	194499139	0.21	99.79
<i>X.tropicalis</i>	2	170236069	236000	170000069	0.14	99.86
<i>X.tropicalis</i>	3	137289692	206000	137083692	0.15	99.85
<i>X.tropicalis</i>	4	133513928	436000	133077928	0.33	99.67
<i>X.tropicalis</i>	5	146597336	406000	146191336	0.28	99.72
<i>X.tropicalis</i>	6	135158710	76000	135082710	0.06	99.94
<i>X.tropicalis</i>	7	117244592	838000	116406592	0.71	99.29
<i>X.tropicalis</i>	8	117649117	982000	116667117	0.83	99.17
<i>X.tropicalis</i>	9	80450090	120000	80330090	0.15	99.85
<i>X.tropicalis</i>	10	39960583	28000	39932583	0.07	99.93

<b><math>tt_e \times I_s</math> hybrid #4</b>						
Sub genome	Chromosome	Total (bp)	Lost (bp)	Remaining (bp)	Lost (%)	Remaining (%)
<i>X.laevis</i>	1L	219879705	218885705	994000	99.55	0.45
<i>X.laevis</i>	2L	181296326	180228326	1068000	99.41	0.59
<i>X.laevis</i>	3L	144228235	143466235	762000	99.47	0.53
<i>X.laevis</i>	4L	144109994	143479994	630000	99.56	0.44
<i>X.laevis</i>	5L	159431385	158707385	724000	99.55	0.45
<i>X.laevis</i>	6L	155092408	154108408	984000	99.37	0.63
<i>X.laevis</i>	7L	126865703	126043703	822000	99.35	0.65
<i>X.laevis</i>	8L	120180497	119382497	798000	99.34	0.66
<i>X.laevis</i>	9_10L	117898509	117462509	436000	99.63	0.37
<i>X.laevis</i>	1S	180018555	179096555	922000	99.49	0.51
<i>X.laevis</i>	2S	159817000	159175000	642000	99.60	0.40
<i>X.laevis</i>	3S	120503335	119983335	520000	99.57	0.43
<i>X.laevis</i>	4S	121299787	120801787	498000	99.59	0.41
<i>X.laevis</i>	5S	136612523	135676523	936000	99.31	0.69
<i>X.laevis</i>	6S	128404278	127736278	668000	99.48	0.52
<i>X.laevis</i>	7S	89697455	89207455	490000	99.45	0.55
<i>X.laevis</i>	8S	98992745	98318745	674000	99.32	0.68
<i>X.laevis</i>	9_10S	104610042	104342042	268000	99.74	0.26
<i>X.tropicalis</i>	1	194899139	432000	194467139	0.22	99.78
<i>X.tropicalis</i>	2	170236069	260000	169976069	0.15	99.85
<i>X.tropicalis</i>	3	137289692	186000	137103692	0.14	99.86
<i>X.tropicalis</i>	4	133513928	316000	133197928	0.24	99.76
<i>X.tropicalis</i>	5	146597336	222000	146375336	0.15	99.85
<i>X.tropicalis</i>	6	135158710	56000	135102710	0.04	99.96
<i>X.tropicalis</i>	7	117244592	822000	116422592	0.70	99.30
<i>X.tropicalis</i>	8	117649117	814000	116835117	0.69	99.31
<i>X.tropicalis</i>	9	80450090	104000	80346090	0.13	99.87
<i>X.tropicalis</i>	10	39960583	28000	39932583	0.07	99.93

<b><math>t_e \times b_s</math> hybrid</b>						
Sub genome	Chromosome	Total (bp)	Lost (bp)	Remaining (bp)	Lost (%)	Remaining (%)
<i>X.borealis</i>	1L	231226000	356000	230870000	0.15%	99.85%
<i>X.borealis</i>	2L	182956000	232000	182724000	0.13%	99.87%
<i>X.borealis</i>	3L	138668000	252000	138416000	0.18%	99.82%
<i>X.borealis</i>	4L	155290000	15020000	140270000	9.67%	90.33%
<i>X.borealis</i>	5L	172066000	706000	171360000	0.41%	99.59%
<i>X.borealis</i>	6L	155492000	164000	155328000	0.11%	99.89%
<i>X.borealis</i>	7L	137928000	178000	137750000	0.13%	99.87%
<i>X.borealis</i>	8L	122646000	91570000	31076000	74.66%	25.34%
<i>X.borealis</i>	9_10L	132722000	388000	132334000	0.29%	99.71%
<i>X.borealis</i>	1S	195332000	9202000	186130000	4.71%	95.29%
<i>X.borealis</i>	2S	164732000	442000	164290000	0.27%	99.73%
<i>X.borealis</i>	3S	127072000	308000	126764000	0.24%	99.76%
<i>X.borealis</i>	4S	125936000	610000	125326000	0.48%	99.52%
<i>X.borealis</i>	5S	135430000	19160000	116270000	14.15%	85.85%
<i>X.borealis</i>	6S	134526000	206000	134320000	0.15%	99.85%
<i>X.borealis</i>	7S	103278000	198000	103080000	0.19%	99.81%
<i>X.borealis</i>	8S	105648000	484000	105164000	0.46%	99.54%
<i>X.borealis</i>	9_10S	109832000	194000	109638000	0.18%	99.82%
<i>X.tropicalis</i>	1	194900000	1152000	193748000	0.59%	99.41%
<i>X.tropicalis</i>	2	170238000	876000	169362000	0.51%	99.49%
<i>X.tropicalis</i>	3	137290000	1012000	136278000	0.74%	99.26%
<i>X.tropicalis</i>	4	133514000	870000	132644000	0.65%	99.35%
<i>X.tropicalis</i>	5	146598000	1800000	144798000	1.23%	98.77%
<i>X.tropicalis</i>	6	135160000	550000	134610000	0.41%	99.59%
<i>X.tropicalis</i>	7	117246000	1958000	115288000	1.67%	98.33%
<i>X.tropicalis</i>	8	117650000	1924000	115726000	1.64%	98.36%
<i>X.tropicalis</i>	9	80452000	1060000	79392000	1.32%	98.68%
<i>X.tropicalis</i>	10	39962000	390000	39572000	0.98%	99.02%

**Table 4.4: Chromosomal distribution of lost vs. remaining DNA in  $t_e \times I_s$ ,  $tt_e \times I_s$ , and  $t_e \times b_s$  hybrids**

Percentage of lost and remaining DNA for each chromosome is shown for all hybrids sequenced. Sub-genomes are color-coded as in Figs 4.3c and 4.7e.

To evaluate the link between the metabolic defects and specific chromosome loss, we used a statistical analysis (Mi et al., 2016) to classify the list of 1803 genes mapped to the regions lost from chromosomes 3L and 4L in  $t_e \times l_s$ . We found that metabolic processes, particularly in glycolysis, were significantly over-represented (Table 4.5). Transcriptome profiling of  $t_e \times l_s$  hybrid embryos at 7 hpf (available online: [https://static-content.springer.com/esm/art%3A10.1038%2Fnature25188/MediaObjects/41586\\_2018\\_BFnature25188\\_MOESM3\\_ESM.xlsx](https://static-content.springer.com/esm/art%3A10.1038%2Fnature25188/MediaObjects/41586_2018_BFnature25188_MOESM3_ESM.xlsx)) revealed that although a large fraction of genes lost from chromosomes 3L and 4L were not differentially expressed compared to wild type embryos (>92%; Fig. 4.5d), 27.1% of the differentially expressed genes related to metabolism (Fig. 4.5e; top), including PDK1 (pyruvate dehydrogenase kinase). Moreover, 36.7% of the significantly under-expressed metabolism genes are found on chromosomes 3L and 4L (Fig. 4.5e; bottom), including GFPT1 (fructose-6-phosphate aminotransferase) and HPDL (4-hydroxyphenylpyruvate dioxygenase).

**Table 4.5**

<b>3L and 4L lost genes overrepresentation test</b>					
Analysis Type	PANTHER Overrepresentation Test (release 20170413)				
Annotation Version and Release Date	PANTHER version 11.1 Released 2016-10-24				
Analyzed List	Client Text Box Input (Xenopus tropicalis)				
Reference List	Xenopus tropicalis (all genes in database)				
Bonferroni correction	TRUE				
PANTHER GO-Slim Biological Process*	Xenopus tropicalis - REFLIST (18238)	Client Text Box Input (843)	Client Text Box Input (expected)	Client Text Box Input (fold Enrichment)	Client Text Box Input (P-value)
biosynthetic process (GO:0009058)	1295	141	100.05	1.41	8.01E-03
nitrogen compound metabolic process (GO:0006807)	1738	179	134.27	1.33	1.40E-02
metabolic process (GO:0008152)	6036	546	466.32	1.17	1.13E-03
<b>3L and 4L lost metabolism genes overrepresentation test</b>					
Analysis Type	PANTHER Overrepresentation Test (release 20170413)				
Annotation Version and Release Date	PANTHER version 11.1 Released 2016-10-24				
Analyzed List	Client Text Box Input (Xenopus tropicalis)				
Reference List	Xenopus tropicalis (all genes in database)				
Bonferroni correction	TRUE				
PANTHER GO-Slim Biological Process*	Xenopus tropicalis - REFLIST (18238)	Client Text Box Input (843)	Client Text Box Input (expected)	Client Text Box Input (fold Enrichment)	Client Text Box Input (P-value)
glycolysis (GO:0006096)	26	6	0.78	7.71	3.71E-02
rRNA metabolic process (GO:0016072)	104	15	3.11	4.82	2.22E-04
DNA replication (GO:0006260)	114	16	3.41	4.69	1.38E-04
tRNA metabolic process (GO:0006399)	104	14	3.11	4.5	1.11E-03
generation of precursor metabolites and energy (GO:0006091)	185	24	5.54	4.33	9.87E-07

**Table 4.5: Overrepresentation test of all or metabolism-only 3L and 4L lost genes.**

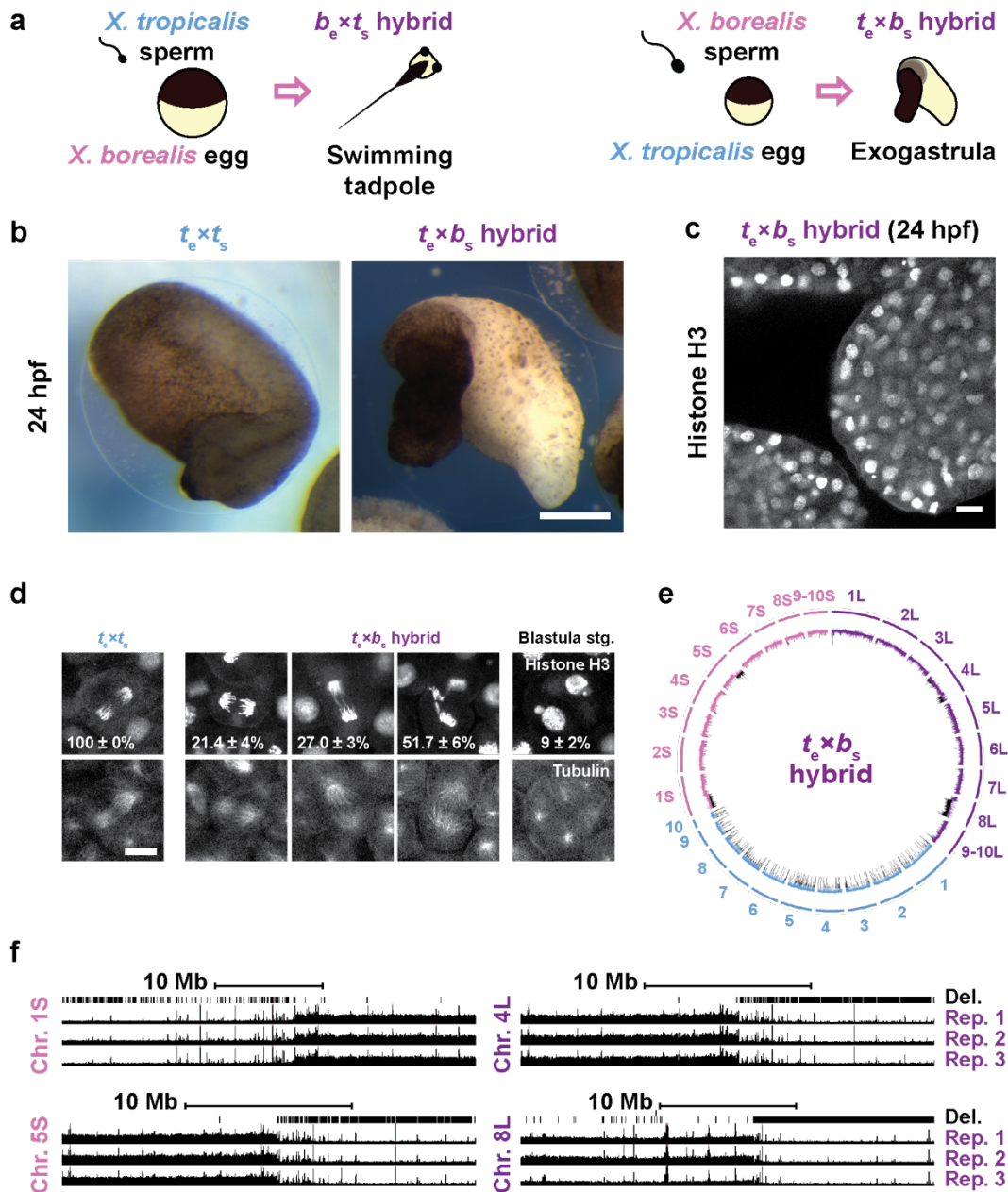
Panther software was used to perform a statistical overrepresentation test on all (top table) or metabolism-only (bottom table) lost genes from chromosomes 3L and 4L.

\* Only over-represented processes are shown in the top table. Only the top five processes based on fold enrichment are shown in the bottom table.

To further characterize the specificity and mechanism underlying  $t_e \times l_s$  hybrid incompatibility, we compared the outcome of cross-fertilizations between *X. tropicalis* and another allotetraploid *Xenopus* species, *X. borealis* (Schmid and Steinlein, 2015). Analogous to hybridization between *X. laevis* and *X. tropicalis*, we observed that *X.*

*borealis* eggs fertilized with *X. tropicalis* sperm ( $b_e \times t_s$ ) were viable while the reverse hybrid ( $t_e \times b_s$ ) was not (Fig. 4.7a). However, the  $t_e \times b_s$  embryos did not lyse, but exogastrulated and survived for hours with intact cells (Fig. 4.7b-c; Video 4.12). Similar to  $t_e \times l_s$ ,  $t_e \times b_s$  embryos displayed chromosome loss through anaphase defects and formation of micronuclei (Fig. 4.7d, Fig. 4.8a-c). Strikingly, whole  $t_e \times b_s$  hybrid genome sequencing revealed that, although the loss was specific for the paternal genome as in the  $t_e \times l_s$  hybrid, specific regions of four different *X. borealis* chromosomes were affected (Fig. 4.7e-f, Table 4.3, 4.4). Furthermore, metabolomics of  $t_e \times b_s$  embryos revealed a distinct profile with less severe alterations than observed for  $t_e \times l_s$  (Fig. 4.7g).

**Figure 4.7**





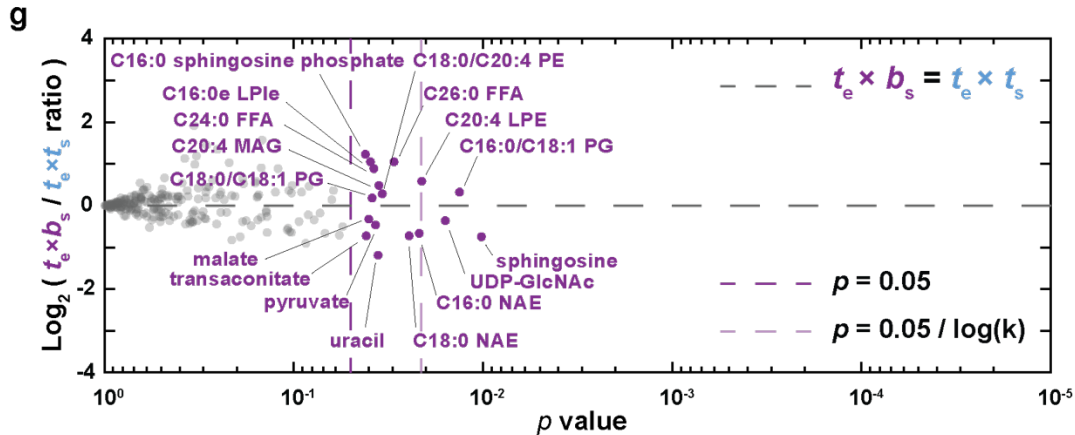


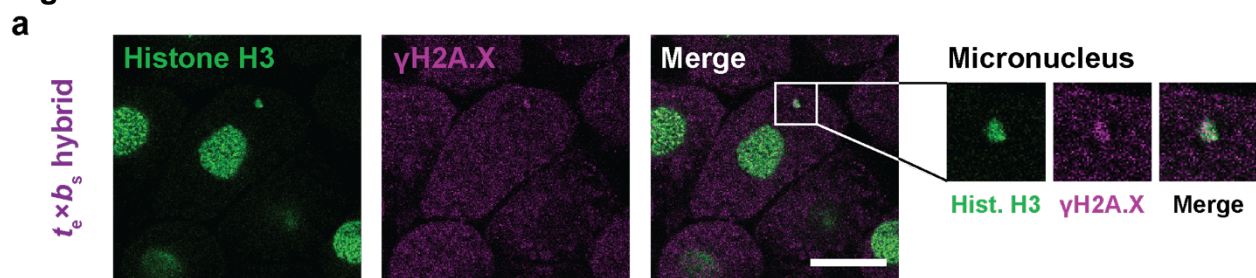
**Figure 4.7: Chromosomal loss in exogastrulating  $t_e \times b_s$  hybrid embryos.**

**a**, Schematic of *X. borealis* and *X. tropicalis* cross-fertilization outcomes. **b**, Representative images of  $t_e \times t_s$  vs.  $t_e \times b_s$  embryos at 24 hpf. Scale bar, 200  $\mu$ m. **c**, Immunofluorescence image of  $t_e \times b_s$  hybrid embryo at 24 hpf showing nuclei and micronuclei. **d**, Immunofluorescence images showing chromosome bridges, mis-segregating chromosomes, and micronuclei throughout  $t_e \times l_s$  hybrid embryos. Scale bars, 20  $\mu$ m. Quantification of  $n = 33$  *X. tropicalis* and 63  $t_e \times b_s$  hybrid anaphases in  $n = 6$  and 12 embryos, respectively, show a significant difference by Fisher 2 by 3 contingency test. Quantification of micronuclei in  $t_e \times b_s$  hybrid embryos is detailed in Fig. 4.8b. **e**, Circle plot of whole genome sequencing data for  $t_e \times b_s$  hybrid embryos aligned and normalized to the genomes of *X. tropicalis* (blue) and *X. borealis* (purple). Underrepresented genome regions (black) represent 9.674% of chromosome 4L, 74.66% of 8L, 4.71% of 1S, and 14.4% of 5S. **f**, Expanded view of chromosome 1S, 5L, 4L and 8L breakpoints with deleted regions indicated in three biological replicates. **g**, Levels of 241 metabolites in *X. tropicalis* and  $t_e \times b_s$  hybrid embryos 7 hpf (see Methods). Note that few metabolites are altered significantly and are distinct from those altered in  $t_e \times l_s$  hybrids (see Fig. 4.6b-c).

**Video 4.12. Characterization of  $t_e \times b_s$  hybrid embryo inviability; *X. tropicalis* vs.  $t_e \times b_s$**

*X. tropicalis* eggs were fertilized with *X. borealis* sperm (left) or *X. tropicalis* sperm (right) and simultaneously imaged in separate dishes. The video plays 20h in 15s (rate of 120 fps) and the scale bar corresponds to 200  $\mu$ m.

**Figure 4.8**



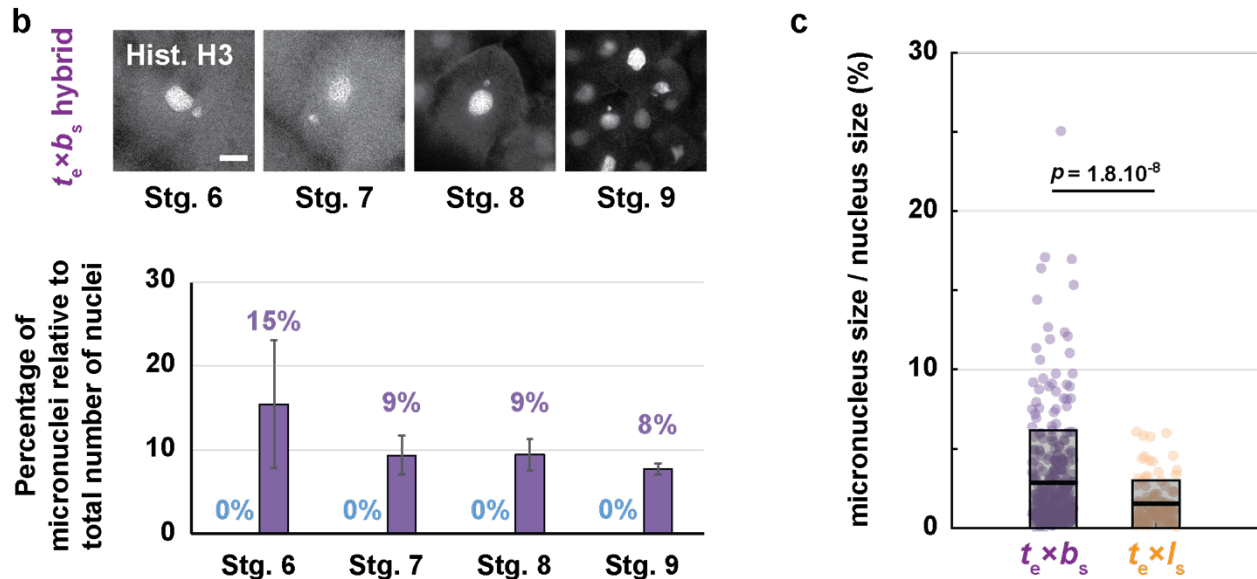


**Figure 4.8: Characterization of micronuclei in  $t_e \times b_s$  hybrid embryos.**

**a**, DNA damage in  $t_e \times b_s$  hybrid embryo micronuclei. Whole mount embryo immunofluorescence was performed in  $t_e \times b_s$  hybrid embryos using anti-histone H3 (left) and anti- $\gamma$ H2A.X (middle) antibodies, corresponding channels are shown in green and magenta, respectively. The merged image is shown on the right. Micronuclei with damaged DNA were observed. Zoomed images of micronuclei are shown on the right in the same left-to-right order. Scale bar is 20  $\mu$ m. **b**, Micronuclei in  $t_e \times b_s$  hybrid embryos at various developmental stages (top). Whole mount embryo immunofluorescence was performed in  $t_e \times b_s$  hybrid embryos using anti-histone H3 antibody at stages 6, 7, 8 and 9. Scale bar is 20  $\mu$ m. Quantification of micronuclei in *X. tropicalis* (blue) and  $t_e \times b_s$  hybrid (purple) embryos (bottom). The percentage of micronuclei was calculated as the number of micronuclei in the imaged portion of the embryo divided by the total number of nuclei in the same imaged portion. The average percentage of micronuclei for several embryos at stage 6 ( $n = 5$   $t_e \times b_s$  hybrid embryos with a total of 125 nuclei), stage 7 ( $n = 7/153$ ), stage 8 ( $n = 9/731$ ) and stage 9 ( $n = 10/2691$ ) is shown. Control *X. tropicalis* embryos from the same mothers were analyzed but no micronuclei were observed at any stages. Error bars indicate the standard error of the mean. **c**, Micronuclei size in  $t_e \times b_s$  and  $t_e \times l_s$  hybrids. Size is plotted as the ratio between the area of the micronucleus and its corresponding nucleus. Each dot represents an individual data point ( $n = 329$  nuclei for  $t_e \times b_s$  shown in purple and  $n = 100$  for  $t_e \times l_s$  shown in orange). The thick black line indicates the average and the grey box corresponds to the standard deviation. Statistical significance was shown using a two-tailed heteroscedastic t-test.

Altogether, our results indicate that hybrid instability in *Xenopus* results primarily from post-zygotic conflicts between the maternal cytoplasm and the paternal genome that lead to the loss of specific genomic regions and downstream gene dosage defects. These findings highlight the role of genome evolution and transmission in defining hybrid fates and speciation.

## 4.2 MATERIALS and METHODS

### Chemicals

Unless otherwise stated, all chemicals were purchased from Sigma-Aldrich, St. Louis, MO.

### Frogs

All animal experimentation in this study was performed according to our Animal Use Protocol approved by the UC Berkeley Animal Care and Use Committee. Mature *X. laevis*, *X. tropicalis*, and *X. borealis* frogs were obtained from NASCO, WI, or the National *Xenopus* Resource (NXR, Woods Hole, MA). Female *X. laevis*, *X. tropicalis*, and *X. borealis* frogs were ovulated with no harm to the animals with 6-, 3-, and 4-month rest intervals, respectively. To obtain testes, males were euthanized by over-anesthesia through immersion in ddH<sub>2</sub>O containing 0.15% MS222 (Tricaine) neutralized with 5 mM sodium bicarbonate prior to dissection, and then frozen at -20°C.

### In vitro fertilization and cross-fertilization

*X. laevis* males were injected with 500 U of human chorionic gonadotropin hormone (hCG) 12-24 h before dissection and testes were stored at 4°C in 1X MR (100 mM NaCl, 1.8 mM KCl, 2 mM CaCl<sub>2</sub>, 1 mM MgCl<sub>2</sub> and 5 mM HEPES-NaOH pH 7.6) for 1-2 weeks. *X. tropicalis* and *X. borealis* males were injected with 250 U and 300 U, respectively, of hCG 12-24 h before dissection and testes were collected in Leibovitz L-15 Medium (Gibco – Thermo Fisher Scientific, Waltham, MA) supplemented with 10% Fetal Bovine Serum (FBS; Gibco) for immediate use.

For *X. tropicalis* egg-based embryos, *X. tropicalis* females were primed with 25 U of hCG 12-24 h before use and boosted with 250 U of hCG on the day of the experiment. As soon as the first eggs were laid (~3 h after boosting), the *X. tropicalis* male was euthanized and dissected. Two *X. tropicalis* or *X. borealis* testes, or 1/3 of a *X. laevis* testis were each added to 1 mL of L-15 10% FBS. *X. tropicalis* females were squeezed gently to deposit eggs onto petri dishes coated with 1.5% agarose in 1/10X MMR (1X MMR: 100 mM NaCl, 2 mM KCl, 2 mM CaCl<sub>2</sub>, 1 mM MgSO<sub>4</sub> and 5 mM HEPES-NaOH pH 7.6, 0.1 mM EDTA). Testes were homogenized using scissors and a pestle in L-15 10% FBS. Any liquid in the petri dishes was removed and the eggs were fertilized with 500 µL of sperm solution per dish. Eggs were swirled in the solution to separate them and incubated for 4 min with the dish slanted. Dishes were then flooded with ddH<sub>2</sub>O, swirled and incubated for 5-10 min. Buffer was exchanged for 1/10X MMR, the eggs incubated for 10 min and jelly coats removed with a 3% cysteine solution (in ddH<sub>2</sub>O-NaOH, pH 7.8). After extensive washing with 1/10X MMR (>4X), embryos were incubated at 23°C. At stage 2-3, fertilized embryos were sorted and placed in fresh 1/10X MMR within new petri dishes coated with 1.5% agarose in 1/10X MMR.

For *X. laevis* egg-based embryos, *X. laevis* females were primed with 100 U of pregnant mare serum gonadotropin (PMSG, National Hormone and Peptide Program, Torrance, CA) at least 48 h before use and boosted with 500 U of hCG 14 hours before the experiment. *X. laevis* females were squeezed gently to deposit eggs onto petri dishes coated with 1.5% agarose in 1/10X MMR. Two *X. tropicalis* testes collected in L-15 10% FBS or 1/3 of a *X. laevis* testes were each added to 1 mL of ddH<sub>2</sub>O and homogenized

using scissors and a pestle. Any liquid in the petri dishes was removed and the eggs were fertilized with 500  $\mu$ L of sperm solution per dish. Eggs were swirled in the solution to individualize eggs as much as possible and incubated for 10 min. Dishes were flooded with 1/10X MMR, swirled and incubated for 10-20 min. Jelly coats were removed with a 2% cysteine solution (in ddH<sub>2</sub>O-NaOH, pH 7.8). After extensive washing (>4X) with 1/10X MMR, embryos were incubated at 23°C. At stage 2-3, fertilized embryos were sorted and placed in fresh 1/10X MMR in new petri dishes coated with 1.5% agarose in 1/10X MMR.

For *X. borealis* egg-based embryos, *X. borealis* females were primed with 60 U of PMSG at least 48 hours before use and boosted with 300 U of hCG 14 h before the experiment. Frogs were kept at 16°C in 1/2X MMR. Eggs were picked from the tub and deposited onto petri dishes coated with 1.5% agarose in 1/10X MMR. Two *X. tropicalis* or *X. borealis* testes were collected and homogenized using scissors and a pestle in L-15 10% FBS. Any liquid in the petri dishes was removed and the eggs were fertilized with 500  $\mu$ L of sperm solution per dish. Eggs were swirled in the solution to individualize eggs as much as possible and incubated for 10 min. Dishes were flooded with 1/10X MMR, swirled and incubated for 10-20 min. Jelly coats were then removed with a 3% cysteine solution (in ddH<sub>2</sub>O-NaOH, pH 7.8). After extensive washing (>4X) with 1/10X MMR, embryos were incubated at 23°C. At stage 2-3, fertilized embryos were sorted and placed in fresh 1/10X MMR in new petri dishes coated with 1.5% agarose in 1/10X MMR. All embryos were staged according to Nieuwkoop and Faber (Nieuwkoop and Faber, 1994).

### **Embryo chemical treatments and video imaging**

Chemical treatments were performed in petri dishes coated with exactly 5 mL of 1.5% agarose in 1/10X MMR covered with 10 mL 1/10X MMR for either regular incubations or video imaging for consistency. Concentrations were calculated relative to the covering volume of 1/10X MMR, no dilution within the volume in the agarose was assumed. Cycloheximide was added at a concentration of 0.1 mg/mL at stage 6.5 from 8 mg/mL stock in DMSO. Hydroxyurea (Thermo Fisher Scientific, Waltham, MA) was added at a concentration of 30 mM at stage 3 from 600 mM stock in ddH<sub>2</sub>O. Triptolide was added at a concentration of 25  $\mu$ M at stage 2 from 25 mM stock in DMSO. Oligomycin was added at a concentration of 40  $\mu$ M at stage 2 from 40 mM stock in DMSO. AP-III-a4 was added at a concentration of 30  $\mu$ M at stage 2 from 1 mM stock in DMSO. Iodoacetic acid was added at a concentration of 50 mM at stage 2 from 1 M stock in ddH<sub>2</sub>O. CP-91,149 was added at a concentration of 270  $\mu$ M at stage 2 from 30 mM stock in DMSO. Corresponding volumes of DMSO or ddH<sub>2</sub>O were added to controls.

Imaging dishes were prepared using a homemade PDMS mold designed to print a pattern of 0.9 mm large wells in agarose that allowed us to image 6 *X. tropicalis* embryos simultaneously within the 3X4 mm camera field of view for each condition. Embryos were imaged from stage 2-3. Treatment and control videos were taken simultaneously using two AmScope MD200 USB cameras (AmScope, Irvine, CA) each mounted on an AmScope SE305R stereoscope. Time lapse movies were acquired at a frequency of 1 frame every 10 s for 20 h and saved as Motion JPEG using a MATLAB (The MathWorks, Inc., Natick, MA) script. Movie post-processing (cropping, concatenation, resizing, addition of scale bar) was done using MATLAB and Fiji (Schindelin et al., 2012). All MATLAB scripts written for this study are available upon request. Two of the scripts used

here were obtained through the MATLAB Central File Exchange: “videoMultiCrop” and “concatVideo2D” by Nikolay S.

### **Embryo ploidy manipulations**

To generate *X. tropicalis* haploid embryos ( $t_e \times [t_s]$  and  $t_e \times [l_s]$ ), fertilizations were conducted as detailed above with slight modifications to accommodate for sperm UV-irradiation. Two *X. tropicalis* testes or 1/3 of a *X. laevis* testis were each added to 1.1 mL of L-15 10% FBS. Testes were homogenized using scissors and a pestle and the solutions spun briefly using a benchtop centrifuge to pellet the tissue. 1 mL of supernatant was transferred into a glass petri dish and irradiated within a Stratalinker UV-Crosslinker (Stratagene, San Diego, CA) with 50,000 microjoules for *X. tropicalis* sperm or 2 times 30,000 microjoules for *X. laevis* sperm, swirling the solution in between the two irradiations. *X. tropicalis* eggs freshly squeezed onto petri dishes coated with 1.5% agarose in 1/10X MMR were then fertilized with 500  $\mu$ L of irradiated sperm solution per dish and processed as described above.

To generate  $[t_e] \times l_s$  cybrid embryos and the haploid  $[t_e] \times t_s$  controls, fertilizations were conducted as detailed above with slight modifications to accommodate for the UV-irradiation of the eggs. Two *X. tropicalis* testes or 2/3 of a *X. laevis* testis were each added to 1.1 mL of L-15 10% FBS. *X. tropicalis* females were squeezed gently to deposit eggs onto petri dishes coated with 1.5% agarose in 1/10X MMR. Excess liquid was removed, eggs were swirled with a pestle to form a monolayer of properly oriented eggs and immediately irradiated within a Stratalinker UV-Crosslinker (Stratagene, San Diego, CA) 2 times with 40,000 microjoules. Testes were homogenized using scissors and a pestle during the irradiation of the eggs. As soon as irradiated, the eggs were fertilized with 500  $\mu$ L of sperm solution per dish and processed as described above.

To prevent polar body formation in either  $t_e \times t_s$  or  $t_e \times l_s$  experiments, fertilizations were conducted as detailed above with slight modifications to accommodate cold treatment. Fertilizations were performed within dishes coated with only 1-1.5 mL, instead of 5 mL, of 1.5% agarose in 1/10X MMR to accelerate cooling. Following the 4-min incubation with sperm, dishes were flooded with ddH<sub>2</sub>O, swirled and incubated for exactly 5 min. Buffer was then exchanged for ice-cold 1/10X MMR, the dishes transferred into a pipette tip box lid placed in a slushy ice bucket, and the eggs were incubated for 10 min. The dishes were then removed from the bucket and the cold buffer was exchanged for RT 1/10X MMR. After 20 min, the jelly coat was removed with a 3% cysteine solution (in ddH<sub>2</sub>O-NaOH, pH 7.8) and the embryos processed as described above.

### **Animal cap assay**

At stage 8, embryos were placed in Danilchik's for Amy Medium (DFA medium; 53 mM NaCl, 5 mM Na<sub>2</sub>CO<sub>3</sub>, 4.5 mM Potassium gluconate, 32 mM Sodium gluconate, 1 mM CaCl<sub>2</sub>, 1 mM MgSO<sub>4</sub>, pH 8.3, 1 g/L BSA and 0.8% Antibiotic Antimycotic Solution) for surgery. Using Dumostar-Biology 55 forceps (Dumont, Montignez, Switzerland), the vitelline membrane was removed and the animal cap was isolated from the embryo. The caps were finally transferred to a new dish or a chamber containing fresh DFA medium for imaging.

### **mRNA, embryo microinjection, and animal cap confocal microscopy**

Plasmids for expression of EB3-GFP and histone H2B-RFP mRNAs were obtained at the 2013 Advanced Imaging in *Xenopus* Workshop from the Wallingford lab (UT Austin, USA). The mRNAs were synthesized using mMessage mMachine SP6 Transcription Kit (Ambion – Thermo Fisher Scientific, Waltham, MA) following supplier protocol. The mRNAs were purified using Phenol-Chloroform extraction, resuspended in ddH<sub>2</sub>O, aliquoted and stored at -80°C.

At stage 2,  $t_e \times l_s$  hybrid embryos were transferred to 1/9X MMR 3% Ficoll. A solution containing 50 pg/nL of H2B-RFP mRNA and 100 pg/nL of EB3-GFP mRNA, concentrations which allowed us to image fluorescent signal as early as stage 9, was loaded into a needle pulled from 1 mm glass capillary tube (TW100F-4, World Precision Instruments, Inc., Sarasota, FL) using a P-87 Micropipette Puller (Sutter Instrument, Navato, CA). Embryos were placed in a mesh-bottomed dish and microinjected in both blastomeres with 1 nL of the mRNA solution using a Picospritzer III microinjection system (Parker, Hollis, NH) equipped with a MM-3 micromanipulator (Narishige, Amityville, NY). Injected embryos were transferred to a new dish and incubated at 23°C in 1/9X MMR 3% Ficoll until stage 8 when they were processed for animal cap isolation as described above. Caps were placed in a chamber filled with DFA medium made using 1x1 cm Gene Frames (Thermo Fisher Scientific, Waltham, MA) between a slide and a coverslip (Thermo Fisher Scientific, Waltham, MA) for confocal microscopy.

### **Embryo whole mount immunofluorescence**

At desired stages, embryos were fixed for 1-3 h using either MAD fixative (2 parts of methanol (Thermo Fisher Scientific, Waltham, MA), 2 parts of acetone (Thermo Fisher Scientific, Waltham, MA), 1 part of DMSO) for most antibodies or MEMFA fixative (0.1 M MOPS pH 7.4, 2 mM EGTA, 1 mM MgSO<sub>4</sub>, 3.7% formaldehyde) for the  $\gamma$ H2A.X antibody. After fixation, embryos were dehydrated in methanol and stored at -20°C. Embryos were then processed as previously described (Lee et al., 2008a) with some modifications. Following gradual rehydration in 0.5X SSC (1X SSC: 150 mM NaCl, 15 mM Na citrate, pH 7.0), embryos were bleached with 1-2% H<sub>2</sub>O<sub>2</sub> (Thermo Fisher Scientific, Waltham, MA) in 0.5X SSC containing 5% formamide for 2-3 h under light, then washed in PBT, a PBS solution containing 0.1% Triton X-100 (Thermo Fisher Scientific, Waltham, MA) and 2 mg/mL bovine serum albumin (BSA). Embryos were blocked in PBT supplemented with 10% goat serum (Gibco – Thermo Fisher Scientific, Waltham, MA) and 5% DMSO for 1-3 h and incubated overnight at 4°C in PBT supplemented with 10% goat serum and the primary antibodies. We used different combinations of the following antibodies: 1:500 mouse anti-beta tubulin (E7; Developmental Studies Hybridoma Bank, Iowa City, IA), 1:500 rabbit anti-histone H3 (ab1791; Abcam, Cambridge, MA), 1:500 rabbit anti-lamin B1 (ab16048; Abcam, Cambridge, MA), 1:500 mouse anti-phospho-histone H2A.X (05-636; EMD Millipore, Merck KGaA, Darmstadt, Germany). Embryos were then washed 4 X 2 h in PBT and incubated overnight in PBT supplemented with 1:500 goat anti-mouse or goat anti-rabbit secondary antibodies coupled either to Alexa Fluor 488 or 568 (Invitrogen – Thermo Fisher Scientific, Waltham, MA) and with 1:200 YO-PRO iodide (Thermo Fisher Scientific, Waltham, MA) if the use of anti-histone H3 antibody as primary was not possible. Embryos were then washed 4 X 2 h in PBT and gradually dehydrated in methanol. Embryos were finally cleared in Murray's clearing medium (2 parts of Benzyl Benzoate, 1 part of Benzyl Alcohol). Embryos were placed either in a chamber made

using a flat nylon washer (Grainger, Lake Forest, IL) attached with nail polish (Sally Hansen, New York, NY) to a slide and covered by a coverslip or a chamber made of silicon grease (Beckman Coulter, Brea, CA) between slide and coverslip, and filled with Murray's clearing medium for confocal microscopy.

### **Confocal microscopy, micronuclei and nuclear size quantification**

Confocal microscopy was performed on a Zeiss LSM 780 NLO Axio Examiner using the Zeiss Zen Software. For animal cap live imaging, histone H2B-RFP and EB3-GFP signals were imaged on a single plane with a frame size of 1024x1024 px every 5 s using a Plan-Apochromat 40x/1.4 Oil objective and laser power of 22%. For imaging of histone H3, embryos were imaged using a Plan-Apochromat 20x/1.0 Water objective and laser power of 12%, on multiple 1024x1024 px plans spaced of 0.68  $\mu\text{m}$  in Z. For characterization of the micronuclei (lamin B1 and  $\gamma\text{H2A-X}$ ), embryos were imaged using a Plan-Apochromat 63x/1.40 Oil objective and laser power of 12%, on multiple plans spaced 0.38  $\mu\text{m}$  in Z. Images are mean averages of 2 scans with a depth of 16 Bits. Pinhole size was always chosen to correspond to 1 airy unit.

Micronuclei were quantified at stages 4, 6, 7, 8 and 9 as the number of observed micronuclei in the dataset divided by the number of nuclei in the dataset. The number of micronuclei at all stages and of nuclei at stage 4 and 6 were counted manually in Fiji. The number of nuclei at stages 7, 8 and 9 was determined automatically through histone H3 fluorescence signal segmentation using Imaris (Bitplane, Zurich, Switzerland). Nuclear area in  $t_e \times t_s$ , *X. tropicalis* and  $t_e \times [t_s]$  was measured in Fiji using the ellipse tool. From this, we calculated the diameter of a circle of the same area, a value that we could directly compare the cell size determined through the measurement of the cell diameter at the nucleus central plan.

### **Embryo nuclei purification**

Embryo nuclei were prepared as previously described (Levy and Heald, 2010) from *X. tropicalis*,  $l_e \times t_s$  hybrid, and *X. laevis* embryos. Briefly, embryos were arrested at stage 8 in late interphase using 150  $\mu\text{g}/\text{mL}$  cycloheximide in 1/10X MMR for 60 min. Then they were washed several times in ELB (250 mM sucrose, 50 mM KCl, 2.5 mM  $\text{MgCl}_2$ , and 10 mM HEPES pH 7.8) supplemented with LPC (10  $\mu\text{g}/\text{mL}$  each leupeptin, pepstatin, chymostatin), cytochalasin D (100  $\mu\text{g}/\text{mL}$ ), and cycloheximide (100  $\mu\text{g}/\text{mL}$ ), packed in a tabletop centrifuge at 200 g for 1 min, crushed with a pestle, and centrifuged at 10,000 g for 10 min at 16°C. The cytoplasmic extract containing endogenous embryonic nuclei was collected, supplemented with 8% glycerol, aliquoted, frozen in liquid nitrogen and stored at -80°C.

### ***Xenopus* egg extracts and related methods**

*X. laevis* (Maresca and Heald, 2006) and *X. tropicalis* (Brown et al., 2007) metaphase arrested egg extracts were prepared and spindle reactions conducted as previously described.

To reconstitute spindle assembly, stage 8 embryo nuclei were used as a source of DNA. Aliquots were thawed, resuspended in 1 mL of ELB, and spun at 1600 g for 5 min at RT. Pelleted nuclei were resuspended in 25  $\mu\text{L}$  of fresh *X. tropicalis* extract and incubated at RT.

To examine kinetochore assembly, *X. laevis* sperm nuclei, prepared as previously described (Murray, 1991), were used as a source of DNA in both *X. laevis* and *X. tropicalis* egg extracts. Cycled chromosomes were prepared and spun-down (Maresca and Heald, 2006) and then processed for immunofluorescence as previously described (Hannak and Heald, 2006). Briefly, the coverslips were incubated for 1 min in cold methanol, washed with PBS+NP40 and blocked overnight in PBS + 5% BSA at 4°C. The anti-Ndc80 (1:300 dilution, Stukenberg lab, University of Virginia) or the anti-CENP-A (1:500 dilution, Straight lab, Stanford University) rabbit antibodies were added for 1 h. After washing with PBS+NP40, the coverslips were incubated with 1:1000 anti-rabbit antibody coupled to Alexa Fluor 488 (Invitrogen – Thermo Fisher Scientific, Waltham, MA) for 30 min and then with 1:1000 Hoechst for 5 min. The coverslips were finally washed and mounted for imaging. Each presented dataset was obtained from 3 different egg extracts with technical duplicates for each.

Spindles and chromosomes were imaged using micromanager software (Edelstein et al., 2014) with an Olympus BX51 microscope equipped with an ORCA-ER or an ORCA-II camera (Hamamatsu Photonics, Hamamatsu city, Japan), and with an Olympus UPlan FL 40X air objective. Spindle measurements were made using Fiji and the spindle tubulin intensity line scan using an automated Java ImageJ plugin developed by Xiao Zhou (Heald lab, UC Berkeley; <https://github.com/XiaoMutt/AiSpindle>).

### **TUNEL assay**

Embryos were fixed in MEMFA as described for embryo whole mount immunofluorescence and processed as previously described (Hensey and Gautier, 1997) with minor modifications. Briefly, after gradual rehydration, embryos were bleached with 1-2% H<sub>2</sub>O<sub>2</sub> in 0.5X SSC containing 5% formamide for 1-2 h under light. After washes in PBS, embryos were incubated in 1X Terminal Deoxynucleotidyl Transferase (TdT) Buffer for 1 h and then overnight in TdT Buffer supplemented with 150 U/ml of TdT enzyme (Invitrogen – Thermo Fisher Scientific, Waltham, MA) and 1 pmol/μL Digoxigenin-11-dUTP (Roche, Basel, Switzerland). After washes in 1 mM EDTA/PBS at 65°C, in PBS and then in MAB (100 mM maleic acid, 150 mM NaCl, pH 7.5), embryos were blocked for 1 h in 2% Blocking Reagent (Roche, Basel, Switzerland) in MAB and then incubated overnight at 4°C in 2% Blocking Reagent in MAB supplemented with 1:3000 anti-Digoxigenin AP antibody (Roche, Basel, Switzerland). After washes in MAB and in AP Buffer (100 mM Tris, pH 9.5, 50 mM MgCl<sub>2</sub>, 100 mM NaCl, 0.1% Tween 20, 2 mM Levamisol), embryos were stained with NBT/BCIP (nitro-blue tetrazolium / 5-Bromo-4-chloro-3-indolyl phosphate; Promega, Sunnyvale, USA) diluted in AP buffer. Reactions were stopped in MAB and embryos fixed overnight in Bouin's solution. After washes in 70% buffered ethanol and in methanol, embryos were imaged in methanol with the ToupView software (ToupTek, Zhejiang, China) using an AmScope MD200 USB camera mounted on M5 stereoscope (Wild Heerbrugg, Gais, Switzerland).

### **Nucleic acid isolation, library construction, and sequencing**

For genomic DNA, embryos at desired stages were incubated overnight in lysis buffer (50 mM Tris-HCl, 5 mM EDTA, 100 mM NaCl, 0.5% SDS) containing 250 μg/mL Proteinase K (Roche, Basel, Switzerland). DNA was isolated using Phenol-Chloroform extraction and ethanol precipitation. To isolate RNAs, embryos at desired stages were homogenize



mechanically in TRIzol® (Thermo Fisher Scientific, Waltham, MA) using up to a 30-gauge needle and processed according to supplier instructions. After resuspension in nuclease-free H<sub>2</sub>O, RNAs were cleaned up using RNeasy kit (Qiagen Inc.) with on-column DNA digestion, following supplier protocol.

Libraries were constructed at the Functional Genomics Lab (FGL), a QB3-Berkeley Core Research Facility at UC Berkeley. For genomic DNA, an S220 Focused-Ultrasonicator (Covaris®) was used to fragment DNA. The fragmented DNA was cleaned and concentrated with the MinElute® PCR Purification kit (Qiagen Inc.). The Library preparation was done on an Apollo 324™ with PrepX™ ILM 32i DNA Library Kits (WaferGen Biosystems, Fremont, CA), and 7 cycles of PCR amplification was used for library fragment enrichment. For RNAs, mRNA enrichment was performed on total RNA using polyA selection with the Invitrogen Dynabeads mRNA Direct kit. The library preparation was done on the Apollo324™ with PrepX™ RNAseq Library Prep Kits (WaferGen Biosystems, Fremont, CA), and 13 cycles of PCR amplification was used for index addition and library fragment enrichment.

Sequencing was performed by the Vincent J. Coates Genomics Sequencing Laboratory at UC Berkeley. All samples have been run as 100 paired-end HiSeq4000 lanes, pooled equimolar after quantification using KAPA Illumina Library quantification qPCR reagents on the BioRad CFX connect. Demultiplexing was performed to allow a single mismatch with Illumina's bcl2fastq version 2.17 software.

### **Genomic DNA sequencing analysis and deletion detection in hybrids**

DNA sequencing reads were mapped to a *X. laevis* - *X. tropicalis* hybrid genome (Xenla9.1 and Xentro9.0) or a *X. borealis* - *X. tropicalis* hybrid genome (Xbo\_04Apr2017 (Mudd and Rokhsar, unpublished) and Xentro9.0) using bwa mem (version 0.7.10-r789) with default settings. Duplicate reads were marked using bamUtil v1.0.2.

Deletions in  $t_e \times l_s$  and  $l_e \times t_s$  hybrids were called by comparing local DNA sequencing read coverage between hybrid ( $t_e \times l_s$  or  $l_e \times t_s$ ) and parental ( $t_e \times t_s$  or  $l_e \times l_s$ ) genomes. The read coverage was determined in 10kb regions, with a 2kb sliding window across the genome. For each 10kb region we calculated the RPKM in  $t_e \times l_s$ ,  $l_e \times t_s$ ,  $t_e \times t_s$  and  $l_e \times l_s$  sequencing tracks. The ratio of median RPKM values in retained regions has a non-zero baseline as expected because of a different size of hybrid and parental genomes. The ratio cut-off for deleted regions was set accordingly at 4-fold and 6-fold for *X. laevis* and *X. tropicalis* sequences, respectively. Lost regions overlapping for more than 30% of their length with gaps were removed and regions within 10kb of each other were merged. Deletions in  $t_e \times b_s$  hybrids were called by identifying reduced genomic DNA signal in  $t_e \times b_s$ . The RPKM read coverage was determined in 10kb regions, with a 2kb sliding window across the genome. Regions with median log<sub>10</sub> RPKM less than -1.25 in the *X. tropicalis* genome and -1.15 in the *X. borealis* genome were marked as deleted. Lost regions overlapping for more than 30% of their length with gaps were removed and regions within 10kb of each other were merged.

### **RNA sequencing analysis**

We mapped RNA-seq reads to the combined primary transcripts of *X. laevis* (JGIv18pV4) and *X. tropicalis* (JGIv91) using bwa mem (version 0.7.10), and discarded all reads mapped in multiple targets for further analysis. To use human gene annotation, which is

more comprehensive than *Xenopus*, we transferred the expression level of these species to human orthologs. Based on the best BLASTP hit to human longest protein sequences (from Ensembl version 80), we merged the read counts of *X. laevis* and *X. tropicalis* genes to corresponding human genes, then performed differential expression analysis with EdgeR (Robinson et al., 2010). An adjusted P-value criterion of less than 0.05 was applied to determine the significance of differential expression. For metabolic gene analysis, we used the list of metabolic genes obtained from the PANTHER database (Mi et al., 2016).

### Metabolomic profiling

Seven hours post-fertilization,  $t_e \times l_s$  hybrid,  $t_e \times b_s$  hybrid, and respective *X. tropicalis* control embryos were collected from 3 independent fertilizations, always using eggs from the same female between the  $t_e \times l_s$  hybrid or the  $t_e \times b_s$  hybrid, and its *X. tropicalis* control. Five samples of 8 embryos each for nonpolar lipid metabolites and 12 embryos each for polar metabolites were rinsed twice in filtered PBS and frozen in liquid nitrogen. Nonpolar lipid metabolites from the 8 embryos were extracted in 3 mL of 2:1 chloroform:methanol and 1 mL of PBS with inclusion of internal standards C12 monoalkylglycerol ether (MAGE) (10 nmol, Santa Cruz Biotechnology) and pentadecanoic acid (10 nmol). Organic and aqueous layers were separated by centrifugation at 1000 g for 5 min and the organic layer was collected, dried under a stream of nitrogen and dissolved in 120  $\mu$ L chloroform. Polar metabolites were extracted from the 12 embryos in 180  $\mu$ L of 40:40:20 (ACN:MeOH:H<sub>2</sub>O) with inclusion of internal standard D3N15 serine (50 nM, Cambridge Isotope Laboratories, Inc. #DNLM-6863). Samples were disrupted by sonication then centrifuged at 21,000 g for 10 min and the supernatant was collected for analysis. Metabolites were separated by liquid chromatography and MS analysis was performed with an electrospray ionization (ESI) source on an Agilent 6430 QQQ LC-MS/MS (Agilent Technologies). The capillary voltage was set to 3.0 kV, and the fragmentor voltage was set to 100 V. The drying gas temperature was 350°C, the drying gas flow rate was 10 l/min, and the nebulizer pressure was 35 psi. Metabolites were identified by single reaction monitoring (SRM) of the transition from precursor to product ions at associated optimized collision energies and retention times as previously described (Louie et al., 2016). Metabolites were quantified by integrating the area under the curve, then normalized to internal standard values and tissue weight. Metabolite levels are expressed as relative abundances as compared to controls. P-values were calculated using a two-tailed homoscedastic t-test. Significance was analyzed for an  $\alpha = 0.05$  threshold as well as that with a Bonferroni-like correction to account for multiple hypothesis comparison. Strict Bonferroni correction is highly conservative and often results in increased type II errors (failing to acknowledge a real effect) and several alternatives exist. Because we compared around 200 compounds between two types of embryos, each with 5 replicates, we used a penalized Bonferroni correction, and divided the  $\alpha$  threshold value by the logarithm of the number of tests ( $\alpha/\log(k)$ ) to decrease the risk for the type II error.

## ACKNOWLEDGMENTS

We thank members of the Heald lab, present and past, for support and fruitful discussions. We thank the students who helped with some of the experiments, Brian Castellano, Jingxun Chen, Stephan Ramos, Armbien Sabillo, and Karen Shih. We are grateful to the Marine Biological Laboratory (MBL) and the National *Xenopus* Resource (NXR), also for organizing the 2013 Advanced Imaging in *Xenopus* Workshop where several techniques used here were taught to RG, and to John Wallingford and Asako Shindo for subsequent support. We thank the Welch, King, Harland, Rokhsar, Barton, and Fletcher labs at UC Berkeley for sharing reagents, materials, and expertise as well as Todd Stukenberg (University of Virginia) and Aaron Straight (Stanford University) for providing us with the Ndc80 and CENP-A antibodies, respectively. Special thanks to Austin Mudd and Daniel Rokhsar for providing early access to the *X. borealis* genome assembly. This work used the Functional Genomics Laboratory, a QB3-Berkeley Core Research Facility at UC Berkeley as well as the Vincent J. Coates Genomics Sequencing Laboratory at UC Berkeley, supported by NIH S10 OD018174 Instrumentation Grant. The confocal microscopy performed in this work was done at the UC Berkeley CRL Molecular Imaging Center, supported by NSF DBI-1041078. RG was initially supported by an EMBO long term fellowship ALTF 836-2013 and for most of this project by an HFSP long term fellowship LT 0004252014-L. RA was supported in part by an NSF REU Summer Fellowship in 2014. RH was supported by NIH R35 GM118183 and the Flora Lamson Hewlett Chair. DKN was supported by NIH R01 CA172667. MK was supported by the UC Berkeley MCB department NIH training grant 4T32GM007232-40. TK was supported by Basic Science Research Program through the National Research Foundation of Korea (NRF) funded by the Ministry of Science, ICT and Future Planning (NRF-2016R1C1B2009302), and the UNIST Research Fund (Grant Number 1.160060.01). GJCV, IVK and GG were supported by R01HD069344 (NICHD).

## AUTHOR CONTRIBUTIONS

RH and RG designed the project. RG performed the molecular, cell and developmental biology experiments, aided by RA, and analyzed the data. MK, together with RG, performed the experiments related to *X. borealis* and analyzed the data. GJCV, IVK and GG prepared and analyzed the hybrid genomes. BM and DKN performed the metabolomic profiling of hybrids. TK and EMM contributed to the transcriptome data analysis. RG prepared the figures and wrote the manuscript with RH, incorporating feedback from all authors.

## Chapter 5: Molecular conflicts disrupting centromere assembly contribute to *Xenopus* hybrid inviability

The following chapter contains material from a publication on which I am the first author (Kitaoka et al., 2022). This article is distributed under the terms of the Creative Commons Attribution License (CC BY 4.0), which permits unrestricted use and redistribution provided that the original author and source are credited.

### ABSTRACT

Although central to evolution, the causes of hybrid inviability that drive reproductive isolation are poorly understood. Embryonic lethality occurs when eggs of the frog *X. tropicalis* are fertilized with either *X. laevis* or *X. borealis* sperm. We observed that distinct subsets of paternal chromosomes failed to assemble functional centromeres, causing their mis-segregation during embryonic cell divisions. Core centromere DNA sequence analysis revealed little conservation among the three species, indicating that epigenetic mechanisms that normally operate to maintain centromere integrity are disrupted on specific paternal chromosomes in hybrids. In vitro reactions combining *X. tropicalis* egg extract with either *X. laevis* or *X. borealis* sperm chromosomes revealed that paternally matched or over-expressed centromeric histone CENP-A and its chaperone HJURP could rescue centromere assembly on affected chromosomes in interphase nuclei. However, whereas the *X. laevis* chromosomes maintained centromeric CENP-A in metaphase, *X. borealis* chromosomes did not, and also displayed ultra-thin regions containing ribosomal DNA. Both centromere assembly and morphology of *X. borealis* mitotic chromosomes could be rescued by inhibiting RNA Polymerase I or by preventing collapse of stalled DNA replication forks. These results indicate that specific paternal centromeres are inactivated in hybrids due to disruption of associated chromatin regions that interfere with CENP-A incorporation, at least in some cases due to conflicts between replication and transcription machineries. Thus, our findings highlight the dynamic nature of centromere maintenance and its susceptibility to disruption in vertebrate interspecies hybrids.

## 5.1 INTRODUCTION

Hybridization between closely related species often leads to embryonic lethality accompanied by defects in genome stability and maintenance, but the cellular and molecular mechanisms underlying post-zygotic barriers that drive reproductive isolation and speciation are largely unknown (Sanei et al., 2011; Maheshwari and Barbash, 2011; Fujiwara et al., 1997; Gernand et al., 2005). Among animals, a number of studies of inviable hybrids resulting from crosses of related *Drosophila* species have revealed an important role for the centromere, the chromosomal site where the kinetochore assembles to mediate chromosome attachment to the mitotic spindle and segregation to daughter cells. Both centromere DNA sequence and protein components including the centromeric histone H3 variant, Centromere Protein A (CENP-A) are rapidly evolving (Malik and Henikoff, 2001; Maheshwari et al., 2015). Localization of exogenously expressed CENP-A to centromeres across *Drosophila* species was shown to require co-expression of its species-matched chaperone CAL1/HJURP, indicating that the CENP-A deposition machinery also co-evolves (Rosin and Mellone, 2016). In turn, kinetochore formation at centromeres depends on specific, epigenetic recognition and stabilization of CENP-A nucleosomes by other factors, including CENP-C, CENP-N, and M18BP1 (Moree et al., 2011; Carroll et al., 2009; Pentakota et al., 2017; Chittori et al., 2018; Tian et al., 2018; Falk et al., 2015; French et al., 2017; Shono et al., 2015; Hori et al., 2017). Thus, co-evolution of centromere DNA and many associated proteins generate barriers to hybrid viability by interfering with assembly of the chromosome segregation machinery.

Increasing evidence suggests that the chromatin environment also plays an important role in centromere assembly and that changes in the nuclear organization are related to hybridization outcomes. For example, disruption of the chromocenter, a domain containing the pericentromeric satellite DNA, is common among *Drosophila* hybrids and may underlie inviability (Jagannathan and Yamashita, 2021). Furthermore, known inviability factors such as hybrid male rescue (Hmr) and lethal hybrid rescue (Lhr) strongly impact chromosome segregation in *Drosophila* hybrids and have been reported to regulate transposable elements and heterochromatic repeats (Thomae et al., 2013; Satyaki et al., 2014), associate with chromatin chaperones adjacent to centromeres (Anselm et al., 2018), and to link pericentromeric and centromeric chromatin to maintain centromere integrity (Lukacs et al., 2021). However, whether these factors play a direct role in centromere function is unclear (Blum et al., 2017). Despite these advances, the relative contribution to hybrid inviability of diverging centromere sequences versus the activity and spatial organization of associated chromatin machineries that promote centromere assembly is poorly understood.

Among vertebrates, hybridization resulting in post-zygotic death has been more difficult to study. *Xenopus* frog species possess interesting evolutionary relationships that include past interspecies hybridization events (Session et al., 2016) and provide an ideal system to study the molecular basis of hybridization outcomes, since cross fertilization experiments are easily performed (Narbonne et al., 2011; Gibeaux et al., 2018), and mechanisms underlying hybrid incompatibility can be uniquely and powerfully investigated in vitro by combining the sperm chromosomes and egg extracts from

different species. We showed previously that interspecies hybrids produced when *X. laevis* or *X. borealis* eggs are fertilized by *X. tropicalis* sperm are viable, while the reverse crosses die before gastrulation and zygotic gene activation by explosive cell lysis or exogastrulation, respectively (Gibeaux et al., 2018). The inviable hybrids displayed chromosome segregation defects during embryonic cleavages, characterized by lagging chromosomes, chromosome bridges, and formation of micronuclei. By whole genome sequencing, specific and distinct paternal chromosome regions were lost from both hybrids prior to embryo death. A fraction of *X. laevis* chromosomes failed to assemble centromeres/kinetochores, likely leading to spindle attachment defects and ultimately chromosome mis-segregation and embryo death (Gibeaux et al., 2018).

To better understand centromere-based *Xenopus* hybrid incompatibilities, here we combine genomic, in vitro, and in vivo analyses. We find that although core centromeric sequences are not conserved, *X. tropicalis* egg cytoplasm supports centromere assembly on *X. laevis* and *X. borealis* chromosomes. However, upon entry into metaphase, conflicts emerge that evict CENP-A from a subset of chromosomes. In the case of *X. laevis*, excess CENP-A and its chaperone HJURP can rescue this defect. In contrast, eviction of CENP-A from *X. borealis* chromosomes could be rescued by dissociating the rRNA polymerase Pol I or by preventing collapse of DNA replication forks. These results indicate that centromere incompatibility is driven primarily by centromere sequence-independent replication-transcription conflicts that disrupt the epigenetic maintenance of CENP-A nucleosomes.

## 5.2 RESULTS

### **Core centromere sequence variation does not underlie *Xenopus* hybrid aneuploidy**

We previously observed chromosome mis-segregation and loss of centromere and kinetochore proteins from a subset of chromosomes in hybrids generated by fertilizing *X. tropicalis* eggs with *X. laevis* sperm. Whole genome sequencing just prior to embryo death revealed consistent deletion of large genomic regions from two paternal chromosomes, 3L and 4L (Gibeaux et al., 2018). We hypothesized that chromosome-specific aneuploidy resulted from divergent centromeric sequences on the affected chromosomes, rendering them incompatible with the maternal *X. tropicalis* centromeric histone CENP-A and its loading machinery. Recent characterization of *X. laevis* centromere sequences by chromatin immunoprecipitation with CENP-A antibodies and sequencing analysis (ChIP-seq) revealed a family of related sequences found in distinct combinations and abundances on different *X. laevis* chromosomes (Smith et al., 2021). However, *X. laevis* centromeres 3L and 4L did not possess any distinguishing features in terms of size or composition. Thus, differences in core centromere DNA sequences do not appear to drive the specific chromosome mis-segregation events and genome loss observed in the inviable *X. tropicalis*/*X. laevis* hybrid.

To expand our analysis, we characterized a second inviable hybrid resulting from fertilization of *X. tropicalis* eggs with sperm from *X. borealis*, a frog species possessing an allotetraploid genome closely related to *X. laevis* (Session et al., 2016). These hybrids display specific and consistent genome loss from a different subset of paternal chromosomes including 1S, 5S, 4L, and 8L (Gibeaux et al., 2018). To determine the extent to which centromere sequences differed across the three *Xenopus* species, CENP-A ChIP-seq was similarly applied to *X. tropicalis* and *X. borealis*. We used an alignment-independent *k*-mer based analysis to identify sequence features of the highly repetitive centromeric arrays in each species without the need for a complete genome sequence (Fig. 5.2A). Comparing the enrichment value (normalized CENP-A *k*-mer counts/normalized input *k*-mer counts) revealed that the majority of individual *k*-mers are enriched in one species, but not the others (Fig. 5.1A). Furthermore, analysis of full-length sequencing reads that contained CENP-A enriched *k*-mers showed that CENP-A nucleosome-associated DNA sequences of the three species bear little relationship to one another (Fig. 5.1B). These findings reinforce the idea that incompatibilities leading to mis-segregation of specific chromosomes are not due to centromere sequence differences. Interestingly, although protein sequence alignments of *X. laevis*, *X. tropicalis*, and *X. borealis* CENP-A showed that they are nearly 90% identical, divergence occurred in both the N-terminus and the CENP-A Targeting Domain (CATD) L1 loop region that provides specificity for recognition of the CENP-A/H4 complex by its dedicated chaperone HJURP (Fig. 5.2B) (Rosin and Mellone, 2016; Foltz et al., 2009; Dunleavy et al., 2009; Hu et al., 2011). Together, these results suggest that as in *Drosophila*, centromere sequences, CENP-A, and its chaperone have co-evolved in *Xenopus* to strengthen specificity of their interactions (Rosin and Mellone, 2017). However, although disruption of these interactions can lead to inviability in flies (Henikoff et al., 2001; Malik and Henikoff, 2009), differences among core centromere sequences and CENP-A

proteins does not explain loss of centromere function on a subset of chromosomes in inviable *Xenopus* hybrids.

**Figure 5.1**

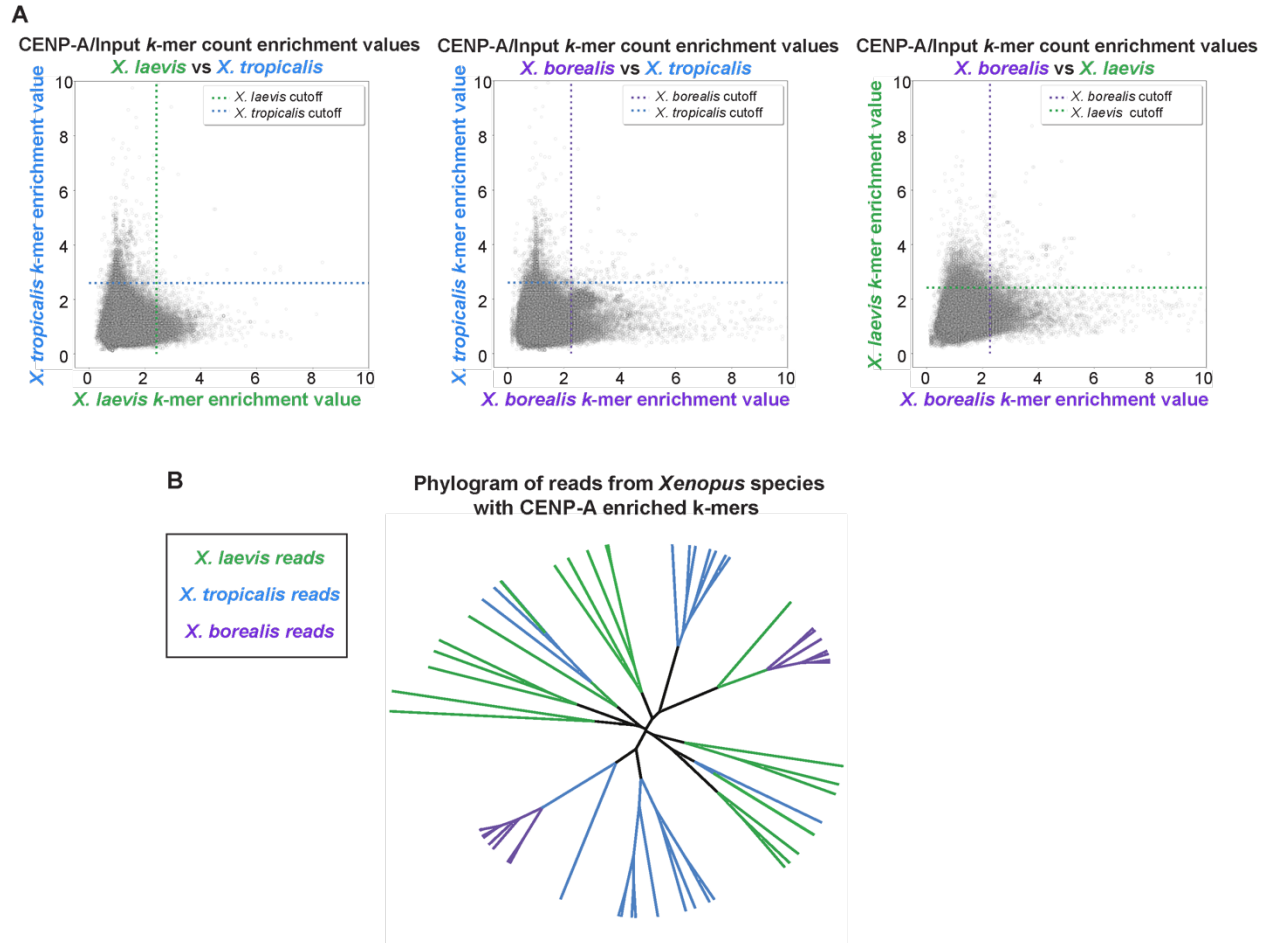


**Figure 5.1: Comparison of *X. laevis*, *X. tropicalis*, and *X. borealis* core centromere sequences**

(A) Scatter plots of *k*-mer enrichment values (normalized CENP-A counts / normalized input counts) compared between species. Only *k*-mers found in both species are plotted. Dotted lines indicate enrichment value for each species that is five median absolute deviations above the median enrichment value to denote highly enriched *k*-mers, which are not well conserved across species. (B) Phylogram of full-length sequencing reads from each *Xenopus* species. Branches are colored according to species of origin. Sequencing reads were selected first by the presence of at least 80 CENP-A enriched 25bp *k*-mers and then by hierarchical clustering. The phylogram illustrates a striking divergence of core centromere sequences.



**Figure 5.2**

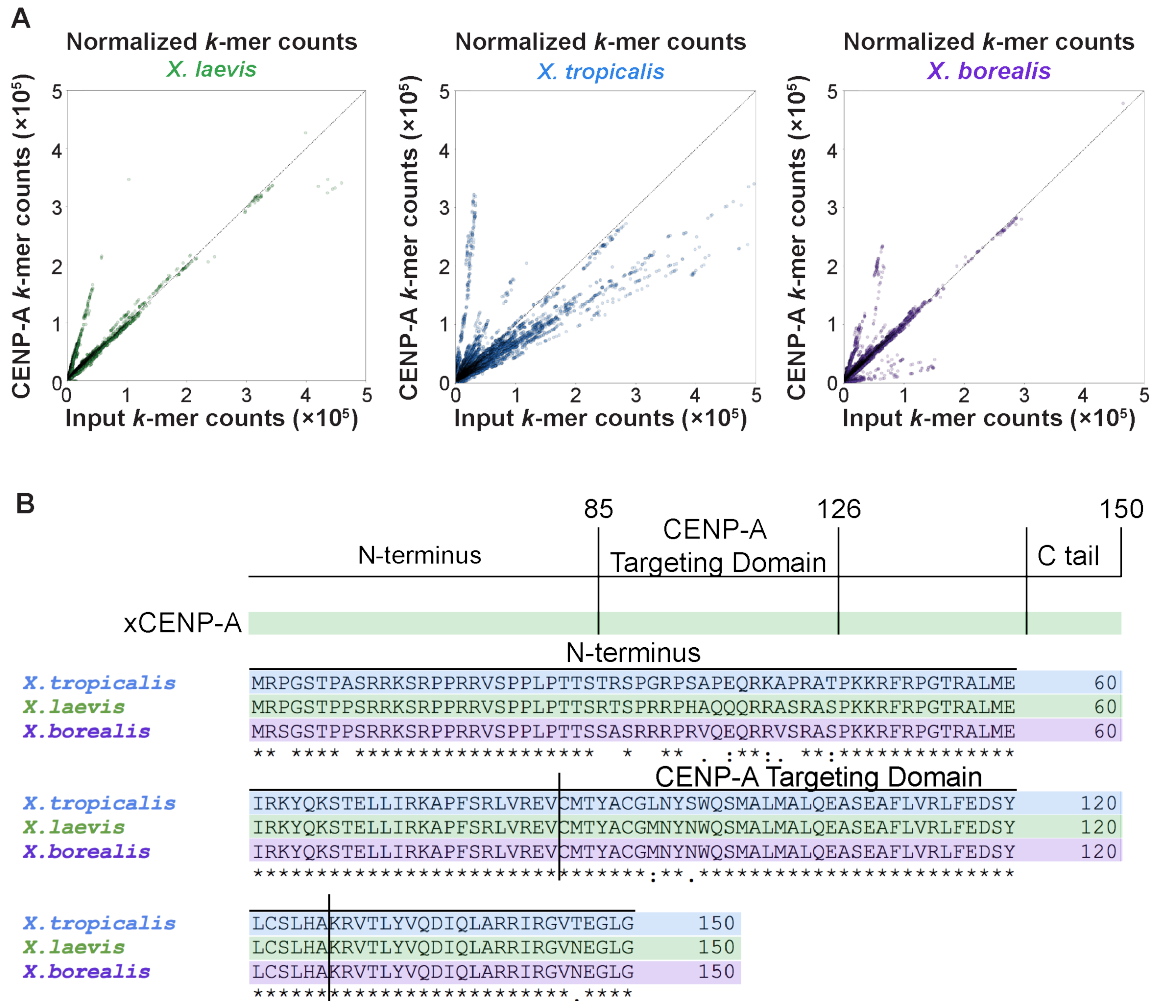


**Figure 5.2: Comparison of centromere DNA and CENP-A protein sequences**

(A) Scatter plots of normalized *k*-mer counts from Input and CENP-A ChIP-seq sequencing libraries from *X. laevis*, *X. tropicalis*, and *X. borealis*. The dotted line ( $x=y$ ) indicates *k*-mers that are equally abundant in both libraries. *k*-mer counts reveal distinct patterns in the three species.

(B) Protein sequence alignment comparing CENP-A across the three *Xenopus* species. Differences are observed in the N-terminal region and the CENP-A targeting domain (CATD).

### CENP-A eviction from a subset of chromosomes requires cell cycle progression

To better understand the process by which specific chromosomes lose centromere function in hybrids, we took advantage of the *Xenopus* egg extract system capable of recapitulating events of the cell division cycle in vitro, including sperm chromosome replication, mitotic chromosome condensation, and centromere/kinetochore formation (Maresca and Heald, 2006; French and Straight, 2017). To monitor centromere assembly, *X. tropicalis*, *X. laevis*, or *X. borealis* sperm nuclei were added to *X. tropicalis* egg extracts and probed for CENP-A at different stages of the cell cycle. Sperm chromosomes of all three species condensed and possessed single centromeric CENP-A foci when added directly to metaphase-arrested *X. tropicalis* extract (Fig. 5.3A, B), consistent with

observations that sperm chromosomes contain CENP-A (Bernad et al., 2011; Milks et al., 2009). However, cycling the extract through interphase to allow sperm decondensation, nuclear envelope formation, and DNA replication in *X. tropicalis* egg cytoplasm resulted in no visible CENP-A on a subset of *X. laevis* and *X. borealis* mitotic chromosomes in the subsequent metaphase, whereas *X. tropicalis* centromeres were not affected (Fig. 5.3A, B).

To determine when in the cell cycle CENP-A was evicted from paternal chromosomes, we examined interphase nuclei in control and hybrid in vitro reactions. The expected number of centromere foci, 18 for *X. laevis* and *X. borealis*, decreased in *X. tropicalis* extract (Fig. 5.3C, Fig 5.4A, B). The loss of CENP-A localization from 2 or 4 paternal *X. laevis* and *X. borealis* chromosomes, respectively, corresponded very well to whole genome sequencing data of hybrid embryos in terms of the number of chromosomes affected (Gibeaux et al., 2018), and indicates that CENP-A is lost from this subset of paternal chromosomes during interphase.

**Figure 5.3**

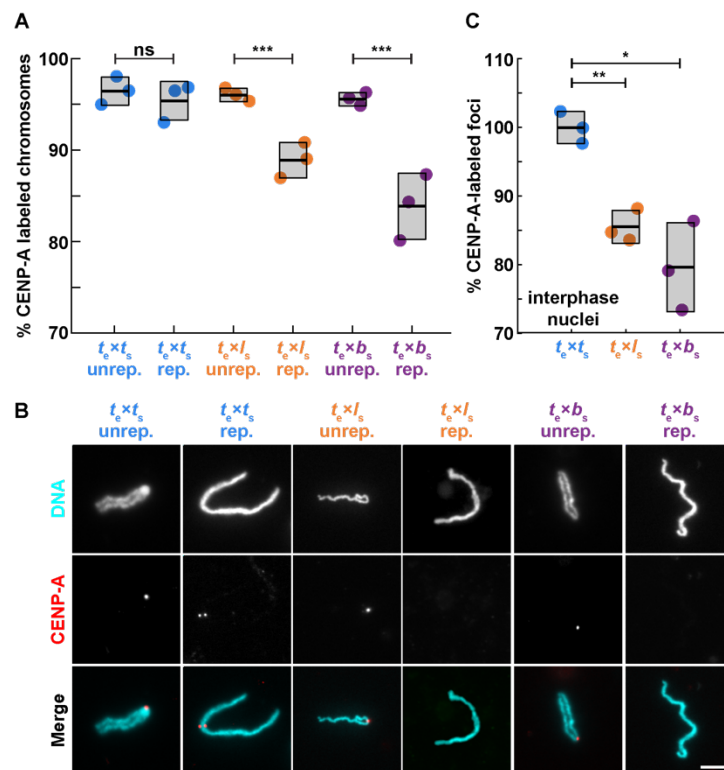


**Figure 5.3: Loss of centromeric CENP-A is cell cycle-dependent**

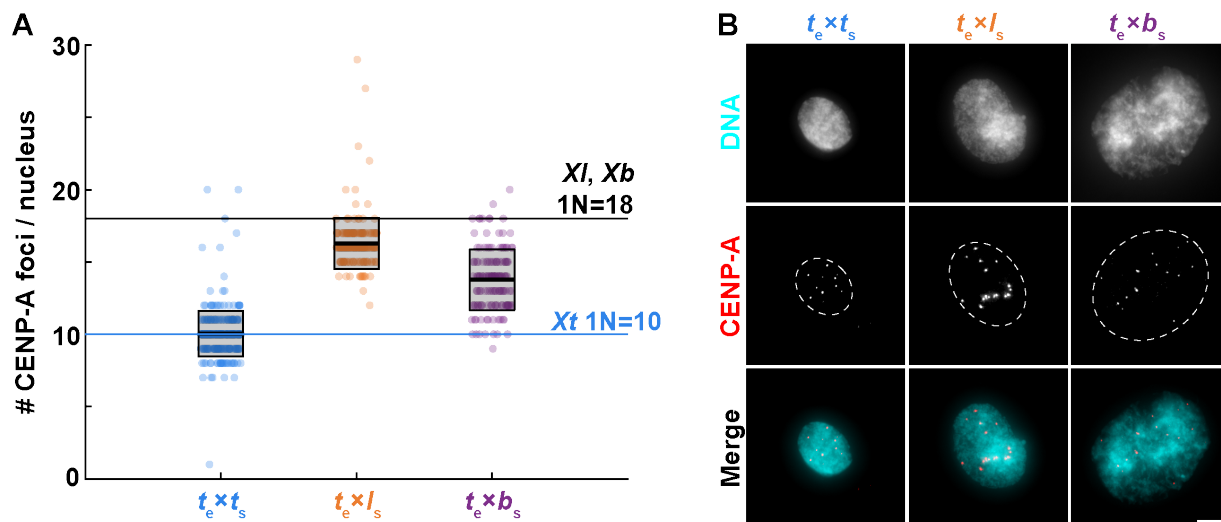
(A) Percentage of mitotic chromosomes with centromeric CENP-A staining in *X. tropicalis* egg extract. Over 95% of *X. tropicalis*, *X. laevis*, and *X. borealis* unreplicated sperm chromosomes added directly to metaphase-arrested *X. tropicalis* egg extracts possess centromeres, as indicated by immunofluorescence of the centromeric histone CENP-A. Following progression through the cell cycle, a fraction of replicated *X. laevis* and *X. borealis* mitotic chromosomes completely lose centromeric CENP-A foci. Unrep., unreplicated chromosomes; rep., replicated chromosomes. N = 3 extracts, N > 275 chromosomes per extract. p-values (left to right) by two-

tailed two-sample unequal variance t-tests: 0.3356, 0.0008, 0.0004; ns, not significant. **(B)** Representative images of mitotic unreplicated and replicated *X. tropicalis*, *X. laevis*, and *X. borealis* chromosomes formed in *X. tropicalis* egg extracts. The chromosomes shown here are not identified, but selected from a population of paternal chromosomes. DNA in cyan, CENP-A in red. Scale bar is 10  $\mu$ m. **(C)** Percentage of total expected CENP-A foci observed in nuclei formed in interphase *X. tropicalis* egg extract. *X. laevis* and *X. borealis* interphase nuclei both lose centromere foci during interphase, prior to entry into metaphase, whereas *X. tropicalis* nuclei do not. From N = 3 extracts, N > 64 nuclei per extract. p-values (top to bottom) by one-way ANOVA with Tukey post-hoc analysis: 0.0025, 0.0133.

Species nomenclature throughout figures denotes egg extract as subscript e and chromosomes as subscript s, for example  $t_e \times l_s$  indicates *X. tropicalis* egg extract combined with *X. laevis* sperm chromosomes. *X. tropicalis* is color-coded blue, while *X. laevis* and *X. borealis* hybrid combinations are orange and purple, respectively.

The recent detailed characterization of *X. laevis* centromere sequences allowed us to test whether the centromere assembly defects observed in egg extract occurred on the same chromosomes disrupted in hybrid embryos (Smith et al., 2021; Gibeaux et al., 2018). Fluorescence in situ hybridization (FISH) probes in combination with CENP-A immunofluorescence identified *X. laevis* chromosomes 3L and 4L, the two chromosomes that lose large genomic regions in hybrid embryos, as those that also lose centromeric CENP-A staining when replicated in *X. tropicalis* egg extract (Fig. 5.4C-E). Thus, the in vitro system reproduces incompatibilities likely to underlie chromosome mis-segregation and ultimately genome loss observed in vivo. These results show that while all paternal sperm chromosomes initially possess CENP-A at their centromeres, a subset evict CENP-A during interphase, indicating that epigenetic mechanisms enable hybrid centromere assembly despite evolutionary differences, but are disrupted on individual chromosomes.

**Figure 5.4**



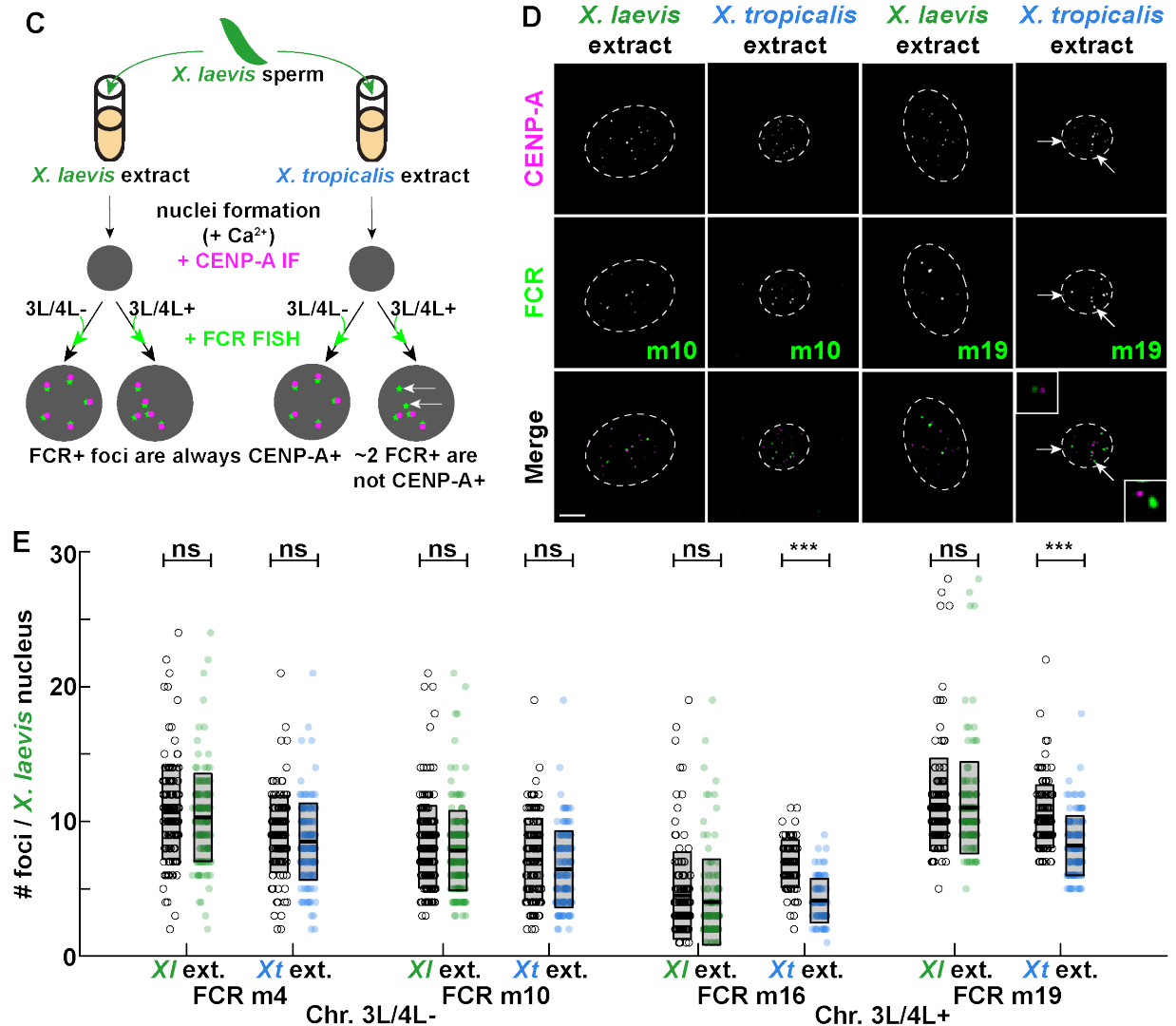


**Figure 5.4: CENP-A is lost from *X. laevis* chromosomes 3L and 4L**

(A) Quantification of the number of CENP-A foci in interphase nuclei assembled in *X. tropicalis* egg extract. Whereas *X. tropicalis* nuclei on average possess 10 foci corresponding to the 10 sperm chromosomes, *X. laevis* and *X. borealis* interphase nuclei possess an average of 16 and 14 CENP-A foci, respectively, which does not match the 18 sperm chromosomes of these species. Note that nuclei in egg extract do not always contain 1 haploid genome perfectly even in the control, but the average surrounds the expected haploid value. Quantification with N = 3 extracts, N > 64 nuclei per extract. (B) Representative images of *X. tropicalis*, *X. laevis* and *X. borealis* nuclei formed in *X. tropicalis* extract. DNA in cyan, CENP-A in red. Scale bar is 5  $\mu$ m. (C) Experimental schematic for specific centromere quantification. *X. laevis* sperm nuclei were cycled into interphase in either *X. laevis* or *X. tropicalis* egg extract. All centromeres were detected by CENP-A immunofluorescence and a subset of centromeres were identified by FCR (frog centromeric repeat) FISH (Smith et al., 2021). Probes prepared from two sequences not present in centromeres of chromosomes 3L or 4L (3L/4L- = m4, m10), were compared with probes made using two sequences present in centromeres of chromosomes 3L and 4L (3L/4L+ = m16, m19). m16 and m19 recognize ~60% of *X. laevis* chromosomes, and are not specific solely to 3L and 4L. In *X. laevis* extract, all FCR+ foci should co-localize with CENP-A, as 18/18 centromeres are maintained. If centromeric CENP-A staining is lost specifically from chromosomes 3L and 4L in

*X. tropicalis* extract, 2 3L/4L+ FCR+ foci should not colocalize with CENP-A (panel A). We note that mitotic chromosome FISH is not compatible with *Xenopus* egg extract, so we used interphase nuclei which appear to be more stable throughout the method to infer chromosome identity. (D) Images of *X. laevis* sperm nuclei formed in *X. laevis* or *X. tropicalis* extract probed by FISH for FCR monomer m10 or m19 (green) and by immunofluorescence of CENP-A (magenta). Insets show the 2 m19 FCR+ foci not co-localized with CENP-A, while all other FCR+ foci co-localize with CENP-A. DNA periphery is marked by the dashed white lines. Scale bar is 5  $\mu$ m. (E) Quantification of CENP-A foci that co-localize with FCR+ foci in *X. laevis* vs. *X. tropicalis* extract. In *X. laevis* extract, all FCR+ foci co-localize with CENP-A. However, in *X. tropicalis* extract, ~2 m16 or m19 FCR+ foci do not co-localize with CENP-A, corresponding to the loss of CENP-A localization on chromosomes 3L and 4L. Quantification with N = 2 extracts, N > 50 nuclei and > 800 centromeres per probe per extract. p-values by two-tailed two-sample unequal variance t-tests (left to right): 0.3562, 0.0916, 0.3708, 0.0499, 0.2426, 2.797e-19, 0.5485, 7.972e-13; ns, not significant. Open circles are FCR+ foci, filled circles represent foci that are both FCR+ and CENP-A+.

### **CENP-A and its chaperone HJURP can rescue *X. laevis* centromere assembly**

We next sought to determine whether enhancing centromere assembly by adding species-matched paternal factors could prevent CENP-A eviction and centromere loss from specific *X. laevis* and *X. borealis* chromosomes formed in *X. tropicalis* extracts. In vitro reactions were supplemented with paternally-matched proteins expressed in reticulocyte lysate, including CENP-A and its dedicated chaperone HJURP, at the onset of interphase (Fig. 5.5A-C). Whereas adding *X. laevis* CENP-A resulted in a partial rescue, CENP-A plus HJURP increased the percentage of replicated *X. laevis* mitotic chromosomes with CENP-A foci to control levels (Fig. 5.6A). In contrast, no combination of *X. borealis* centromere factors tested, including CENP-A, HJURP, and CENP-C (Erhardt et al., 2008; Roure et al., 2019), restored CENP-A foci to replicated *X. borealis* mitotic chromosomes (Fig. 5.6B). Notably, however, examination of interphase nuclei in *X. borealis* sperm/*X. tropicalis* egg extract reactions prior to metaphase entry revealed that CENP-A localization was initially fully rescued, with the expected number of CENP-A-positive foci corresponding to the number of chromosomes (Fig. 5.6C). These results indicate that exogenous species-matched CENP-A can restore proper centromere formation on all chromosomes during interphase of for both *X. laevis* and *X. borealis*, but that CENP-A is not maintained on a subset of *X. borealis* chromosomes upon entry into mitosis.

The ability to mix and match egg extract, sperm chromosomes, and exogenous centromere assembly factors enabled evaluation of CENP-A/centromere compatibilities across species. For example, despite striking differences in core centromere sequences between *X. laevis* and *X. borealis* (Fig. 5.1), the CATDs of the two species' CENP-A sequences are identical (Fig. 5.2B), and exogenous CENP-A from either species equivalently restored centromere assembly on *X. laevis* mitotic chromosomes replicated in *X. tropicalis* egg extract (Fig. 5.6A). Further, we observed that addition of excess exogenous *X. tropicalis* CENP-A could also increase the percentage of *X. laevis* mitotic chromosomes with centromere foci to control levels, although *X. borealis* chromosomes could not be rescued under any condition tested (Fig. 5.6B, D). Together, our results indicate that enhancing the pathway that drives CENP-A incorporation into centromeric chromatin can overcome whatever is destabilizing centromeres on specific *X. laevis*

centromeres and raised the question of why the *X. borealis* chromosomes are refractory to this rescue.

**Figure 5.5**

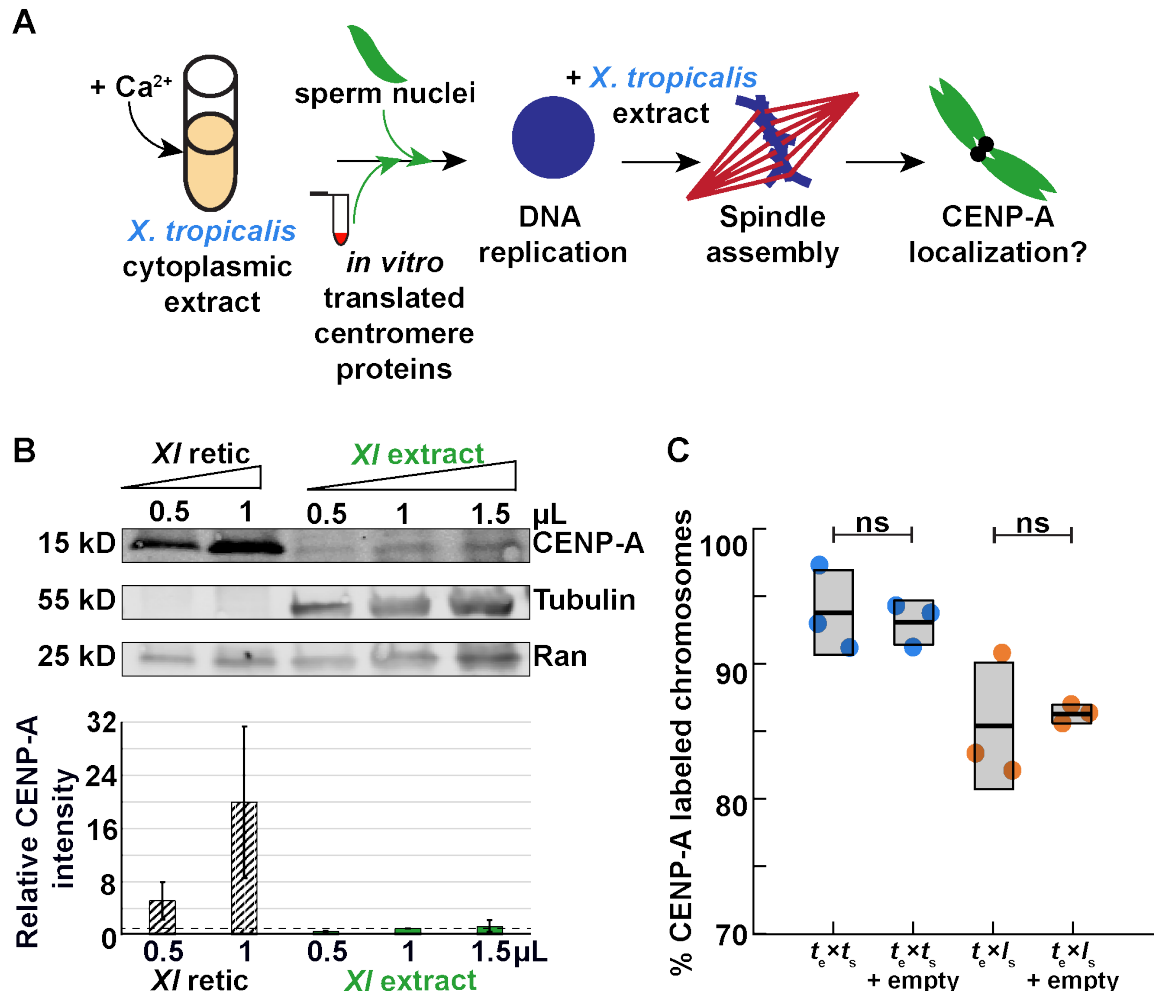


**Figure 5.5: Driving CENP-A assembly with proteins expressed in reticulocyte lysate**

(A) Experimental schematic of extract reactions in which reticulocyte lysate is added at the onset of interphase to mimic the timing of CENP-A deposition in G1. (B) Representative Western blot of *X. laevis* CENP-A protein expressed in reticulocyte lysate and quantification of three blots showing band intensity normalized to CENP-A levels in 1 μL of *X. laevis* egg extract (dotted line). CENP-A is approximately twenty times more concentrated in reticulocyte lysate compared to *X. laevis* extract, with amounts added to chromosome/nuclear assembly reactions corresponding to 8 or 80 times endogenous CENP-A levels. (C) Percentage of replicated *X. laevis* or *X. tropicalis* chromosomes with CENP-A staining in *X. tropicalis* extract supplemented with unprogrammed reticulocyte lysate. Lysates containing empty expression vectors have no effect on centromere staining. Quantification from N = 3 extracts, N > 298 chromosomes per extract. p-values (left to right) by two-tailed two-sample unequal variance t-tests: 0.7433, 0.7755; ns, not significant.

**Figure 5.6**

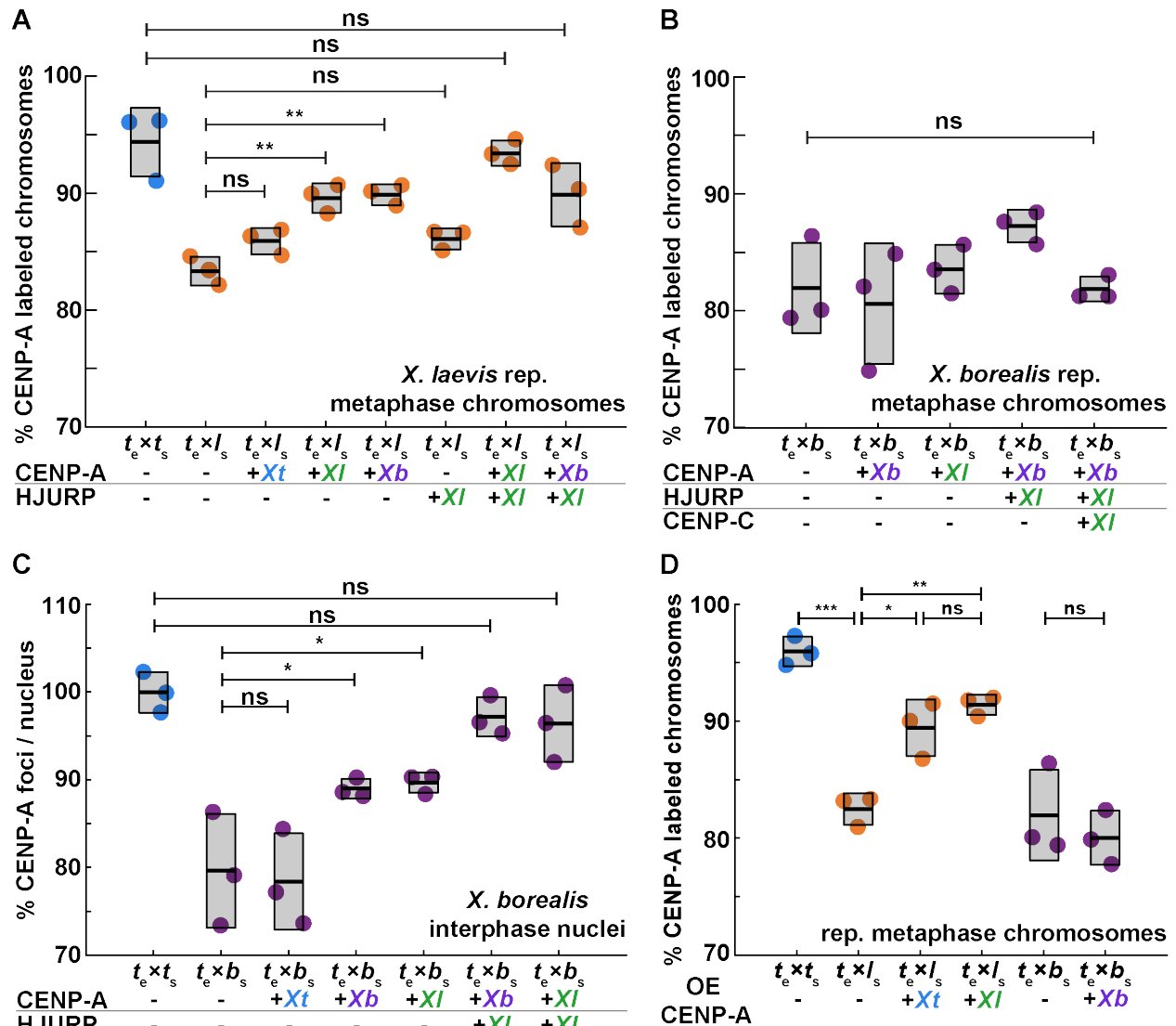


**Figure 5.6: Driving CENP-A assembly rescues centromere localization in interphase, which persists on mitotic *X. laevis*, but not on *X. borealis* chromosomes**

(A) Percentage of replicated *X. laevis* chromosomes with centromeric CENP-A staining in *X. tropicalis* extract supplemented with in vitro translated CENP-A and HJURP proteins from different *Xenopus* species. *X. laevis* chromosomes are fully rescued with species-matched centromere proteins. Quantification with N = 3 extracts, N > 315 chromosomes per extract. p-values (top to bottom) by one-way ANOVA with Tukey post-hoc analysis: 0.1734, 0.9999, 0.5522, 0.0057, 0.0086, 0.6281. (B) Percentage of replicated *X. borealis* chromosomes with centromeric CENP-A staining in *X. tropicalis* extract supplemented with in vitro translated centromere proteins from different *Xenopus* species. No combination or increased amounts of centromeric proteins CENP-A (CA), HJURP (HJ), and CENP-C (CC) restored CENP-A localization on *X. borealis* mitotic chromosomes. Quantification with N = 3 extracts, N > 216 chromosomes per extract. p-value by one-way ANOVA = 0.0786. (C) Percentage of CENP-A-labeled centromeric foci in *X. borealis* nuclei assembled in *X. tropicalis* extract supplemented with in vitro translated centromere proteins from different *Xenopus* species. Driving centromere assembly with species-matched proteins fully

restores formation of centromere foci in interphase, but CENP-A staining is subsequently lost in metaphase (panel B). Quantification with N = 3 extracts, N > 67 nuclei per extract. p-values (top to bottom) by one-way ANOVA: 0.9996, 0.0562, 0.0433, 0.9690, 0.9109. **(D)** Percentage of replicated *X. laevis* or *X. borealis* chromosomes with centromeric CENP-A staining in *X. tropicalis* extract supplemented with excess (~80X endogenous levels) of in vitro translated *X. laevis* or *X. tropicalis* CENP-A. Whereas centromere staining is fully rescued on *X. laevis* mitotic chromosomes by CENP-A from either species, *X. borealis* centromere staining is not affected. Quantification with N = 3 extracts, N > 204 chromosomes per extract. p-values (top to bottom, then left to right) by one-way ANOVA with Tukey post-hoc analysis: 0.0042, 0.0001, 0.0249, 0.8845, 0.88946. **A-C**: Centromere proteins were added at ~8X endogenous levels. **A-D**: ns, not significant.

### ***X. borealis* chromosome defects result from mitotic replication stress**

A clue as to why *X. borealis* mitotic chromosomes behave differently than *X. laevis* chromosomes in the in vitro hybrid extract system emerged with observation of their morphology. Although a subset of replicated *X. laevis* mitotic chromosomes formed in *X. tropicalis* extract lacked centromeres, they otherwise appeared normal. In contrast, 7-10% of *X. borealis* mitotic chromosomes displayed ultra-thin regions of 2-3  $\mu\text{m}$  in length following replication, although centromeres on these chromosomes appeared largely intact (Fig. 5.7A, B; Fig. 5.8A, B). We reasoned that incomplete DNA replication leading to fork stalling and subsequent collapse in mitosis, termed replication stress, caused the formation of fragile sites (Gómez-González and Aguilera, 2019; Deng et al., 2019). Consistent with this idea, adding low doses of the DNA polymerase inhibitor aphidicolin that leads to replication stress (Deng et al., 2019; Kabeche et al., 2018; Durkin and Glover, 2007) triggered formation of ultra-thin regions on *X. tropicalis* and *X. laevis* mitotic sperm chromosomes that had progressed through the cell cycle in *X. tropicalis* extract, and slightly exacerbated morphological defects of *X. borealis* chromosomes (Fig. 5.8C-E). Notably, however, the aphidicolin-induced replication stress did not significantly affect CENP-A localization efficiency (Fig. 5.8F), indicating that replication stress per se does not interfere with CENP-A loading and maintenance.

To determine whether the *X. borealis* chromosome morphology and mitotic centromere defects were due to replication stress, we blocked collapse of stalled mitotic replication forks by adding an inhibitor of the ATPase p97 (Fig. 5.8C), which is required for replication helicase removal (Maric et al., 2014; Deng et al., 2019). We observed a complete rescue of CENP-A localization and chromosome morphology on *X. borealis* chromosomes (Fig. 5.7C, D). Consistent with the factors known for this pathway of mitotic replication fork collapse and breakage (Deng et al., 2019), Aurora A and Plk1 kinase inhibitors added to *X. tropicalis* extracts at low doses that avoided mitotic defects also rescued *X. borealis* chromosome morphology and CENP-A localization, but did not affect *X. laevis* or *X. tropicalis* chromosomes (Fig. 5.7E, F). Finally, *X. laevis* or *X. tropicalis* chromosomes treated with aphidicolin followed by p97 inhibition displayed very few chromosome defects (Fig. 5.8C, D). Combined, these data reveal that a subset of *X. borealis* chromosomes experience mitotic replication stress in *X. tropicalis* cytoplasm, and that this is coupled to CENP-A eviction. Remarkably, however, centromere loss appears to occur on a different subset of mitotic chromosomes than those with ultra-thin regions.



**Figure 5.7**

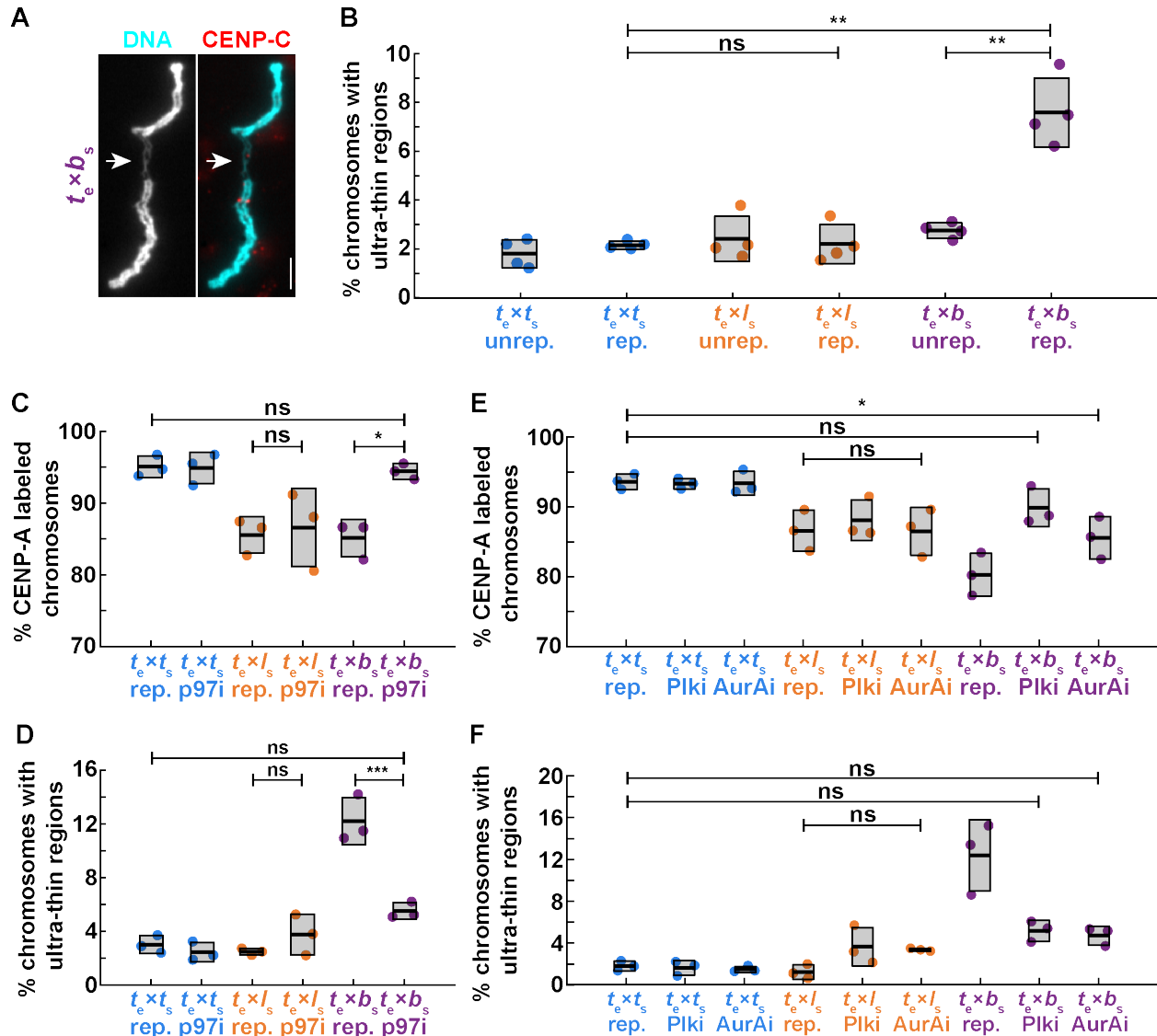
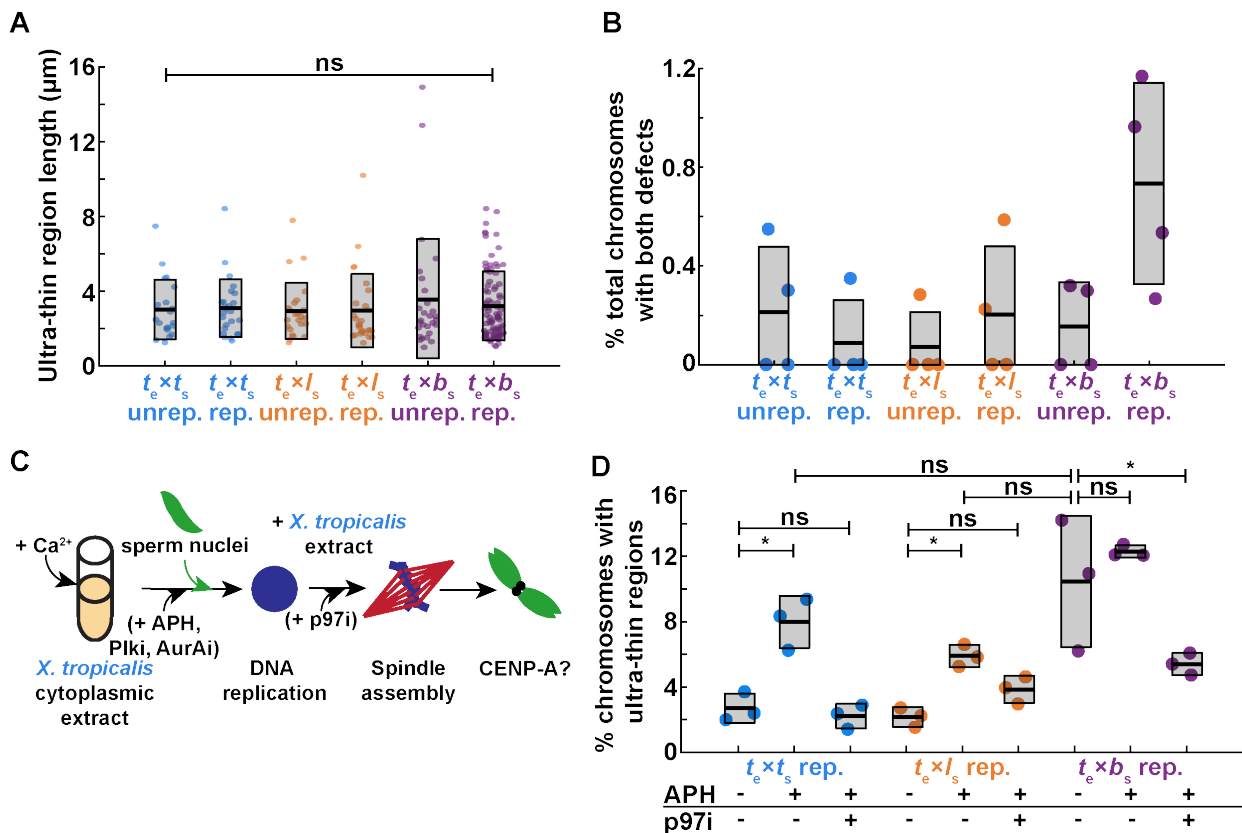


**Figure 5.7: Mitotic replication stress leads to *X. borealis* centromere and chromosome morphology defects**

(A) Representative image showing an ultra-thin region of a mitotic *X. borealis* chromosome formed in *X. tropicalis* egg extract. Note that the chromosome has an intact centromere. DNA in cyan, CENP-A in red. Scale bar is 5  $\mu$ m. (B) Percentage of unreplicated and replicated mitotic chromosomes with ultrathin morphology defects in *X. tropicalis* extract. A low percentage of *X. tropicalis*, *X. laevis* or *X. borealis* unreplicated chromosomes display ultra-thin regions. After cycling through interphase, only *X. borealis* chromosomes exhibit a significant increase in this defect. Quantification with N = 3 extracts, N > 310 chromosomes per extract. p-values (top to bottom, then left to right) by one-way ANOVA with Tukey post-hoc analysis: 2.9352e-7, 0.9999, 1.6475e-6. (C) Percentage of replicated chromosomes with centromeric CENP-A staining in *X. tropicalis* extracts treated with solvent control or 10  $\mu$ M p97 ATPase inhibitor NMS-873 (p97i). Inhibition of p97 restores CENP-A staining on *X. borealis* mitotic chromosomes, but does not affect *X. tropicalis* or *X. laevis* chromosomes. p-values (top to bottom, then left to right) by one-way ANOVA with Tukey post-hoc analysis: 0.9997, 0.9978, 0.0204. (D) Percentage of

chromosomes with ultrathin regions in *X. tropicalis* extracts treated with solvent control or 10  $\mu$ M p97 ATPase inhibitor NMS-873 (p97i). Inhibition of p97 rescues *X. borealis* chromosome morphology defects, but does not affect *X. tropicalis* or *X. laevis* chromosomes. p-values (top to bottom, then left to right) by one-way ANOVA with Tukey post-hoc analysis: 0.1114, 0.6903, 6.2572e-5. (E) Percentage of replicated chromosomes with centromeric CENP-A staining in *X. tropicalis* extracts treated with solvent control, 1  $\mu$ M Polo-like kinase 1 inhibitor BI-2536 (Plk1i), or 1  $\mu$ M Aurora A kinase inhibitor MLN-8237 (AurAi). CENP-A localization is fully or partially rescued on *X. borealis* mitotic chromosomes, whereas *X. tropicalis* or *X. laevis* chromosomes are not affected. p-values (top to bottom) by one-way ANOVA with Tukey post-hoc analysis: 0.0276, 0.7003, 0.9999. (F) Percentage of chromosomes with ultrathin regions in *X. tropicalis* extracts treated with solvent control, 1  $\mu$ M Polo-like kinase 1 inhibitor BI-2536 (Plk1i), or 1  $\mu$ M Aurora A kinase inhibitor MLN-8237 (AurAi). Inhibition of Plk1 and AurA rescued *X. borealis* mitotic chromosome morphology defects, but did not affect *X. tropicalis* or *X. laevis* chromosomes. p-values (top to bottom) by one-way ANOVA with Tukey post-hoc analysis: 0.2882, 0.1525, 0.5887. C, D: N = 3 extracts, N > 179 chromosomes per extract. E, F: N = 3 extracts, N > 155 chromosomes per extract. B-F: ns, not significant.

**Figure 5.8**



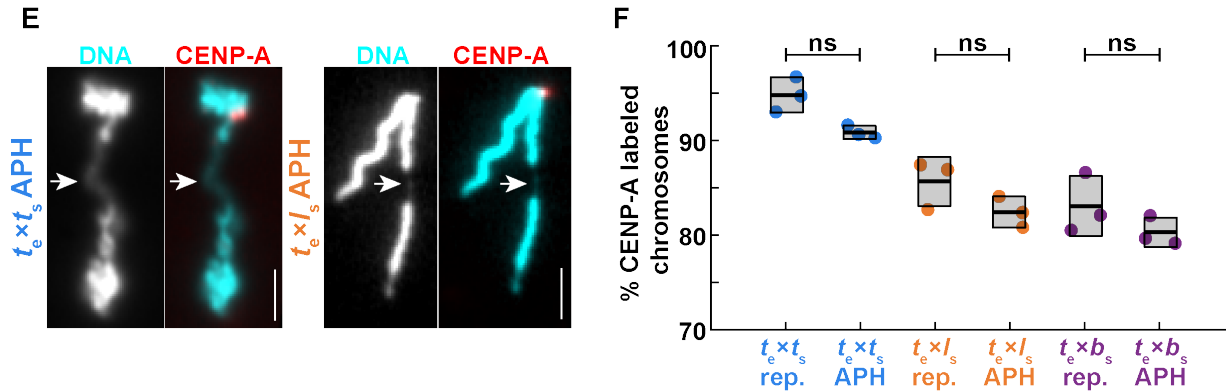


**Figure 5.8: Characterization of chromosome morphology defects that can be induced by aphidicolin and rescued by p97 inhibition**

(A) Quantification of ultra-thin region lengths, which average  $\sim 2\text{-}3\ \mu\text{m}$  on mitotic chromosomes of all three *Xenopus* species. p-value by one-way ANOVA = 0.8712. (B) Percentage of *X. tropicalis*, *X. laevis*, and *X. borealis* chromosomes with ultra-thin regions that have also lost CENP-A staining. Only a small fraction of chromosomes with ultra-thin regions also show centromere loss. Across all species, only  $\sim 0.2\text{-}0.6\%$  of all chromosomes exhibit both morphological and centromere defects, corresponding to 1-4 chromosomes out of  $\sim 350$  total chromosomes per extract. (C) Experimental schematic illustrating when inhibitors are added to *X. tropicalis* extract reactions. (D) Percentage of mitotic chromosomes with ultrathin regions in *X. tropicalis* extracts treated with solvent control or  $10\ \mu\text{g}/\text{mL}$  aphidicolin (APH) to inhibit DNA replication, and with or without  $10\ \mu\text{M}$  p97 ATPase inhibitor NMS-873 (p97i) to prevent removal of stalled replication forks. Aphidicolin increased the prevalence of ultra-thin chromosome regions on *X. tropicalis* and *X. laevis* chromosomes, but did not significantly exacerbate these regions on *X. borealis* chromosomes. Inhibition of p97 rescued the chromosome morphology defects. Quantification from  $N = 3$  extracts,  $N > 138$  chromosomes per extract. p-values (top to bottom, then left to right) by two-tailed two-sample unequal variance t-tests: 0.6106, 0.0217, 0.9986, 0.8708, 0.9999, 0.9159, 0.0151, 0.0023. (E) Representative images of *X. tropicalis* and *X. laevis* mitotic chromosomes following aphidicolin treatment. DNA in cyan, CENP-A in red. Scale bar is  $5\ \mu\text{m}$ . (F) Percentage of replicated chromosomes with centromeric CENP-A staining in *X. tropicalis* extracts treated with solvent control or  $10\ \mu\text{g}/\text{mL}$  aphidicolin. Inhibition of DNA replication does not affect centromere formation on any species' chromosomes. p-values (left to right) by two-tailed two-sample unequal variance t-tests: 0.0523, 0.1554, 0.2679. **A, B:**  $N = 3$  extracts,  $N > 20$  chromosomes per condition. **D, F:**  $N = 3$  extracts,  $N > 150$  chromosomes per extract. **A, D, F:** ns, not significant.

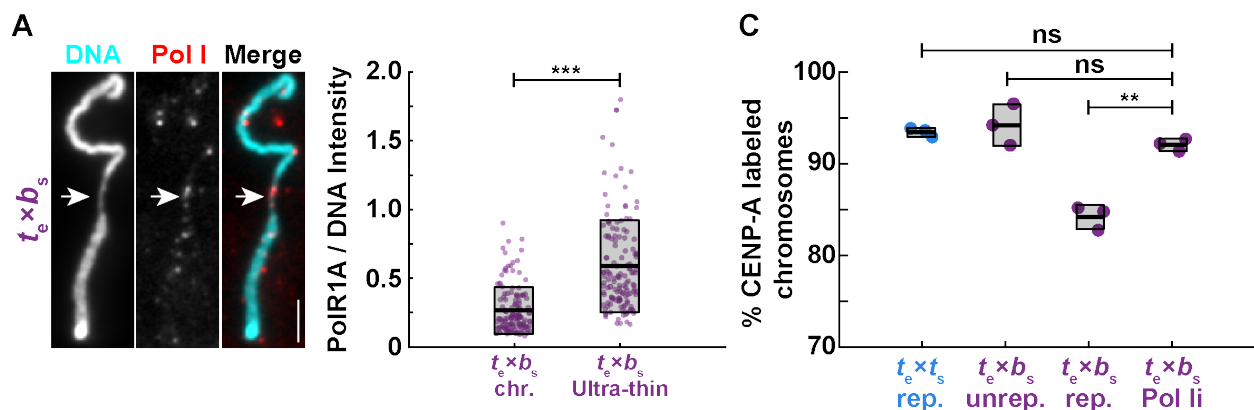
### Replication-transcription conflicts lead to centromere defects

The fragile sites observed on *X. borealis* chromosomes were reminiscent of secondary constrictions that occur at repetitive, late-replicating regions such as ribosomal DNA (rDNA; Durica and Krider, 1977; Durkin and Glover, 2007). In *Xenopus*, the rDNA transcription machinery associates with mitotic chromosomes early in development and in egg extract (Roussel et al., 1996; Gébrane-Younès et al., 1997; Bell and Scheer, 1997; Bell et al., 1997), even though rDNA transcription and nucleolus formation occur after zygotic genome activation (Shiokawa et al., 1994; Newport and Kirschner, 1982). We therefore tested whether ultra-thin regions of *X. borealis* chromosomes replicated in *X. tropicalis* extract contained rDNA by performing immunofluorescence using antibodies against RNA polymerase I (Pol I) and the rDNA transcription regulator upstream binding

factor (UBF). Both proteins were consistently enriched on the ultra-thin regions of *X. borealis* mitotic chromosomes assembled in *X. tropicalis* egg extract (Fig. 5.9A, B).

To test whether RNA Pol I occupancy at rDNA of *X. borealis* chromosomes contributed to the observed defects, *X. tropicalis* extract reactions were treated with the inhibitor BMH-21, which has been shown to dissociate the polymerase from chromatin (Peltonen et al., 2014; Colis et al., 2014). Strikingly, *X. borealis* chromosome morphology defects as well as CENP-A localization were rescued (Fig. 5.9C, D). Together, these data suggest that the replication stress experienced by *X. borealis* mitotic chromosomes occurs at rDNA loci, and that defects in rDNA chromatin dynamics act to destabilize a subset of *X. borealis* centromeres. In contrast, centromere formation on *X. laevis* chromosomes was not rescued by RNA Pol I inhibition (Fig. 5.10A, B), further indicating differences in the mechanisms underlying their incompatibility with *X. tropicalis*. However, we observed that inhibition of RNA polymerase II (Pol II) with triptolide partially rescued CENP-A localization to *X. laevis* chromosomes in *X. tropicalis* extract, whereas *X. borealis* chromosomes were not affected (Fig. 5.9E), and no species' chromosomes were rescued by inhibition of RNA Pol III (Fig. 5.10C, D). Therefore, a common theme in hybrid incompatibility among *Xenopus* species may be replication-transcription conflicts that contribute to eviction of CENP-A from a subset of mitotic chromosomes. However, whereas this occurs at rDNA on *X. borealis* chromosomes and depends on RNA Pol I, *X. laevis* defects are driven, at least in part, by RNA Pol II-induced defects. These observations lead to the model that epigenetic mechanisms promoting CENP-A incorporation at centromeres are disrupted by the presence or activity of RNA polymerases that cause under-replication at specific chromosome loci. Whereas *X. laevis* defects can be overcome by driving CENP-A incorporation at centromeres, *X. borealis* defects can only be rescued by blocking replication stress at rDNA, either by preventing fork collapse or by removing RNA Pol I.

**Figure 5.9**



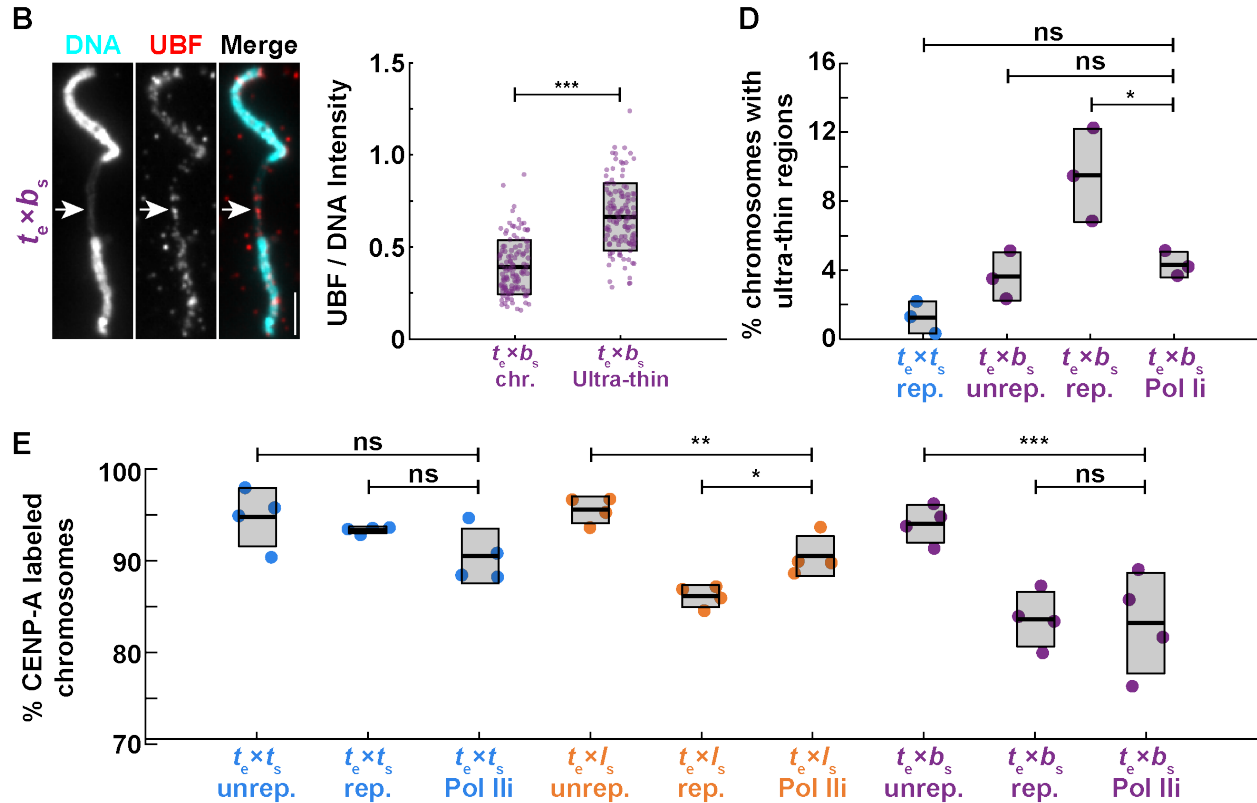


**Figure 5.9: Replication-transcription conflicts at rDNA on *X. borealis* chromosomes can be rescued by inhibiting RNA Pol I**

(A) Representative images and fluorescence intensity quantification of RNA Pol I staining relative to DNA on ultrathin and normal regions of *X. borealis* mitotic chromosomes, revealing enrichment of Pol I on ultra-thin regions. Quantification with N = 3 extracts, N = 140 chromosomes. p-value =  $9.4793 \times 10^{-20}$  by two-tailed two-sample unequal variance t-tests. (B) Representative images and fluorescence intensity quantification of UBF staining relative to DNA on ultrathin and normal regions of *X. borealis* mitotic chromosomes, revealing enrichment of UBF on ultra-thin regions. Quantification with N = 3 extracts, N = 62 chromosomes. p-value =  $4.5004 \times 10^{-13}$  by two-tailed two-sample unequal variance t-tests. (C) Percentage of mitotic chromosomes with centromeric CENP-A staining in *X. tropicalis* extracts treated with solvent control or 1  $\mu$ M BMH-21 to inhibit RNA Pol I (Pol Ii), which fully rescues CENP-A localization on replicated *X. borealis* chromosomes. p-values (top to bottom) by one-way ANOVA with Tukey post-hoc analysis: 0.9794, 0.7979, 0.0005. (D) Percentage of mitotic chromosomes with ultrathin regions in *X. tropicalis* extracts treated with solvent control or 1  $\mu$ M BMH-21 (Pol Ii). Pol I inhibition also rescues *X. borealis* chromosome morphology defects. p-values (top to bottom) by one-way ANOVA with Tukey post-hoc analysis: 0.5078, 0.9999, 0.0469. (E) Percentage of chromosomes with centromeric CENP-A staining in *X. tropicalis* extracts treated with solvent control or 25  $\mu$ M triptolide to inhibit RNA Pol II (Pol Iii). *X. laevis* chromosomes are partially rescued, while *X. tropicalis* and *X. borealis* chromosomes are not affected. Quantification with N = 3 extracts, N > 322 chromosomes per extract. p-values (top to bottom, then left to right) by one-way ANOVA with Tukey post-hoc analysis: 0.4785, 0.8797, 0.0052, 0.0125, 0.0003, 0.9999. A, B: DNA in cyan, Pol I in red. Scale bar is 5  $\mu$ m. C, D: N = 3 extracts, N > 172 chromosomes per extract. C-E: ns, not significant.

**Figure 5.10**

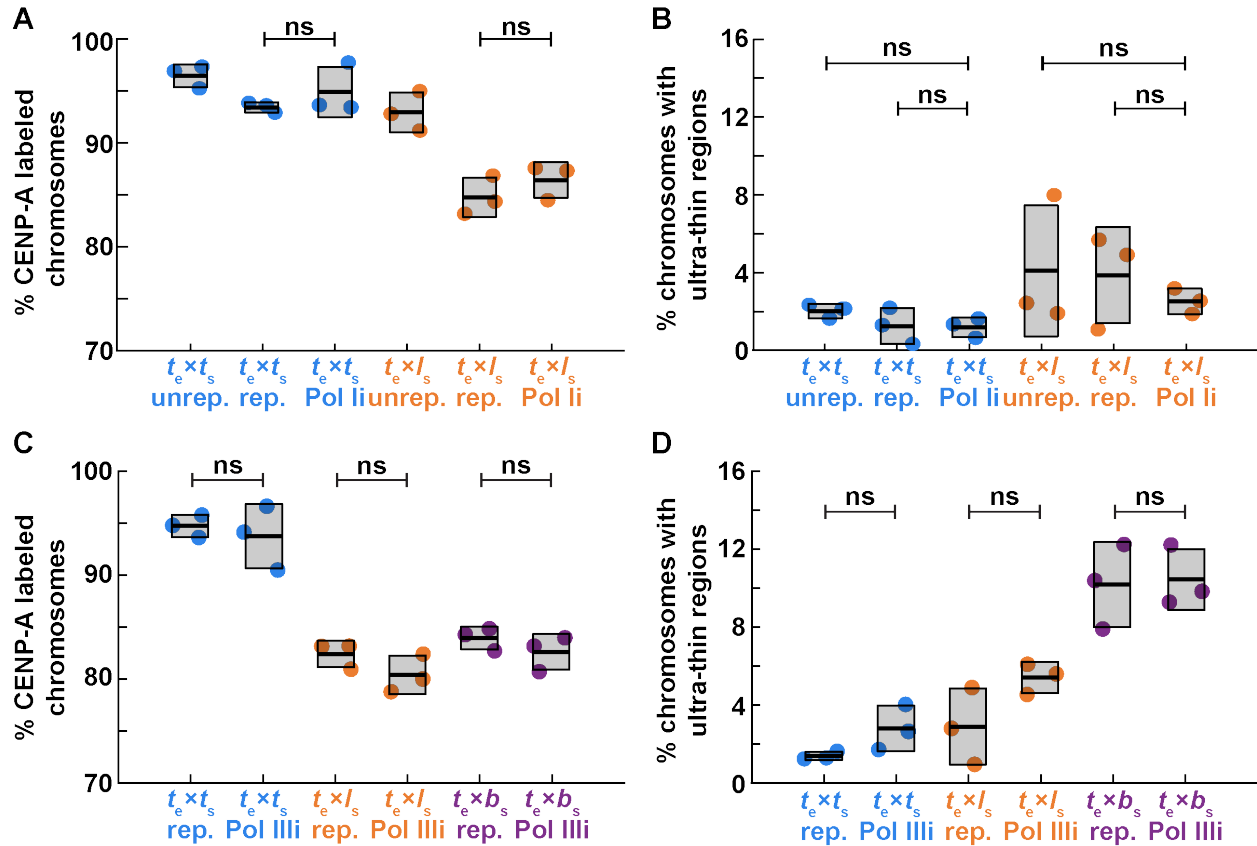


**Figure 5.10: Pol I transcription inhibition does not affect *X. tropicalis* or *X. laevis* chromosomes, while Pol III inhibition had no effect on any species**

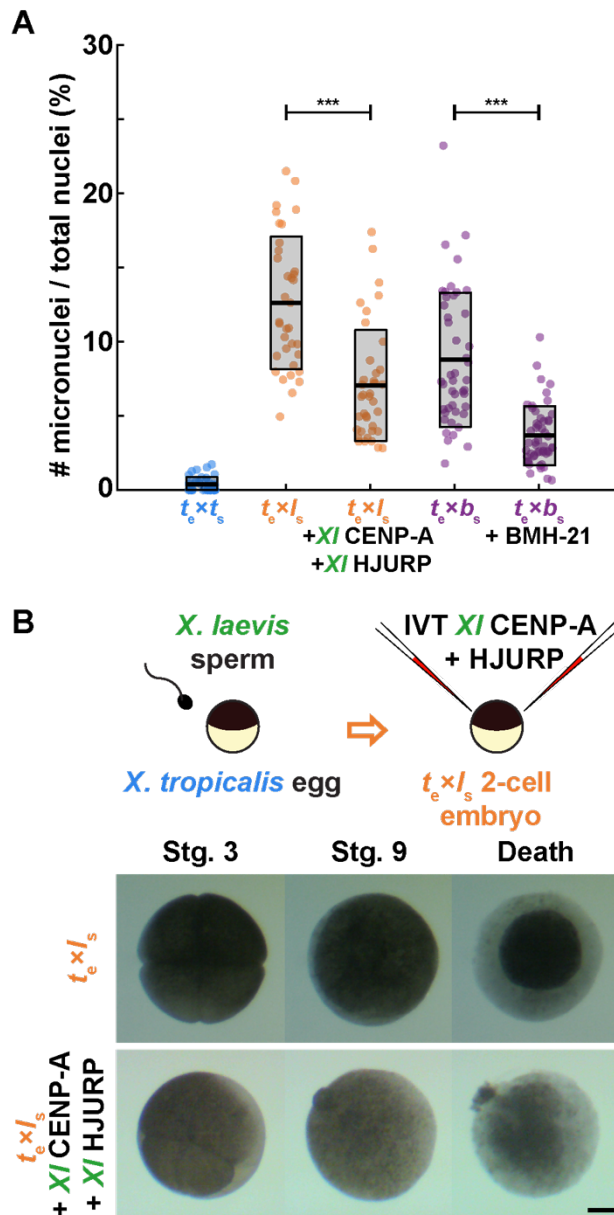
(A, B) The percentage of *X. tropicalis* or *X. laevis* mitotic chromosomes formed in *X. tropicalis* egg extract with centromeric CENP-A staining (A) or ultrathin regions (B) is unchanged upon treatment with 1  $\mu$ M BMH-21 to inhibit RNA Pol I (Pol Ii). Quantification with N = 3 extracts, N > 113 chromosomes per extract. p-values by one-way ANOVA with Tukey post-hoc analysis: (A, left to right) 0.9702, 0.9413, (B, left to right, then top to bottom) 0.9995, 0.9711, 1, 0.9882. (C, D) The percentage of *X. tropicalis*, *X. laevis*, or *X. borealis* mitotic chromosomes formed in *X. tropicalis* egg extract with centromeric CENP-A staining (C) or ultrathin regions (D) is unchanged upon treatment with 20  $\mu$ M ML-69218 to inhibit RNA Pol III (Pol IIIi). Quantification with N = 3 extracts, N > 179 chromosomes per extract. p-values by one-way ANOVA with Tukey post-hoc analysis: (C, left to right) 0.9389, 0.7506, 0.9416, (D, left to right) 0.8431, 0.3540, 0.9999. **A-D:** ns, not significant.

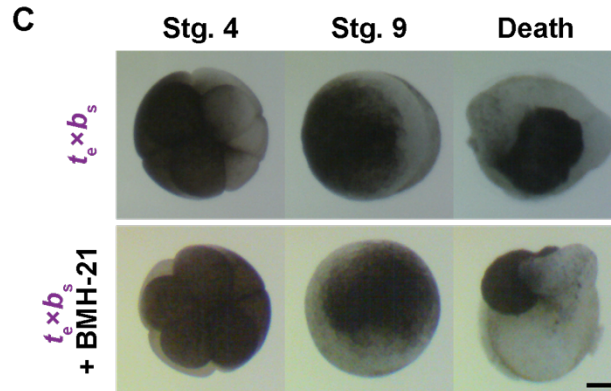
### Chromosome mis-segregation can be reduced in hybrid embryos, but inviability persists

To determine whether the incompatibility mechanisms identified through this work are responsible for hybrid inviability in vivo, we performed rescue experiments on cross-fertilized embryos. In vitro translated, paternally-matched CENP-A and HJURP proteins were microinjected into both blastomeres of the 2-cell hybrid embryo produced by fertilizing *X. tropicalis* eggs with *X. laevis* sperm, while *X. tropicalis*/*X. borealis* hybrid embryos were treated with RNA Pol I inhibitor BMH-21. Fewer micronuclei were observed in both cases, indicating a decrease in mitotic errors in hybrid embryos, although not to

the low levels seen in wild-type *X. tropicalis* embryos (Fig. 5.11A, Fig. 5.12). Thus, the basis of chromosome defects identified using our in vitro egg extract assays also contribute to chromosome segregation defects in vivo. However, despite this partial rescue, treated hybrids died at the same time and in the same manner as untreated sibling controls (Fig. 5.11B, C, Movie 5.1, 5.2). While it is possible that a complete rescue of chromosome segregation defects in the hybrid embryos is required for viability, we predict that other mechanisms that we have not yet identified also contribute, which can be uniquely addressed using a combination of in vitro and in vivo approaches in *Xenopus*.

**Figure 5.11**

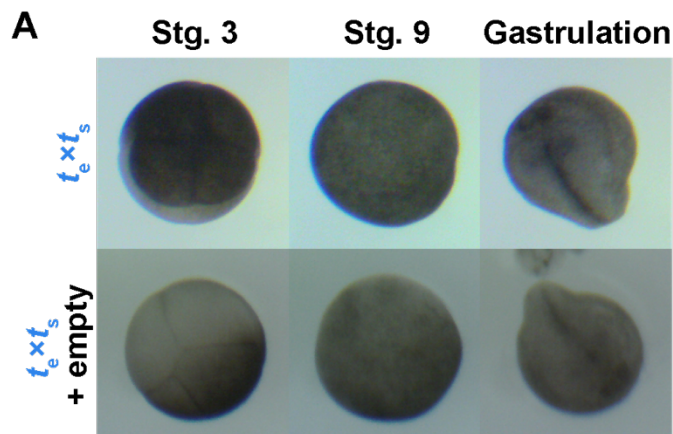




**Figure 5.11: Treatments that rescue CENP-A localization in egg extracts reduce micronuclei formation in hybrid embryos, but inviability persists**

(A) Quantification of chromosome mis-segregation events as measured by the number of micronuclei compared to total nuclei in treated hybrid embryos. *X. tropicalis* eggs fertilized with *X. laevis* sperm were microinjected with *X. laevis* CENP-A/HJURP, while *X. tropicalis* eggs fertilized with *X. borealis* sperm were treated with Pol 1 inhibitor BMH-21. Embryos were fixed at stage 9 (7 hpf) just before gastrulation and hybrid death. The number of micronuclei was significantly reduced in both cases, but not to control levels measured in *X. tropicalis* eggs fertilized with *X. tropicalis* sperm. N = 3 clutches for each hybrid, N > 15 embryos and > 200 cells per embryo. p-values (left to right) by two-tailed two-sample unequal variance t-tests: 2.111e-7, 2.651e-9; ns, not significant. (B) Schematic of experiment and movie frames of *X. tropicalis* eggs fertilized with *X. laevis* sperm microinjected at the two-cell stage with *X. laevis* CENP-A/HJURP, increasing centromeric protein concentration by ~44.5%. Microinjected hybrid embryos die at the same time and in the same manner as uninjected hybrid controls. N = 10 embryos across 4 clutches. Scale bar is 200  $\mu\text{m}$ . (C) Movie frames of *X. tropicalis* eggs fertilized with *X. borealis* sperm that were incubated from the two-cell stage with 1  $\mu\text{M}$  RNA Pol I inhibitor, BMH-21. Treated hybrid embryos die at the same time and in the same manner as untreated hybrid controls. N = 12 embryos across 2 clutches. Scale bar is 200  $\mu\text{m}$ .

**Figure 5.12**





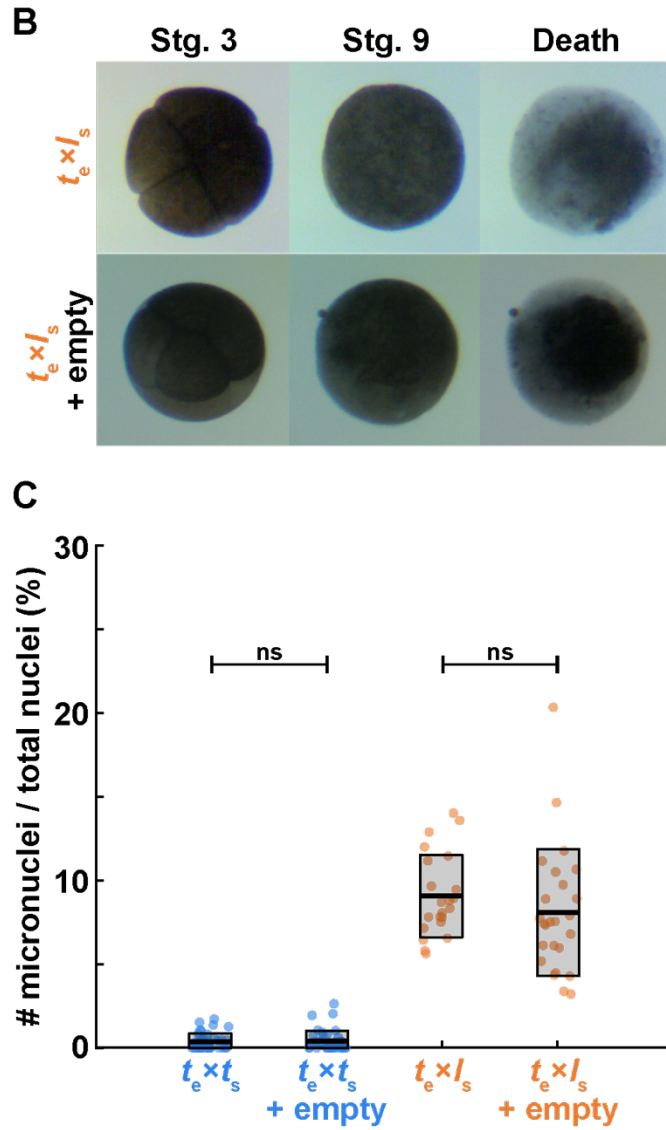


**Figure 5.12: Microinjection with reticulocyte lysate does not affect embryo development or chromosome segregation.**

(A) Movie frames of untreated *X. tropicalis* embryos and embryos microinjected at the two-cell stage with empty reticulocyte lysate into both blastomeres show that embryonic development is not affected by the procedure. N = 15 embryos across 3 clutches. Scale is 200  $\mu$ m. (B) Movie frames of untreated *X. tropicalis*/*X. laevis* hybrid embryos and hybrid embryos microinjected at the two-cell stage with empty reticulocyte lysate into both blastomeres show that the embryonic death phenotype is not affected by the procedure. N = 12 embryos across 2 clutches. Scale is 200  $\mu$ m. (C) Quantification of the number of micronuclei compared to total nuclei in stage 9 *X. tropicalis* embryos or *X. tropicalis*/*X. laevis* hybrid embryos microinjected with empty reticulocyte lysate. The prevalence of micronuclei is unaffected by the procedure. p-values (left to right) by two-tailed two-sample unequal variance t-tests: 0.749, 0.288; ns, not significant.

**MOVIE 5.1: Microinjection of *X. laevis* CENP-A and HJURP in vitro translated proteins into  $t_e \times l_s$  hybrids does not rescue viability.**

*X. tropicalis* eggs were fertilized with *X. laevis* sperm and microinjected with in vitro translated paternally-matched CENP-A and HJURP (right) at stage 2. Embryos were imaged in separate

dishes from stage 3 in 1/10X MMR. The movie plays 20 h in 15s (rate of 120 frames per second). Scale bar corresponds to 200  $\mu\text{m}$ .

**MOVIE 5.2: Treatment with RNA Polymerase I inhibitor BMH-21 does not rescue  $t_e \times b_s$  hybrid viability.**

*X. tropicalis* eggs were fertilized with *X. borealis* sperm and incubated with 1  $\mu\text{M}$  BMH-21 in 1/10X MMR (right) from stage 2. The movie plays 20 h in 15s (rate of 120 frames per second). Scale bar corresponds to 200  $\mu\text{m}$ .

### 5.3 DISCUSSION

Centromeric DNA sequences and centromere and kinetochore proteins have been shown to rapidly co-evolve, which is thought to counteract female meiotic drive and maintain faithful chromosome segregation (Malik and Henikoff, 2001; Malik et al., 2002; Kumon et al., 2021; Pontremoli et al., 2021; Hooff et al., 2017). Our study reveals very low conservation of core centromere DNA sequences across three *Xenopus* species, and differences in protein sequences of *Xenopus* CENP-A and its chaperone HJURP are also observed, indicating co-evolution. However, robust epigenetic mechanisms must operate to maintain centromere compatibility in *Xenopus* hybrids, since many crosses are viable (De Robertis and Black, 1979; Woodland and Ballantine, 1980; Bürki, 1985; Narbonne et al., 2011), and only a subset of chromosomes display centromere/kinetochore defects in inviable hybrids (Gibeaux et al., 2018). Thus, neither differences in centromere sequences nor co-evolved centromere/kinetochore proteins contribute directly to *Xenopus* hybrid inviability.

The *Xenopus* egg extract and sperm chromosome reconstitution system uniquely allowed us to identify mechanisms by which centromere formation is disrupted on specific chromosomes in inviable interspecies hybrids. For *X. tropicalis* eggs fertilized with *X. borealis* sperm, in vitro experiments indicate that defects are due to replication stress at rDNA, since both CENP-A localization and chromosome morphology can be rescued by either preventing replication fork collapse or evicting RNA Pol I (Roussel et al., 1996; Bell et al., 1997; Deng et al., 2019). However, it is unclear why distinct subsets of paternal chromosomes appear to possess ultra-thin regions versus centromere defects. We propose that clustering of repetitive elements including rDNA, pericentromeric, and centromeric repeats during interphase brings together different chromosomal loci and their associated machineries. Normally, such clustering is observed at chromocenters, which may function to stabilize centromeres and promote CENP-A deposition in early G1 of the cell cycle (Brändle et al., 2022; Stellfox et al., 2013). Although discrete chromocenters or other nuclear bodies such as nucleoli have not been observed to form in egg extracts, loci interactions may nevertheless occur during interphase that are disrupted in hybrid reactions and affect four specific *X. borealis* chromosomes due to defects in rDNA replication. While addition of excess CENP-A and its chaperone HJURP can rescue centromere assembly on these chromosomes during interphase, the burst of DNA replication that occurs when metaphase-arrested extract is added (Deng et al., 2019) may simultaneously lead to fork breakage and CENP-A loss. Understanding how formation of fragile sites and centromere loss are related will require a complete *X. borealis* genome assembly that includes rDNA and other repetitive sequences.

Our findings highlight the dynamic interplay between machineries that promote and disrupt centromere assembly. For in vitro reactions reconstituting *X. tropicalis* eggs fertilized with *X. laevis* sperm, the disruption does not involve Pol I or replication stress. Centromere defects appear less severe in this hybrid reaction and can be fully rescued by addition of either species-matched or overexpressed CENP-A/HJURP and partially rescued by Pol II eviction, treatments that may reinforce epigenetic machineries that maintain centromeres. Thus, distinct mechanisms underlie centromere disruption in the

two inviable hybrids, but defects in both cases are consistent with observations that aberrant polymerase occupancy or transcription adjacent to the centromere can compromise its assembly (Rošić et al., 2014; Grenfell et al., 2016a; Bobkov et al., 2018).

An open question is how the incompatibilities we have characterized in vitro manifest in hybrid embryos in vivo. Whole genome sequencing of the *X. tropicalis* egg/*X. laevis* sperm hybrid just prior to embryo death combined with preliminary Hi-C analysis indicates that the long arms of chromosomes 3L and 4L have been largely eliminated, but the centromere persists on the short arm allowing it to be retained (Gibeaux et al., 2018). One possible explanation is that under-replication of repetitive sequences adjacent to the centromere in this hybrid initially disrupts centromere assembly, but after chromosome breakage, the adjacent, troublesome sequences are removed and the centromere stabilizes on the short arm while the long arm lacking the centromere frequently ends up in micronuclei and is eventually degraded. Because micronuclei are observed throughout embryogenesis in both inviable hybrids (Gibeaux et al., 2018), multiple rounds of chromosome mis-segregation and instability likely occur that give rise to the terminal karyotype. In the *X. tropicalis* egg/*X. borealis* sperm inviable hybrid that experiences replication stress, a pathway involving p97-mediated extraction and degradation of the replicative helicase that leads to fork breakage and microhomology-mediated end joining events likely operates, which has been well characterized in *Xenopus* egg extracts (Deng et al., 2019). Detailed genomic analysis of chromosome deletions and rearrangements in hybrid embryos will shed light on how replication-transcription conflicts give rise to specific chromosome defects, while additional in vitro experiments will reveal underlying molecular mechanisms.

Death of inviable *Xenopus* hybrids occurs at gastrulation when the zygotic genome undergoes widespread transcriptional activation, and the distinct death phenotypes observed upon fertilization of *X. tropicalis* eggs with either *X. laevis* or *X. borealis* sperm may be due to the different sets of genes affected by the loss of specific chromosomal loci. However, despite a reduction in micronuclei upon hybrid embryo treatments that rescued centromere formation in vitro, death was not delayed or the phenotypes altered in any way. Therefore, we hypothesize that other incompatibilities also contribute to hybrid inviability. In particular, mismatches between mitochondrial and nuclear-encoded genes have been shown to underlie inviability in some hybrids (Lee et al., 2008b; Ma et al., 2016).

In conclusion, our findings identify defects in epigenetic centromere maintenance that contribute to hybrid inviability. The combination of in vivo, in vitro, and genomic approaches possible in *Xenopus* promise to provide further mechanistic insights into the molecular basis of hybrid fates and speciation.

## 5.4 MATERIALS AND METHODS

### Lead Contact and Materials Availability

All data and materials are available upon request. Further information and requests for resources and reagents should be directed to Rebecca Heald ([bheald@berkeley.edu](mailto:bheald@berkeley.edu)).

### Experimental Model and Subject Details

All frogs were used and maintained in accordance with standards established by the UC Berkeley Animal Care and Use Committee and approved in our Animal Use Protocol. Mature *Xenopus laevis*, *X. tropicalis*, and *X. borealis* frogs were obtained from Nasco (Fort Atkinson, WI) or the National *Xenopus* Resource (Woods Hole, MA). *Xenopus* frogs were housed in a recirculating tank system with regularly monitored temperature and water quality (pH, conductivity, and nitrate/nitrite levels). *X. laevis* and *X. borealis* were housed at 20-23°C, and *X. tropicalis* were housed at 23-26°C. All animals were fed Nasco frog brittle.

### Chemicals

Unless otherwise states, all chemicals were purchased from Sigma-Aldrich, St. Louis, MO.

### Frog care

*X. laevis*, *X. tropicalis*, and *X. borealis* females were ovulated with no harm to the animals with a 6-, 3-, and 4-month rest interval, respectively, as previously described (Kitaoka et al., 2018). To obtain testes, males were euthanized by over-anesthesia through immersion in ddH<sub>2</sub>O containing 0.15% MS222 (Tricaine) neutralized with 5 mM sodium bicarbonate prior to dissection, and then frozen at -20°C.

### CENP-A ChIP-seq and data analysis

CENP-A MNase ChIP-seq was performed as previously described (Smith et al., 2021). Briefly, livers were extracted from adult *X. borealis* animals and flash frozen. Upon thawing, livers were diced on ice, rinsed in PBS, and buffer 1 (2.5 mM EDTA, 0.5 M EGTA, 15 mM Tris-HCl pH 7.4, 15 mM NaCl, 60 mM KCl, 15 mM sodium citrate 0.5 mM spermidine, 0.15 mM spermine, 340 mM sucrose, supplemented with 0.1 mM PMSF) was added and the tissue dounced using pestle A 12 times. A syringe with 18-gauge needle was backfilled with nuclei mixture and expelled into 2 mL tubes with additional buffer 1. Nuclei were spun at 6,000g for 5 min at 4°C, and washed 3 times with buffer 3 (2.5 mM EDTA, 0.5 M EGTA, 15 mM Tris-HCl pH 7.4, 15 mM NaCl, 60mM KCl, 15 mM sodium citrate 0.5 mM spermidine, 0.15 mM spermine, 340 mM sucrose, supplemented with 0.1 mM PMSF). Nuclei quality was checked and nuclei were counted by hemocytometer. ~5-10 million nuclei were used per IP reaction.

For MNase digestion, CaCl<sub>2</sub> was added to each reaction tube to 5 mM together with 300 U of MNase. Digestion was performed at RT for 30 min and reaction was quenched with 10 mM EDTA and 5 mM EGTA. Nuclei were lysed with 0.05% IGEPAL CA-630 in ice for 10 min. Following an initial spin 1,500g 5 min 4°C, the pellet was resuspended in 500 µL buffer 3 + 200 mM NaCl and rotated overnight at 4°C to extract mononucleosomes. Samples were precleared, input fractions were taken and CENP-A

mononucleosomes were isolated with 10 µg rabbit anti *X. laevis* CENP-A antibody prebound to protein A dynabeads in 200 µL TBST with rotation overnight at 4°C. Beads were washed and eluted, mononucleosomal DNA was isolated with Ampure beads, and sequencing libraries were prepared using NEBNext kit for Illumina sequencing which was performed on a NovaSeq instrument with paired end 150bp sequencing.

*X. laevis* and *X. tropicalis* CENP-A CHIP-seq datasets were used from previously described studies (Smith et al., 2021; Bredeson et al., 2021). CENP-A ChIP and Input libraries from each species were processed to identify CENP-A enriched *k*-mers using the *k*-mer counting pipeline that normalizes *k*-mer counts by sequencing depth of each library (<https://github.com/straightlab/xenla-cen-dna-paper>). For this study 25bp *k*-mers were used and kmc was run with ci=10, indicating that *k*-mers must be found 10 times in the dataset to be considered. This was chosen so that more *k*-mers were identified from each species to make comparisons more likely.

A phylogram was generated using a method similar to that previously described (Smith et al., 2021). From each species full length ChIP-seq reads were selected based on the presence of at least 80 CENP-A enriched *k*-mers. The reads from each species that met this criterion were then clustered by sequence similarity using cd-hit-est (Fu et al., 2012) using sequential rounds of clustering by 98%, 95%, and 90% identical by sequence. The 20 top clusters from each species were then selected for phylogram generation using Geneious (7.1.4) Tree Builder with the following settings: Genetic Distance Model=Tamura-Nei, Tree building method=Neighbor-joining, Outgroup=No outgroup, Alignment Type=Global alignment, Cost Matrix=93% similarity. Colors for each species were added manually.

### **Protein sequence alignments**

Multiple sequence alignments were performed using Clustal Omega (default parameters). Sequence similarities were determined by pair-wise alignments using EMBOSS Needle (default parameters).

### ***Xenopus* egg extracts**

*X. tropicalis* metaphase-arrested egg extracts and spindle reactions were prepared as previously described (Hannak and Heald, 2006; Brown et al., 2007; Maresca and Heald, 2006). Briefly, freshly laid, metaphase II-arrested eggs were collected, dejellied, packed and crushed by centrifugation. The cytoplasmic layer was collected with a syringe and 18G needle, then supplemented with 10 µg/mL of leupeptin, pepstatin, and chymostatin (LPC), 20 µM of cytochalasin B, and energy mix (3.75 µM creatine phosphate, 0.5 µM ATP, 0.5 µM MgCl<sub>2</sub>, 0.05 µM EGTA). Typical reactions contained 20 µL CSF extract, sperm nuclei at a final concentration of 500 nuclei/µL, and rhodamine-labeled porcine brain tubulin at a final concentration of 50 µg/mL.

### **Chromosome immunofluorescence**

Spindle reactions were prepared, spun-down, and processed for immunofluorescence as previously described (Hannak and Heald, 2006; Maresca and Heald, 2006). Briefly, the extract reactions were fixed for 5-10 min with 2% formaldehyde and spun down at 5,500 rpm (5821.9 x g) for 20 min at 16°C. The coverslips were incubated for 30 s in cold methanol, washed in PBS + 0.1% NP40, and blocked overnight in PBS + 3% BSA at 4°C.

We used rabbit anti-xCENPA, 1:500 (Milks et al., 2009; Moree et al., 2011), mouse anti-myc (9E10 clone, 1:500), rabbit anti-POLR1A (Novus Biologicals, 1:500), and mouse anti-UBTF (Abnova, 1:500) antibodies. Primary antibodies were added for 1 h in PBS + 3% BSA. After washing with PBS + 0.1% NP40, the coverslips were incubated with 1:1000 anti-rabbit or mouse secondary antibodies coupled to Alexa Fluor 488 or 568 (Invitrogen), respectively, for 30 min and then with 1:1000 Hoechst (Invitrogen) for 5 min. The coverslips were then washed and mounted for imaging with Vectashield (Vector Labs). Each presented dataset was obtained from three independent egg extracts.

### **Nuclear DNA FISH for FCR centromeric sequences**

Nuclear DNA FISH using probes against various FCR monomers was performed as previously described (Smith et al., 2021). Briefly, pJET1.2 plasmids containing 150 bp FCR monomer sequences were PCR-amplified and fluorescently labeled using random hexamer priming and Klenow (exo-) polymerase (New England Biolabs). Both Alexa Fluor 488 and 568 dUTP-conjugated fluorophores were used. Probes were desalted to remove unincorporated nucleotides, then precipitated and cleaned before resuspension in hybridization buffer (65% formamide, 5X SSC, 5X Denhardtts with 1% blocking reagent (Roche), 0.5 mg/mL salmon sperm DNA added fresh). Each experiment used 4 uL of probe mixed with 4 uL of hybridization buffer.

Nuclei were assembled in egg extract, spun down onto coverslips, and probed with CENP-A antibody as previously described in (Levy and Heald, 2010) and detailed above. Samples proceeded to FISH by fixation in 2.5% formaldehyde in PBS for 10 min, washed in PBS, and dehydrated with increasing concentrations of 70-100% ice-cold ethanol. Coverslips were blocked for 30 min in hybridization buffer. Probes were warmed and mixed with hybridization buffer before being added to samples, flipping coverslips onto glass slides for hybridization. These “sandwiches” were incubated at 80°C for 10 min, then incubated overnight at 37°C. Coverslips were removed from glass slides carefully with 4X SSC, washed thoroughly in SSC, stained with Hoechst and mounted with Vectashield (Vector Labs).

### **Protein expression in reticulocyte lysate**

To generate plasmids for expression of species-specific *X. laevis*, *X. tropicalis*, and *X. borealis* CENP-A, total RNA was isolated from stage 9 embryos. Embryos were homogenized mechanically in TRIzol (Thermo Fisher Scientific) using up to a 30-gauge needle and processed according to manufacturer’s instructions. After resuspension in nuclease-free H<sub>2</sub>O, RNAs were cleaned using a RNeasy kit (Qiagen) according to manufacturer’s instructions, and cDNA was synthesized using the SuperScript III First Strand Synthesis system (Thermo Fisher Scientific) according to the manufacturer’s instructions. The *X. laevis*, *X. tropicalis*, and *X. borealis* CENP-A sequences were then PCR-amplified from the cDNA. The amplified sequence was then subcloned into a pCS2+ vector using Gibson assembly. The constructs were then amplified using XL1-Blue competent *E. coli* (Agilent).

The TnT Sp6-coupled rabbit reticulocyte system (Promega) was used for in vitro transcription/translation (IVT) of plasmid DNA according to the manufacturer’s protocol. 2-10% of the final egg extract reaction volume was added prior to addition of sperm nuclei; for CENP-A, this corresponds to 8-80 times endogenous protein levels.

## Western blots

Increasing volumes of egg extracts and reticulocyte lysate were subject to SDS-PAGE and wet transferred to PVDF membranes. Blots were blocked with PBS + 0.1% Tween + 5% milk for 1 h, probed with primary antibodies diluted in PBS + 0.1% Tween + 5% milk for 1 h, rinsed 3x over a 10 m period with PBS + 0.1% Tween, then probed with secondary antibodies (Rockland Immunochemicals; goat anti-rabbit DyLight 800 and donkey anti-mouse DyLight 680, 1:10,000) diluted in PBS + 0.1% Tween for 30 m. Blots were scanned on an Odyssey Infrared Imaging System (Li-Cor Biosciences). Band intensities were quantified using FIJI.

## Drug treatments

*X. tropicalis* extract was supplemented with the following drugs and concentrations: Aphidicolin (DNA replication inhibitor, 10 µg/mL), BMH-21 (RNA Polymerase I inhibitor, 1 µM), NMS-873 (p97 inhibitor, 10 µM), MLN-8237 (Aurora A inhibitor, 1 µM, Selleck Chemicals), BI-2536 (Polo kinase 1 inhibitor, 1 µM, Selleck Chemicals), Triptolide (RNA Polymerase II inhibitor, 25 µM)

## Chromosome and nuclei imaging

Chromosomes were imaged using Micromanager 1.4 software (Edelstein et al., 2014) and nuclei were imaged using Olympus cellSens Dimension 2 software on an upright Olympus BX51 microscope equipped with an ORCA-ER or ORCA-Spark camera (Hamamatsu Photonics) and Olympus UPlan 60X/NA 1.42 oil objective. All images across all datasets were taken using the same exposure settings.

## In vitro fertilization and cross-fertilizations

In vitro fertilization and cross-fertilizations were performed as previously described (Gibeaux et al., 2018; Gibeaux and Heald, 2019; Kitaoka et al., 2018). *X. laevis*, *X. borealis*, and *X. tropicalis* males were injected with 500, 300, and 250 U, respectively, of human chorionic gonadotropin hormone (hCG) 12-24 h before dissection. Testes were collected in Leibovitz L-15 Medium (Gibco, Thermo Fisher Scientific) supplemented with 10% fetal bovine serum (FBS; Gibco) for immediate use. *X. tropicalis* females were primed with 10 U of hCG 12-18 h before use and boosted with 250 U of hCG on the day of the experiment. As soon as the first eggs were laid (~3 h after boosting), the male was euthanized and dissected. Two *X. tropicalis* testes or one *X. laevis* or *X. borealis* testis were added to 1 mL of L-15 + 10% FBS. *X. tropicalis* females were squeezed gently to deposit eggs onto glass Petri dishes (Corning) coated with 1.5% agarose in 1/10X MMR (1X MMR: 100 mM NaCl, 2 mM KCl, 2 mM CaCl<sub>2</sub>, 1 mM MgSO<sub>4</sub>, 0.1 mM EDTA, 5 mM HEPES-NaOH pH 7.6) Testes were homogenized using a pestle in L-15 + 10% FBS to create sperm solution. Any liquid in the Petri dishes was removed, and the eggs were fertilized with 500 µL of sperm solution per dish. Eggs were swirled in the solution to separate them and incubated for 5 min with the dish slanted. Dishes were flooded with ddH<sub>2</sub>O and incubated for 10 min. ddH<sub>2</sub>O was exchanged for 1/10X MMR and incubated for 10 min. The jelly coats were removed with a 3% cysteine solution (in ddH<sub>2</sub>O-NaOH, pH 7.8). After extensive washing with 1/10X MMR (at least four times), embryos were incubated at 23°C until the first cleavage at 1 hour post fertilization (hpf). Fertilized



embryos were then sorted and placed in a mesh-bottomed dish for microinjection as described below.

### **Embryo microinjection**

At stage 2 (2-cell embryo), embryos were transferred to a 1/9X MMR + 3% Ficoll. IVT reticulocyte lysate was backloaded into a needle pulled from a 1 mm glass capillary tube (TW 100F-4, World Precision Instruments) using a P-87 Micropipette Puller (Sutter Instrument). Embryos were placed in a mesh-bottomed dish and microinjected in both blastomeres with 2 nL of the IVT reticulocyte lysate using a Picospritzer III microinjection system (Parker) equipped with a MM-3 micromanipulator (Narishige). Injected embryos were transferred to a new dish and incubated at 23°C in 1/9X + 3% Ficoll for several hours, then buffer exchanged for 1/10X MMR overnight.

### **Embryo video imaging**

Imaging dishes were prepared using an in-house PDMS mold designed to print a pattern of 0.9 mm large wells in agarose that allowed us to image six *X. tropicalis* embryos simultaneously within the 3 mm x 4 mm camera field of view for each condition. Embryos were imaged from stage 3 after microinjection. Treatment and control videos were taken simultaneously using two AmScope MD200 USB cameras (AmScope), each mounted on an AmScope stereoscope. Time-lapse movies were acquired at a frequency of one frame every 10 s for 20 h and saved as Motion JPEG using a Matlab (The MathWorks) script. Movie post-processing (cropping, concatenation, resizing, and addition of scale bar) was done using Matlab and FIJI (Schindelin et al., 2012). All Matlab scripts written for this study are available upon request. Two of the scripts used here were obtained through the MATLAB Central File Exchange: 'videoMultiCrop' and 'concatVideo2D' by 'Nikolay S'.

### **Embryo whole-mount immunofluorescence**

Embryos were fixed at the desired stages for 1-3 h using MAD fixative (2:2:1 methanol: acetone: DMSO). After fixation, embryos were dehydrated in methanol and stored at -20°C. Embryos were then processed for immunofluorescence as previously described (Gibeaux et al., 2018). Briefly, embryos were gradually rehydrated in 0.5X SSC (1X SSC: 150 mM NaCl, 15 mM Na citrate, pH 7.0), then bleached with 2% H<sub>2</sub>O<sub>2</sub> in 0.5X SSC with 5% formamide for 2 h under light. Embryos were washed with PBT (1X PBS, 0.1% Triton X-100, 2 mg/mL bovine serum albumin). Embryos were blocked in PBT supplemented with 10% goat serum and 5% DMSO for 1-3 h and incubated overnight at 4°C in PBT supplemented with 10% goat serum and primary antibodies. We used mouse anti-beta-tubulin (E7, Developmental Studies Hybridoma Bank, 1:300 dilution) and rabbit anti-histone H3 (Abcam, 1:500 dilution). Embryos were then washed 4 x 2 h in PBT and incubated overnight at 4°C in PBT supplemented with goat anti-mouse and goat anti-rabbit secondary antibodies coupled to Alexa Fluor 488 and 568 (Invitrogen). Embryos were then washed 4 x 2 h in PBT and gradually dehydrated in methanol. Finally, embryos were cleared in Murray's clearing medium (2:1 benzyl benzoate: benzyl alcohol). Embryos were placed in a reusable chamber (Thermo Fisher) for confocal microscopy.

### **Confocal microscopy**

Confocal microscopy was performed on an inverted Zeiss LSM 800 using the Zeiss Zen software, a Plan-Achromat 20X/0.8 air objective and laser power 0.5-2%, on multiple 1024x1024 pixel plans spaced of 0.68  $\mu\text{m}$  in Z. Images are mean averages of two scans with a depth of 16 bits. Pinhole size always corresponded to 1 Airy unit.

### **Quantification and Statistical Analysis**

Quantification of CENP-A localization on mitotic chromosomes was determined manually in a dataset of 100 images from one extract. Quantification of ultra-thin chromosomal regions was also determined manually in parallel from the same datasets. Only single chromosomes were counted. Each dataset had ~150-400 chromosomes. The average of each extract was calculated as a percentage of total chromosome number. Averages were plotted in Matlab, and statistical significance and p-values were determined with two-tailed, two-sample unequal variance t-tests or one-way ANOVA with Tukey post-hoc analysis in Microsoft Excel. The number of egg extracts used, individual chromosomes counted, and p-values are listed in the figure legends. For all box plots, the thick line inside the box indicates the average across biological replicates, and the upper and lower box boundaries indicate the standard deviation.

PolR1A and UBF fluorescent intensity on *X. borealis* ultra-thin chromosomes were quantified in FIJI by measuring the intensity of the stretched region specifically and comparing it to a random non-stretched region on the same chromosome. All intensity measurements were normalized to the samples' Hoechst intensity.

Micronuclei in embryos were quantified at the relevant stages as the number of observed micronuclei divided by the number of nuclei, counted manually in FIJI. Statistical significance was determined by two-tailed, two-sample unequal variance t-tests.

## **ACKNOWLEDGEMENTS**

We thank Daniel Rokshar, Austin Mudd, Sofia Medina-Ruiz, and Mariko Kondo for early access to *X. borealis* CENP-A, CENP-C, HJURP, and H3 sequences. We also thank students Elizabeth Turcotte, Costa Bartolutti, Justin Peng, and Christian Erikson for help with experiments to MK. We are grateful to the Welch, King, Dernberg, Karpen, Lewis, and Rokshar laboratories at UC Berkeley for sharing reagents, discussions, and expertise. We thank all past and present members of the Heald laboratory, Coral Y. Zhou, Gary Karpen, Dirk Hockemeyer, Rasmus Nielsen, and Mark J. Khoury for continuous support and fruitful discussions. M.K. was supported by a National Science Foundation (NSF) GRFP fellowship. O.K.S. was supported by a National Institutes of Health (NIH) T32 GM113854-02 and an NSF GRFP fellowship. A.F.S. was supported by NIH NIGMS R01 GM074728. R.H. was supported by NIH MIRA grant R35 GM118183 and the Flora Lamson Hewlett Chair.

## **AUTHOR CONTRIBUTIONS**

Conceptualization, Funding acquisition: RH, MK  
Methodology, Investigation, Visualization: MK, OKS  
Supervision: AFS, RH  
Manuscript preparation: MK, RH, OKS, AFS

## **DECLARATION OF INTERESTS**

The authors declare no competing interests.

## Chapter 6: Conclusions

*Xenopus* frog systems stand out as the ideal system to investigate a wide variety of biological questions, ranging from spindle assembly and size scaling to speciation. The combination of in vitro cytoplasmic extracts and in vivo embryos create a versatile biological and evolutionary toolbox with unparalleled access to probe cellular dynamics and potential mismatches in a vertebrate system. Throughout this work, we have seen species-specific mechanisms in play around the central theme of cell division, some which are more conserved than others. My thesis research highlights the importance of conducting comparative studies with various species to understand fundamental mechanisms that not only provide insight into speciation and reproductive isolation but also demonstrate the evolutionary divergence of highly conserved and essential processes.

How does the architecture of the mitotic spindle contribute to its essential and conserved function of faithfully segregating chromosomes? We discover that even closely related *Xenopus* species have unique microtubule distributions across the length of the spindle from pole-to-pole, even though they share size scaling mechanisms (Chapter 2). How do specific microtubule associated proteins, like TPX2 and katanin, that create unique spindle shapes, sizes, and organization lend themselves to optimize spindle function? One approach would be to compare many more frog species' spindles to find patterns that predict spindle architecture by examining sequence divergence, expression levels, and additional mechanisms. Adapting new techniques that allow us to see more deeply and clearly into the dense microtubule networks will also be a valuable avenue to explore. We took inspiration from others to adapt expansion microscopy for the cell-free extract system (Chapter 3). In combination with the biochemical power of the egg extract, the increased resolution from expansion microscopy promises to provide a window into the complex and dense organizational network of microtubules and associated proteins in the spindle, allowing us to understand how unique architectures form and function across cell types, sizes, and species.

Why is there such a variety of spindle structures and divergence of cell division components, like the centromere, across species, especially given the universal function and importance of cell division in early embryogenesis and organismal viability? It is tempting to speculate that this provides a selfish, chromosome-based mechanism to generate post-zygotic speciation barriers against hybridization events between species. We discovered several cell biological and genomic consequences of chromosome/centromere mismatches in inviable hybrids (Chapter 4-5), but many further questions follow.

How do incompatibility mechanisms manifest in hybrid embryos, and what other mechanisms underlie hybrid inviability and chromosomal defects? We showed that while the *X. tropicalis/X. borealis* hybrid does not suffer from metabolic crisis, the *X. tropicalis/X. laevis* hybrid has dramatic losses of key metabolic intermediates and TCA cycle components, such as lactic acid, pyruvate, and citrate, strongly suggesting mis-regulation

of cellular respiration and mitochondrial function (Chapter 4). Various studies have pointed to mitochondrial-nuclear mismatches as driving incompatibility between species (Lee et al., 2008b; Jhuang et al., 2017; Chou et al., 2010; Meiklejohn et al., 2013; Moran et al., 2021). While the mitochondrial genome is very small compared to its nuclear counterpart, encoding only 13 genes, many components required for mitochondrial function are encoded by and require coordination between both genomes (Friedman and Nunnari, 2014). This generates the potential for mutations or evolutionary divergence in either genome to cause incompatibilities that decrease fitness and function. Mitochondrial morphology undergoes several changes throughout development as it adapts to the changing needs of the developing organism and is thought to reflect the function and fate of cell types, with fission-fusion cycles dictating the transition between sheet-like and tubular morphology to regulate cellular respiration, ATP production, calcium homeostasis, and apoptosis (Friedman and Nunnari, 2014). It is possible that the *X. tropicalis* egg mitochondria cannot support *X. laevis* or *X. borealis* nuclei in part due to mito-nuclear conflicts. It will be interesting to observe mitochondrial dynamics and morphology in hybrid and pure species embryos to further understand underlying mismatches and malfunctions. Additionally, inviable *Xenopus* hybrids die as the zygotic genome begins to activate. They suffer unique deaths (i.e., explosive cellular lysis vs. exogastrulation) that do not seem to share metabolic or developmental pathways. It will be of particular interest to characterize genes on the affected chromosomes in each hybrid, and determine how gene dosage and/or compensation affects hybrid embryo lethality. By combining classical *Xenopus* embryology techniques with high resolution imaging and genomic methods, such as long-read genome and RNA sequencing, we can begin to understand the developmental regulation and consequences of hybrid inviability.

One exciting discovery from this work is that hybrid incompatibility stems from repetitive sequences in the genome (Chapter 5), in line with increasing evidence that the chromatin environment is important for hybridization outcomes (Jagannathan and Yamashita, 2021). Despite their close relationship in evolution and origin from the same ancient interspecies hybridization event (Session et al., 2016), *X. laevis* and *X. borealis* paternal genomes experience distinct chromosomal defects when hybridized with *X. tropicalis*. However, centromeric localization of CENP-A is lost in both species, and rDNA is additionally affected in *X. borealis* chromosomes. Centromeres and rDNA make up the two most repetitive regions of the genome, and share several characteristics, such as their larger size and late replication timing (Gómez-González and Aguilera, 2019). Centromere sequences and associated proteins are extremely divergent and rapidly evolving (Henikoff et al., 2001; Malik and Henikoff, 2001). On the other hand, the rDNA sequence is among the most conserved in the genome, leading non-coding regions and transcriptional machinery to diverge instead (Bell et al., 1989). Our results highlight the vulnerability of these key regions in hybrids, and we speculate that these repetitive elements create domains within the nucleus that are somehow disrupted in hybrids.

The identification of rDNA as a specific affected region of *X. borealis* chromosomes in *X. tropicalis* cytoplasm opens more questions and future directions about the regulation of rDNA in these inviable hybrids. rDNA encodes the components of protein-producing ribosomes, and is present in multiple copies across multiple organisms in one or more

repetitive arrays (Long and Dawid, 1980). Expression of rRNA is considered a vitally important mechanism to control the energy expenditure of the cell, as it can control how much protein is translated for cellular functions (Murayama et al., 2008). Chromosome banding studies have showed that the rDNA arrays can map to single (*Xenopus*) or multiple (human) chromosomes (Long and Dawid, 1980; Schmid and Steinlein, 1991; Henderson et al., 1972), and cluster together to form nucleolar organizer regions (NORs), which support dynamic production and maintenance of the loci, including transcription, processing, and protein synthesis (Bell et al., 1989; Roussel et al., 1996).

Nucleolar dominance was originally discovered in interspecies hybrids, notably the viable crosses of *X. laevis* and *X. borealis* (Honjo and Reeder, 1973; Cassidy and Blackler, 1974) as well as other hybrids (Durica and Krider, 1977; Chen et al., 1998). The phenomenon occurs when rDNA loci are preferentially expressed from only one parental species and the loci from the other species is actively silenced throughout embryogenesis and in adult tissues. In the case of *Xenopus* hybrids between *X. laevis* and *X. borealis*, *X. laevis* rDNA is always preferentially expressed regardless of which species is maternal. *X. borealis* rDNA is only expressed if it is the singular source of rDNA in the hybrid, i.e., the *X. laevis* parent does not contribute any rDNA (Honjo and Reeder, 1973). The two species' rDNA sequences have minimal divergence, but dominance has been attributed to increased enhancer copy numbers at the promoter in the *X. laevis* array, potentially allowing more transcription factor binding and polymerase complex activation (Reeder and Roan, 1984; Miesfeld and Arnheim, 1984). Additionally, it has been proposed that the *X. laevis* promoter sequence functions well with *X. borealis* transcriptional machinery, but the reverse is not true as *X. borealis* rRNA expression is slow to activate even without any competing *X. laevis* rDNA (Honjo and Reeder, 1973; Reeder and Roan, 1984). Interestingly, adult somatic cells possess only one nucleolus per nucleus instead of the expected two (Michalak et al., 2015), but hybrids from *X. laevis* and *X. borealis* are viable and fertile in both directions, so it is unclear how the number of nucleoli reflect the regulation of rRNA expression and function in hybrids.

Nucleolar dominance can also occur within a species, which regulates rRNA expression and dosage (Warsinger-Pepe et al., 2020). For example, only a subset of NORs are expressed in humans (Roussel et al., 1996). It remains unclear how or why specific rDNA loci are silenced or activated, though there appears to be a threshold that cells can sense to upregulate expression, such as when rDNA repeats have diminished and undergo amplification to restore copy number in the germline (Lu et al., 2018).

Previous investigations of nucleolar dominance with *Xenopus* hybrids have yet to use *X. tropicalis* as either the maternal or paternal species. Do *X. tropicalis* sperm-based viable hybrids demonstrate similar signatures of nucleolar dominance? Do inviable hybrids show nucleolar dominance or other mis-regulation at rDNA? Do these defects stem specifically from replication-transcription conflicts as a result of mismatched polymerase machinery? How might these connect or interact with the centromeric defects seen in inviable hybrids? Preliminary data from my thesis research suggests that the domains containing rDNA and centromeres are not yet organized in the first cell cycle, though this organization emerges as the embryo reaches and passes zygotic genome

activation. However, previous work has suggested the presence of nucleolar-centromeric interactions that affect the transcriptional output from both genomic regions (Ochs and Press, 1992; Wong et al., 2007; Bury et al., 2020). In addition, it is clear that the *X. borealis* chromosomes that show a centromeric defect are different from the ones with ultra-thin rDNA regions, suggesting that there may be a mechanism where the two genomic regions interact negatively in interphase and lead to their mitotic chromosome defects. Despite the lack of rDNA transcription and nucleolar domain formation in egg extract, combining egg extracts with various DNA sources that have already established NORs and nucleoli will allow for more carefully controlled manipulation and dissection of the underlying molecular mechanisms involved in rDNA regulation, dynamics, and disruption due to hybridization and incompatibility. Investigation of the surrounding chromatin environment, including heterochromatic domain formation, in a hybrid context will complement the existing work done in *Drosophila*, where specific satellite DNA-protein interactions are required for chromocenter formation and appropriate clustering of chromosomes (Jagannathan et al., 2018). Disruption of these interactions lead to micronuclei formation and cell death in the germline, leading to hybrid sterility (Jagannathan and Yamashita, 2021).

Importantly, it is still unclear why distinct subsets of specific chromosomes are affected in inviable hybrids, while others appear unperturbed. Species-specificity of centromere assembly factors alone does not explain this phenomenon. Why can *X. tropicalis* cytoplasm support centromere formation on all *X. laevis* or *X. borealis* paternal chromosomes except for the 2-4 affected ones? At least in the case of the affected *X. laevis* 3L and 4L chromosomes, it is clear that they do not possess unique centromeric features that distinguish them from the other 16 *X. laevis* chromosomes (Smith et al., 2021). We speculate that this is likely true for *X. borealis* chromosomes as well, though further genomic analysis and mapping of the core centromeric sequences to an *X. borealis* genome assembly will provide more clarity. In addition, we still do not fully understand the fate of these mis-segregated chromosomes and how the terminal hybrid karyotype is reached. Preliminary data from chromosome conformation capture (Hi-C) of inviable hybrids revealed that the long arms of *X. laevis* 3L and 4L are completely lost, likely through micronuclei formation and chromothripsis (Crasta et al., 2012; Zhang et al., 2015), but the remaining short arms still maintain the centromeric DNA. Most micronuclei and lagging chromosomes in hybrid embryos are acentric and lack CENP-A foci, and only ~10% of cells contain micronuclei (Gibeaux et al., 2018; Kitaoka et al., 2022). This suggests a mechanism where the centromere on the affected chromosomes is reactivated once the “problematic” region adjacent to it is broken. We require a deeper understanding of the mechanisms at play underlying chromosome fragility coupled with a chromosome-level knowledge of the underlying genomic architecture and sequence organization to probe the mystery of chromosome-specific defects in hybrids.

Throughout this work, we have been limited by the lack of *X. borealis* genomic data. Therefore, we began to generate long-read PacBio and Bionano genomic sequencing reads that will be used to assemble the first *X. borealis* genome. Our goal is to provide this resource to the broader *Xenopus* community, as many current studies are hampered by the inability to access and use large genomic datasets despite advances in

other technologies. We hope to ask further detailed questions about the genomic architecture and evolution of *Xenopus* frog species. In particular, we are interested in asking what changes occur in inviable hybrids, such as chromosomal deletions and rearrangements, that lead to the terminal karyotype with loss of specific paternal DNA, and how these are connected to the mechanisms already uncovered (Chapters 4-5). We expect these studies to shed light on the molecular mechanisms occurring during hybridization and their role in genome and organismal evolution.

My thesis work has demonstrated the power of the *Xenopus* egg extract in vitro system as a powerful cell biological system capable of recapitulating cell cycle dynamics, scaling, and novel hybrid incompatibility mechanisms (Chapters 2-5). In addition, it will likely serve as a useful system to examine what happens when these mechanisms are challenged. My thesis has taken advantage of three *Xenopus* species to create various hybrids that can address a wide range of questions surrounding speciation. Viable *Xenopus* hybrids have been used to understand size scaling and zygotic genome activation mechanisms (Gibeaux, Miller et al., 2018; Jukam et al., 2021), and more detailed study of *X. laevis*/*X. borealis* hybrids could shed further light on the definition of species by understanding their physiology, cell biology, and genomic architecture. The inviable *Xenopus* hybrids are extremely unique in that hybrid death occurs before the F1 generation can reach gastrulation, let alone adulthood. While this does not allow for detailed genetic studies across generations, it provides a powerful cell biological, developmental, and evolutionary lens to examine specific mechanistic mismatches during early embryogenesis (Gibeaux et al., 2018; Kitaoka et al., 2022). Future studies that combine these approaches with high quality, long read genome assemblies to uncover chromosomal consequences will shed light on these questions. Thus, *Xenopus* species and hybrids promise to reveal novel insights into size scaling, speciation, hybrid incompatibility, and cell division dynamics.



## References

- Akiyoshi, B., and K. Gull. 2014. Discovery of unconventional kinetochores in kinetoplastids. *Cell*. 156:1247–1258. doi:10.1016/j.cell.2014.01.049.
- Alfaro-Aco, R., A. Thawani, and S. Petry. 2017. Structural analysis of the role of TPX2 in branching microtubule nucleation. *J. Cell Biol.* 216:983–997. doi:10.1083/jcb.201607060.
- Anselm, E., A.W. Thomae, A.A. Jeyaprakash, and P. Heun. 2018. Oligomerization of Drosophila Nucleoplasmin-Like Protein is required for its centromere localization. *Nucleic Acids Res.* 46:11274–11286. doi:10.1093/nar/gky988.
- Baudat, F., J. Buard, C. Grey, A. Fledel-Alon, C. Ober, M. Przeworski, G. Coop, and B. de Massy. 2009. PRDM9 is a Major Determinant of Meiotic Recombination Hotspots in Humans and Mice. *Science (80-. ).* 327:836–840. doi:10.1002/da.22291.
- Bell, P., C. Mais, B. McStay, and U. Scheer. 1997. Association of the nucleolar transcription factor UBF with the transcriptionally inactive rRNA genes of pronuclei and early *Xenopus* embryos. *J. Cell Sci.* 110:2053–2063.
- Bell, P., and U. Scheer. 1997. Prenucleolar bodies contain coilin and are assembled in *Xenopus* egg extract depleted of specific nucleolar proteins and U3 RNA. *J. Cell Sci.* 110:43–54. doi:10.1242/jcs.110.1.43.
- Bell, S.P., C.S. Pikaard, R.H. Reeder, and R. Tjian. 1989. Molecular mechanisms governing species-specific transcription of ribosomal RNA. *Cell*. 59:489–497. doi:10.1016/0092-8674(89)90032-9.
- Bernad, R., P. Sánchez, T. Rivera, M. Rodríguez-Corsino, E. Boyarchuk, I. Vassias, D. Ray-Gallet, A. Arnaoutov, M. Dasso, G. Almouzni, and A. Losada. 2011. *Xenopus* HJURP and condensin II are required for CENP-A assembly. *J. Cell Biol.* 192:569–582. doi:10.1083/jcb.201005136.
- Blow, J.J., and R.A. Laskey. 1986. Initiation of DNA replication in nuclei and purified DNA by a cell-free extract of *Xenopus* eggs. *Cell*. 47:577–587. doi:10.1016/0092-8674(86)90622-7.
- Blower, M.D., E. Feric, K. Weis, and R. Heald. 2007. Genome-wide analysis demonstrates conserved localization of messenger RNAs to mitotic microtubules. *J. Cell Biol.* 179:1365–1373. doi:10.1083/jcb.200705163.
- Blum, J.A., S. Bonaccorsi, M. Marzullo, V. Palumbo, Y.M. Yamashita, D.A. Barbash, and M. Gatti. 2017. The Hybrid Incompatibility Genes Lhr and Hmr Are Required for Sister Chromatid Detachment During Anaphase but Not for Centromere Function. *Genetics*. 207:1457–1472. doi:10.1534/genetics.117.300390/-/DC1.1.
- Bobkov, G.O.M., N. Gilbert, and P. Heun. 2018. Centromere transcription allows CENP-A to transit from chromatin association to stable incorporation. *J. Cell Biol.* 217:1957–1972. doi:10.1083/jcb.201611087.
- Brändle, F., B. Frühbauer, and M. Jagannathan. 2022. Principles and functions of pericentromeric satellite DNA clustering into chromocenters. *Semin. Cell Dev. Biol.* doi:10.1016/j.semcdb.2022.02.005.
- Bredeson, J. V., A.B. Mudd, S. Medina-Ruiz, T. Mitros, O.K. Smith, K.E. Miller, J.B. Lyons, S.S. Batra, J. Park, K.C. Berkoff, C. Plott, J. Grimwood, J. Schmutz, G. Aguirre-Figueroa, M.K. Khokha, M. Lane, I. Philipp, M. Laslo, J. Hanken, G.

- Kerdivel, N. Buisine, L.M. Sachs, D.R. Buchholz, T. Kwon, H. Smith-Parker, M. Gridi-Papp, M.J. Ryan, R.D. Denton, J.H. Malone, J.B. Wallingford, A.F. Straight, R. Heald, D. Hockemeyer, R.M. Harland, and D.S. Rokhsar. 2021. Conserved chromatin and repetitive patterns reveal slow genome evolution in frogs. *bioRxiv*. 2021.10.18.464293.
- Brown, D.D., I.B. Dawid, and R.H. Reeder. 1977. *Xenopus borealis* misidentified as *Xenopus mulleri*. *Dev. Biol.* 59:266–267. doi:10.1016/0012-1606(77)90263-9.
- Brown, D.D., and K. Sugimoto. 1973. The Structure and Evolution of Ribosomal and 5 S DNAs in *Xenopus laevis* and *Xenopus mulleri*. *Cold Spring Harb. Symp. Quant. Biol.* 38:501–5.
- Brown, D.D., P.C. Wensink, and E. Jordan. 1972. A comparison of the ribosomal DNA's of *Xenopus laevis* and *Xenopus mulleri*: the evolution of tandem genes. *J. Mol. Biol.* 63:57–73.
- Brown, K.S., M.D. Blower, T.J. Maresca, T.C. Grammer, R.M. Harland, and R. Heald. 2007. *Xenopus tropicalis* egg extracts provide insight into scaling of the mitotic spindle. *J. Cell Biol.* 176:765–70. doi:10.1083/jcb.200610043.
- Bürki, E. 1985. The expression of creatine kinase isozymes in *Xenopus tropicalis*, *Xenopus laevis laevis*, and their viable hybrid. *Biochem. Genet.* 23:73–88. doi:10.1007/BF00499114.
- Bury, L., B. Moodie, L.S. McKay, K.H. Miga, and I.M. Cheeseman. 2020. Alpha-satellite RNA transcripts are repressed by centromere-nucleolus associations. *bioRxiv*. 9:e59770. doi:DOI: <https://doi.org/10.7554/eLife.59770>.
- Carroll, C.W., K.J. Milks, and A.F. Straight. 2010. Dual recognition of CENP-A nucleosomes is required for centromere assembly. *J. Cell Biol.* 189:1143–1155. doi:10.1083/jcb.201001013.
- Carroll, C.W., M.C.C. Silva, K.M. Godek, L.E.T. Jansen, and A.F. Straight. 2009. Centromere assembly requires the direct recognition of CENP-A nucleosomes by CENP-N. *Nat. Cell Biol.* 11:896–902. doi:10.1038/ncb1899.
- Cassidy, D.M., and A.W. Blackler. 1974. Repression of nucleolar organizer activity in an interspecific hybrid of the genus *Xenopus*. *Dev. Biol.* 41:84–96. doi:10.1016/0012-1606(74)90285-1.
- Cavazza, T., and I. Vernos. 2016. The RanGTP Pathway: From Nucleo-Cytoplasmic Transport to Spindle Assembly and Beyond. *Front. Cell Dev. Biol.* 3:82. doi:10.3389/fcell.2015.00082.
- Chang, H., J. Wang, Y. Tian, J. Xu, X. Gou, and J. Cheng. 2012. The TPX2 gene is a promising diagnostic and therapeutic target for cervical cancer. *Oncol. Rep.* 27:1353–1359. doi:10.3892/or.2012.1668.
- Chang, P., M.K. Jacobson, and T.J. Mitchison. 2004. Poly(ADP-ribose) is required for spindle assembly and structure. *Nature.* 432:645–649. doi:10.1038/nature03061.
- Cheeseman, I.M. 2014. The Kinetochore. *Cold Spring Harb. Perspect. Biol.* 6:1–19. doi:10.1007/978-0-387-69076-6.
- Chen, C.C., M.L. Dechassa, E. Bettini, M.B. Ledoux, C. Belisario, P. Heun, K. Luger, and B.G. Mellone. 2014. CAL1 is the *Drosophila* CENP-A assembly factor. *J. Cell Biol.* 204:313–329. doi:10.1083/jcb.201305036.
- Chen, F., P.W. Tillberg, and E.S. Boyden. 2015. Expansion microscopy. *Science (80-. ).* 347:543–548. doi:10.1126/science.1260088.

- Chen, J., L. Comai, and C.S. Pikaard. 1998. Gene dosage and stochastic effects determine the severity and direction of uniparental ribosomal RNA gene silencing (nucleolar dominance) in *Arabidopsis* allopolyploids. *Proc. Natl. Acad. Sci. U. S. A.* 95:14891–14896. doi:10.1073/pnas.95.25.14891.
- Chittori, S., J. Hong, H. Saunders, H. Feng, R. Ghirlando, A.E. Kelly, Y. Bai, and S. Subramaniam. 2018. Structural mechanisms of centromeric nucleosome recognition by the kinetochore protein CENP-N. *Science (80-. )*. 359:339–343. doi:10.1126/science.aar2781.
- Chou, J., Y. Hung, K. Lin, H. Lee, and J. Leu. 2010. Multiple Molecular Mechanisms Cause Reproductive Isolation between Three Yeast Species. *PLoS Biol.* 8:e1000432. doi:10.1371/journal.pbio.1000432.
- Chozinski, T.J., A.R. Halpern, H. Okawa, H.-J. Kim, G.J. Tremel, R.O.L. Wong, and J.C. Vaughan. 2016. Expansion microscopy with conventional antibodies and fluorescent proteins. *Nat. Methods.* 13:485–488. doi:10.1038/nmeth.3833.
- Chretien, D., F. Metz, F. Verde, E. Karsenti, and R.H. Wade. 1992. Lattice defects in microtubules: Protofilament numbers vary within individual microtubules. *J. Cell Biol.* 117:1031–1040. doi:10.1083/jcb.117.5.1031.
- Clute, P., and Y. Masui. 1992. Development of Microtubule-Dependence of the Chromosome Cycle at the Midblastula Transition in *Xenopus laevis* Embryos: (*Xenopus/cell cycle/chromosomes/microtubules/midblastula transition*). *Dev. Growth Differ.* 34:27–36. doi:10.1111/j.1440-169X.1992.00027.x.
- Colis, L., K. Peltonen, P. Sirajuddin, H. Liu, S. Sanders, G. Ernst, J.C. Barrow, and M. Laiho. 2014. DNA intercalator BMH-21 inhibits RNA polymerase I independent of DNA damage response. *Oncotarget.* 5:4361–4369. doi:10.18632/oncotarget.2020.
- Cooper, J.L., and S. Henikoff. 2004. Adaptive evolution of the histone fold domain in centromeric histones. *Mol. Biol. Evol.* 21:1712–1718. doi:10.1093/molbev/msh179.
- Cortes-Silva, N., J. Ulmer, T. Kiuchi, E. Hsieh, G. Cornilleau, I. Ladid, F. Dingli, D. Loew, S. Katsuma, and I.A. Drinnenberg. 2020. CenH3-Independent Kinetochore Assembly in Lepidoptera Requires CCAN, Including CENP-T. *Curr. Biol.* 30:561-572.e10. doi:10.1016/j.cub.2019.12.014.
- Crasta, K., N.J. Ganem, R. Dagher, A.B. Lantermann, E. V. Ivanova, Y. Pan, L. Nezi, A. Protopopov, D. Chowdhury, and D. Pellman. 2012. DNA breaks and chromosome pulverization from errors in mitosis. *Nature.* 482:53–58. doi:10.1038/nature10802.
- Crowder, M.E., M. Strzelecka, J.D. Wilbur, M.C. Good, G. Von Dassow, and R. Heald. 2015. A comparative analysis of spindle morphometrics across metazoans. *Curr. Biol.* 25:1542–1550. doi:10.1016/j.cub.2015.04.036.
- Das, A., E.M. Smoak, R. Linares-Saldana, M.A. Lampson, and B.E. Black. 2017. Centromere inheritance through the germline. *Chromosoma.* 126:595–604. doi:10.1007/s00412-017-0640-y.
- Decarreau, J., M. Wagenbach, E. Lynch, A.R. Halpern, J.C. Vaughan, J. Kollman, and L. Wordeman. 2017. The tetrameric kinesin Kif25 suppresses pre-mitotic centrosome separation to establish proper spindle orientation. *Nat. Cell Biol.* 19:384–390. doi:10.1038/ncb3486.
- Deng, L., R.A. Wu, R. Sonnevile, O. V. Kochenova, K. Labib, D. Pellman, and J.C. Walter. 2019. Mitotic CDK Promotes Replisome Disassembly, Fork Breakage, and Complex DNA Rearrangements. *Mol. Cell.* 73:915-929.e6.

- doi:10.1016/j.molcel.2018.12.021.
- Dion-Cote, A.-M., and D.A. Barbash. 2017. Beyond speciation genes : an overview of genome stability in evolution and speciation. *Curr. Opin. Genet. Dev.* 47:17–23. doi:10.1016/j.gde.2017.07.014.
- Dobzhansky, T. 1937. Genetic Nature of Species Differences. *Am. Nat.* 71:404–420.
- Drinnenberg, I.A., D. deYoung, S. Henikoff, and H.S. Malik. 2014. Recurrent loss of CenH3 is associated with independent transitions to holocentricity in insects. *Elife.* 3:1–19. doi:10.7554/eLife.03676.
- Dunleavy, E.M., N.L. Beier, W. Gorgescu, J. Tang, S. V. Costes, and G.H. Karpen. 2012. The Cell Cycle Timing of Centromeric Chromatin Assembly in *Drosophila* Meiosis Is Distinct from Mitosis Yet Requires CAL1 and CENP-C. *PLoS Biol.* 10:1–16. doi:10.1371/journal.pbio.1001460.
- Dunleavy, E.M., and M. Collins. 2017. Centromere Dynamics in Male and Female Germ Cells. *Prog Mol Subcell Biol.* 56:357–375. doi:10.1007/978-3-319-58592-5.
- Dunleavy, E.M., D. Roche, H. Tagami, N. Lacoste, D. Ray-Gallet, Y. Nakamura, Y. Daigo, Y. Nakatani, and G. Almouzni-Pettinotti. 2009. HJURP Is a Cell-Cycle-Dependent Maintenance and Deposition Factor of CENP-A at Centromeres. *Cell.* 137:485–497. doi:10.1016/j.cell.2009.02.040.
- Durica, D.S., and H.M. Krider. 1977. Studies on the ribosomal RNA cistrons in interspecific *Drosophila* hybrids. I. Nucleolar dominance. *Dev. Biol.* 59:62–74. doi:10.1016/0012-1606(77)90240-8.
- Durkin, S.G., and T.W. Glover. 2007. Chromosome Fragile Sites. *Annu. Rev. Genet.* 41:169–192. doi:10.1146/annurev.genet.41.042007.165900.
- Earnshaw, W.C., and B.R. Migeon. 1985. Three related centromere proteins are absent from the inactive centromere of a stable isodicentric chromosome. *Chromosoma.* 92:290–296. doi:10.1007/BF00329812.
- Earnshaw, W.C., and N. Rothfield. 1985. Identification of a family of human centromere proteins using autoimmune sera from patients with scleroderma. *Chromosoma.* 91:313–321. doi:10.1007/BF00328227.
- Edelstein, A.D., M. a Tsuchida, N. Amodaj, H. Pinkard, R.D. Vale, and N. Stuurman. 2014. Advanced methods of microscope control using  $\mu$ Manager software. *J. Biol. Methods.* 1:10. doi:10.14440/jbm.2014.36.
- Edwards, N.S., and A.W. Murray. 2005. Identification of *Xenopus* CENP-A and an Associated Centromeric DNA Repeat. *Mol. Biol. Cell.* 16:1800–1810. doi:10.1091/mbc.E04.
- Elinson, R.P. 1977a. Macrocephaly and microcephaly in hybrids between the bullfrog *Rana catesbeiana* and the mink frog *Rana septentrionalis*. *J. Herpetol.* 11:94–96.
- Elinson, R.P. 1977b. Amphibian Hybrids: A Genetic Approach to the Analysis of Their Developmental Arrest. *Differentiation.* 9:3–9.
- Elinson, R.P. 1981. Genetic Analysis of Developmental Arrest in an Amphibian Hybrid (*Rana catesbeiana*, *Rana clamitans*). *Dev. Biol.* 81:167–176.
- Elinson, R.P., and A. Briedis. 1981. Triploidy Permits Survival of an Inviabile Amphibian Hybrid. *Dev. Genet.* 2:357–367.
- Elting, M.W., P. Suresh, and S. Dumont. 2018. The Spindle: Integrating Architecture and Mechanics across Scales. *Trends Cell Biol.* xx:1–15.

- doi:10.1016/j.tcb.2018.07.003.
- Erhardt, S., B.G. Mellone, C.M. Betts, W. Zhang, G.H. Karpen, and A.F. Straight. 2008. Genome-wide analysis reveals a cell cycle-dependent mechanism controlling centromere propagation. *J. Cell Biol.* 183:805–818. doi:10.1083/jcb.200806038.
- Evans, B.J., T.F. Carter, E. Greenbaum, V. Gvodík, D.B. Kelley, P.J. McLaughlin, O.S.G. Pauwels, D.M. Portik, E.L. Stanley, R.C. Tinsley, M.L. Tobias, and D.C. Blackburn. 2015. Genetics, Morphology, Advertisement Calls, and Historical Records Distinguish Six New Polyploid Species of African Clawed Frog (*Xenopus*, Pipidae) from West and Central Africa. *PLoS One.* 10:1–51. doi:10.1371/journal.pone.0142823.
- Fachinetti, D., H. Diego Folco, Y. Nechemia-Arbely, L.P. Valente, K. Nguyen, A.J. Wong, Q. Zhu, A.J. Holland, A. Desai, L.E.T. Jansen, and D.W. Cleveland. 2013. A two-step mechanism for epigenetic specification of centromere identity and function. *Nat. Cell Biol.* 15:1056–1066. doi:10.1038/ncb2805.
- Falk, S.J., L.Y. Guo, N. Sekulic, E.M. Smoak, T. Mani, G.A. Logsdon, K. Gupta, L.E.T. Jansen, G.D. Van Duyne, S.A. Vinogradov, M.A. Lampson, and B.E. Black. 2015. CENP-C reshapes and stabilizes CENP-A nucleosomes at the centromere. *Science (80-. ).* 348:699–704.
- Ferree, P.M., and D.A. Barbash. 2009. Species-specific heterochromatin prevents mitotic chromosome segregation to cause hybrid lethality in *Drosophila*. *PLoS Biol.* 7:e1000234. doi:10.1371/journal.pbio.1000234.
- Flemming, W. 1882. Zellsubstanz, kern und zelltheilung. *F.C.W. Vogel, Leipzig.* 419.
- Foltz, D.R., L.E.T. Jansen, A.O. Bailey, J.R. Yates, E.A. Bassett, S. Wood, B.E. Black, and D.W. Cleveland. 2009. Centromere-Specific Assembly of CENP-A Nucleosomes Is Mediated by HJURP. *Cell.* 137:472–484. doi:10.1016/j.cell.2009.02.039.
- Foltz, D.R., L.E.T. Jansen, B.E. Black, A.O. Bailey, J.R. Yates, and D.W. Cleveland. 2006. The human CENP-A centromeric nucleosome-associated complex. *Nat. Cell Biol.* 8:458–469. doi:10.1038/ncb1397.
- Ford, P.J., and R.D. Brown. 1976. Sequences of 5S ribosomal RNA from *Xenopus mulleri* and the evolution of 5S gene-coding sequences. *Cell.* 8:485–93.
- Forejt, J., P. Jansa, and E. Parvanov. 2021. Hybrid sterility genes in mice (*Mus musculus*): a peculiar case of PRDM9 incompatibility. *Trends Genet.* 37:1095–1108. doi:10.1016/j.tig.2021.06.008.
- French, B.T., and A.F. Straight. 2017. The Power of *Xenopus* Egg Extract for Reconstitution of Centromeres and Kinetochores Function. *Prog Mol Subcell Biol.* 56:59–84. doi:10.1007/978-3-319-58592-5.
- French, B.T., F.G. Westhorpe, C. Limouse, and A.F. Straight. 2017. *Xenopus laevis* M18BP1 Directly Binds Existing CENP-A Nucleosomes to Promote Centromeric Chromatin Assembly. *Dev. Cell.* 42:190–199.e10. doi:10.1016/j.devcel.2017.06.021.
- Friedman, J.R., and J. Nunnari. 2014. Mitochondrial form and function. *Nature.* 505:335–343. doi:10.1038/nature12985.
- Fu, J., M. Bian, G. Xin, Z. Deng, J. Luo, X. Guo, H. Chen, Y. Wang, Q. Jiang, and C. Zhang. 2015. TPX2 phosphorylation maintains metaphase spindle length by regulating microtubule flux. *J. Cell Biol.* 210:373–383. doi:10.1083/jcb.201412109.
- Fu, L., B. Niu, Z. Zhu, S. Wu, and W. Li. 2012. CD-HIT: Accelerated for clustering the

- next-generation sequencing data. *Bioinformatics*. 28:3150–3152. doi:10.1093/bioinformatics/bts565.
- Fujiwara, A., S. Abe, E. Yamaha, F. Yamazaki, and M.C. Yoshida. 1997. Uniparental chromosome elimination in the early embryogenesis of the inviable salmonid hybrids between masu salmon female and rainbow trout male. *Chromosoma*. 106:44–52. doi:10.1007/s004120050223.
- Gambarotto, D., F.U. Zwettler, M. Le Guennec, M. Schmidt-Cernohorska, D. Fortun, S. Borgers, J. Heine, J.-G. Schloetel, M. Reuss, M. Unser, E.S. Boyden, M. Sauer, V. Hamel, and P. Guichard. 2018. Imaging cellular ultrastructures using expansion microscopy (U-ExM). *Nat. Methods*. 16:1. doi:10.1038/s41592-018-0238-1.
- Gao, R., S.M. Asano, and E.S. Boyden. 2017. Q&A: Expansion microscopy. *BMC Biol*. 15:50. doi:10.1186/s12915-017-0393-3.
- Gatlin, J.C., A. Matov, A.C. Groen, D.J. Needleman, T.J. Maresca, G. Danuser, T.J. Mitchison, and E.D. Salmon. 2009. Spindle Fusion Requires Dynein-Mediated Sliding of Oppositely Oriented Microtubules. *Curr. Biol*. 19:287–296. doi:10.1016/j.cub.2009.01.055.
- Gébrane-Younès, J., N. Fomproix, and D. Hernandez-Verdun. 1997. When rDNA transcription is arrested during mitosis, UBF is still associated with non-condensed rDNA. *J. Cell Sci*. 110:2429–2440.
- Gernand, D., T. Rutten, A. Varshney, M. Rubtsova, S. Prodanovic, and C. Bru. 2005. Uniparental Chromosome Elimination at Mitosis and Interphase in Wheat and Pearl Millet Crosses Involves Micronucleus Formation , Progressive Heterochromatinization , and DNA Fragmentation. *Plant Cell*. 17:2431–2438. doi:10.1105/tpc.105.034249).
- Gert, K.R., and A. Pauli. 2020. Species-specific mechanisms during fertilization. 1st ed. Elsevier Inc. 1–24 pp.
- Gibeaux, R., R. Acker, M. Kitaoka, G. Georgiou, I. Van Kruijsbergen, B. Ford, E.M. Marcotte, D.K. Nomura, T. Kwon, G.J.C. Veenstra, and R. Heald. 2018. Paternal chromosome loss and metabolic crisis contribute to hybrid inviability in *Xenopus*. *Nature*. 553:337–341. doi:10.1038/nature25188.
- Gibeaux, R., and R. Heald. 2019. Generation of *Xenopus* Haploid, Triploid, and Hybrid Embryos. *Methods Mol. Biol*. 1920:303–315. doi:10.1007/978-1-61779-210-6.
- Gibeaux, R., K. Miller, R. Acker, T. Kwon, R. Heald, and R.K. Miller. 2018. *Xenopus* Hybrids Provide Insight Into Cell and Organism Size Control. *Front. Physiol*. 9:1–11. doi:10.3389/fphys.2018.01758.
- Glotzer, M., A.W. Murray, and M.W. Kirschner. 1991. Cyclin is degraded by the ubiquitin pathway. *Nature*. 349:132–138. doi:10.1038/349132a0.
- Goda, T., A. Abu-Dayya, S. Carruthers, M.D. Clark, D.L. Stemple, and L.B. Zimmerman. 2006. Genetic screens for mutations affecting development of *Xenopus tropicalis*. *PLoS Genet*. 2:e91. doi:10.1371/journal.pgen.0020091.
- Gómez-González, B., and A. Aguilera. 2019. Transcription-mediated replication hindrance : a major driver of genome instability. *Genes Dev*. 33:1008–1026. doi:10.1101/gad.324517.119.Freely.
- Good, M.C., M.D. Vahey, A. Skandarajah, D.A. Fletcher, and R. Heald. 2013. Cytoplasmic Volume Modulates Spindle Size During Embryogenesis. *Science (80-. )*. 342:856–860. doi:10.1126/science.1243147.

- Goshima, G. 2011. Identification of a TPX2-like microtubule-associated protein in *Drosophila*. *PLoS One*. 6. doi:10.1371/journal.pone.0028120.
- Graham, C.F., and R.W. Morgan. 1966. Changes in the cell cycle during early amphibian development. *Dev. Biol.* 14:439–460. doi:10.1016/0012-1606(66)90024-8.
- Grainger, R.M. 2012. *Xenopus tropicalis* as a Model Organism for Genetics and Genomics: Past, Present and Future. *Methods Mol. Biol.* 917:3–15. doi:10.1007/978-1-61779-992-1.
- Grenfell, A.W., R. Heald, and M. Strzelecka. 2016a. Mitotic noncoding RNA processing promotes kinetochore and spindle assembly in *Xenopus*. *J. Cell Biol.* 214:133–141. doi:10.1083/jcb.201604029.
- Grenfell, A.W., M. Strzelecka, M.E. Crowder, K.J. Helmke, A.L. Schlaitz, and R. Heald. 2016b. A versatile multivariate image analysis pipeline reveals features of *Xenopus* extract spindles. *J. Cell Biol.* 213:127–136. doi:10.1083/jcb.201509079.
- Grill, S.W., J. Howard, E. Schäffer, E.H.K. Stelzer, and A.A. Hyman. 2003. The distribution of active force generators controls mitotic spindle position. *Science (80- )*. 301:518–521. doi:10.1126/science.1086560.
- Griswold, M.D., R.D. Brown, and G.P. Tocchini-Valentini. 1974. An Analysis of the Degree of Homology Between 28S rRNA from *Xenopus laevis* and *Xenopus Mulleri*. *Biochem. Biophys. Res. Commun.* 58:1093–1103.
- Le Guennec, M., N. Klena, D. Gambarotto, M.H. Laporte, A.M. Tassin, H. van den Hoek, P.S. Erdmann, M. Schaffer, L. Kovacic, S. Borgers, K.N. Goldie, H. Stahlberg, M. Bornens, J. Azimzadeh, B.D. Engel, V. Hamel, and P. Guichard. 2020. A helical inner scaffold provides a structural basis for centriole cohesion. *Sci. Adv.* 6. doi:10.1126/sciadv.aaz4137.
- Guse, A., C.W. Carroll, B. Moree, C.J. Fuller, and A.F. Straight. 2011. In vitro centromere and kinetochore assembly on defined chromatin templates. *Nature*. 477:354–358. doi:10.1038/nature10379.
- Halpern, A.R., G.C.M. Alas, T.J. Chozinski, A.R. Paredez, and J.C. Vaughan. 2017. Hybrid Structured Illumination Expansion Microscopy Reveals Microbial Cytoskeleton Organization. *Am. Chem. Soc. Nano.* 11:12677–12686. doi:10.1021/acsnano.7b07200.
- Halpin, D., P. Kalab, J. Wang, K. Weis, and R. Heald. 2011. Mitotic spindle assembly around RCC1-coated beads in *Xenopus* egg extracts. *PLoS Biol.* 9. doi:10.1371/journal.pbio.1001225.
- Hamilton, L. 1957. Androgenic haploids of a toad, *Xenopus laevis*. *Nature*. 179:159.
- Hannak, E., and R. Heald. 2006. Investigating mitotic spindle assembly and function in vitro using *Xenopus laevis* egg extracts. *Nat. Protoc.* 1:2305–2314. doi:10.1038/nprot.2006.396.
- Hatch, E.M., A.H. Fischer, T.J. Deerinck, and M.W. Hetzer. 2013. Catastrophic nuclear envelope collapse in cancer cell micronuclei. *Cell*. 154:47–60. doi:10.1016/j.cell.2013.06.007.
- Hayward, D., and J.G. Wakefield. 2014. Chromatin-mediated microtubule nucleation in *Drosophila* syncytial embryos. *Commun. Integr. Biol.* 7. doi:10.4161/cib.28512.
- Heald, R., R. Tournebise, T. Blank, R. Sandaltzopoulos, P. Becker, A. Hyman, and E. Karsenti. 1996. Self-organization of microtubules into bipolar spindles around

- artificial chromosomes in *Xenopus* egg extracts. *Nature*. 382:420–5. doi:10.1038/382420a0.
- Helmke, K.J., and R. Heald. 2014. TPX2 levels modulate meiotic spindle size and architecture in *Xenopus* egg extracts. *J. Cell Biol.* 206:385–393. doi:10.1083/jcb.201401014.
- Helmke, K.J., R. Heald, and J.D. Wilbur. 2013. Interplay between spindle architecture and function. 306. 1st ed. Elsevier Inc. 83–125 pp.
- Henderson, A.S., D. Warburton, and K.C. Atwood. 1972. Location of ribosomal DNA in the human chromosome complement. *Proc. Natl. Acad. Sci. U. S. A.* 69:3394–3398. doi:10.1073/pnas.69.11.3394.
- Henikoff, S., K. Ahmad, and H.S. Malik. 2001. The Centromere Paradox : Stable Inheritance with Rapidly Evolving DNA. *Science (80- )*. 293:1098–1102. doi:10.1126/science.1062939.
- Hensey, C., and J. Gautier. 1997. A developmental timer that regulates apoptosis at the onset of gastrulation. *Mech. Dev.* 69:183–195. doi:10.1016/S0925-4773(97)00191-3.
- Herberg, S., K.R. Gert, A. Schleiffer, and A. Pauli. 2018. The Ly6 / uPAR protein Bouncer is necessary and sufficient for species-specific fertilization Authors. *bioRxiv*. 1033:1–42. doi:10.1101/354688.
- Hirano, T., and T.J. Mitchison. 1991. Cell cycle control of higher-order chromatin assembly around naked DNA in vitro. *J. Cell Biol.* 115:1479–1489. doi:10.1083/jcb.115.6.1479.
- Hirsch, N., L.B. Zimmerman, and R.M. Grainger. 2002. *Xenopus*, the next generation: *X. tropicalis* genetics and genomics. *Dev. Dyn.* 225:422–33. doi:10.1002/dvdy.10178.
- Holland, A.J., and D.W. Cleveland. 2012. Losing balance: The origin and impact of aneuploidy in cancer. *EMBO Rep.* 13:501–514. doi:10.1038/embor.2012.55.
- Honjo, T., and R.H. Reeder. 1973. Preferential transcription of *Xenopus laevis* ribosomal RNA in interspecies hybrids between *Xenopus laevis* and *Xenopus mulleri*. *J. Mol. Biol.* 80:217–228. doi:10.1016/0022-2836(73)90168-X.
- Hooff, J.J., E. Tromer, L.M. Wijk, B. Snel, and G.J. Kops. 2017. Evolutionary dynamics of the kinetochore network in eukaryotes as revealed by comparative genomics. *EMBO Rep.* 18:1559–1571. doi:10.15252/embr.201744102.
- Hori, T., W.H. Shang, M. Hara, M. Ariyoshi, Y. Arimura, R. Fujita, H. Kurumizaka, and T. Fukagawa. 2017. Association of M18BP1/KNL2 with CENP-A Nucleosome Is Essential for Centromere Formation in Non-mammalian Vertebrates. *Dev. Cell.* 42:181-189.e3. doi:10.1016/j.devcel.2017.06.019.
- Hu, H., Y. Liu, M. Wang, J. Fang, H. Huang, N. Yang, Y. Li, J. Wang, X. Yao, Y. Shi, G. Li, and R.M. Xu. 2011. Structure of a CENP-A-histone H4 heterodimer in complex with chaperone HJURP. *Genes Dev.* 25:901–906. doi:10.1101/gad.2045111.
- Jagannathan, M., R. Cummings, and Y.M. Yamashita. 2018. A conserved function for pericentromeric satellite DNA. *Elife*. 7:e34122. doi:10.7554/eLife.34122.
- Jagannathan, M., and Y. Yamashita. 2018. Evolution Repeats Itself in Building a Species Barrier. *Dev. Cell.* 47:527–528. doi:10.1016/j.devcel.2018.11.025.
- Jagannathan, M., and Y.M. Yamashita. 2021. Defective Satellite DNA Clustering into Chromocenters Underlies Hybrid Incompatibility in *Drosophila*. *Mol. Biol. Evol.*



- 38:4977–4986. doi:10.1093/molbev/msab221.
- Jansen, L.E.T., B.E. Black, D.R. Foltz, and D.W. Cleveland. 2007. Propagation of centromeric chromatin requires exit from mitosis. *J. Cell Biol.* 176:795–805. doi:10.1083/jcb.200701066.
- Jenness, C., D.J. Wynne, and H. Funabiki. 2018. Protein Immunodepletion and Complementation in *Xenopus laevis* Egg Extracts. *Cold Spring Harb. Protoc.* 1–6. doi:10.1101/pdb.prot097113.
- Jhuang, H., H. Lee, and J. Leu. 2017. Mitochondrial – nuclear co-evolution leads to hybrid incompatibility through pentatricopeptide repeat proteins. *EMBO Rep.* 18:87–101. doi:10.15252/embr.201643311.
- Jiang, K., L. Rezabkova, S. Hua, Q. Liu, G. Capitani, A.F.M. Altelaar, A.J.R. Heck, R.A. Kammerer, M.O. Steinmetz, and A. Akhmanova. 2017. Microtubule minus-end regulation at spindle poles by an ASPM-katanin complex. *Nat. Cell Biol.* 19:480–492. doi:10.1038/ncb3511.
- Joly, N., L. Martino, E. Gigant, J. Dumont, and L. Pintard. 2016. Microtubule-severing activity of the AAA+ ATPase Katanin is essential for female meiotic spindle assembly. *Development.* 143:3604–3614. doi:10.1242/dev.140830.
- Jukam, D., R.R. Kapoor, A.F. Straight, and J.M. Skotheim. 2021. The DNA-to-cytoplasm ratio broadly activates zygotic gene expression in *Xenopus*. *Curr. Biol.* 31:4269–4281.e8. doi:10.1016/j.cub.2021.07.035.
- Kabeche, L., H.D. Nguyen, R. Buisson, and L. Zou. 2018. A mitosis-specific and R loop-driven ATR pathway promotes faithful chromosome segregation SUPP. *Science (80-. )*. 359:108–114. doi:10.1126/science.aan6490.
- Kajtez, J., A. Solomatina, M. Novak, B. Polak, K. Vukušić, J. Rüdiger, G. Cojoc, A. Milas, I. Šumanovac Šestak, P. Risteski, F. Tavano, A.H. Klemm, E. Roscioli, J. Welburn, D. Cimini, M. Glunčić, N. Pavin, and I.M. Tolić. 2016. Overlap microtubules link sister k-fibres and balance the forces on bi-oriented kinetochores. *Nat. Commun.* 7. doi:10.1038/ncomms10298.
- Kalab, P., and R. Heald. 2008. The RanGTP gradient - a GPS for the mitotic spindle. *J. Cell Sci.* 121:1577–86. doi:10.1242/jcs.005959.
- Kalab, P., R.T. Pu, and M. Dasso. 1999. The Ran GTPase regulates mitotic spindle assembly. *Curr. Biol.* 9:481–484. doi:10.1016/S0960-9822(99)80213-9.
- Kalab, P., K. Weis, and R. Heald. 2002. Visualization of a Ran-GTP gradient in interphase and mitotic *Xenopus* egg extracts. *Science.* 295:2452–2456. doi:10.1126/science.1068798.
- Kalitsis, P., and K.H.A. Choo. 2012. The evolutionary life cycle of the resilient centromere. *Chromosoma.* 121:327–340. doi:10.1007/s00412-012-0369-6.
- Kitaoka, M., R. Heald, and R. Gibeaux. 2018. Spindle assembly in egg extracts of the Marsabit clawed frog, *Xenopus borealis*. *Cytoskeleton.* 75:244–257. doi:10.1002/cm.21444.
- Kitaoka, M., O.K. Smith, A.F. Straight, and R. Heald. 2022. Molecular conflicts disrupting centromere assembly contribute to *Xenopus* hybrid inviability. *bioRxiv*. doi:https://doi.org/10.1101/2022.03.06.483208.
- Kumon, T., J. Ma, R.B. Akins, D. Stefanik, C.E. Nordgren, J. Kim, M.T. Levine, and M.A. Lampson. 2021. Parallel pathways for recruiting effector proteins determine centromere drive and suppression. *Cell.* 1–15. doi:10.1016/j.cell.2021.07.037.

- Kuppu, S., E.H. Tan, H. Nguyen, A. Rodgers, L. Comai, S.W.L. Chan, and A.B. Britt. 2015. Point Mutations in Centromeric Histone Induce Post-zygotic Incompatibility and Uniparental Inheritance. *PLoS Genet.* 11:1–18. doi:10.1371/journal.pgen.1005494.
- Kursel, L.E., and H.S. Malik. 2017. Recurrent gene duplication leads to diverse repertoires of centromeric histones in *Drosophila* species. *Mol. Biol. Evol.* 34:1445–1462. doi:10.1093/molbev/msx091.
- Kursel, L.E., H. McConnell, A.F.A. De La Cruz, and H.S. Malik. 2021. Gametic specialization of centromeric histone paralogs in *Drosophila virilis*. *Life Sci. Alliance.* 4:1–14. doi:10.26508/lsa.202000992.
- Lee, C., E. Kieserman, R.S. Gray, T.J. Park, and J. Wallingford. 2008a. Whole-Mount Fluorescence Immunocytochemistry on *Xenopus* Embryos. *Cold Spring Harb. Protoc.* 3:1–5. doi:10.1101/pdb.prot4957.
- Lee, H.Y., J.Y. Chou, L. Cheong, N.H. Chang, S.Y. Yang, and J.Y. Leu. 2008b. Incompatibility of Nuclear and Mitochondrial Genomes Causes Hybrid Sterility between Two Yeast Species. *Cell.* 135:1065–1073. doi:10.1016/j.cell.2008.10.047.
- Leister, D.E., and I.B. Dawid. 1975. Mitochondrial Ribosomal Proteins in *Xenopus laevis* / *X. mulleri* Interspecific Hybrids. *J. Mol. Biol.* 96:119–123.
- Levy, D.L., and R. Heald. 2010. Nuclear Size Is Regulated by Importin A and Ntf2 in *Xenopus*. *Cell.* 143:288–298. doi:10.1016/j.cell.2010.09.012.
- Levy, D.L., and R. Heald. 2016. Biological scaling problems and solutions in amphibians. *Cold Spring Harb. Perspect. Biol.* 8. doi:10.1101/cshperspect.a019166.
- Liska, A.J., A. V. Popov, S. Sunyaev, P. Coughlin, B. Habermann, A. Shevchenko, P. Bork, E. Karsenti, and A. Shevchenko. 2004. Homology-based functional proteomics by mass spectrometry: Application to the *Xenopus* microtubule-associated proteome. *Proteomics.* 4:2707–2721. doi:10.1002/pmic.200300813.
- Lohka, M.I., and J.L. Maller. 1985. Induction of nuclear envelope breakdown, chromosome condensation, and spindle formation in cell-free extracts. *J. Cell Biol.* 101:518–523. doi:10.1083/jcb.101.2.518.
- Lohka, M.J., and Y. Masui. 1983. Formation in vitro of sperm pronuclei and mitotic chromosomes induced by amphibian ooplasmic components. *Science (80- ).* 220:719–721. doi:10.1126/science.6601299.
- Long, E.O., and I.B. Dawid. 1980. Repeated genes in eukaryotes. *Annu. Rev. Biochem.* 49:727–764. doi:10.1146/annurev.bi.49.070180.003455.
- Loughlin, R., R. Heald, and F. Nédélec. 2010. A computational model predicts *Xenopus* meiotic spindle organization. *J. Cell Biol.* 191:1239–1249. doi:10.1083/jcb.201006076.
- Loughlin, R., J.D. Wilbur, F.J. McNally, F.J. Nédélec, and R. Heald. 2011. Katanin contributes to interspecies spindle length scaling in *Xenopus*. *Cell.* 147:1397–1407. doi:10.1016/j.cell.2011.11.014.
- Louie, S.M., E.A. Grossman, L.A. Crawford, L. Ding, R. Camarda, T.R. Huffman, D.K. Miyamoto, A. Goga, E. Weerapana, and D.K. Nomura. 2016. GSTP1 Is a Driver of Triple-Negative Breast Cancer Cell Metabolism and Pathogenicity. *Cell Chem. Biol.* 23:567–78. doi:10.1016/j.chembiol.2016.03.017.
- Lu, K.L., J.O. Nelson, G.J. Watase, N. Warsinger-Pepe, and Y.M. Yamashita. 2018.

- Transgenerational dynamics of rDNA copy number in drosophila male germline stem cells. *Elife*. 7:1–20. doi:10.7554/eLife.32421.
- Lukacs, A., A.W. Thomae, P. Krueger, T. Schauer, A. V. Venkatasubramani, N.Y. Kochanova, W. Aftab, R. Choudhury, I. Forne, and A. Imhof. 2021. The integrity of the HMR complex is necessary for centromeric binding and reproductive isolation in *Drosophila*. *PLoS Genet*. 17:1–27. doi:10.1371/journal.pgen.1009744.
- Ma, H., N. Marti Gutierrez, R. Morey, C. Van Dyken, E. Kang, T. Hayama, Y. Lee, Y. Li, R. Tippner-Hedges, D.P. Wolf, L.C. Laurent, and S. Mitalipov. 2016. Incompatibility between Nuclear and Mitochondrial Genomes Contributes to an Interspecies Reproductive Barrier. *Cell Metab*. 24:283–294. doi:10.1016/j.cmet.2016.06.012.
- Ma, N., J. Titus, A. Gable, J.L. Ross, and P. Wadsworth. 2011. TPX2 regulates the localization and activity of Eg5 in the mammalian mitotic spindle. *J. Cell Biol*. 195:87–98. doi:10.1083/jcb.201106149.
- Maheshwari, S., and D.A. Barbash. 2011. The Genetics of Hybrid Incompatibilities. *Annu. Rev. Genet*. 45:331–355. doi:10.1146/annurev-genet-110410-132514.
- Maheshwari, S., E.H. Tan, A. West, F.C.H. Franklin, L. Comai, and S.W.L. Chan. 2015. Naturally Occurring Differences in CENH3 Affect Chromosome Segregation in Zygotic Mitosis of Hybrids. *PLoS Genet*. 11:1–20. doi:10.1371/journal.pgen.1004970.
- Malik, H.S., and S. Henikoff. 2001. Adaptive evolution of Cid, a centromere-specific histone in *Drosophila*. *Genetics*. 157:1293–1298. doi:10.1093/genetics/157.3.1293.
- Malik, H.S., and S. Henikoff. 2009. Major Evolutionary Transitions in Centromere Complexity. *Cell*. 138:1067–1082. doi:10.1016/j.cell.2009.08.036.
- Malik, H.S., D. Vermaak, and S. Henikoff. 2002. Recurrent evolution of DNA-binding motifs in the *Drosophila* centromeric histone. *Proc. Natl. Acad. Sci. U. S. A*. 99:1449–54. doi:10.1073/pnas.032664299.
- Maresca, T.J., and R. Heald. 2006. Methods for studying spindle assembly and chromosome condensation in *Xenopus* egg extracts. *Methods Mol. Biol. (Clifton, NJ)*. 322:459–474. doi:10.1007/978-1-59745-000-3\_33.
- Maric, M., T. Maculins, G. De Piccoli, and K. Labib. 2014. Cdc48 and a ubiquitin ligase drive disassembly of the CMG helicase at the end of DNA replication. *Science (80-. )*. 346. doi:10.1126/science.1253596.
- Marimuthu, A.M.P.A., R. Maruthachalam, and R. Bondada. 2021. Epigenetically mismatched parental centromeres trigger genome elimination in hybrids. 1–19.
- Mastronarde, D.N., K.L. McDonald, R. Ding, and J.R. McIntosh. 1993. Interpolar spindle microtubules in PTK cells. *J. Cell Biol*. 123:1475–1489. doi:10.1083/jcb.123.6.1475.
- Masui, Y., and C.L. Markert. 1971. Cytoplasmic control of nuclear behavior during meiotic maturation of frog oocytes. *J. Exp. Zool*. 129–146. doi:10.1016/S0248-4900(99)80004-5.
- McDonald, K.L., E.T. O’Toole, D.N. Mastronarde, and J.R. McIntosh. 1992. Kinetochore microtubules in PTK cells. *J. Cell Biol*. 118:369–383. doi:10.1083/jcb.118.2.369.
- McKinley, K.L., and I.M. Cheeseman. 2016. The molecular basis for centromere identity and function. *Nat. Rev. Mol. Cell Biol*. 17:16–29. doi:10.1038/nrm.2015.5.
- McNally, K., A. Audhya, K. Oegema, and F.J. McNally. 2006. Katanin controls mitotic and meiotic spindle length. *J. Cell Biol*. 175:881–891. doi:10.1083/jcb.200608117.
- Meiklejohn, C.D., M.A. Holmbeck, M.A. Siddiq, D.N. Abt, D.M. Rand, and K.L.

- Montooth. 2013. An Incompatibility between a Mitochondrial tRNA and Its Nuclear-Encoded tRNA Synthetase Compromises Development and Fitness in *Drosophila*. *PLoS Genet.* 9:e1003238. doi:10.1371/journal.pgen.1003238.
- Mellone, B.G., K.J. Grive, V. Shteyn, S.R. Bowers, I. Oderberg, and G.H. Karpen. 2011. Assembly of *drosophila* centromeric chromatin proteins during mitosis. *PLoS Genet.* 7. doi:10.1371/journal.pgen.1002068.
- Mendiburo, M.J., J. Padeken, S. Fülöp, A. Schepers, and P. Heun. 2011. *Drosophila* CENH3 Is Sufficient for Centromere Formation. *Science (80-. )*. 334:686–690.
- Mi, H., S. Poudel, A. Muruganujan, J.T. Casagrande, and P.D. Thomas. 2016. PANTHER version 10: Expanded protein families and functions, and analysis tools. *Nucleic Acids Res.* 44:D336–D342. doi:10.1093/nar/gkv1194.
- Michalak, K., S. Maciak, Y.B. Kim, G. Santopietro, J.H. Oh, L. Kang, H.R. Garner, and P. Michalak. 2015. Nucleolar dominance and maternal control of 45S rDNA expression. *Proc. R. Soc. B Biol. Sci.* 282:20152201. doi:10.1098/rspb.2015.2201.
- Miesfeld, R., and N. Arnheim. 1984. Species-specific rDNA transcription is due to promoter-specific binding factors. *Mol. Cell. Biol.* 4:221–227. doi:10.1128/mcb.4.2.221.
- Mihola, O., Z. Trachtulec, C. Vlcek, J.C. Schimenti, and J. Forejt. 2009. A Mouse Speciation Gene Encodes a Meiotic Histone H3 Methyltransferase. *Science (80-. )*. 323:373–5.
- Milks, K.J., B. Moree, and A.F. Straight. 2009. Dissection of CENP-C – directed Centromere and Kinetochore Assembly. *Mol. Biol. Cell.* 20:4246–4255. doi:10.1091/mbc.E09.
- Miller, K.E., A.M. Session, and R. Heald. 2019. Kif2a Scales Meiotic Spindle Size in *Hymenochirus boettgeri*. *Curr. Biol.* 29:3720-3727.e5. doi:10.1016/j.cub.2019.08.073.
- Mitchison, T., and M. Kirschner. 1984a. Microtubule assembly nucleated by isolated centrosomes. *Nature.* 312:232–237. doi:10.1038/312232a0.
- Mitchison, T., and M. Kirschner. 1984b. Dynamic instability of microtubule growth. *Nature.* 312:237–242. doi:10.1038/312237a0.
- Moran, B.M., C.Y. Payne, D.L. Powell, E.N.K. Iverson, S.M. Banerjee, Q.K. Langdon, T.R. Gunn, F. Liu, R. Matney, K. Singhal, R.D. Leib, O. Hernandez-Perez, R. Corbett-Detig, M. Scharl, J.C. Havird, and M. Schumer. 2021. A Lethal Genetic Incompatibility between Naturally Hybridizing Species in Mitochondrial Complex I. *bioRxiv.* 2021.07.13.452279.
- Moree, B., C.B. Meyer, C.J. Fuller, and A.F. Straight. 2011. CENP-C recruits M18BP1 to centromeres to promote CENP-A chromatin assembly. *J. Cell Biol.* 194:855–871. doi:10.1083/jcb.201106079.
- Müller-Reichert, T., R. Kiewisz, and S. Redemann. 2018. Mitotic spindles revisited – new insights from 3D electron microscopy. *J. Cell Sci.* 131:jcs211383. doi:10.1242/jcs.211383.
- Murayama, A., K. Ohmori, A. Fujimura, H. Minami, K. Yasuzawa-Tanaka, T. Kuroda, S. Oie, H. Daitoku, M. Okuwaki, K. Nagata, A. Fukamizu, K. Kimura, T. Shimizu, and J. Yanagisawa. 2008. Epigenetic Control of rDNA Loci in Response to Intracellular Energy Status. *Cell.* 133:627–639. doi:10.1016/j.cell.2008.03.030.
- Murray, A.W. 1991. Cell Cycle Extracts. *Methods Cell Biol.* 36:581–605.

- doi:10.1016/S0091-679X(08)60298-8.
- Murray, A.W., and M.W. Kirschner. 1989. Cyclin synthesis drives the early embryonic cell cycle. *Nature*. 339:275–280.
- Narbonne, P., D.E. Simpson, and J.B. Gurdon. 2011. Deficient induction response in a *Xenopus* nucleocytoplasmic hybrid. *PLoS Biol.* 9:e1001197. doi:10.1371/journal.pbio.1001197.
- Neumayer, G., C. Belzil, O.J. Gruss, and M.D. Nguyen. 2014. TPX2: Of spindle assembly, DNA damage response, and cancer. *Cell. Mol. Life Sci.* 71:3027–3047. doi:10.1007/s00018-014-1582-7.
- Newport, J., and M. Kirschner. 1982. A major developmental transition in early *xenopus* embryos: I. characterization and timing of cellular changes at the midblastula stage. *Cell*. 30:675–686. doi:10.1016/0092-8674(82)90272-0.
- Newport, J.W., and M.W. Kirschner. 1984. Regulation of the cell cycle during early *Xenopus* development. *Cell*. 37:731–742. doi:10.1016/0092-8674(84)90409-4.
- Nieuwkoop, P.D., and J. Faber. 1994. Normal table of *Xenopus laevis* (Daudin). Garland Publishing.
- Ochs, R.L., and R.I. Press. 1992. Centromere autoantigens are associated with the nucleolus. *Exp. Cell Res.* 200:339–350. doi:10.1016/0014-4827(92)90181-7.
- Palmer, D.K., K. O'Day, and R.L. Margolis. 1990. The centromere specific histone CENP-A is selectively retained in discrete foci in mammalian sperm nuclei. *Chromosoma*. 100:32–36. doi:10.1007/BF00337600.
- Palmer, D.K., K. O'Day, H.L.E. Trong, H. Charbonneau, and R.L. Margolis. 1991. Purification of the centromere-specific protein CENP-A and demonstration that it is a distinctive histone. *Proc. Natl. Acad. Sci. U. S. A.* 88:3734–3738. doi:10.1073/pnas.88.9.3734.
- Peltonen, K., L. Colis, H. Liu, R. Trivedi, M.S. Moubarek, H.M. Moore, B. Bai, M.A. Rudek, C.J. Bieberich, and M. Laiho. 2014. A targeting modality for destruction of RNA polymerase I that possesses anticancer activity. *Cancer Cell*. 25:77–90. doi:10.1016/j.ccr.2013.12.009.
- Pentakota, S., K. Zhou, C. Smith, S. Maffini, A. Petrovic, G.P. Morgan, J.R. Weir, I.R. Vetter, A. Musacchio, and K. Luger. 2017. Decoding the centromeric nucleosome through CENP-N. *Elife*. 6:e33442. doi:10.7554/eLife.33442.
- Petry, S. 2016. Mechanisms of Mitotic Spindle Assembly. *Annu. Rev. Biochem.* 85:659–683. doi:10.1146/annurev-biochem-060815-014528.
- Petry, S., A.C. Groen, K. Ishihara, T.J. Mitchison, and R.D. Vale. 2013. Branching microtubule nucleation in *xenopus* egg extracts mediated by augmin and TPX2. *Cell*. 152:768–777. doi:10.1016/j.cell.2012.12.044.
- Phadnis, N., E.P. Baker, J.C. Cooper, K.A. Frizzell, E. Hsieh, A.F.A. de la Cruz, J. Shendure, J.O. Kitzman, and H.S. Malik. 2015. An essential cell cycle regulation gene causes hybrid inviability in *Drosophila*. *Science (80-. )*. 350:1552–1555. doi:10.1126/science.aac7504.
- Ponjavić, I., K. Vukušić, and I.M. Tolić. 2021. Expansion microscopy of the mitotic spindle. *Methods Cell Biol.* 161:247–274. doi:10.1016/bs.mcb.2020.04.014.
- Pontremoli, C., D. Forni, U. Pozzoli, M. Clerici, R. Cagliani, and M. Sironi. 2021. Kinetochore proteins and microtubule-destabilizing factors are fast evolving in eutherian mammals. *Mol. Ecol.* 30:1505–1515. doi:10.1111/mec.15812.

- Powell, D.L., M. Garcia, M. Keegan, P. Reilly, K. Du, A.P. Diaz-Loyo, S. Banerjee, D. Blakkan, D. Reich, P. Andolfatto, G. Rosenthal, M. Scharl, and M. Schumer. 2020. Natural hybridization reveals incompatible alleles that cause melanoma in swordtail fish. *Science* (80-. ). 736:1–21. doi:10.1101/2019.12.12.874586.
- Presgraves, D.C. 2010. The molecular evolutionary basis of species formation. *Nat. Rev. Genet.* 11:175–180. doi:10.1038/nrg2718.
- Presgraves, D.C., L. Balagopalan, S.M. Abmayr, and H.A. Orr. 2003. Adaptive evolution drives divergence of a hybrid inviability gene between two species of *Drosophila*. *Nature*. 423:715–719. doi:10.1038/nature01679.
- Raychaudhuri, N., R. Dubruielle, G.A. Orsi, and H.C. Bagheri. 2012. Transgenerational Propagation and Quantitative Maintenance of Paternal Centromeres Depends on Cid / Cenp-A Presence in *Drosophila* Sperm. *PLOS Biol.* 10. doi:10.1371/journal.pbio.1001434.
- Reber, S.B., J. Baumgart, P.O. Widlund, A. Pozniakovsky, J. Howard, A.A. Hyman, and F. Jülicher. 2013. XMAP215 activity sets spindle length by controlling the total mass of spindle microtubules. *Nat. Cell Biol.* 15:1116–1122. doi:10.1038/ncb2834.
- Redemann, S., I. Lantzsch, N. Lindow, S. Prohaska, and M. Srayko. 2018. A Switch in Microtubule Orientation during *C. elegans* Meiosis. *Curr. Biol.* 28:2991–2997. doi:10.1016/j.cub.2018.07.012.
- Reeder, R.H., and J.G. Roan. 1984. The mechanism of nucleolar dominance in xenopus hybrids. *Cell.* 38:39–44. doi:10.1016/0092-8674(84)90524-5.
- Régnier, V., P. Vagnarelli, T. Fukagawa, T. Zerjal, E. Burns, D. Trouche, W. Earnshaw, and W. Brown. 2005. CENP-A Is Required for Accurate Chromosome Segregation and Sustained Kinetochore Association of BubR1. *Mol. Cell. Biol.* 25:3967–3981. doi:10.1128/mcb.25.10.3967-3981.2005.
- De Robertis, E.M., and P. Black. 1979. Hybrids of *Xenopus laevis* and *Xenopus borealis* express proteins from both parents. *Dev. Biol.* 68:334–339. doi:10.1016/0012-1606(79)90267-7.
- Robinson, M.D., D.J. McCarthy, and G.K. Smyth. 2010. edgeR: a Bioconductor package for differential expression analysis of digital gene expression data. *Bioinformatics.* 26:139–40. doi:10.1093/bioinformatics/btp616.
- Rošić, S., F. Köhler, and S. Erhardt. 2014. Repetitive centromeric satellite RNA is essential for kinetochore formation and cell division. *J. Cell Biol.* 207:335–349. doi:10.1083/jcb.201404097.
- Rosin, L., and B.G. Mellone. 2016. Co-evolving CENP-A and CAL1 Domains Mediate Centromeric CENP-A Deposition across *Drosophila* Species. *Dev. Cell.* 37:136–147. doi:10.1016/j.devcel.2016.03.021.
- Rosin, L.F., and B.G. Mellone. 2017. Centromeres Drive a Hard Bargain. *Trends Genet.* 33:101–117. doi:10.1016/j.tig.2016.12.001.
- Roure, V., B. Medina-Pritchard, V. Lazou, L. Rago, E. Anselm, D. Venegas, A.A. Jeyaprakash, and P. Heun. 2019. Reconstituting *Drosophila* Centromere Identity in Human Cells. *Cell Rep.* 29:464-479.e5. doi:10.1016/j.celrep.2019.08.067.
- Roussel, P., C. André, L. Comai, and D. Hernandez-Verdun. 1996. The rDNA transcription machinery is assembled during mitosis in active NORs and absent in inactive NORs. *J. Cell Biol.* 133:235–246. doi:10.1083/jcb.133.2.235.
- Sakai, C., F. Konno, O. Nakano, T. Iwai, T. Yokota, J. Lee, C. Nishida-Umehara, A.

- Kuroiwa, Y. Matsuda, and M. Yamashita. 2007. Chromosome elimination in the interspecific hybrid medaka between *Oryzias latipes* and *O. hubbsi*. *Chromosom. Res.* 15:697–709. doi:10.1007/s10577-007-1155-9.
- Sanei, M., R. Pickering, K. Kumke, S. Nasuda, and A. Houben. 2011. Loss of centromeric histone H3 (CENH3) from centromeres precedes uniparental chromosome elimination in interspecific barley hybrids. *PNAS.* 108:E498–E505. doi:10.1073/pnas.1103190108/-/DCSupplemental.www.pnas.org/cgi/doi/10.1073/pnas.1103190108.
- Satyaki, P.R. V, T.N. Cuykendall, K.H.C. Wei, N.J. Brideau, H. Kwak, S. Aruna, P.M. Ferree, S. Ji, and D.A. Barbash. 2014. The Hmr and Lhr Hybrid Incompatibility Genes Suppress a Broad Range of Heterochromatic Repeats. *PLoS Genet.* 10. doi:10.1371/journal.pgen.1004240.
- Sauer, G., R. Körner, A. Hanisch, A. Ries, E.A. Nigg, and H.H.W. Silljé. 2005. Proteome analysis of the human mitotic spindle. *Mol. Cell. Proteomics.* 4:35–43. doi:10.1074/mcp.M400158-MCP200.
- Sawin, K.E., and T.J. Mitchison. 1991. Mitotic Spindle Assembly by Two Different Pathways in Vitro. *J. Cell Biol.* 112:925–940.
- Schindelin, J., I. Arganda-Carreras, E. Frise, V. Kaynig, M. Longair, T. Pietzsch, S. Preibisch, C. Rueden, S. Saalfeld, B. Schmid, J.-Y. Tinevez, D.J. White, V. Hartenstein, K. Eliceiri, P. Tomancak, and A. Cardona. 2012. Fiji: an open-source platform for biological-image analysis. *Nat. Methods.* 9:676–682. doi:10.1038/nmeth.2019.
- Schmid, M., and C. Steinlein. 1991. Chromosome banding in Amphibia - XVI. High-resolution replication banding patterns in *Xenopus laevis*. *Chromosoma.* 101:123–132. doi:10.1007/BF00357062.
- Schmid, M., and C. Steinlein. 2015. Chromosome Banding in Amphibia. XXXII. the Genus *Xenopus* (Anura, Pipidae). *Cytogenet. Genome Res.* 145:201–217. doi:10.1159/000433481.
- Scrofani, J., T. Sardon, S. Meunier, and I. Vernos. 2015. Microtubule nucleation in mitosis by a RanGTP-dependent protein complex. *Curr. Biol.* 25:131–140. doi:10.1016/j.cub.2014.11.025.
- Seehausen, O., R.K. Butlin, I. Keller, C.E. Wagner, J.W. Boughman, P.A. Hohenlohe, C.L. Peichel, G.-P. Saetre, C. Bank, A. Brannstrom, A. Brelsford, C.S. Clarkson, F. Eroukhmanoff, J.L. Feder, M.C. Fischer, A.D. Foote, P. Franchini, C.D. Jiggins, F.C. Jones, A.K. Lindholm, K. Lucek, M.E. Maan, D.A. Marques, S.H. Martin, B. Matthews, J.I. Meier, M. Most, M.W. Nachman, E. Nonaka, D.J. Rennison, J. Schwarzer, E.T. Watson, A.M. Westram, and A. Widmer. 2014. Genomics and the origin of species. *Nat Rev Genet.* 15:176–192. doi:10.1038/nrg3644.
- Session, A.M., Y. Uno, T. Kwon, J.A. Chapman, A. Toyoda, S. Takahashi, A. Fukui, A. Hikosaka, A. Suzuki, M. Kondo, S.J. van Heeringen, I. Quigley, S. Heinz, H. Ogino, H. Ochi, U. Hellsten, J.B. Lyons, O. Simakov, N. Putnam, J. Stites, Y. Kuroki, T. Tanaka, T. Michiue, M. Watanabe, O. Bogdanovic, R. Lister, G. Georgiou, S.S. Paranipe, I. van Kruijsbergen, S. Shu, J. Carlson, T. Kinoshita, Y. Ohta, S. Mawaribuchi, J. Jenkins, J. Grimwood, J. Schmutz, T. Mitros, S. V. Mozaffari, Y. Suzuki, Y. Haramoto, T.S. Yamamoto, C. Takagi, R. Heald, K. Miller, C. Haudenschild, J. Kitzman, T. Nakayama, Y. Izutsu, J. Robert, J. Fortriede, K.

- Burns, V. Lotay, K. Karimi, Y. Yasuoka, D.S. Dichmann, M.F. Flajnik, D.W. Houston, J. Shendure, L. DuPasquier, P.D. Vize, A.M. Zorn, M. Ito, E.M. Marcotte, J.B. Wallingford, Y. Ito, M. Asashima, N. Ueno, Y. Matsuda, G.J.C. Veenstra, A. Fujiyama, R.M. Harland, M. Taira, and D.S. Rokhsar. 2016. Genome evolution in the allotetraploid frog *Xenopus laevis*. *Nature*. 538:336–343. doi:10.1038/nature19840.
- Shiokawa, K., R. Kurashima, and J. Shinga. 1994. Temporal control of gene expression from endogenous and exogenously- introduced DNAs in early embryogenesis of *Xenopus laevis*. *Int. J. Dev. Biol.* 38:249–255. doi:10.1387/ijdb.7526881.
- Shono, N., J.I. Ohzeki, K. Otake, N.M.C. Martins, T. Nagase, H. Kimura, V. Larionov, W.C. Earnshaw, and H. Masumoto. 2015. CENP-C and CENP-I are key connecting factors for kinetochore and CENP-A assembly. *J. Cell Sci.* 128:4572–4587. doi:10.1242/jcs.180786.
- Shukla, M., P. Tong, S.A. White, P.P. Singh, A.M. Reid, S. Catania, A.L. Pidoux, and R.C. Allshire. 2018. Centromere DNA Destabilizes H3 Nucleosomes to Promote CENP-A Deposition during the Cell Cycle. *Curr. Biol.* 28:3924-3936.e4. doi:10.1016/j.cub.2018.10.049.
- Sim, J., C.E. Park, I. Cho, K. Min, J.-S. Lee, Y. Chong, J. Kim, J.S. Kang, K.D. Piatkevich, E.E. Jung, S.-K. Kwon, Y.-G. Yoon, E.S. Boyden, and J.-B. Chang. 2021. Whole-ExM: Expansion microscopy imaging of all anatomical structures of whole larval zebrafish. *bioRxiv*. 2021.05.18.443629.
- Smith, O.K., C. Limouse, K.A. Fryer, N.A. Teran, K. Sundararajan, R. Heald, and A.F. Straight. 2021. Identification and characterization of centromeric sequences in *Xenopus laevis*. *Genome Res.* 31:958–967. doi:10.1101/gr.267781.120.
- Stellfox, M.E., A.O. Bailey, and D.R. Foltz. 2013. Putting CENP-A in its place. *Cell. Mol. Life Sci.* 70:387–406. doi:10.1007/s00018-012-1048-8.
- Swartz, S.Z., L.S. McKay, K.-C.C. Su, L. Bury, A. Padeganeh, P.S. Maddox, K.A. Knouse, and I.M. Cheeseman. 2019. Quiescent Cells Actively Replenish CENP-A Nucleosomes to Maintain Centromere Identity and Proliferative Potential. *Dev. Cell.* 51:35-48.e7. doi:10.1016/j.devcel.2019.07.016.
- Tang, S., and D.C. Presgraves. 2009. Evolution of the Drosophila Nuclear Pore Complex Results in Multiple Hybrid Incompatibilities. *Science (80-. ).* 7:779–782.
- Terradas, M., M. Martín, L. Tusell, and A. Genescà. 2009. DNA lesions sequestered in micronuclei induce a local defective-damage response. *DNA Repair (Amst)*. 8:1225–34. doi:10.1016/j.dnarep.2009.07.004.
- Thomae, A.W., G.O.M. Schade, J. Padeken, M. Borath, I. Vetter, E. Kremmer, P. Heun, and A. Imhof. 2013. A Pair of Centromeric Proteins Mediates Reproductive Isolation in Drosophila Species. *Dev. Cell.* 27:412–424. doi:10.1016/j.devcel.2013.10.001.
- Tian, T., X. Li, Y. Liu, C. Wang, X. Liu, G. Bi, X. Zhang, X. Yao, Z.H. Zhou, and J. Zang. 2018. Molecular basis for CENP-N recognition of CENP-A nucleosome on the human kinetochore. *Cell Res.* 28:374–378. doi:10.1038/cr.2018.13.
- Tillberg, P.W., F. Chen, K.D. Piatkevich, Y. Zhao, C.-C. (Jay) Yu, B.P. English, L. Gao, A. Martorell, H.-J. Suk, F. Yoshida, E.M. DeGennaro, D.H. Roossien, G. Gong, U. Seneviratne, S.R. Tannenbaum, R. Desimone, D. Cai, and E.S. Boyden. 2016. Protein-retention expansion microscopy of cells and tissues labeled using standard



- fluorescent proteins and antibodies. *Nat. Biotechnol.* 34:987–992. doi:10.1038/nbt.3625.
- Tranfield, E.M., X. Heiligenstein, I. Peristere, and C. Antony. 2014. Correlative light and electron microscopy for a free-floating spindle in *Xenopus laevis* egg extracts. 124. 1st ed. Elsevier Inc. 111–128 pp.
- Vastag, L., P. Jorgensen, L. Peshkin, R. Wei, J.D. Rabinowitz, and M.W. Kirschner. 2011. Remodeling of the metabolome during early frog development. *PLoS One.* 6. doi:10.1371/journal.pone.0016881.
- Vukusic, K., R. Buda, B. Agneza, A. Milas, N. Pavin, and I.M. Tolic. 2017. Microtubule Sliding within the Bridging Fiber Pushes Kinetochore Fibers Apart to Segregate Chromosomes. *Dev. Cell.* 43:11–23. doi:10.1016/j.devcel.2017.09.010.
- Walczak, C.E., I. Vernos, T.J. Mitchison, E. Karsenti, and R. Heald. 1998. A model for the proposed roles of different microtubule-based motor proteins in establishing spindle bipolarity. *Curr. Biol.* 8:903–13. doi:10.1016/S0960-9822(07)00370-3.
- Warsinger-Pepe, N., D. Li, and Y.M. Yamashita. 2020. Regulation of nucleolar dominance in *Drosophila melanogaster*. *Genetics.* 214:991–1004. doi:10.1101/690198.
- Weir, J.R., A.C. Faesen, K. Klare, A. Petrovic, F. Basilico, J. Fischböck, S. Pentakota, J. Keller, M.E. Pesenti, D. Pan, D. Vogt, S. Wohlgemuth, F. Herzog, and A. Musacchio. 2016. Insights from biochemical reconstitution into the architecture of human kinetochores. *Nature.* 537:249–253. doi:10.1038/nature19333.
- Wellauer, P.K., and R.H. Reeder. 1975. A Comparison of the Structural Organization of Amplified Ribosomal DNA from *Xenopus mulleri* and *Xenopus laevis*. *J. Mol. Biol.* 94:151–61.
- Westhorpe, F.G., and A.F. Straight. 2014. The Centromere: Epigenetic Control of Chromosome Segregation during Mitosis. *Cold Spring Harb. Perspect. Biol.* 7:1–26. doi:a015818.
- Wilbur, J.D., and R. Heald. 2013. Mitotic spindle scaling during *Xenopus* development by *kif2a* and importin  $\alpha$ . *Elife.* 2013:1–17. doi:10.7554/eLife.00290.
- Wong, L.H., K.H. Brettingham-Moore, L. Chan, J.M. Quach, M.A. Anderson, E.L. Northrop, R. Hannan, R. Saffery, M.L. Shaw, E. Williams, and K.H.A. Choo. 2007. Centromere RNA is a key component for the assembly of nucleoproteins at the nucleolus and centromere. *Genome Res.* 17:1146–1160. doi:10.1101/gr.6022807.
- Woodland, H.R., and J.E.M. Ballantine. 1980. Paternal gene expression in developing hybrid embryos of *Xenopus laevis* and *Xenopus borealis*. *J. Embryol. Exp. Morphol.* 60:359–372.
- Wühr, M., Y. Chen, S. Dumont, A.C. Groen, D.J. Needleman, A. Salic, and T.J. Mitchison. 2008. Evidence for an Upper Limit to Mitotic Spindle Length. *Curr. Biol.* 18:1256–1261. doi:10.1016/j.cub.2008.07.092.
- Yanai, I., L. Peshkin, P. Jorgensen, and M.W. Kirschner. 2011. Mapping gene expression in two *Xenopus* species: evolutionary constraints and developmental flexibility. *Dev. Cell.* 20:483–96. doi:10.1016/j.devcel.2011.03.015.
- Yu, C.J., N. Barry, A.T. Wassie, A. Sinha, F. Chen, G. Haspel, M.B. Goodman, and E.S. Boyden. 2020. Expansion microscopy of *C. elegans*. *Elife.* 9:1–78.
- Zhang, C.Z., A. Spektor, H. Cornils, J.M. Francis, E.K. Jackson, S. Liu, M. Meyerson, and D. Pellman. 2015. Chromothripsis from DNA damage in micronuclei. *Nature.*

522:179–184. doi:10.1038/nature14493.

Zheng, Y., M.L. Wong, B. Alberts, and T. Mitchison. 1995. Nucleation of microtubule assembly by a  $\gamma$ -tubulin-containing ring complex. *Nature*. 378:578–583.